



**Ultrasonic instrument for accurate measurements of spatial parameters
in blood vessels**

Mohammad H. Mani, MEng

**Thesis submitted to the University of Nottingham
for the degree of Doctor of Philosophy**

May 2016

Abstract

The present research is aimed at the development of an ultrasonic medical instrument capable of measuring the intima-media thicknesses (IMT) of artery walls that are considered by medical practitioners as good indicators of the risk of atherosclerosis. This overcomes two notable limitations of the instruments available at present – insufficient axial resolution and lack of synchronisation to the heart cycle that make the measurements difficult to use, e.g., for annual screening of patients and like-for-like comparisons. These limitations were addressed by using a combination of on-the-fly averaging and interleaved sampling for acquiring echo waveforms, and triggering the scans at a particular instant of the heart cycle.

The developed electronic instrumentation consisted of a battery powered electrocardiogram (ECG) monitor that transmitted the ECG data using an infrared link to the ECG processor that triggered the scans. Such architecture eliminated any possibility of accidentally connecting the patient to a source of voltage capable of causing serious injury and of causing radio frequency interference to medical equipment located in a close proximity. The algorithm for detecting the R-waves from noisy ECGs was fully verified with simulated and experimental ECG records, and implemented in firmware on board the ECG processor. The rate of R-wave detection of the developed algorithm is 88.24% out of 204 heartbeats recorded.

In order to ease the interpretation of the recorded echoes, both mathematical and physical simulations of tubular objects were carried out. The calculated resolution of the system was estimated 2.5 μ m. Spatial resolution of 15 μ m was achieved during the in-vivo experiments. Some of the factors that might have caused this difference have been discussed with suggestions on possible methods of improvements.

The set of experimental waveforms recorded in vivo demonstrated the correct operation of the developed instrument, appropriate consistency and some features that were expected and described in the literature. The developed instrument seems ready for application to a broader group of subjects.

Publications

1. M.Mani, A.N.Kalashnikov, "In vivo verification of an intelligent system for accurate measurement of intima-media thicknesses", *In: Advanced information systems and technologies (AIST-2013)*, Sumy, Ukraine, 2013, pp.124-127.
2. He Yin, M. Mani, O. Sonbul, A.N. Kalashnikov, "Measurement time as a limiting factor for the accurate acquisition of repeatable waveforms", *IEEE international conference on Intelligent Data Acquisition and Advanced Computing Systems*", Berlin, Germany, 2013, 4 p., in press.
3. M.Mani, A.N. Kalashnikov, "Intelligent system for accurate measurement of intima-media thickness as markers of atherosclerosis", in: *Advanced information system and technologies (AIST-2012)*, Sumy, Ukraine, 2012, pp.180 – 183.
4. E.Otoakhia, T.Jenmanachaiyakun, A.Afaneh, S.Alzebda, M.Mani, O.Sonbul, A.Kalashnikov, "Embedded web server for remote laboratory access for undergraduate students studying electronic engineering", in: *2011 IEEE International Symposium on Circuits and Systems*, Rio de Janeiro, Brazil, pp.337-340.
5. O. Bener, M. Mani, O. Sonbul, A. Bener, A. Kalashnikov, "Intrinsically safe and RF interface free device for synchronisation of ultrasonic scans with the heart activity", In *4th International conference Sensor Electronics and Microsystems Technology*" (SEMST-4), Odessa, Ukraine, 2010, p.133.

Presentations

1. "Measurement time as a limiting factor for the accurate acquisition of repeatable waveforms", oral, IEEE international conference on Intelligent Data Acquisition and Advanced Computing Systems, Berlin, Germany, September 2013, presented by Dr Sonbul.
2. "In vivo verification of an intelligent system for accurate measurement of intima-media thicknesses", oral, Advanced information systems and technologies AIST-2013, Sumy, Ukraine, May 2013.
3. "Intelligent system for accurate measurement of intima-media thickness as markers of atherosclerosis", oral, Advanced information system and technologies AIST-2012, Sumy, Ukraine, May 2012.
4. "Embedded web server for remote laboratory access for undergraduate students studying electronic engineering", oral, 2011 IEEE International Symposium on Circuits and Systems, Rio de Janeiro, Brazil, May 2011, presented by Dr Kalashnikov.
5. "Novel instrumentation for accurate measurement of the thickness of blood vessels in vivo", poster, Transitional imaging priority, University of Nottingham, UK, April 2011.
6. "Synchronization of vascular ultrasonic scans with heart activity using ECG signals", PhD poster presentations, University of Nottingham, UK, October 2010.
7. "Intrinsically safe and RF interface free device for synchronisation of ultrasonic scans with the heart activity", oral, 4th International conference "Sensor Electronics and Microsystems Technology" (SEMST-4), Odessa, Ukraine, June-July 2010, presented by Dr Kalashnikov.

Acknowledgments

I would like to express my gratitude and appreciation to my supervisor, Dr. Alexander Kalashnikov, for giving me the opportunity, his selfless help and guidance throughout this PhD.

I would like to thank my second supervisor, Prof. Barrie Hayes-Gill, for his support and useful suggestions during my PhD.

I would also like to thank my parents and my brother for providing me with the chance to do my PhD; for their support and help during all these years.

Finally, thanks should go to all the colleagues at the Ultrasonic laboratory at the University of Nottingham Electrical and Electronic Engineering department, for all their motivations, help and support over the years.

Contents

1.1 - Cardiovascular system and its operation	1
1.1.1 - Purpose of the cardiovascular system.....	1
1.1.2 - Operation of the heart	3
1.1.3 - Abnormalities in the cardiovascular system	3
1.2 - Atherosclerosis and its diagnosis.....	4
1.3 - Intima media Thickness as marker for atherosclerosis	5
1.4 - Ultrasound measurement of the IMT	7
1.5 - Significant causes of uncertainty in conventional IMT measurements.....	9
1.5.1 - IMT variation during the heart cycle	9
1.5.2 -Resolution of ultrasonic scans	11
1.6 - Prior developments in the applied ultrasonic research group.....	13
1.6.1 - High accuracy and high speed ultrasound acquisition	13
1.6.2 - O. Benner’s MPhil	16
1.7 - Aims and Objectives.....	17
1.7.1 - Aim	17
1.7.2 - Objectives	18
1.8 - Thesis structure.....	18
1.8.1 - Development of a wireless ECG Monitor	18
1.8.2 - Development of triggering algorithm for ultrasonic scans	19
1.8.3 - Experimental study of reflections from tubular objects	20
1.8.4 - Development of in vivo experimental protocol and system verification	20
References	22
2.1 - Development of the wireless link between the ECG monitor and processor	29
2.1.1 - Selection of the wireless link technology	29

2.1.2 –Development of the IR link	35
2.1.2.1 – Selection of the modulation scheme	35
2.1.2.2 – Infrared transceivers.....	35
2.2 – Operation and implementation of the ECG Monitor	38
2.2.1 - Relation of electrocardiogram to the cardiac cycle.....	38
2.2.2 - Experimental recording of an ECG.....	40
2.2.2.1 - Placement of the ECG electrodes.....	40
2.2.2.2 - ECG leads	40
2.2.2.3 - Signal to Noise Ratio (SNR)	44
2.2.3 - Commercial ECG Monitors.....	44
2.2.4 - Analysis of ECG monitor Schematics	46
2.2.5 - Development of the schematic for the custom ECG monitor	48
2.2.5.1 - Design of the analogue section	49
2.2.5.2 - Selection of the instrumentation amplifiers.....	53
2.2.6 – Implementation of the ECG monitor.....	55
2.2.6.1 –PCB design	57
2.3 – Conclusions and summary	60
References	62
3.1 – Requirements of the ECG Processor	66
3.2 – ECG Processor development.....	67
3.2.1 – First prototype	67
3.2.2 – Level converter design	71
3.2.2.1 – ECG processor to DAQ level converter	71
3.2.2.2 – DAQ to UPR amplifier level converter	75
3.2.3 – Final design of the ECG processor.....	76
3.3 – Establishing and debugging the IR link	79
3.4 – Development and testing of the algorithm for triggering the ultrasonic scans.....	81

3.4.1 – Simulating an ECG signal	81
3.4.2 – Detection of the R-wave.....	82
3.4.2.1 – Methodology	82
3.4.2.2 – R-wave detection algorithm with static threshold	85
3.4.2.3 – Use of time stamps	86
3.4.2.4 – Experimental verification	87
3.4.2.5 – Adaptive calculation of the threshold	87
3.4.2.6 – Operating procedures of the ECG processor	94
3.4.2.7 – Using a potentiometer to set the post R-wave delay.....	95
3.5 – Conclusion	98
References	101
4.1. Methodology of physical modelling.....	103
4.2 - Commissioning of the test rig	105
4.2.1 – Purpose and requirements.....	105
4.2.2 – Test rig components	106
4.2.2.1 – The container	107
4.2.2.2 – Phantom clamp	107
4.2.2.3 – Transducer holder.....	108
4.3 - Experimental Procedure	110
4.3.1 – Software parameters	111
4.3.2 – Test rig settings	112
4.3.3 – Preliminary experiments	113
4.4 – Experimental records for the phantom experiments	117
4.4.1 – Phantom 1.....	118
4.4.2 – Phantom 2.....	121
4.4.3 – Phantom 3.....	124
4.4.2 – Verification of the results.....	126
4.5 – Conclusion	133

References	136
5.1 - Experimental protocol	139
5.1.1 - Connection diagram for the instrumentation.....	139
5.1.2 - Setting up the ECG instrumentation	141
5.1.3 - Setting up the ultrasonic scanner.....	144
5.1.4 - Getting appropriate ultrasonic A-scan.....	149
5.1.4.1 - Identification of the transducer elements	149
5.1.4.2 - Placement of the transducer on the neck of the patient.....	151
5.1.4.3 - Selecting the right transducer for a complete <i>in vivo</i> measurement session.....	154
5.1.5 - Collecting a set of waveforms for an <i>in vivo</i> measurement session ..	156
5.1.6 - Protocol summary	158
5.2 - Check for consistency of the acquired records	158
5.3 - Propagation delay estimation	164
5.4 - Estimation of the SNR for the recorded waveforms.....	168
5.5 - Discussion on possible improvement to experimental procedures and data processing	169
5.6 - Conclusions	170
References	172
6.1 Summery	179
6.2 - Knowledge contributions.....	180
6.2.1 - Development of the ECG Monitor.....	180
6.2.2 - Development of the ECG processor and triggering procedure	181
6.2.3 - Phantom Experiments.....	182
6.2.4 - Concluding Remarks	183
6.3 - Future Work.....	184

List of Figures

Figure 1.1 - Cardiovascular system [1.1]	1
Figure 1.2 - Three types of cells in blood [1.1].....	2
Figure 1.3 - Main chambers of the heart [1.2]	3
Figure 1.4 - Intima-media Thickness [1.20].....	6
Figure 1.5 - Responses of a 20 MHz transducer recorded with different number of averages and sampling frequency: (a) 2 averages, 80 MHz; (b) 2 averages, 2.16 GHz; (c) 512 averages, 80 MHz (d) 512 averages, 2.16 GHz [1.62, figure 9]	15
Figure 1.6 - Block diagram of the entire instrument.....	18
Figure 2.1 – Block diagram of the overall system	34
Figure 2.2 - IR link; pin connections for the ECG monitor	37
Figure 2.3 - IR link; pin connections for the ECG processor	38
Figure 2.4 - Typical ECG waveform and its different parts [2.20, Figure1]	39
Figure 2.5 - Nine lead configuration (left [2.22, figure 15.8]) and three leads configuration (right[2.22, figure 15.1]) for ECG recordings.....	41
Figure 2.6 - Developed ECG leads from PCB board and shielded cables	42
Figure 2.7 - 3rd PCB design (left) and 2nd PCB design (right) outputs	44
Figure 2.8 - Example of an ECG circuit schematic [2.24, figure 37]	47
Figure 2.9 - Example of an ECG circuit schematic [2.24, figure 36]	47
Figure 2.10 - Overall schematic	48
Figure 2.11 - Schematic of the first design	50
Figure 2.12 - First vero board assembled	50
Figure 2.13 - Schematic of the second vero board.....	51
Figure 2.14 - Assembled second vero board	52
Figure 2.15 – Block diagram of the ECG Monitor	55
Figure 2.16 - Direct connection of the right leg to the ground of the ECG monitor	56
Figure 2.17 – Low pass filter connected to the output of the instrumental amplifier	56
Figure 2.18 – Frequency response of the low pass filter shown in figure 2.19 ..	57
Figure 2.19 - MCP1640 application circuit [2.21, p.2]	58
Figure 2.20 - PCB layout of the final ECG monitor	59

Figure 2.21 - Third PCB assembled.....	59
Figure 2.22 - ECG taken from commercial machine (top) and experimentally taken ECG (bottom, y-axis in mV, x-axis in mS)	60
Figure 3.1 - Block diagram of the ECG processor.....	66
Figure 3.2 – Converting voltage levels in the ECG processor.....	66
Figure 3.3 – Block diagram of the first design of the ECG processor.....	68
Figure 3.4 - USB pin out	69
Figure 3.5 - PCB of the first ECG processor.....	70
Figure 3.6 - First ECG processor assembled.....	70
Figure 3.7 - Schematic of 5V to 1V amplifier.....	72
Figure 3.8 - Breadboard design for the ECG processor to DAQ level converter .	72
Figure 3.9 -Assembled on a breadboard ECG processor to DAQ level converter	73
Figure 3.10 - EAGLE design of the ECG processor to DAQ level converter	74
Figure 3.11 - Schematic of the DAQ to UPR level converter	75
Figure 3.12 - Breadboard design of the DAQ to UPR level converter	75
Figure 3.13 – Assembled on a breadboard DAQ to UPR level converter	76
Figure 3.14 Operation of the DAQ to UPR level conversion (red curve – input signal from the PicoScope, blue curve – output signal to the UPR).....	76
Figure 3.15 – Block diagram of the final design of the ECG processor	77
Figure 3.16 - PCB layout of the final ECG processor board.....	78
Figure 3.17 - Assembled second ECG processor board	78
Figure 3.18 - FS USB board with IR transmitter module (left - shown separately, right - shown connected)	79
Figure 3.19 - Microchip IR transmitter/receiver board connected to a PC.....	80
Figure 3.20 - Effect of different levels of noise on the simulated ECG.....	82
Figure 3.21 - Simulation of the R wave detection (calculated threshold is shown starting from the sample 1000; the triggers are shown by low value horizontal lines) – X-axis represents sample number and the Y-axis is in mV	86
Figure 3.22 - Experimental ECG with trigger 0 to 20 seconds (amplitude in mV vs time in mS).....	87
Figure 3.23 - 60s Experimentally recorded ECG	88
Figure 3.24 - Results of processing experimental data in MATLAB for R-wave detection	89
Figure 3.25 - Calculation of moving average threshold (red curve) using the accumulator	90

Figure 3.26 - Simulation of the R-wave detection using re-calculated threshold	90
Figure 3.27 - Operation of the ECG monitor with re-calculated threshold (red line – ECG, blue line – narrow time markers and wider trigger events)	91
Figure 3.28 - Experimental ECG (red curve) and the ECG processor output (blue line) with all the debugging information	91
Figure 3.29 - Experimental test with threshold calculation and R-wave detection	92
Figure 3.30 - Experimental test with threshold calculation and R-wave detection	92
Figure 3.31 - Experimental test with threshold calculation and R-wave detection	93
Figure 3.32 - Resetting the ECG Monitor (blue curve – ECG trace before digitization in the ECG monitor, red curve – output trigger signal of the ECG processor).....	94
Figure 3.33 – LED indicates that DelayFactor equates to 3	96
Figure 3.34 - ECG trace used for verifying set delays.....	97
Figure 4.1 - Schematic of different parts of the experiment setup (1 – supporting legs, 2 – tube holders, 3 – test tube, 4 – test tank).....	106
Figure 4.2 - Test cell and transducer rails.....	107
Figure 4.3 - Tube holders.....	108
Figure 4.4 - Transducer holder.....	108
Figure 4.5 - Assembled setup with a phantom and transducer	109
Figure 4.6 - Different positions of the transducer relative to the centre relative to the cross-section view of the tube.....	110
Figure 4.7 – Software parameters for phantom experiments.....	111
Figure 4.8 - Reflections from a flattened piece of an ABS plastic tube shown at different scales	114
Figure 4.9 - Reflections from the original ABS tube.....	116
Figure 4.10 - An illustration to possibility of appearance of additional echoes in the recorded waveforms	117
Figure 4.11 – Cross section of phantom 1	118
Figure 4.12 - Cross section of phantom 2.....	121
Figure 4.13 - Cross section of phantom 3.....	124

Figure 4.14 - Waveform collected for the second phantom at the centre during the morning, afternoon and evening examinations (from the top to the bottom respectively)	128
Figure 4.15 - Waveforms recorded for different phantoms at position 16 (top – for the tube 1, middle and bottom – for the tube 2)	130
Figure 4.16 - Reflections and reverberations from the phantom	132
Figure 4.17 - An experimental waveform used for the acoustic impedance evaluation of the phantom	132
Figure 5.1 - Interconnection of custom build, previously developed and off the shelf instruments used for in vivo measurements (1 – patient; 2 – electrodes (right arm RA, left arm LA and right leg RL); 3 – ECG monitor; 4 – ECG processor; 5 – Oscilloscope; 6 – Personal Computer; 7 – DAQ Board on the PC; 8 – ultrasonic pulser receiver (UPR); 9 – ultrasound transducer).....	140
Figure 5.2 - Photograph of the setup for an experiment (1 – patient; 2 – ECG electrodes connector; 3 – ECG monitor; 4 – ECG processor; 5 – Oscilloscope; 6 – conductive gel for the ECG electrodes; 7- coupling gel for the ultrasound transducer).....	141
Figure 5.3 - Output signal of the ECG front end showing rapid increase	142
Figure 5.4 - Output signal of the ECG front end showing unacceptable increase in noise	143
Figure 5.5 - Placement, connections and indicators for the ECG instrumentation	144
Figure 5.6 - Screenshot of the control panel	145
Figure 5.7 - Operation of the level converter on the ECG processor board (blue trace – input from the DAQ board, red trace- output to the UPR)	147
Figure 5.8 - UPR setup window	147
Figure 5.9 - Trigger signal at the input of the UPR and the excitation pulse it produces.....	148
Figure 5.10 - Photograph of the transducer and its mating connector (1 - transducer’s head, 2 and 4 – transducer’s connecting pins, 3 – mating connector to the transducer)	149
Figure 5.11 - Experimentally determined pin-out of the transducer (0 denotes grounded pins, red cells with crosses showed either unused pins or connections to malfunctioning elements, numbers in the green cells relate to the order of the elements placement from one side of the transducer’s head).....	150

Figure 5.12 - Aluminium prism used to determine positions of array elements	151
Figure 5.13 - Examples of ultrasonic array placements for taking RCA scans .	152
Figure 5.14 - Photographs of the subject and equipments taken during in vivo measurement session	153
Figure 5.15 - An example of experimental waveform and its relation to arterial interfaces [5.15, figure 1]	155
Figure 5.16 - Pins of the array's mating connector were connected to the UPR using	156
Figure 5.17 - Setting and conditions for IMT measurement.....	157
Figure 5.18 - Three valid waveforms recorded for session 1, delay 1 that show no consistency.....	159
Figure 5.19 - Session 4 - Delay 4 ; First record.....	160
Figure 5.20 - Session 4 - Delay 4 ; Second record.....	160
Figure 5.21 - Session 4 - Delay 4; Third record.....	160
Figure 5.22 - Session 4 - Delay 4; Fourth record.....	160
Figure 5.23 - Session 4 - Delay 4; Fifth record.....	161
Figure 5.24 - Five consistent valid waveforms recorded for session 4, delay 4 [5.18].....	162
Figure 5.25 - Additional reflections in the recorded waveforms at around 10.5 and 15 μ s	163
Figure 5.26 - Distances measured from the printouts for the propagation delays estimation.....	165
Figure 5.27 - Recorded waveforms for session 4, delay 1 with markers.....	166
Figure 5.28 - Recorded waveforms for session 4, delay 2 with markers.....	166
Figure 5.29 - Recorded waveforms for session 4, delay 3 with markers.....	166
Figure 5.30 - Recorded waveforms for session 4, delay 4 with markers.....	166
Figure 5.31 - Reduction of the ECA diameter from the bulb to the point of measurement (background image taken from [5.20, figure 507])	167
Figure 5.32 - A typical cardiovascular behaviour of the arterial pressure and ECG signal [5.21]. Vertical lines depict time instants when the echo waveforms could have been taken to result in the estimated propagation delays.	168

List of Tables

Table 2.1 - Number of affected pacemakers [2.18].....	31
Table 2.2 - Number of affected implantable cardiac defibrillators (ICDs)	32
Table 2.3 - Test results: interference from 0.6 W analogue mobile phones [2.9]	33
Table 2.4 - Infrared Encoder/decoder	36
Table 2.5 - SNR comparison of the 2nd and final prototypes tested using commercial and developed electrodes.....	43
Table 2.6 - A list of some commercially available ECG monitors	45
Table 2.7 - Different OPAMPS available for ECG measurements (data taken from respective datasheets).....	54
Table 3.1 - Purposes of the USB socket pins	69
Table 3.2 - Changes in the post R-wave delays for different positions of the potentiometer's dial	97
Table 4.1 - Waveforms recorded for phantom 1.....	120
Table 4.2 - Waveforms recorded for phantom 2	123
Table 4.3 - Waveforms recorded for phantom 3	125
Table 5.1 - Consistency analysis for recorded waveforms at different sessions with different delays (number of valid records / number of consistent records)	164
Table 5.2 - Measured lengths and estimated ultrasound propagation delays ..	166
Table 5.3 - SNR calculation of the system	168

1 - Introduction

1.1 - Cardiovascular system and its operation

1.1.1 - Purpose of the cardiovascular system

The cardiovascular system consists of many parts such as the heart, arteries and veins. It functions as the network connecting all the parts of a body together to enable essential body functions. The heart pumps blood around the body. Blood transports vital materials (such as nutrients and dissolved oxygen), messages (hormones) and blood cells to all the body organs (figure 1.1). Arteries transport oxygenated blood whilst veins deal with de-oxygenated blood.

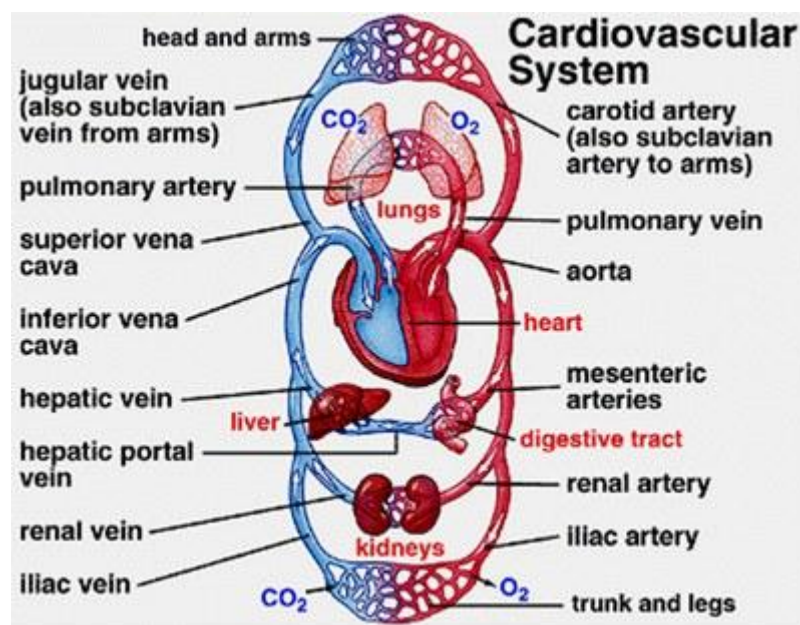


Figure 1.1 - Cardiovascular system [1.1]

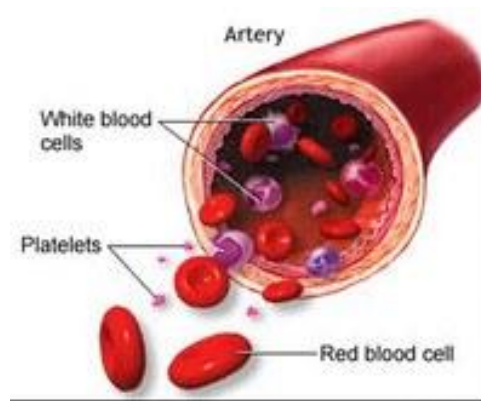


Figure 1.2 - Three types of cells in blood [1.1]

There are three types of cells in blood (figure 1.2):

- white blood cells detect and kill foreign bodies or infections, helping the immune system to fight infections effectively and efficiently;
- red blood cells are the carriers of the oxygen. When blood goes through the lungs, oxygen binds with a protein inside the red blood cells and is then consumed throughout the body;
- Platelets are the cells that stick to any cuts in the arteries, healing internal or external cuts. “In addition to being the cellular effector of hemostasis [1.1], platelets are rapidly deployed to sites of injury or infection, and potentially modulate inflammatory processes by interacting with leukocytes [1.2] and by secreting cytokines [1.3], chemokines [1.4], and other inflammatory mediators”.

The cardiovascular system also acts as the temperature regulator in the body. When the core temperature deviates from the healthy range, the blood flow is re-directed either to the surface of skin (in the case of increased temperature) or away from the skin (in the case of decreased temperature) to maintain the constant temperature of most important organs [1.5].

1.1.2 - Operation of the heart

The human heart consists of four main chambers shown in figure 1.3:

- Left Atrium
- Right Atrium
- Left Ventricle
- Right Ventricle

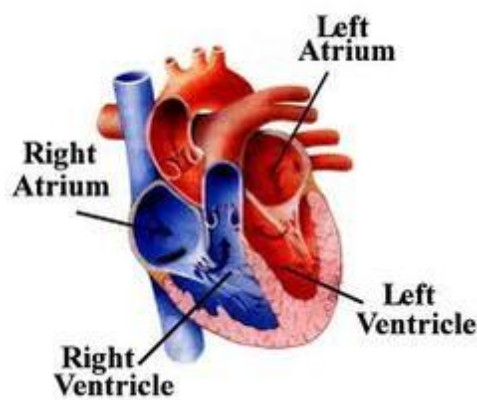


Figure 1.3 - Main chambers of the heart [1.2]

The upper chambers are the blood inlets to the heart. The left atrium is connected to the lungs; blood enriched with oxygen enters the left atrium whilst de-oxygenated blood from the veins enters the right atrium. When both atriums are full, the top side of the heart contracts and pushes the blood into the ventricles. The left ventricle is connected to the aorta, the largest artery in the body [1.3] which distributes the blood to all the other arteries. The right ventricle pushes de-oxygenated blood through the lungs, with blood enriched with oxygen. The left ventricle collects enriched blood from the lungs [1.4, 1.5].

1.1.3 - Abnormalities in the cardiovascular system

Some abnormalities can be caused by the heart itself, such as arrhythmia or abnormal heart beat [1.6]. A major abnormality is chronic heart failure,

where, due to damage to the left ventricle's muscle the heart is not able to pump blood to other parts of the body [1.7]. Some abnormalities relate to the delivery of blood, e.g. chronic venous insufficiency, where the blood cannot be sent back to the heart from the lower limbs [1.8]; symptomatic congenital heart disease, when abnormalities in the heart itself or important veins disturb the cardiovascular system operation [1.9]; and atherosclerosis related to increases in arterial thickness that partially blocks the blood flow [1.10].

1.2 – Atherosclerosis and its diagnosis

“Atherosclerosis (also known as arteriosclerotic vascular disease or ASVD) is a condition in which an artery wall thickens, as a result of a build-up of fatty materials such as cholesterol. It is caused by the formation of multiple plaques within the arteries” [1.10].

“Atherosclerosis typically begins in early adolescence, and is usually found in most major arteries, yet is asymptomatic and not detected by most diagnostic methods during life. According to United States data for the year 2004, for about 65% of men and 47% of women, the first symptom of atherosclerotic cardiovascular disease is heart attack or sudden cardiac death (death within one hour of onset of the symptom). Most artery flow disrupting events occur at locations with less than 50% lumen narrowing (~20% stenosis is average)” [1.11] Stenosis is defined as abnormal narrowing of blood vessels [1.12].

Traditionally, atherosclerosis was diagnosed using angiography (dissolution in the blood of a contrast agent visible in X-rays, and taking an X-ray image of the arteries in question [1.13]), or stress testing (making the cardiac system work harder than usual by physical exercise or drugs [1.14]). Angiography does not provide the resolution required, and exposes the patient to X-rays that are disadvantageous. Stress testing provides useful information at the last stages of atherosclerosis, only with narrowing of about 75% or greater. That is why other methods are being developed actively.

Newer methods are divided into anatomic ones that use medical instrumentation and imaging, and physiologic ones that are based on chemical analysis.

Examples of anatomic methods include coronary calcium scoring by computer tomography (CT), carotid IMT (intimal media thickness) measurement by ultrasound, and intravascular ultrasound (IVUS) [1.14].

A study by A. F. Kopp et al [1.15] showed that, by using a CT scan, it was possible to detect over 50% stenosis of 102 patients. The CT scan machine that was used in the study provided only 3mm resolution for 3D imaging. The method involved taking 3D images combined with angiography for stenosis measurement in patients.

Another research by L. Kaufman [1.16] reports spatial resolutions ranging from 1 to 1.7mm that has been reached in phantom simulations, using various CT scanners. In this study, aluminium wires were submerged in water to measure the spatial resolution of CT scanners to be used for coronary calcium scoring. The results showed that the scanners' operation could change over time. For this reason a standard spatial resolution should be considered for CT scanners for the calcium scoring purpose. Additionally, post-processing corrections may be required for accurate and consistent measurements.

Physiologic methods, such as Thermal Heterogeneity [1.17] are less expensive and safer compared to Anatomic Methods. These methods cannot detect the disease; however, they show its progression. However, they lack the accuracy of the anatomic methods, thus cannot be used for early detection of atherosclerosis.

1.3 – Intima media Thickness as marker for atherosclerosis

The thickness of the two inner artery layers, tunica intima and tunica media, is called the intima-media thickness (IMT, shown in figure 1.4) and can be used as a marker to detect and monitor the progression of atherosclerosis

[1.18, 1.19]. Figure 1.4 shows some examples of the IMT and lumen diameter changes comparing to the normal case.

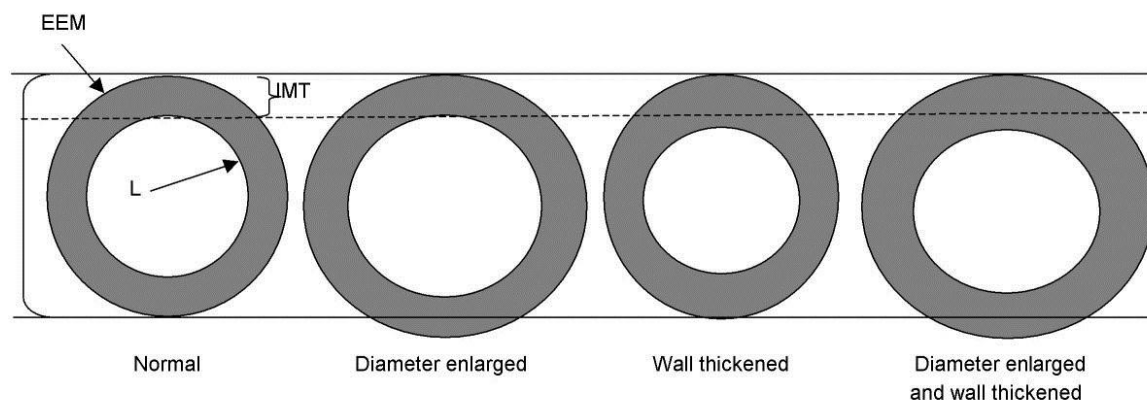


Figure 1.4 - Intima-media Thickness [1.20]

Changes in IMT are affected by a variety of different factors such as gender, age and general health of the patients. A study by Michiel L. Bots and Albert Hofman has shown that the thickness of the arterial wall does increase adaptively as the subject gets older. This is to keep the blood pressure inside the artery constant, representing a response to shear stress on the artery [1.21]. This change however, is only considered adaptive due to age factor for IMTs up to 1.1mm. Beyond this point, the thickening occurs more rapidly and represents the presence of atherosclerosis [1.21]. During the early stages of atherosclerosis, IMT increases to prevent the lumen from getting smaller in diameter. This phenomenon will result in an increase of the artery size [1.22].

Measuring the IMT, however, only helps in the detection and progression of atherosclerosis in the overall cardiovascular system, and will not detect the exact point at which the artery is getting blocked. Thickening of the IMT is an adaptive response to a change in the blood pressure in the artery [1.23-1.25]. Therefore, measuring the IMT can only be used as the marker for the presence of atherosclerosis and its effect on the blood flow in the body. According to a study by M.L. Bots et al. [1.25] when the IMT in the Common Carotid Artery (CCA) is greater than 0.89 mm, its value can be used as a good predictor of low priority arterial diseases. In this study, the ankle-arm index was used to monitor the association between the IMT increase and atherosclerosis. Ankle-arm index is the ratio of the systolic blood pressure at the lower leg, to systolic blood pressure at the arm (P_{leg}/P_{arm}). Reduction in P_{leg} would then result in the

reduction of the ankle-arm index, which is a sign of blocked artery somewhere in the body. M.L. Bots [1.25] found out that the increase in IMT is directly connected to the reduction in the ankle-arm index, which proved a connection between thickening of the artery wall to atherosclerosis.

It is very important to consider all the factors that may cause changes in IMT, as some of them may not be related to any cardiovascular disease. Factors such as age [1.24, 1.27, 1.28], smoking [1.29, 1.30] and high blood pressure [1.24] all have notable effect on increased IMT.

1.4 – Ultrasound measurement of the IMT

Since the importance of the IMT measurement with regard to diagnosis of atherosclerosis, was accepted by the medical community, there have been many studies to develop methods for reliable and consistent IMT measurements. As most of main arteries in the human body are not easily accessible, it is necessary to find methods to measure the IMT in vivo using superficial (i.e. located close to the skin) arteries. This can be achieved using ultrasound examination of common carotid (CCA), external carotid (ECA) and internal carotid (ICA) arteries. As a result, ultrasound scans became very common in the field of cardiovascular disease detection, when there was a need to measure the thickness of an artery wall.

One way to measure IMT is to use intravascular ultrasound (IVUS). This method uses a probe that is surgically inserted into an artery with the transducer at the tip of the probe. The transducer sends live images to the computer as the probe penetrates the artery. Two main disadvantages of IVUS outweigh its potential accuracy. These are the time required for the examination procedure, and the fact that it must be performed by trained professionals at an operating theatre. This is due to the fact that IVUS is a highly interventional procedure [1.31]. These disadvantages also lead to high cost of examination.

Using non-invasive ultrasonography is seen as a better option by the medical community, as it is considered safe, and does not have any long term side effects reported by patients [1.32]. Ultrasound waves can heat soft tissues

[1.33] and supposedly be harmful if the patient is subjected to the radiation for a long time. However, the risk of medical ultrasound scans is considered to be so low that these scans are widely used, e.g. to detect any pregnancy abnormalities [1.34].

One method of using B-mode ultrasound scans is to monitor the diameter of the artery during one complete cardiac cycle, and determine minimum and maximum values diameter of the artery. This can be used to measure the arterial stiffness, which is also considered another way to predict atherosclerosis [1.35].

Another method to use B-mode scans for IMT measurement is to apply edge detection technology to scanned images. A study by R.H. Selzer et al [1.36] showed that a computerized method, with automatic tracking of the lumen-intima and media-adventia layers, can be used for precise IMT measurements in short and long term [1.37]. Although the results from B-mode ultrasound scans and edge tracking processing were found to be reproducible [1.37] and made the IMT readings more accurate [1.38], the complexity and cost added by the edge-detection processing may make these scans unavailable to certain patients. Additionally, any image processing technologies operate individual pixels of the image, and cannot provide measurement accuracy better than the pixel size. As it is discussed below, conventional instrumentation cannot achieve pixel sizes required for confident detection of the progression of atherosclerosis.

Although Selzer et al [1.36] did improve the IMT measurement in 24 subjects by recording ECG alongside of the B-scans; the scans were not triggered based on the ECG. This means that large number of scans is required to cover a complete cardiac cycle to be able to relate the IMT to heart activity. An improvement to this approach, which was implemented in this project and explained in more details in chapter 2, is the integration of an ECG monitor with A-mode ultrasound scans. This integration means that each scan can be triggered at a specific point of the cardiac cycle.

1.5 – Significant causes of uncertainty in conventional IMT measurements

Non-invasive measurements of the IMT face two main difficulties that need to be addressed, to ensure high accuracy of the results. Addressing these issues is essentially the purpose of the present study.

1.5.1 - IMT variation during the heart cycle

As discussed in section 1.3, the IMT changes depending on the variations in the blood pressure inside the artery under examination. Some in vivo studies showed different values for this change. For the common carotid artery the average range over the heart cycle was reported as 0.037 mm in one study [1.39] and 0.041 mm in another [1.40]. As the IMT normally thickens between 10 μm to 30 μm in a year [1.39], it is very important to somehow overcome the variation in IMT during the heart cycle, returning consistent measurements for any given part of the artery.

One possible approach to overcome this issue is to use the so called 4-dimensional (4D) ultrasound scans. 4D ultrasound scans are the collection of 3D scans taken in real-time, and display them along with the time axis (sometimes along with the electrocardiogram trace). These are mostly used for scanning pregnant women, who want to see movements of their babies in the early pregnancy stages. However, this technology could also be used to measure the IMT in real-time, finding the maximum and/or minimum values from the successive scans. Real-time imaging techniques, combined with clear 3D scans of the artery, may be the most reliable solution in IMT measurements. However, this approach is not very cost-effective due to the cost of the equipment required for 4D ultrasound scans. For instance, one Mindray ultrasound scanner with 4D scan capabilities costs \$42,000 [1.41]. This amount of money is not available to all medical communities. Therefore, using this technology, despite the possible accuracy and advantages, is not feasible for all hospitals and clinics.

A second option is to synchronise the scans with the heart cycle of the patient. This option requires a heart monitor connected to the ultrasound scanner, which triggers the scans at some definitive moment of the heart cycle, providing the necessary consistency for the IMT estimates. If synchronisation between the scans and heart activity is established, then setting a fixed time delay with respect to the a.m. definitive moment for the successive scans, only allows for collecting a few representative waveforms. Otherwise, recording many ultrasonic scans with the hope that they will cover all the important phases of the heart cycle is required. An additional advantage of having scans synchronised is the lower volume of scans that need to be analysed. This is important when the analysis is performed by humans.

There are several methods to monitor the cardiac cycle with each having its own advantages and disadvantages. Some of these options include:

- Arterial Blood Pressure (ABP) (also referred to as blood pressure) is the changing pressure inside the blood vessels when the heart pumps blood throughout the body [1.42]. Blood pressure is measured at the highest value (systolic pressure) and lowest value (diastolic pressure). Systolic pressure appears near the start of the cardiac cycle [1.43]. ABP has been used to monitor the cardiac cycle non-invasively [1.44];
- Electrocardiogram (ECG): ECG is the trace of the voltage generated by the heart to produce contractions in the muscles required for each heartbeat. This voltage can be detected by placing electrodes on the skin, and gives accurate monitoring for the cardiac cycle [1.45];
- Doppler Ultrasound: in addition to the blood pressure, the blood velocity during a cardiac cycle changes as well [1.46]. Doppler Ultrasound can be used to measure the blood flow rate [1.47] and can be used to detect the cardiac motion [1.48];
- Photoplethysmogram (PPG): PPG is often taken by using a pulse oximeter, which measures the changes in the light absorption of the skin, which changes during the cardiac cycle [1.49]; in a PPG waveform each cardiac cycle is marked by a peak [1.50].

After analysing the above options for monitoring the cardiac cycle for triggering the ultrasonic scans, it was decided that Electrocardiogram was the least expensive, most reliable and easiest option to use in in this study. Although most of these approaches are non-invasive methods of detecting the cardiac cycle accurately, the ECG is the signal that is specifically generated to operate the heart in the body. Therefore, it could provide the most accurate solution for cardiac cycle monitoring. There are a number of studies that have taken advantage of the ECG triggering to get more accurate results when taking IMT measurements [1.51]. In a study by J. Meinders et al [1.52], an ECG trace was used to detect the cardiac cycle and used as a marker to trigger the ultrasound waves for the IMT measurements.

These studies and the ones similar to them have proven that the cardiac cycle, monitored by the ECG, is the most suitable marker for the IMT measurements to ensure more accurate and consistent results are obtained during each trial.

There are also commercial ultrasound scanners that have embedded ECG measurements unit to assist experimenters in taking more accurate measurements during IMT examinations. For instance, the Acuson Cypress from Simens [1.53] allows the user to monitor the cardiac cycle using ECG signal from the patient. Another example is the SonixTouch[1.54] which enables the examiner to monitor the raw ECG during examination and add a delay between the detection and triggering the ultrasound.

The combination of ECG monitoring and the high resolution system, the experiments explained and discussed in chapter 5 of this thesis achieved a relatively high accuracy in the measurements.

1.5.2 -Resolution of ultrasonic scans

When ultrasonic waves are sent from a transducer through the human body, layers formed of different tissues will interact with the waves, partially absorbing and reflecting the wave's energy. Reflections from layers of different acoustic impedance (echoes) are picked up by the ultrasound transducer, and

are used to present the results of the scans. The accuracy of localisation of any layer depends on the resolution of the ultrasound transducer used to perform the measurement. Lateral resolution is the minimum distance that can be detected between two objects that are placed perpendicularly to the axis of the transducer. This parameter is determined by the ultrasound wavelength and the dimensions of the transducer. However, it is not of high importance to this study.

Axial resolution is the minimum distance detected between two reflectors when they are placed on the axis of the transducer. Since the two artery layers of interest are located one after another on the transducer's axis, the axial resolution must be as high as possible to measure the thickness of the artery wall accurately. The axial resolution can be calculated using the following equation [1.55]:

$$\text{Axial resolution} = \frac{\text{spatial pulse length}}{2} \quad , \quad (1.1)$$

where spatial pulse length is the length of one excited pulse by the transducer. It defines the pixel size for the ultrasonic scans. The spatial pulse length is proportional to the interval between the subsequent echo samples taken in the time domain τ and the ultrasound velocity c , i.e.

$$\text{Spatial pulse length} = \tau \times c = \frac{c}{f_s} \quad (1.2)$$

where f_s is the sampling frequency.

For a typical sampling frequency of 50-100 MHz, employed by conventional ultrasonic instruments, the axial resolution is between 15-30 μm . Based on the changes in the IMT in a year mentioned in section 1.5.1 (10-15 μm per year) that is insufficient for monitoring the progression of atherosclerosis for yearly screening.

Spatial resolution is the ability to distinguish two objects separated in space. Spatial resolution of an ultrasound scanner is dependent on the transducer used. The frequency of the transducer will affect resolution which sets the minimum distance between the two objects before they will be seen as one single object. The axial resolution is also affected by the pulse length and sampling frequency. The developed system in this research project tries to

improve the axial resolution mainly by increasing the sampling rate by means explained in chapter 5 and therefore increase the accuracy of the IMT measurement using ultrasound.

1.6 – Prior developments in the applied ultrasonic research group

The development of an accurate IMT measurement instrument is a very complex task that could not be effectively tackled by a single PhD study on its own. However, there were two important preliminary developments completed in the applied ultrasonic research group described below. These were used as starting points for this study.

1.6.1 – High accuracy and high speed ultrasound acquisition

Traditional ultrasonic systems perform measurements by recording the signal reflected from the test object, and estimating the amplitude and time delay of the reflection to either form an image, or to estimate the reflector's properties non-destructively [1.56]. If the echo signal is captured several times, and noisy copies are combined together, then the Signal to Noise Ratio (SNR) of the images could increase [1.57], making them clearer and easier to interpret. However, any misalignment in the timing of the noisy copies can degrade the average [1.58]. Any noise present in addition to the signal of interest leads to increases in the uncertainty of the estimated ultrasonic parameters [1.59], and for this reason should be reduced as much as possible.

Another obstacle for achieving high accuracy waveform acquisition is related to the limitations on the sampling frequency imposed by inexpensive analogue-to-digital converters. For MHz-range frequencies, fast ADCs (flash ADCs [1.60] or pipelined ADC) require many comparators and buffers that limit the achievable sampling frequency of these parts. There are two methods to increase this sampling frequency. One possibility is to use several differently clocked "slow" ADCs and combine their output samples. This approach is adopted on chip by the vendors of the high speed digital storage oscilloscopes - DSOs (ADC interleaving, e.g., [1.60]), but result in substantial cost and size

increases when used on a PCB. Additionally, there is a need to tackle the inevitable mismatch of separate ADCs appearing when they are not implemented on the same die [1.61]. Another approach is to digitize the signal of interest many times asynchronously, measure the relative delays of individual records, and combine the recorded waveforms accordingly. Using this approach, it is possible to characterize the signal beyond the limitation of the Nyquist frequency. If the signal is repetitive, this method captures multiple instances of the signal and combines all based on their time delay. The main requirement of this method is that the signal must be repetitive, so that the ADC can capture the signal many times, independent from the external clock of the system.

This approach is called differently depending on DSO vendors, e.g., random interleaved sampling (RIS) by LeCroy [1.61a]. However it was shown that using RIS requires excessive time to collect an appropriate number of records, especially if averaging is required in addition to high sampling rate [1.61b].

Synchronous on-the-fly averaging and accurate interleaved sampling, which overcome the a.m. limitations of conventional approaches, were successfully combined in high accuracy waveform acquisition architecture developed in the applied ultrasonic laboratory of Nottingham University [1.62]. Waveforms, recorded using this architecture, show clear improvement in accuracy achieved through averaging and accurate interleaved sampling (figure 1.5).

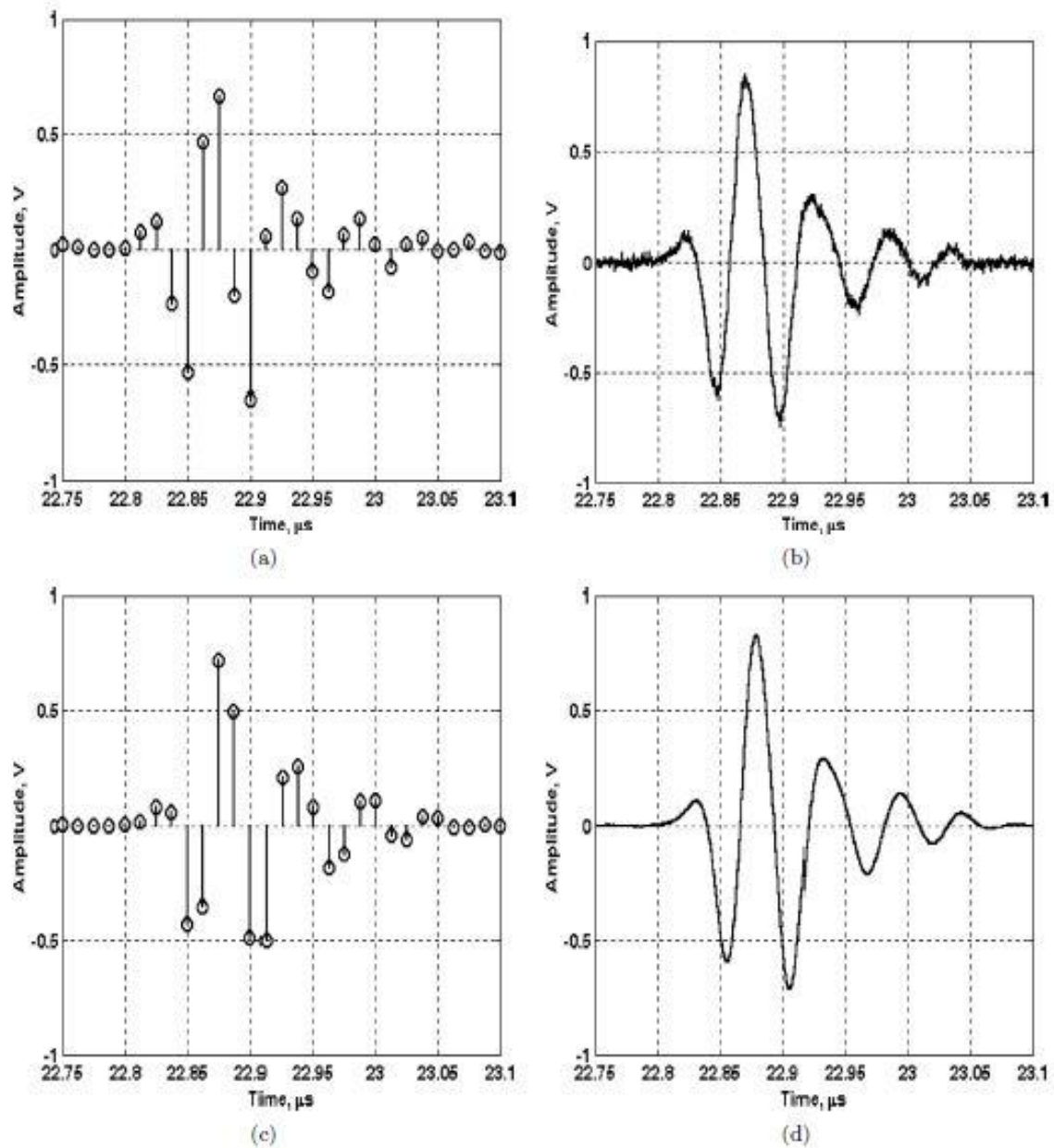


Figure 1.5 - Responses of a 20 MHz transducer recorded with different number of averages and sampling frequency: (a) 2 averages, 80 MHz; (b) 2 averages, 2.16 GHz; (c) 512 averages, 80 MHz (d) 512 averages, 2.16 GHz [1.62, figure 9]

Availability of an instrument, utilising this architecture, in the applied ultrasonic laboratory provided an opportunity to potentially meet the accuracy requirement for the IMT measurement.

D. Baldassarre et al [1.63] reported that only 5.9% of IMTs, measured in vivo, were reproducible. This shows the difficulty of measuring the IMT consistently, using the existing medical instrumentation. In another research

study, A. Ray et al [1.64] have designed a protocol to measure the IMT by ultrasound. They used an ultrasonic machine to take black and white images of the carotid artery at a particular sector of the artery. Presence of plaques in the artery, and whether the IMTs had the normal or abnormal size were judged by trained practitioners. They concluded that “clinicians can be trained well enough in six weeks to accurately and efficiently detect carotid plaques in an outpatient setting.” [1.64] However, the second conclusion was that “IMT abnormalities were less accurately detected in the office-based approach and may require a specialized vascular laboratory” [1.64]. Therefore, equipping practicing clinicians with the high accuracy IMT measurement instrument seems as a viable improvement to the existing practices.

Most of the IMT measurement methods, described in the literature, used either B-mode ultrasound scans or 3D ultrasound imaging. Therefore, higher accuracy of the measurement of the IMT can lead to more accurate diagnoses at the early stages of heart diseases. Using high accuracy ultrasonic data acquisition architecture can enable increase in the sampling frequency of the echo waveforms. In turn, these increases will improve the theoretical axial resolution of the instrument, which is defined in the pulse-echo mode as the sampling interval times the ultrasound velocity divided by two.

1.6.2 – O. Benner’s MPhil

In a research study, O. Benner [1.65] developed a wired ECG monitor that was connected to the ultrasound scanner (section 1.6.1) to synchronize the cardiac cycle with ultrasonic measurements, and recorded some waveforms. However, there were several issues that could not be resolved by his development. First of all, the developed ECG monitor was connected to the rest of the system by wires, which made it difficult to apply the instrument in a hospital environment due to safety concerns. That is because any mains powered electronic equipment that has electrical contact with the patient should be approved by a regulatory body before such a use.

Secondly, triggering the ultrasound scans was found to be severely affected by the presence of high amplitude noise in the ECG trace. Triggering the scanner at a particular point of the cardiac cycle is very important for accurate IMT measurements. The observed high level of artifacts made it impossible to achieve reliable and consistent records of the artery examined at the same point of the heart cycle.

Thirdly, the transducer used in the study was a 20 MHz transducer with the diameter of 1.27cm placed on the neck of the subject. The diameter of the transducer was bigger than the artery's diameter. This meant that the reflections from the entire artery resulted in very convoluted waveforms, which were difficult to analyse and extract information from. This complexity of the recorded echoes was attributed to ultrasound wave diffraction on the curved shapes of the arteries.

For these reasons the developed instrument, despite being fully operational, was unable to produce consistent waveforms that could be interpreted, and led to inaccurate measurements of the IMT.

1.7 – Aims and Objectives

1.7.1 - Aim

An example was given in section 1.4, where Selzer et al [1.36] measured IMT in 24 subjects using B-Mode ultrasound with ECG recorded at the same time. Post processing techniques can also be applied such as edge detection. This project aims to develop an electronic instrument for accurate measurement of the IMT, which is to be achieved by improving the measurement resolution and synchronising ultrasonic scans with the heart activity. Combination of high resolution, high speed measurement system, and monitoring the heart activity will enable fast and accurate measurements of IMT in A-mode ultrasound scans

The overall system is shown in figure 1.6. The objectives set for the project include development of the sub-systems shown below, and their integration.

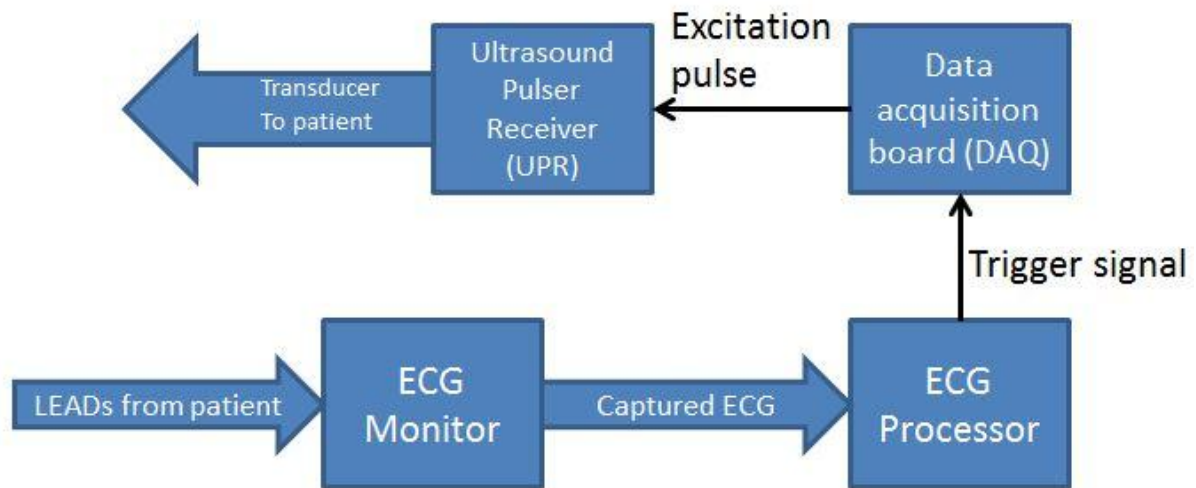


Figure 1.6 - Block diagram of the entire instrument

1.7.2 - Objectives

In order to achieve the main goal of the project it is necessary to set objectives that break the body of the project into smaller and manageable tasks. Each objective is related to subsequent objectives and the overall aim of the project. Each of these objectives required substantial development and experimental effort on their own. Finally they were combined together to achieve the overall aim of the project. Objectives that were set to meet the aim of the projects are as follow:

1. Development of a wireless ECG monitor
2. Development of triggering algorithm for ultrasonic scans
3. Experimental study of reflections from tubular objects
4. Development of the in vivo experimental protocol and system verification

1.8 – Thesis structure

1.8.1 - Development of a wireless ECG Monitor

The first objective is to overcome the ECG safety issue that prevented the previous development from being used at medical hospitals. This objective is to

be met by analysing wireless communication solutions available on the market, and select one that has the following characteristics:

- is robust and provides enough data bandwidth
- does not use much power, to enable operation from a battery
- can be employed at medical installations without causing much interference.

The ECG Monitor itself will be designed and developed to be battery operated, where in the unlikely case of malfunction the low voltage and current of the battery is not harmful to the patient. The ECG Processor will receive the data from the ECG monitor and trigger the ultrasonic scans. It can be connected to a mains powered power supply and other equipment like the ultrasonic scanner, because there is no electrical contact between the ECG processor and the patient.

Chapter 2 discusses the development and experimental results obtained during design and verification of the wireless ECG monitor.

1.8.2 - Development of triggering algorithm for ultrasonic scans

The ECG processor should consistently trigger ultrasonic scans at the required instant of the heart cycle by analysing the ECG. Although deep analysis of the ECG signal is not required for triggering, the process of capturing and detecting elements in the signal becomes even more complicated. This is because of the presence of electrical noise and interference as it was experienced in the previous project. The processing algorithm needs to be reliable not to miss a possibility of triggering the scan when the condition is right. It also needs to be fast enough to ensure that the condition is detected before it is too late to trigger the scan at the required instant of the heart cycle. The algorithm should be tested with simulated and recorded data, and be compatible with the available processing power of conventional microcontrollers.

The steps taken to develop the ECG Processor and the algorithm, used to enable the accurate triggering of the ultrasound pulses, followed by the results of experimental verification of the ECG Monitor and ECG processor, operating together, are described in Chapter 3.

1.8.3 - Experimental study of reflections from tubular objects

Human arteries can have uneven diameter, wall thickness, twists, stenosis, and experience dimensional changes throughout the heart cycle etc. These factors complicate the interpretation of ultrasonic scans. However, it is possible to examine some man-made object with fixed and well known properties in order to get experimental data on what to predict in vivo. Generally speaking, use of phantoms is less flexible compared to the use of mathematical models. For example, boundary conditions can be easily changed in simulation, but may require another phantom and attachments when conducting physical modelling. This objective is essential for verification of the computerised simulation results, and development of the experimental in vivo measurement protocol, which is the next objective.

Chapter 4 discusses the requirements for selecting appropriate phantoms for physical simulations; the experimental protocol to obtain reproducible results from the phantom experiments, and the analysis of the experimental results obtained from these experiments.

1.8.4 - Development of in vivo experimental protocol and system verification

To confirm the accuracy of the obtained results using the developed system, one requirement is to be able to repeat each experiment and produce consistent results every time. During one examination, there are many important parameters that need to be taken into account, to ensure the results are reliable, accurate and consistent. Therefore, it is necessary to develop a method to ensure that all the relevant parameters are set as required every time.

The first step to verify that the system operates correctly is to make sure the results are reproducible; this means that under the same conditions the results from different experiments are the same. As the placement of the

transducer plays an important role in the outcome of the experiments, it may not be possible to have the exact same setup in every session. Therefore, the robustness of the system is to be confirmed by repeating each measurement at least three times, and different reality checks to be applied for this purpose. The measurements should be conducted at different times of day on several occasions. They should results in some estimates that agree with literature data related to IMT measurements. Finally, the IMT should be extracted from in vivo experimental records.

Chapter 5 provides a protocol that fully describes the experimental procedures, providing step by step instructions to be followed before, during and after any IMT measurements. It should be detailed enough to allow another researcher to follow it closely, and repeat the results obtained by the protocol's developer when using the same instrumentation and subject.

The protocol for the in vivo experiments and the analysis of the recorded data are also presented in Chapter 5. Discussion in the chapter covers some of limitations and problems, which were encountered when real-time in vivo measurements were conducted.

References

- 1.1 – Wikipedia (2014; September). "Hemostasis"[Online]. Available: <http://en.wikipedia.org/wiki/Hemostasis>
- 1.2 – Wikipedia (2014; September). "White Blood Celss"[Online]. Available: http://en.wikipedia.org/wiki/White_blood_cell
- 1.3 – Wikipedia (2014;September). "Cytokine"[Online]. Available: <http://en.wikipedia.org/wiki/Cytokine>
- 1.4 – Wikipedia (2014; September). "Chemokine"[Online]. Available: <http://en.wikipedia.org/wiki/Chemokine>
- 1.5 – PTDirect. "Major Functions of the Cardiovascular System"[Online]. Available: <http://www.ptdirect.com/training-design/anatomy-and-physiology/cardiovascular-system/major-functions-of-the-cardiovascular-system-2013-a-closer-look>
- 1.3 – QuizLet. "Cardiology Heart Chambers"[Online]. Available: <http://quizlet.com/4833709/cardiology-heart-chambers-flash-cards/>
- 1.4 – British Heart Foundation. "How your heart works"[Online]. Available: <http://www.bhf.org.uk/heart-health/how-your-heart-works.aspx>
- 1.5 – Down's heart group. "The Normal Heart"[Online]. Available: <http://www.dhg.org.uk/information/normalheart.aspx>
- 1.6 – National Heart Lung and Blood institute (July; 2011). "What Is an Arrhythmia?"[Online]. Available: <http://www.nhlbi.nih.gov/health/health-topics/topics/arr/>
- 1.7 – Scottish Intecollegiate Guidelines Network (2007). "Chronic Heart Failue"[Online]. Available: <http://www.sign.ac.uk/pdf/pat95.pdf>
- 1.8 – J. White, C. Ryjewski. "Chronic Venous Insufficiency", PERSPECT VASC SURG ENDOVASC THER 2005, vol. 17, no. 4, pp.319-327, 2005
- 1.9 – S. Mitchell et al. "Congenital Heart Disease in 56,109 Births Incidence and Natural History", Circulation, vol. 43, pp. 323 – 332, 1971

- 1.10 – A.Maton, R.L.J.Hopkins, C.W.McLaughlin, S.Johnson, M.Q.Warner, D.LaHart, and J.D.Wright, *Human Biology and Health*, Englewood Cliffs, New Jersey, USA, 1993.
- 1.11 – Wikipedia (2010; August). "Atherosclerosis"[Online]. Available: <http://en.wikipedia.org/wiki/Atherosclerosis>
- 1.12 – Wikipedia (2013; August). "Stenosis"[Online]. Available: <http://en.wikipedia.org/wiki/Stenosis>
- 1.13 – Wikipedi (2010; July). "Angiography"[Online]. Available: <http://en.wikipedia.org/wiki/Angiography>
- 1.14 – Wikipedia (2010; July). "Cardiac stress test"[Online]. Available: http://en.wikipedia.org/wiki/Cardiac_stress_test
- 1.15 – A.F.Kopp et al. "Non-invasive coronary angiography with high resolution multidetector-row computed tomography", *European Heart Journal*, vol.23, pp. 1714-1725, 2002
- 1.16 – L. Kaufman et al. "Coronary calcium scoring: modelling, predicting and correcting for the effect of CT scanner spatial resolution on Agatston and volume scores", *Physics in medicine and biology*, vol. 48, pp. 1423 – 1436, 2003
- 1.17 – C. Stefanadis et al. "Thermal Heterogeneity Within Human Atherosclerotic Coronary Arteries Detected In Vivo", *Circulation* vol. 99, pp. 1965 – 1971, 1999
- 1.18 – S. Bernard et al. "Incremental predictive value of carotid ultrasonography in the assessment of coronary risk in a cohort of asymptomatic type 2 diabetic subjects". *Diabetes Care* vol. 28, pp. 1158-1162, 2005
- 1.19 – Aminbakhsh, A. Mancini. "Carotid intima-media thickness measurements: what defines an abnormality? A systematic review", *Invest Med*, vol. 4, pp. 149-157, 1999
- 1.20 – M. Eigenbrodt et al. "B-mode ultrasound common carotid artery intima-media thickness and external diameter: cross-sectional and longitudinal associations with carotid atherosclerosis in a large population sample", *Cardiovascular Ultrasound*, March 2008

1.21 – M. Bots, A. Hofman. "Increased Common carotid Intima-media thickness; adaptive response of a reflection of atherosclerosis", *Stroke*, vil. 12, pp. 2442 – 2447, 1997

1.22 – C. Bonithon-kopp et al. "Factors of carotid arterial enlargement in a population aged 59 to 71 years", *Stroke*, vol. 37, pp. 1103 – 1105, 2006

1.23 – M. Bots et al. "Common carotid Intima-media thickness and risk of stroke and myocardial infraction", *Stroke*, vol. 37, pp. 1913 – 1916, 2006

1.24 – J. Gariepy et al. "Sex and topographic differences in associations between large-artery wall thickness and coronary risk profile in a French working cohort: the AXA Study", *Arterioscler Thromb Vasc Biol*, vol. 4, pp. 584-590, 1998

1.25 – A. Poli et al. "Ultrasonographic measurement of the common carotid artery wall thickness in hypercholesterolemic patients. A new model for the quantitation and follow-up of preclinical atherosclerosis in living human subjects", *Atherosclerosis*, vol3, pp.253-261, 1988

1.26 – M. Bots et al. "Common carotid Intima-media thickness and lower extremity arterial atherosclerosis; The Rotterdam study", *Arterioscler Thromb*, vol. 14, pp 1885 – 1891, 1994

1.27 – S. Ebrahim et al. "Carotid Plaque, Intima Media Thickness, Cardiovascular Risk Factors, and Prevalent Cardiovascular Disease in Men and Women, The British Regional Heart Study", *Stroke*, vol. 30, pp.841-850, 1999

1.28 – G. Howard et al. "Carotid artery intimal-medial thickness distribution in general populations as evaluated by B-mode ultrasound. ARIC Investigators", *Stroke*, vol. 9, pp. 1297-1304, 1993

1.29 – R. Karim et al. "Significantly higher incidence of carotid atherosclerosis found in Japanese type 2 diabetic patients with early nephropathy", *Diabetes* vol. 66, pp. 161-163, 2004

1.30 – G. Bolinder et al. "Smokeless tobacco use and atherosclerosis: an ultrasonographic investigation of carotid intima media thickness in healthy middle-aged men" *Atherosclerosis*, vol. 132, pp. 95-103, 1997

- 1.31 – J. Sandham. "Intravascular ultrasound (IVUS)"[Online]. Available: <http://www.ebme.co.uk/arts/ivus/>
- 1.32 – N. Hangiandreou. "AAPM/RSNA Physics Tutorial for Residents: Topics in US, B-mode US: Basic Concepts and New Technology". *Radiographics*, vol. 23, pp. 1019-1033, 2003
- 1.33 – Physiomontreal, "Ultrasound"[Online]. Available: <http://www.physiomontreal.com/Ultrasound.pdf>
- 1.34 – MedlinePlus (2013; March) "Pregnancy ultrasound"[Online]. Available: <http://www.nlm.nih.gov/medlineplus/ency/article/003778.htm>
- 1.35 – U. Francesco et al. "Arterial Stiffness and Risk of Coronary Heart Disease and Stroke", *Circulation*, vol. 113, pp. 657 – 663, 2006
- 1.36 – R. Selzer, H. Hodis. "Evaluation of computerized edge tracking for quantifying intima-media thickness of the common carotid artery from B-mode ultrasound images", *Atherosclerosis*, vol. 154, no.1, pp.185-193, 2001
- 1.37 – Robert H Selzer, Wendy J Mack, "Improved common carotid elasticity and intima-media thickness measurements from computer analysis of sequential ultrasound frames" , *Atherosclerosis*, vol. 154, pp. 185 – 193, 2001
- 1.38 – I. Wendelhag, Q. Liang. "A New Automated Computerized Analyzing System Simplifies Readings and Reduces the Variability in Ultrasound Measurement of Intima-Media Thickness", *Stroke*, vol.11, pp. 2195 – 2200, 1997.
- 1.39 – J. Polka et al. "Variations in common carotid artery intima-media thickness during the cardiac cycle: implications for cardiovascular risk assessment". *Journal of the American society of Echocardiography*, vol. 25, no. 9, pp. 1023 – 1028, 2012
- 1.40 – J. Polka et al. "Changes in Carotid Intima-Media Thickness During the Cardiac Cycle: The Multi-Ethnic Study of Atherosclerosis" *Journal of the American Heart association*, doi: 10.1161/JAHA.112.001420.

- 1.41 – Absolute Medical Equipment. "Mindray DC-7 3D/4D Ultrasound Machine"[Online]. Available: <http://www.absolutemed.com/Medical-Equipment/Ultrasound-Machines/Mindray-DC-7-3D-4D-Ultrasound-Machine>
- 1.42 – Wikipedia (2013; September). "Blood Pressure"[Online]. Available: http://en.wikipedia.org/wiki/Blood_pressure
- 1.43 – WelchAllyn (2008). "Blood Pressure Training Guide"[Online]. Available: http://www.welchallyn.com/documents/Blood%20Pressure%20Management/7171WAWorkbook_AUG5.pdf
- 1.44 – R. Mukkamala et al. "Continuous Cardiac Output Monitoring by Peripheral Blood Pressure Waveform Analysis", IEEE TRANSACTIONS ON BIOMEDICAL ENGINEERING, VOL. 53, NO. 3, pp. 459 – 467, 2006
- 1.45 – Texas Instrument (2007; September). "Heart-Rate and EKG Monitor Using the MSP430FG439"[Online]. Available: <http://www.ti.com/lit/an/slaa280a/slaa280a.pdf>
- 1.46 – C. Riva et al. "Blood Velocity and Volumetric Flow Rate in Human Retinal Vessels", Investigative Ophthalmology and Visual Science, vol. 26, no. 8, pp. 1124 – 1132, 1985
- 1.47 – "Blood Flow Hemodynamics, Cardiac Mechanics, and Doppler Echocardiography"[Online]. Available: http://samples.jbpub.com/9780763779351/79351_CH04_BulwerSec.pdf
- 1.48 – S. Shakespeare et al. "The information content of Doppler ultrasound Signals from the fetal heart", Medical and Biological Eng. & Computing, vol. 39, pp. 619 – 626, 2001
- 1.49 – K. Shelley, S. Shelley. "Pulse Oximeter waveform: Photoelectric Plethsmography", in Clinical Monitoring, pp. 420 – 428, 2001
- 1.50 – Wikipedia (2013; September). "Photoplethysmogram"[Online]. Available: <http://en.wikipedia.org/wiki/Photoplethysmogram>
- 1.51 – J. Gonzalez, "Reproducibility of Carotid Intima-Media Thickness Measurements in Young Adults", Radiology, vol. 247, no. 2, pp. 465- 471, 2008

1.52 - J. Meinders, "Assessment of spatial inhomogeneities in intima media thickness along an arterial segment using its dynamic behavior", Am J Physiol Heart Circ Physiol, vol. 13, pp 384 – 391, 2003

1.53 – BKUltrasound, "SonixTouch Q+"[Online], Available:

<http://www.bkultrasound.com/ultrasonix/systems/sonixtouchq>

1.54- Siemens, "ACUSON Cypress Cardiovascular system PLUS"[Online],

Available: <https://www.healthcare.siemens.co.uk/ultrasound/options-and-upgrades/upgrades/acuson-cypress-cardiovascular-plus-option>

1.55 – Echocardiographer. "Axial, Lateram and Temporal Resolution"[Online].

Available: <http://echocardiographer.org/Echo%20Physics/Axresolution.html>

1.56 – A. K.Holmes, J. Laybourn-Parry, J.D. Parry, M. E.Unwin, and R. E. Challis, "Ultrasonic imaging of biofilms utilizing echoes from the biofilm/air interface," IEEE Trans. Ultrason., Ferroelect., Freq. Contr., vol. 52, pp. 185–192, Jan. 2006.

1.57 – Wikipedia. (2013; July). "Signal averaging"[Online]. Available:

http://en.wikipedia.org/wiki/Signal_averaging

1.58 – A. N. Kalashnikov, R. E. Challis, M. E. Unwin, and A. K.Holmes, "Effects of frame jitter in data acquisition systems," IEEE Trans. Instrum. Meas., vol. 54, pp. 2177–2183, 2005.

1.59 – A. N. Kalashnikov and R. E. Challis, "Errors and uncertainties in the measurement of ultrasonic wave attenuation and phase velocity," IEEE Trans. Ultrason., Ferroelect., Freq. Contr., vol.52, pp. 1754–1768, 2005.

1.60 – Wikipedia. (2013; July). "Flash ADC"[Online]. Available:

http://en.wikipedia.org/wiki/Flash_ADC

1.61 – C. Vogel, "The impact of combined channel mismatch effects in time-interleaved ADCs," IEEE Trans. Instrum. Meas., vol. 54, pp. 415–427, 2005.

1.62 – Alexander N. Kalashnikov. "High-Accuracy Data Acquisition Architectures for Ultrasonic Imaging", IEEE Transactions on Ultrasonics, Ferroelectrics and Frequency Control, vol. 54, no. 8, pp. 1596 – 1605, August 2007

1.63 – D. Baldassarre et al. “Common carotid intima-media thickness measurement. A method to improve accuracy and precision”, *Stroke*, vol. 8, pp. 1588 – 1592, 1994

1.64 – A. Ray et al. “Accuracy of carotid plaque detection and intima-media thickness measurement with ultrasonography in routine clinical practice” *European Journal of International Medicine*, vol. 1, pp. 35-39, 2010

1.65 – O. Benner, “Synchronisation of vascular ultrasonic scans with heart activity using ECG signals”, MPhil thesis, Dept. Elect. Eng., Nottingham univ., Nottingham, UK

2 – Development of the ECG monitor

The ECG Monitor is the circuitry connected to the patient to capture an Electrocardiogram, which is then used for triggering the ultrasound imaging system. The process of designing and developing the ECG Monitor was one of the most important parts of the research project as not only the safety of the patient was a very important matter, but also the reliability of the electronics and operation of the board had a considerable impact on the results achieved by the overall system.

Wireless communication between the ECG monitor and ECG processor, which generates the trigger signal at the desired stage of a heart cycle (chapter 3), makes the overall system safe to be connected to the patient. It also makes the design electromagnetically compatible with other electronic devices in hospitals. Other than safety, the link between ECG Monitor and ECG Processor needs to be reliable as the timing of the trigger plays an important role in the outcome of the experiments.

This chapter presents the development process of the ECG monitor and discusses the importance of using infrared communication to avoid any interference with other systems in a hospital environment if applicable. It also details the process of improving the designs.

2.1 - Development of the wireless link between the ECG monitor and processor

2.1.1 - Selection of the wireless link technology

The Electrocardiogram of a patient is taken by placing electrodes directly on her/his skin. Although the voltage applied to these electrodes is safe, there is a slight possibility of appearance of injury-capable voltage from the mains powered equipment due to malfunction. This possibility relates not only to the power connection of the ECG circuit itself, but also to the battery powered equipment that utilises wired data communication. Any equipment that falls in

these categories requires rigorous testing by approved bodies before being used on patients, which makes this option unfeasible for the present research due to the required cost and time. The only solution that enables safe testing on human volunteers is to use a battery powered ECG monitor which wirelessly communicates the data to the device that would trigger the ultrasonic scans. Most commonly used options for wireless communication currently include radio frequency (RF) and optical communications.

RF communication can be implemented using a local transceiver providing physical level link (PHY) only. These transceivers usually operate in the unlicensed industrial, scientific and medical (ISM) radio band at centre frequencies of either 433.92 or 866.50 MHz [2.1]. A number of manufacturers offer transceiver chipsets (e.g., Maxim [2.2]), modules (e.g., RFM [2.3]) or microcontrollers with built in RF transmitters (e.g., Microchip [2.4]) for these frequencies. Using any of these options requires development or adoption of firmware for low level signaling, error checking etc. Alternatively, a complete standardized solution can be used which enables built in high level protocol features like secure communication, data integrity check, automated secure pairing etc. Most notable examples of such protocols include Bluetooth [2.5], ZigBee [2.6] and WiFi [2.7], which can be realized in embedded systems using a single chip or a module. For instance, the AT86RF212 from ATMEL is an RF transceiver with built in ZigBee protocol [2.8].

Despite the simplicity and convenience of using the above mentioned RF communication methods, they can cause unacceptable RF interference (RFI, also called electromagnetic interference EMI) to medical electronic devices operated in close proximity.

There are various factors that complicate detection of EMI-caused malfunction of medical devices. Sporadic appearance of EMI contributes to an estimated 25% of medical devices service calls, which resulted in the report “no problem found” [2.9]. Spotting, measuring and tracking EMI sources require sophisticated and expensive equipment that is not readily available at medical installations.

Since the use of medical electronic devices became more popular in the early 1990s, there was a large increase in the number of reports linking

malfunction of these devices to RFI. For example, it was reported that an external pacemaker was affected when medical technicians started using their radio, which caused "excruciating pain" to the patient. Another report indicated that a heart monitor in a nursery produced false readings because of the RFI from a base station, located on the wall outside the building. When the base station was moved 25 feet away from the nursery, the heart monitor resumed normal operations [2.9, p.5].

An analysis of 150,000 incident reports that involved cardiac medical devices filed in the USA between 1984 and 1995, showed that RFI caused malfunction in at least 456 cases. In most cases some kind of intervention was needed to prevent adverse outcomes [2.10].

A number of experiments conducted by various researchers, concentrated on different aspects of EMI affecting medical devices. A study by graduate school of Information Science and Technology of Hokkaido University in Japan, showed that the presence of EMI caused by RF identification tags worn by the personnel, had direct effect on some active implantable medical devices, in particular pacemakers and defibrillators (AIMD) (table 2.1, 2.2 [2.11]).

Table 2.1 - Number of affected pacemakers [2.18]

Freq. of RFID interrogator	Total number of pacemakers tested	Number of affected pacemakers	Percentage	Maximum distance (cm)
Low frequency (LF)	450	161	29.3	16
High frequency (HF)	912	39	4.3	23
Ultra high frequency (UHF)	952	40	4.2	20
2.4 GHz	304	0	0	20

Table 2.2 - Number of affected implantable cardiac defibrillators (ICDs) [2.18]

Freq. of RFID interrogator	Total number of Implantable Cardiac Defibrillators (ICDs) tested	Number of affected ICDs	Percentage	Maximum distance (cm)
Low frequency (LF)	82	6	7.3	4
High frequency (HF)	25	1 only for gate-type	4	3
Ultra high frequency (UHF)	N/A	0	0	N/A
2.4 GHz	N/A	0	0	N/A

Even though it seems that higher frequencies of RF signals have less effect on some AIMDs, these frequencies are reserved and licensed; and may not be available to manufacturers of medical instruments. Another study investigated the sensitivity of a wheelchair and a ventilator to EMI, within a frequency range from 0 to 1000 MHz both devices were found susceptible to emissions at some frequencies [2.10]. Finally, a ubiquitous mobile phone (although an outdated analogue one) caused malfunction to different medical devices at close range (table 2.3,).

Table 2.3 – Test results: interference from 0.6 W analogue mobile phones [2.9]

Device	Effect	Proximity
Infusion pump	Flow sensor triggered – causes pump to stop	0.2m of the flow sensor
Incubator	Temperature settings fluctuate, causing the heating element to turn on	0.1m of the LED display
ECG/Apnea	False apnea alarm	0.1m of monitor
Ventilator	Change in delivered gas volume	.03m of right side
Oxygen monitor	Oxygen saturation reading increases	0.13m of monitor

In order to limit the harmful effect of the RFI on medical devices, various international bodies, such as the Centre for Devices and Radiological Health of the US Food and Drug Administration (FDA), have established relevant standards on RF emissions and/or RFI immunity [2.9, p.22]. As a result, devices used in medical environments need to be tested for RFI immunity, if their malfunction could cause a potential threat to patients. Additionally, parts of the spectrum (?) are dedicated by licensing bodies to medical use in order to prevent RFI; an example is the Wireless Medical Telemetry Service (WMTS) spectrum exclusively allocated to its purpose by the Federal Communication Commission (FCC) in the USA [2.12].

RFI caused by wireless communication not only leads to malfunction of other devices, but also increase the level of noise in readings of medical instruments. This is because processing of most bio signals requires high gain amplifiers that amplify RFI-induced noise too.

In summary, using RF communications in medical devices requires a considerable amount of research and development to ensure their compliance to regulatory requirements. These devices need to be subjected to a series of different tests at approved laboratories in order to be used in hospitals [2.13].

For the purpose of this project, technically convenient RF communication was not used in order to avoid the need of going through all the compulsory tests and licensing. A viable alternative to RF communication is infrared (IR)

communication technology [2.14]. IR only operates at short range and line of sight and is widely used domestically for various remote controls. It was also a very popular wireless communication option among laptops and mobile phones, however, this use faded away with the market acceptance of the USB communication for this purpose.

Development of an IR link was deemed viable due to the availability of low cost integrated components from many suppliers. These components allow for setting up a two-way low bitrate line of sight IR communication link at a short range.

As a result of the above considerations, infrared communication is the most viable option to connect the ECG Monitor to ECG Processor. A Block diagram of the overall system is presented in figure 2.1.

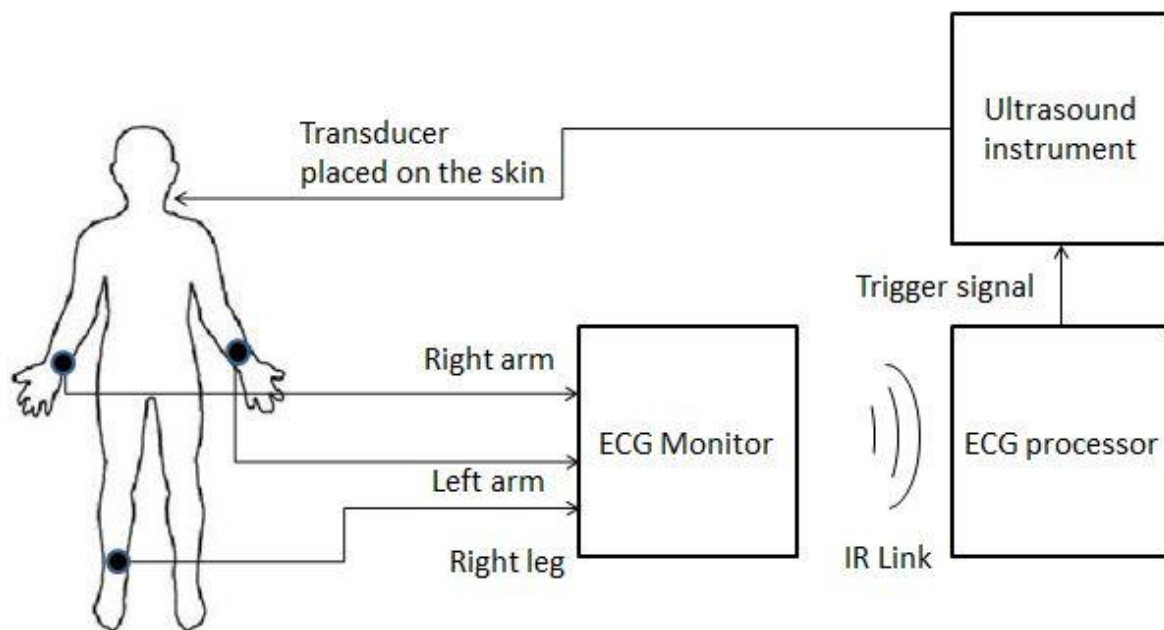


Figure 2.1 – Block diagram of the overall system

2.1.2 -Development of the IR link

2.1.2.1 - Selection of the modulation scheme

Amplitude modulation assumes changing the amplitude of the carrier signal based on the variation in the value of the information signal. When this modulation is applied, there could be some communication imperfections because of possible fluctuations in the analogue signal levels due to noise. In contrast to this, transmission of a digital bit stream consisting of zeros and ones requires switching the carrier ON or OFF only, which substantially increases the noise immunity. This is due to the fact that the receiver only needs to detect the presence of the carrier, rather than the exact amplitude (ON/OFF keying - OOK). The minimal time difference between the subsequent switches determines the data transmission rate (bitrate).

The main disadvantage of using this method is the continuous current consumption when the transmitter is in the ON state. Since the ECG monitor is battery operated, any reduction in its power consumption (e.g. by shortening the IR ON time) is beneficial to the user. Therefore the ON state in IR links is commonly represented by only a fraction of the complete bit transmit period ([2.15, p. 7 - 10]).

2.1.2.2 - Infrared transceivers

An infrared transceiver is used to convert an input binary electrical signal to IR light and vice versa. These devices are offered by several manufacturers, and operate at the maximum baud rate for up to 115 kbps. A number of different transceivers were evaluated to find the most suitable option.

TFDU4300 [2.16] and TFDU4101 [2.17] transceivers have the maximum range of communication of 1 m. They allow the use of an external resistor, which reduces the transmitted power, hence the current consumption is lower at the expense of the shorter communication distance. TFBS4650 has a typical range of 30 cm, and the maximum of 50 cm with the extended power specification [2.18]. Among available IR transceivers, the TFDU devices are specifically suggested for medical data recording by their manufacturer [2.16,

2.17], whereas the suggested applications for other transceivers are PCs and PDAs only (e.g., [2.18]).

IR transceivers can be directly connected to the microcontroller's serial communication, Tx and Rx pins. Dedicated firmware is required to handle the transmission and reception of the bit stream, especially if the consumed power reduction features mentioned above are used. However the microcontroller needs to spend a substantial percentage of its running time, coding/decoding IR messages. A better alternative is to use an intermediate IR encoder/decoder IC that bridges the microcontroller and IR transceiver, delivering energy efficient features in hardware. In order to ease the integration among electronic components, one vendor was used. Microchip's IR interface ICs were compared for this purpose. Table 2.4 includes some of the available encoder/decoder components from Microchip that could be used to simplify the IR link design.

Table 2.4 - Infrared Encoder/decoder

Product Name	Features
MCP23016	Extra I/O pins for LEDs and buttons [2.19, p.9]
MCP215x	Independent UART and IR baud rate [2.19, p.7]
MCP250xx	On-chip memory to save configurations [2.19, p.4]
MCP2122	Baud rate up to 115kbits/s, low power mode, UART to IrDA standard encoder/decoder [2.15]

The first three options in table 2.4 include a built-in protocol handler, which establishes connection between any compatible IR-enabled devices. This is also responsible for restoring the connectivity of the established bridge when necessary. If at any point the communication is disrupted, the handler will stop transmission, re-establish the connection and restart the communication. This feature is useful for many devices, and assists in avoiding the difficulty of manually establishing the connection.

Presence of the handler protocol, whilst easing connection of various devices like mobile phones and laptops, can be a disadvantage of the IR link for ECG communication due to its impact on the real-time operation of the link. In the case of lost connection between the two linked devices (caused by

intermittent malfunction of any of them or temporary obstruction of their optical path), the ECG communication should continue even if a few samples are lost, in order to enable real time monitoring of the heart cycle. A device with built in protocol handler will switch to the handshake routine instead to restore the connection, which takes a few seconds. MCP2122 is a simple encoder/decoder that does not include a built in protocol handler, thus it is selected for the purpose of this project.

The developed ECG trigger circuit uses two different microcontrollers. PIC18F1330 with lower power consumption (nanoWatt technology) is used for the ECG monitor, whilst USB enabled PIC18F14K50 is used for the ECG processor. Connections between the microcontrollers and other circuit elements are shown in figure 2.2 for the ECG Monitor, and figure 2.3 for the ECG processor. Both devices feature a three-colour LED for IR link debugging purposes.

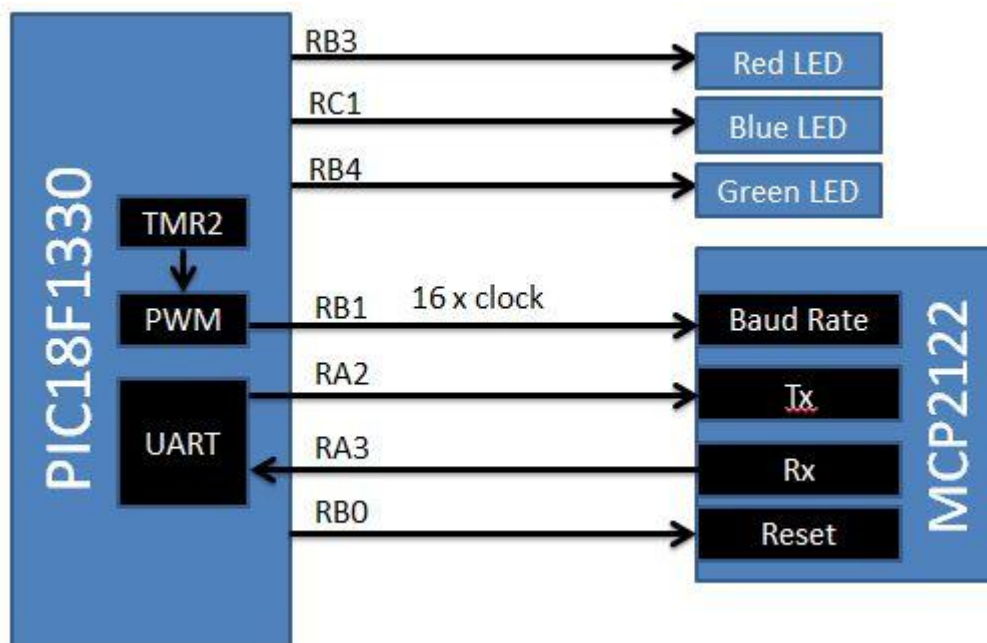


Figure 2.2 - IR link; pin connections for the ECG monitor

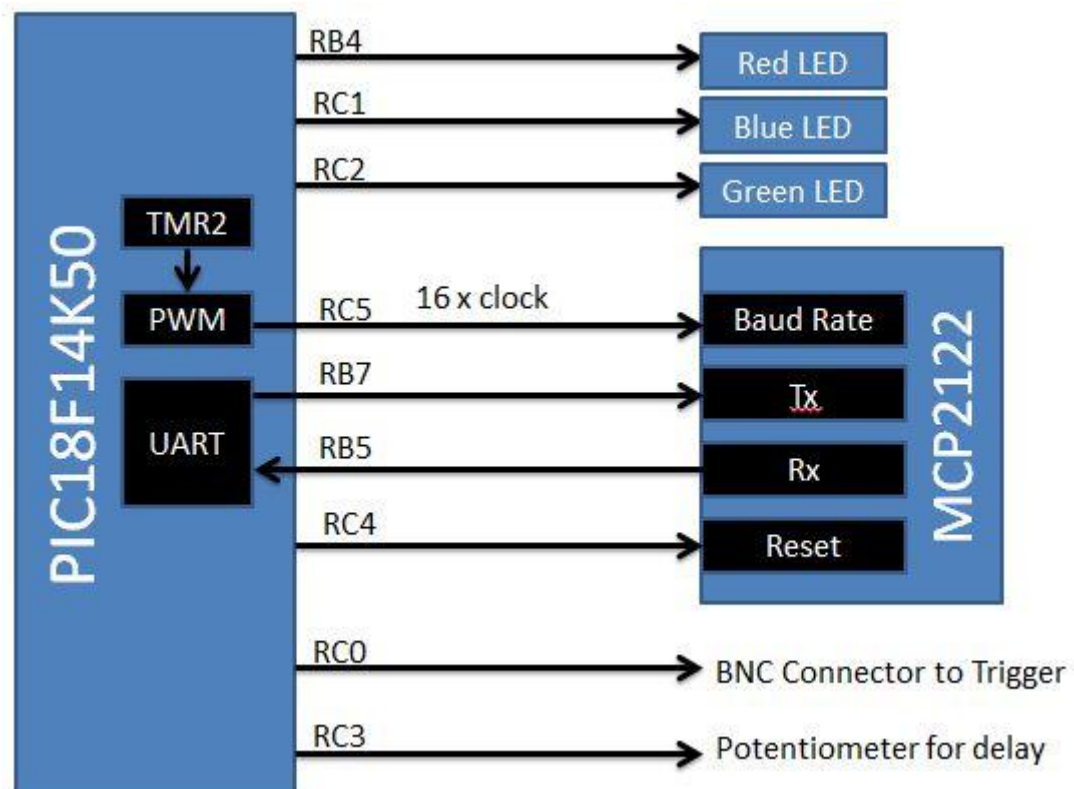


Figure 2.3 - IR link; pin connections for the ECG processor

2.2 – Operation and implementation of the ECG Monitor

2.2.1 - Relation of electrocardiogram to the cardiac cycle

As the heart cycle progresses through different phases, various currents are generated when electric charges follow the movements of blood in different heart chambers, as they contract. These electrical signals are called the electrocardiogram (ECG).

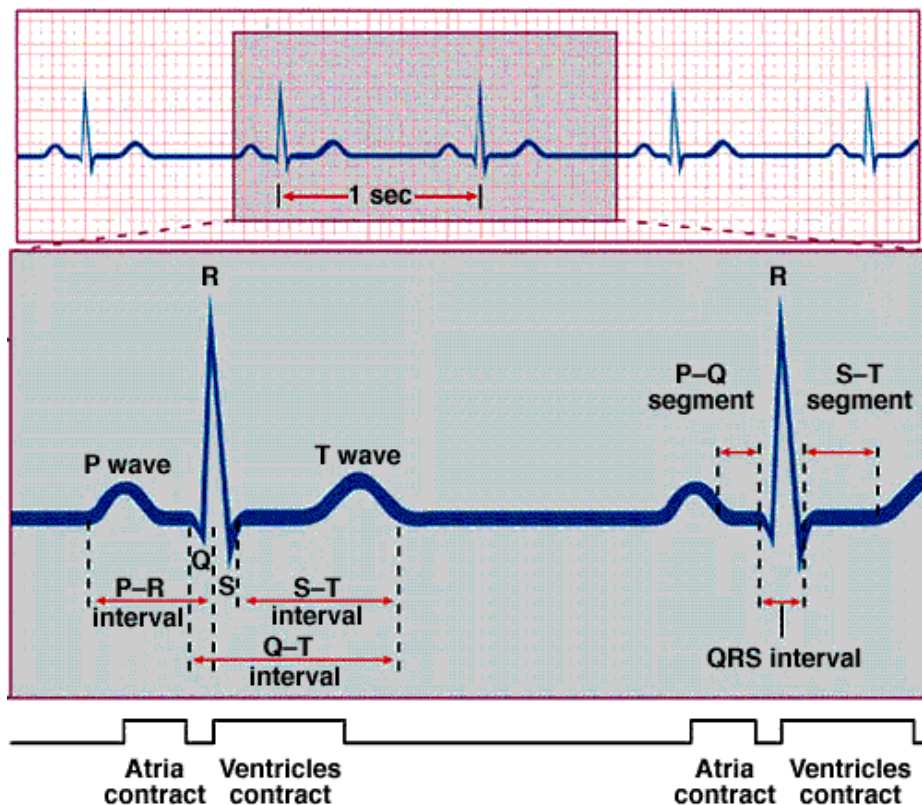


Figure 2.4 - Typical ECG waveform and its different parts [2.20, Figure1]

Distinct parts of the ECG, which are commonly called waves, are shown in figure 2.4. The P wave occurs when the atria of the heart contracts and sends the blood to the ventricles. Between the P and Q waves there is the time when blood fills the ventricles. The Q wave corresponds to the downward movement of the electrical current through the heart [2.21].

The R wave and S wave are produced when the electrical current travels back up through the right and left ventricles. The R wave corresponds to current travelling through the left ventricle. The time required for this travel is smaller than the travel time for the current through the right ventricle (that produces the S wave) by a fraction of a second. At the end of each cardiac cycle, the heart walls relax which results in the appearance of the T wave, before the start of the following cardiac cycle. The ECG signal can be interpreted and used to detect certain problems with the heart activity; abnormalities in the ECG can explain chest pain and detect symptoms of different heart diseases [2.21].

2.2.2 - Experimental recording of an ECG

2.2.2.1 - Placement of the ECG electrodes

Although muscles are better conductors than bones, muscle movement produces an electrical signal which may cause interference to the ECG being recorded. For this reason the electrodes are commonly placed on bony parts of the body. Bones do not produce electrical signals, so the interference is lower. (The electrodes must be placed at the same distance to the body on both hands, as far from the body as possible to reduce interference.

2.2.2.2 - ECG leads

A lead is the potential difference between two ECG electrodes. Three ECG leads (leads 1, 2, and 3 discussed below) are used most commonly. There are nine leads available overall (figure 2.5 [2.22]):

Lead1: Positive difference between LA and RA

Lead2: Positive difference between LL and RA

Lead3: Positive difference between LL and LA

Leads V1 to V6: $Lead V_x = V_x - \frac{(LA+RA+LL)}{3}$

where LA is Left Arm, RA is Right Arm, LL is Left Leg

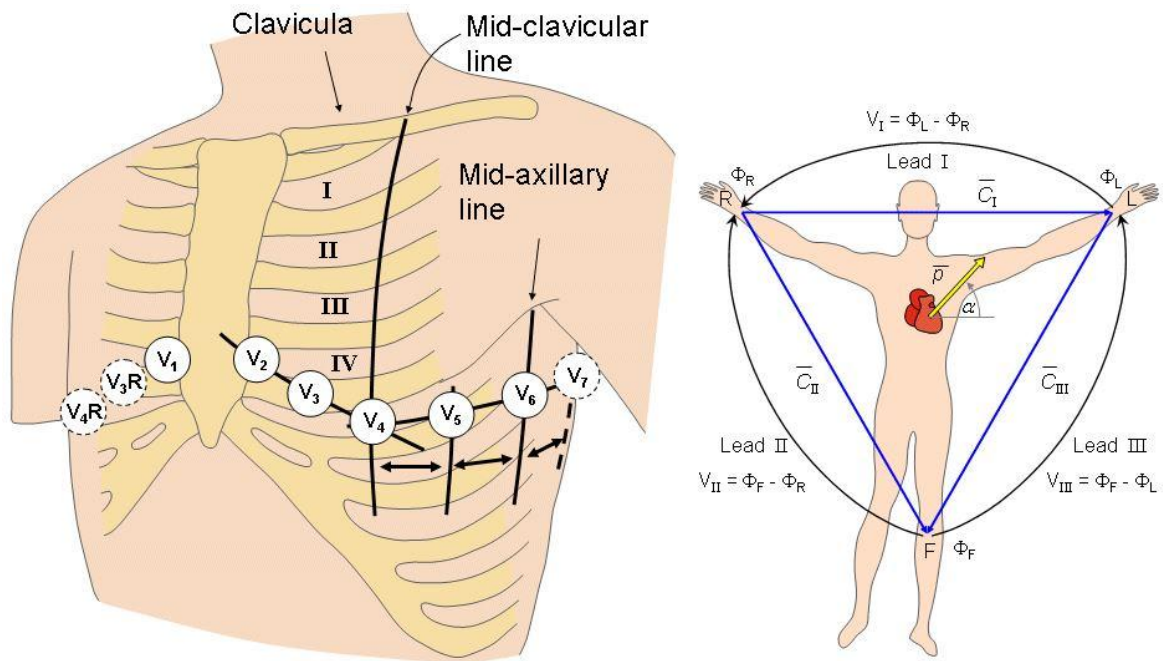


Figure 2.5 - Nine lead configuration (left [2.22, figure 15.8]) and three leads configuration (right[2.22, figure 15.1]) for ECG recordings

In most commercial devices, three electrodes are used: one on the left arm (LA), one on the right arm (RA), and one on the left leg (LL). Some devices may include an extra electrode on the right leg (RL).

Commercially available disposable electrodes are widely used by health departments for taking ECG waveforms. These electrodes are usually placed and secured on the skin with adhesive materials and sometimes include conductive gel for better contact with the skin. However, these electrodes are one-time use only and need to be disposed of after they are used. Since the ECG monitor is tested many times to verify its operation and operation of other parts of the system, using commercial electrodes is excessive. Therefore a set of electrodes are developed that can be used as many times as necessary.

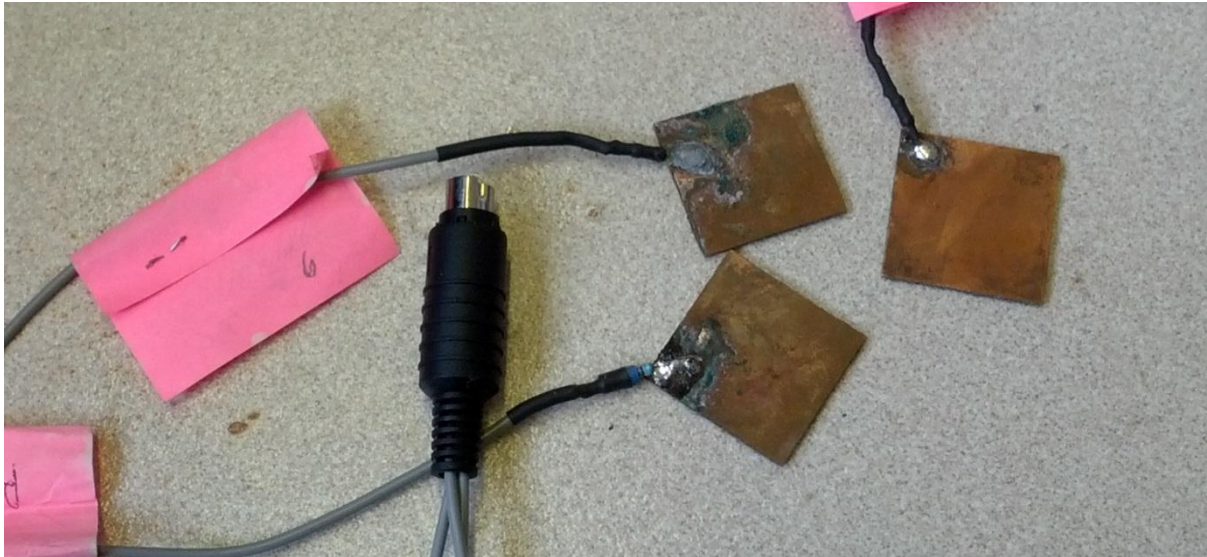


Figure 2.6 - Developed ECG leads from PCB board and shielded cables

These electrodes are made out of approximately 2cm by 2cm PCB squares, which are connected to the ECG monitor by shielded cables, to reduce the effect of any possible interference (figure 2.6). A comparison is done to check the signal quality of the developed electrodes against commercial ones to ensure the quality of these electrodes. Waveforms are captured from the output of the operational amplifier using both electrodes, and then Signal-to-Noise ratio (SNR) of both signals are compared.

The signal to noise ratio of each system is calculated by measuring the RMS of the signal and comparing that to the RMS of the captured noise of the system according to following equation:

$$nRMS = RMS \text{ of Noise}$$

$$aRMS = RMS \text{ of over all recorded signal}$$

$$sRMS = \sqrt{aRMS^2 - nRMS^2}$$

$$SNR = 20 \times \log_{10}\left(\frac{sRMS}{nRMS}\right)$$

The results of the SNR calculations are presented in table 2.5.

Table 2.5 - SNR comparison of the 2nd and final prototypes tested using commercial and developed electrodes

Board/Electrodes	nRMS(mV)	aRMS(mV)	sRMS(mV)	SNR(dB)
2 nd prototype/Commercial electrodes	0.0295	0.1864	0.1841	15.8970
2 nd prototype/Developed electrodes	0.0295	0.1912	0.1899	16.1205
Final prototype/Commercial electrodes	6.2215	41.2156	40.7433	16.3232
Final prototype/Developed electrodes	0.2441	2.0852	2.0709	18.5705

The developed electrodes proved to have a better SNR value compared to those available commercially. Although this can be due to the amount of conductive gel used between the electrodes and the skin, results show that the electrodes can be used with the ECG Monitor to test the system. To keep the conductivity of the electrodes before and after each experiment, the electrodes were cleaned to make sure the gel is not dried on the surface of the electrodes. The improvement on the final board increases the SNR of the system which both helps the R-wave detection of explained in Chapter 3 but also since the ECG signal is cleaner than before; it has the potential to be used for monitoring patient's status during the examination.

The difference between the two boards could be due to the following factors:

- Disconnecting the main power supply from the 3rd design – 50 Hz signal
- Having connection corrections on the 2nd design – possible noise due to bad connections

The improvement of the captured signal over the second and third design iteration can be seen in figure 2.23. There is visible reduction in the noise in the 3rd design.

As shown in table 2.5, there is a difference between the noise RMS value of the final board for the commercial and the developed electrodes. This difference could mainly be caused by the amount of conductive gel was used for the developed electrodes and the gel available in the commercial electrodes

considering that the commercial electrodes were not used for a period of time from the start of the project up to the point of taking these measurements.

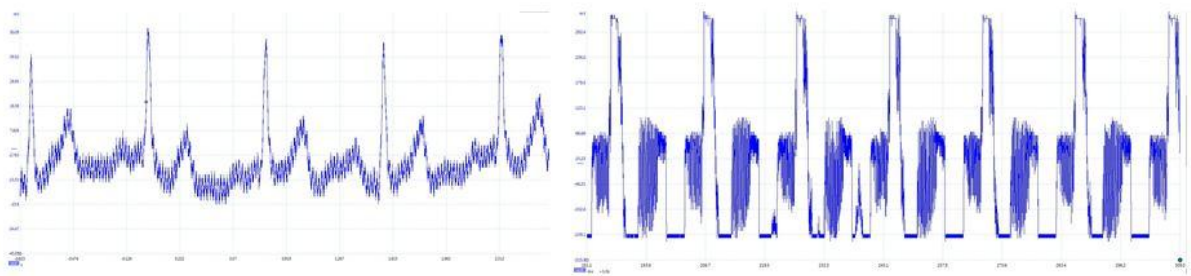


Figure 2.7 - 3rd PCB design (left) and 2nd PCB design (right) outputs

Both ECG traces in figure 2.7 were captured with the developed electrodes in the laboratory with a short delay between the experiments. In order to get clearer signals to measure the SNR of both boards, these signals were captured with the IR communication on as the IR operation interfered with the electronics on the board and added significant amount of noise (see chapter 5.1.2).

2.2.2.3 - Signal to Noise Ratio (SNR)

Based on the results obtained from different experiments with several devices, the ECG signal level was normally about 1 mV only. The level of the noise measured at a single ECG electrode was about 100 mV. Therefore, it was necessary to significantly reduce the noise and amplify the actual ECG signal at the same time.

A differential amplifier is required to reduce the in-phase interference captured from the patient's body. This reduces the noise, however, keeps the level of the ECG low. Then the instrumental amplifier with a certain amount of gain raises the ECG signal to about 2V p-p. This level is sufficient to be fed to the ADC of a microcontroller.

2.2.3 - Commercial ECG Monitors

Various devices, with different features, were developed to record an ECG. Some of them are listed in table 2.5 below. It was necessary to analyse

the market for available ECG monitors to investigate their feasibility for the purpose of this project.

Table 2.6 - A list of some commercially available ECG monitors

Name	Power	Cost	Weight	No. of leads	Comment
Welch Allyn CP250	Mains and battery	£1649	2 kg	12	- Lead off detection
Welch Allyn CP100	Mains and battery	£1,524.95	N/A	12	- Lead off detection
SECA CT3000i	Mains and battery	£1236.75	2.9 kg	12	-
SECA CT6i	Mains and batter	£1915.75		12	-
SECA CTP6i	Mains and battery	£1189.60	5 kg	12	- RS232 - 3.5 hours battery life
SECA CT8000i	Mains and battery	£1741.15	2.5 kg	12	- standalone and PC connectivity
SECA CT 8000p	Mains and battery	£2905.15	N/A	12	- All parameters including filters are programmed through on-screen menu
GE Healthcare MAC400	Mains and battery	N/A	1.3 kg	12	- 0.1Hz to 20 Hz filter - 4hours of battery life
GE Healthcare MAC800	Mains and Battery	N/A	3.0 kg	12	- 90dB CMRR - 0.04Hz to 150Hz configurable filter

There are several issues with the use of commercially available devices. The first and most obvious reason is their cost. Most reliable ECG monitors cost over £1,000; that is a significant outlay for a PhD research project's budget. Additionally there are specific legal limitations that prohibit unauthorised use and modification of off-the-shelf ECG monitors, required to trigger an ultrasonic scan.

Another limitation of these machines is their weight. They are heavy because they are capable of printing ECG traces or displaying the traces on the

device's built in screen. In particular, the lightest device from table 2.4 is over 1kg. Therefore it is difficult to move the device around the patient if necessary for the convenience of taking ultrasonic scans.

For the reasons stated above, it was necessary to develop a custom ECG monitor for this project which would:

- operate from a battery and thus be safe to the patient;
- Use an IR link to transmit the ECG data to the ECG processor that trigger an ultrasonic scan.

2.2.4 - Analysis of ECG monitor Schematics

Some of the open source ECG monitor schematics are available online [2.23]. Additionally a number of reference designs are published by manufacturers of instrumentation amplifiers, in the device's datasheets and application notes. For example, figures 2.8 and 2.9 present recommended ECG application circuits for INA333 produced by Texas Instruments [2.24]. The Schematic in figure 2.7 features a single supply voltage, three electrode inputs, right leg driver, enabling amplification by a factor of 1,000, and a low pass filter with a cut off frequency of 150 Hz [2.24].

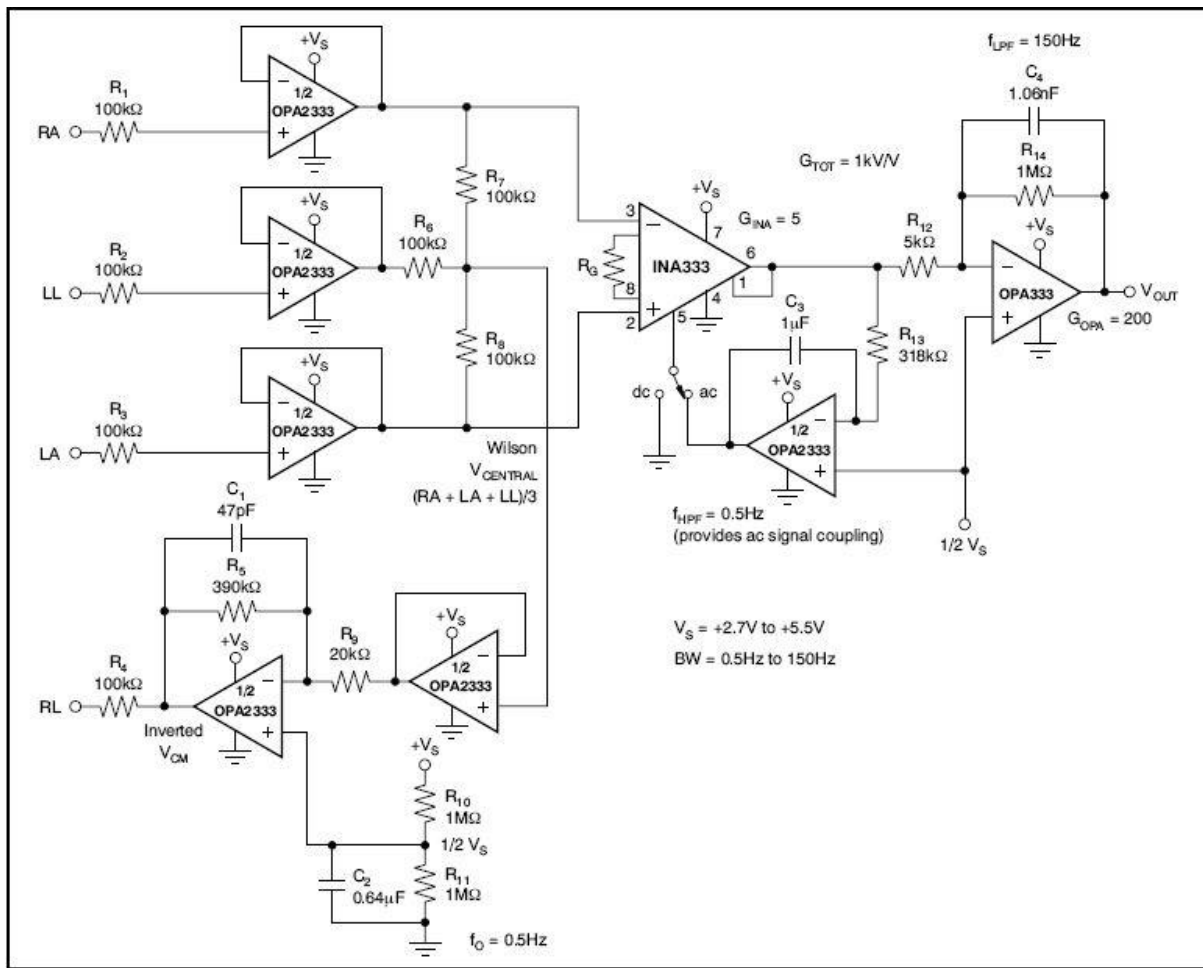


Figure 2.8 - Example of an ECG circuit schematic [2.24, figure 37]

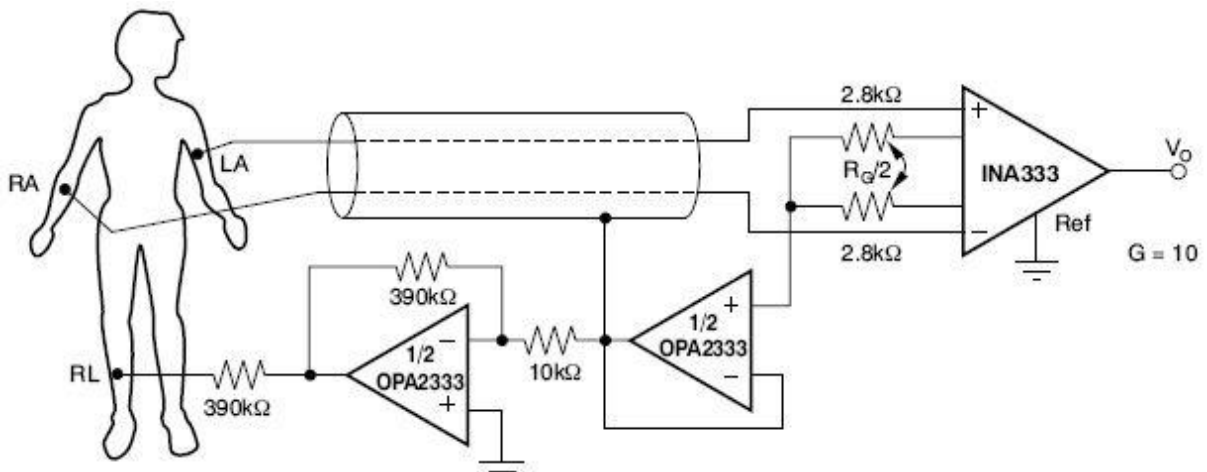


Figure 2.9 - Example of an ECG circuit schematic [2.24, figure 36]

Another example from the same datasheet (figure 2.9) requires fewer components, however, needs a dual supply voltage, provides a gain of 10, and

does not include any low pass filter. These and other available designs were compared and custom ECG monitor circuitry was developed as detailed in the following sections.

2.2.5 - Development of the schematic for the custom ECG monitor

In the schematics designed in this project, the analogue and digital parts of the circuit are separated. This is to reduce the effect of the interference caused by the digital circuitry on the sensitive ECG signal path (figure 2.10).

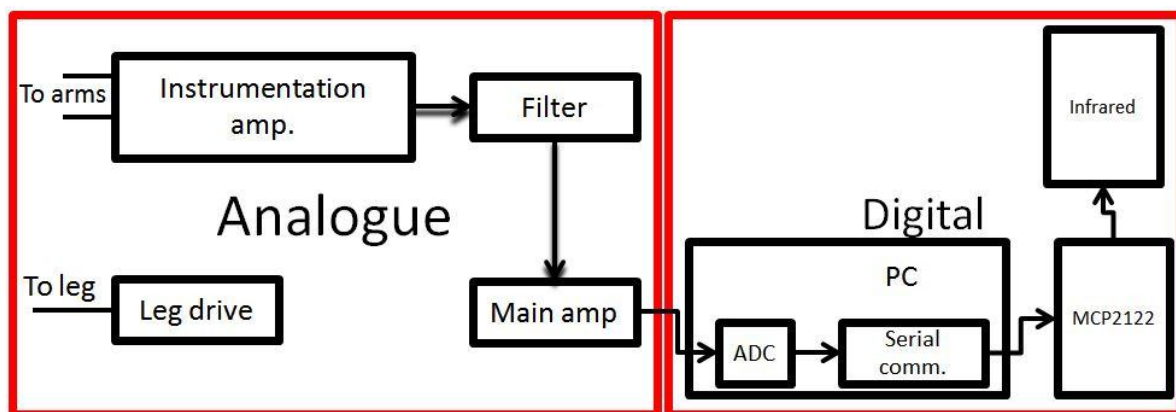


Figure 2.10 - Overall schematic

The analogue part is responsible for three main tasks. First, the instrumentation amplifier senses the ECG signal. This amplifier is connected to the arm electrodes via shielded cables. Shielding reduces the amount of interference from the nearby environment. Then the ECG signal goes through a band pass filter with the pass band frequency from 0.5 Hz to 40 Hz. This filter aims to reduce the baseline drift (appearing at below 0.5 Hz) and to eliminate interference from the mains at 50Hz fundamental frequency and its harmonics. The filtered signal is amplified by the main amplifier to achieve the desired amplitude. There is also a leg driver circuit in the analogue part. The leg driver is connected to the right leg of the patient in order to provide the reference voltage to the patient's body which also helps with reducing the baseline drift.

From the output of the main amplifier, the signal enters the digital section of the device via the analogue to digital convertor built into the microcontroller. The ECG trace is digitised and sent to the serial communication module, built into the PIC micro controller. This module transfers the data to the MCP2122, where it is encoded and passed on to the IR transmitter to be sent wirelessly to the ECG processor.

2.2.5.1 - Design of the analogue section

When designing a new board, several important factors have to be considered. The input impedance of the operational amplifier must be as high as possible. This is to reduce the effect of the change of voltage source on the input current. Also there needs to be a path to ground for the input current. It is common to use two equal resistors between the inputs and the ground.

The design procedure was completed in three steps. The schematic was drawn using LTspice software [2.25]. Then the circuit was simulated to achieve further improvements. When the schematic was completed, a vero board was designed using LochMaster software [2.26]. Then the design was implemented and experimentally tested. When the robustness of the design was verified, the PCB was developed and sent to the manufacturer. There were three vero boards and two PCBs designed and manufactured for this project. The first vero board design was based on the schematic developed in a previous masters project at Nottingham University (figures 2.11 and 2.12) [2.28].

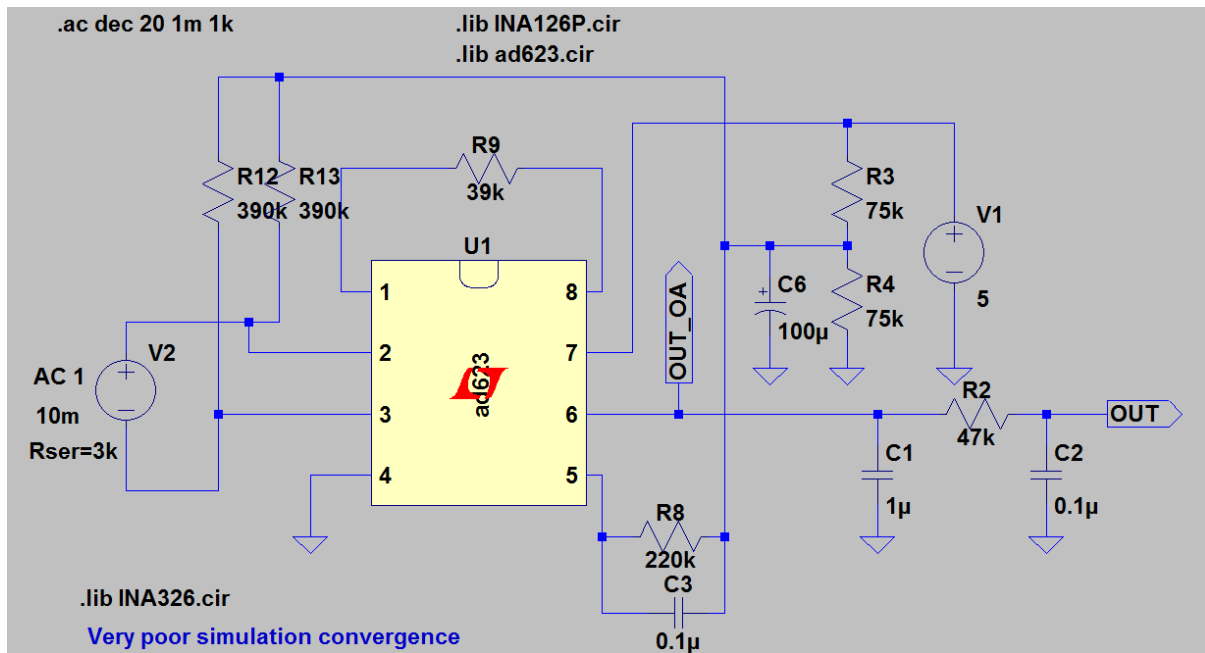


Figure 2.11 - Schematic of the first design

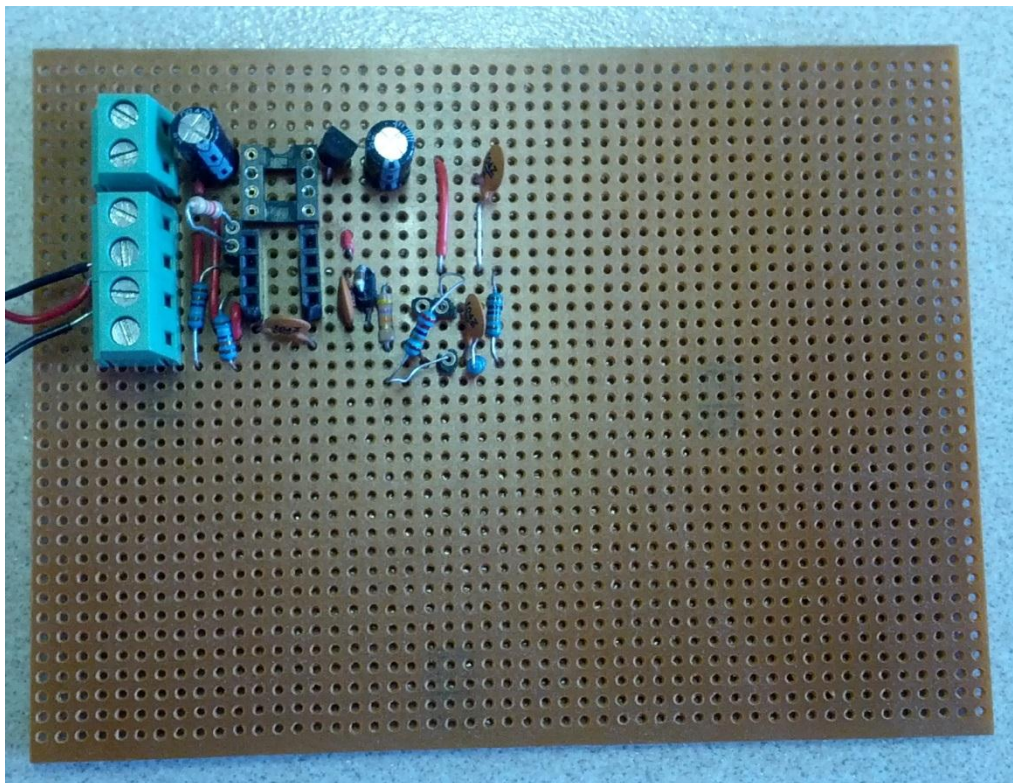


Figure 2.12 - First vero board assembled

In this design, there are two resistors (R12, R13) at the input of the ECG instrumentation amplifier, which provide the current path to the ground. There are two terminals to connect right and left arms to the op-amp. The left leg

electrode is connected to the ground potential. There are three low pass filters (R2, C1, and C2) at the output of the ECG instrumentation amplifier. The mid-point of the supply voltage (R3, R4, and C6) is used to set up the baseline voltage via parallel connection of R8 and C3. R9 sets the gain of the stage.

Most of the instrumentation amplifiers used for taking ECGs have the same pin out. Therefore, they can be connected to the same socket to evaluate their performance for this application.

There are several issues with this design, it is not reliable and does not give consistent results. More importantly, the insufficient gain results in the output signal with very low amplitude.

After testing this board and facing the above issues, a new board was developed shown in figures 2.14, 2.15 and 2.16.

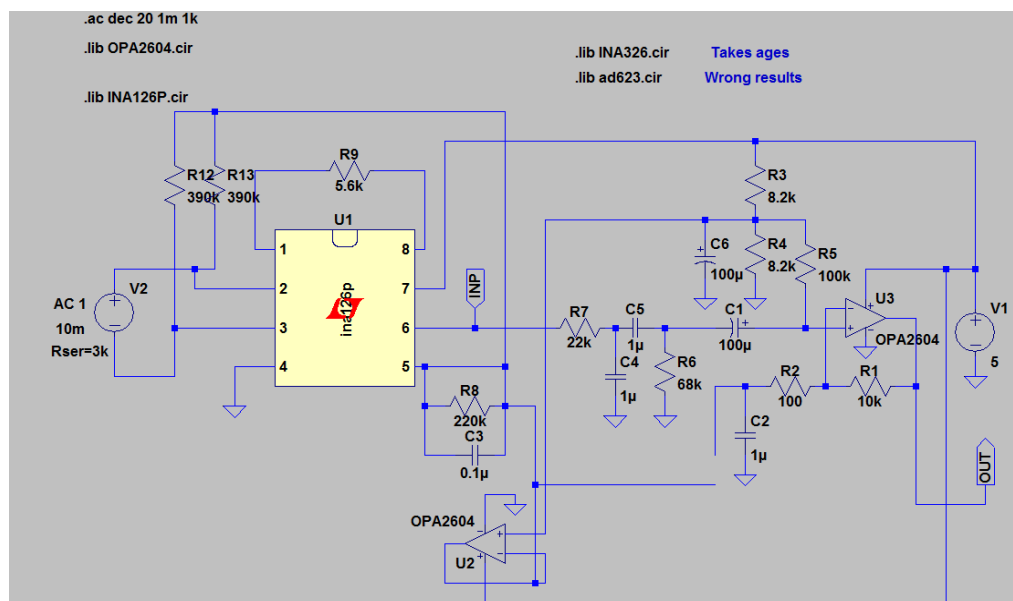


Figure 2.13 - Schematic of the second vero board

This board has two main advantages over the previous one:

1. The low pass filter is more accurate and has better performance;
2. There is an operational amplifier stage after the filter, which amplifies the ECG signal by the factor of 100.

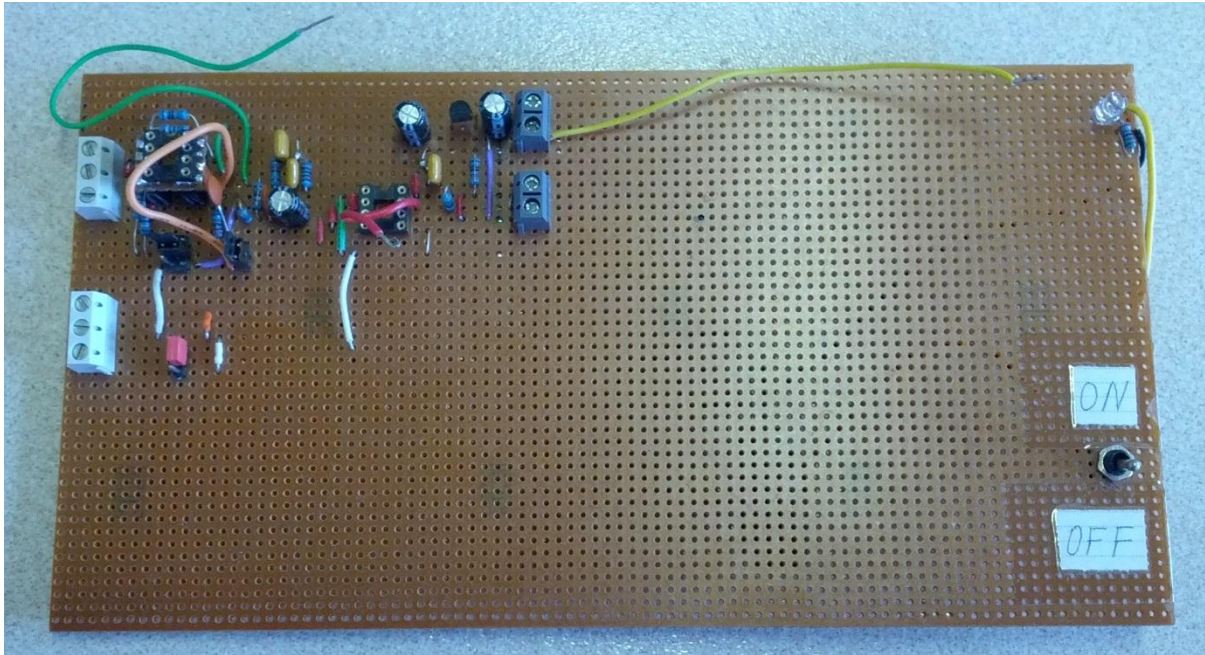


Figure 2.14 - Assembled second vero board

The second board has a fixed gain for the ECG op-amp, however it provides more options. Firstly there is a terminal dedicated to the leg. Therefore, either leg can be connected to the board. There is an improved filter at the output. This band pass filter has the pass band of 0.5 to 40 Hz, allowing reduction of the baseline drift. This results in a better and clearer ECG trace.

The board accommodates several jumpers. These jumpers assist in testing the board with different connections.

For example, the ref pin of the ECG op-amp can either be connected to 2.5 V output of the unused amplifier, or can be connected to the 2.5 V through the parallel resistor R8 and capacitor C3.

The other jumper provides the option of the input resistors to be connected to ground, the 2.5 V from the voltage divider, or 2.5 V from output of the amplifier.

The last jumper located at the bottom of the board enables the leg to be connected either to ground, or 2.5 V from the output of the amplifier.

These options were experimentally tested and the results were as follows:

- feeding the ref pin from the output of the amplifier reduced the noise;

- when the left leg was connected to the ground, the ECG trace was lost;
- when the left leg was connected to the output of the amplifier, the ECG noise level was reduced;
- connecting the input resistors to a proper 2.5 V source reduced the noise.

2.2.5.2 - Selection of the instrumentation amplifiers

Various instrumentation amplifiers are available for capturing an ECG signal, which are widely used in commercial ECG monitors. Each of these amplifiers has different and sometimes unique options which would be ideal for different cases. A number of instrumentation amplifiers were considered for this project. These are shown in table 2.6.

After comparing the properties of these amplifiers, two amplifiers, AD622 and INA126, were selected as the primary candidates for the ECG monitor. This is due to their use in some reference designs, wide availability and pin compatibility.

Both amplifiers were tested under the same conditions to prevent the possibility of any changes in the environment and the patient affecting the results. Also, the patient was in a relaxed state with closed eyes. It was observed on numerous occasions that if the patient was not in a relaxed state, recording consistent ECG waveforms was not possible.

Table 2.7 - Different OPAMPS available for ECG measurements (data taken from respective datasheets)

Part name	Gain Accuracy	Supply current, mA	Max. input offset, nA	Input bias, nA	CMRR gain, dB	Differential gain, dB	Noise at 1 kHz, nV/ $\sqrt{\text{Hz}}$	Bandwidth, Hz	Settling time, ms	Cost, £
AD633	0.35%	0.575	200	25	90	120	35	800	20	3.33
AD627	0.1%	0.085	200	10	77	120	38	80	135	4.24
AD622	0.15%	1.5	123	5	98	120	12	800	10	4.66
INA126	0.02%	0.2	250	25	95	100	35	200	30	1.67
INA131	0.02%	3	50	2	120	125	12	70	100	6.67
INA332	0.07%	0.49	200	500	73	N/A	46	2000	1.7	2.00
INA118	0.02%	0.18	50	5	110	N/A	10	500	15	5.08
INA121	0.001	0.450	200	4	100	N/A	20	600	20	6.08
INA337	0.08%	2.4	100	2	120	N/A	97	1	130	4.00
INA116	N/A	N/A	3	N/A	95	100	28	800	N/A	N/A
MAX 4209	0.25%	0.25	20	.001	135	125	140	750	15	1.53
LTC6800	0.1%	1.2	100	4 nA	120	N/A	>100	200	4 ms	3.32

2.2.6 - Implementation of the ECG monitor

In order to make sure that all available options are tested and the most suitable is selected for the ECG monitor, three different designs were implemented on the first PCB board. Having three different designs on the same board enables the possibility of changing the circuit in use while the ECG was taken, giving instant comparison among different designs.

These three options follow the same concept of operating the board, to ensure the safety of patients and quality of the results. The overall structure for the ECG Monitor is shown in figure 2.15.

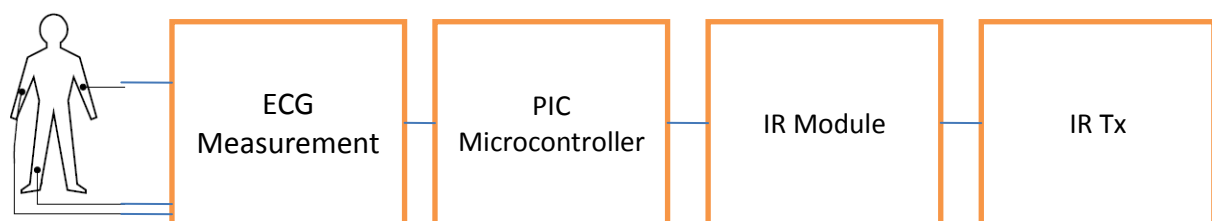


Figure 2.15 – Block diagram of the ECG Monitor

The ECG waveform is picked up by electrodes placed on both arms and the right leg of the patient, and is fed to the analogue part of the circuit. After filtering out the noise and amplifying the actual ECG signal, the resultant analogue signal is digitized by the PIC Microcontroller; the digital bitstream is sent to the ECG Processor via IR circuitry. The options for the schematics implemented on the board are relevant to the ECG measurement only if the rest of the device is kept the same.

Three options implemented on the PCB are shown in figures 2.8, 2.9 and 2.16. Figure 2.8 shows a right leg driver that supplies the potential proportional to the instrumentation's amplifier midpoint voltage for a bipolar power supply. Figure 2.9, bottom part, depicts such a driver operating from unipolar power supply. Direct connection of the right leg to the ground of the ECG monitor is shown in figure 2.16. Any of these options could be selected by operating jumpers on the PCB.

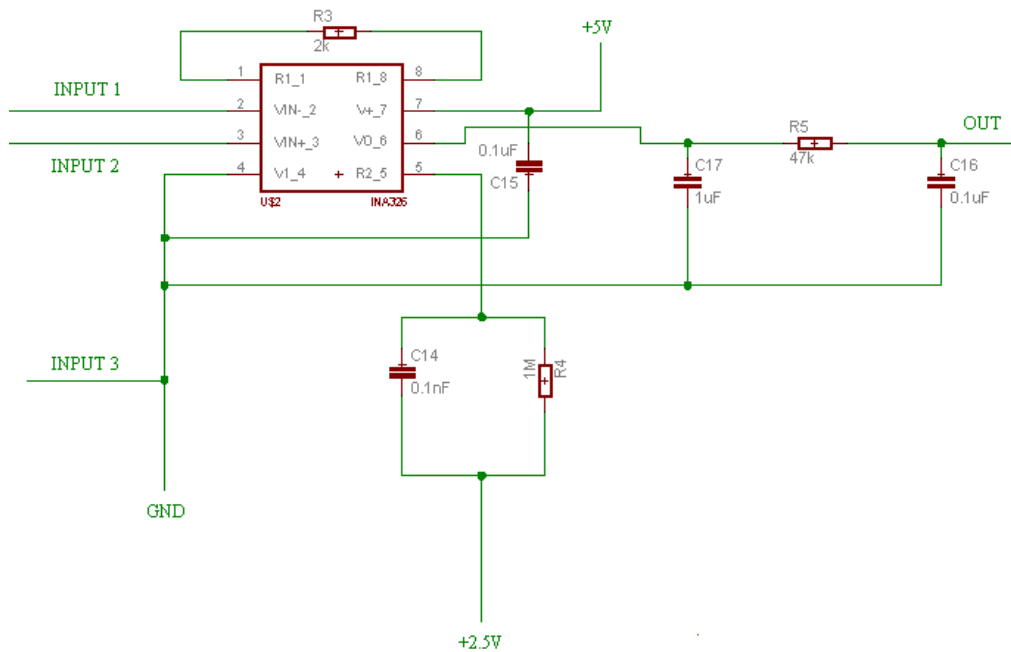


Figure 2.16 - Direct connection of the right leg to the ground of the ECG monitor

The output voltage of the instrumentation amplifier was filtered by the low pass filter shown in figure 2.17. Its frequency response is shown in figure 2.18. The low pass filter is required to eliminate the high frequency caused by muscle movements during examinations. The low amplitude signals due to the muscle movements are picked by the electrodes, and will distort the ECG signal. These distortions will have an impact on the detection of the R-wave, which is used as the trigger marker; therefore, they must be eliminated as much as possible.

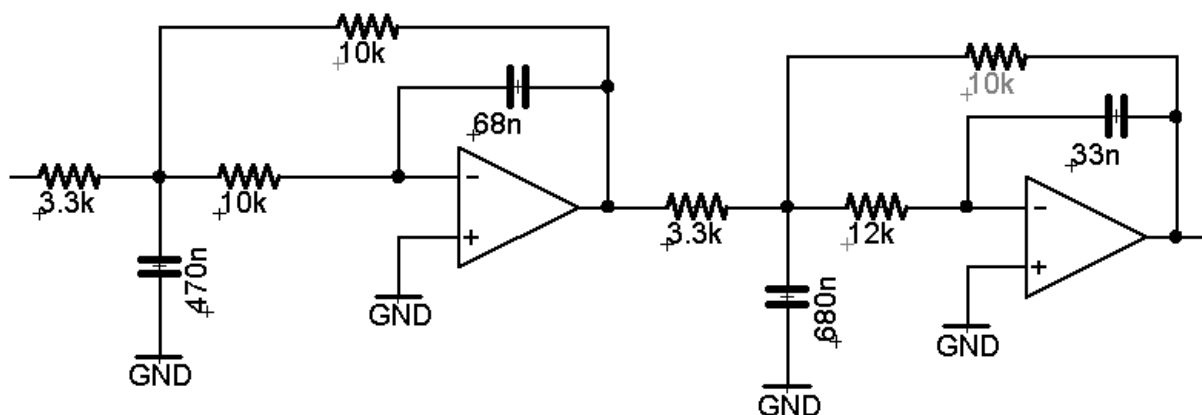


Figure 2.17 – Low pass filter connected to the output of the instrumental amplifier

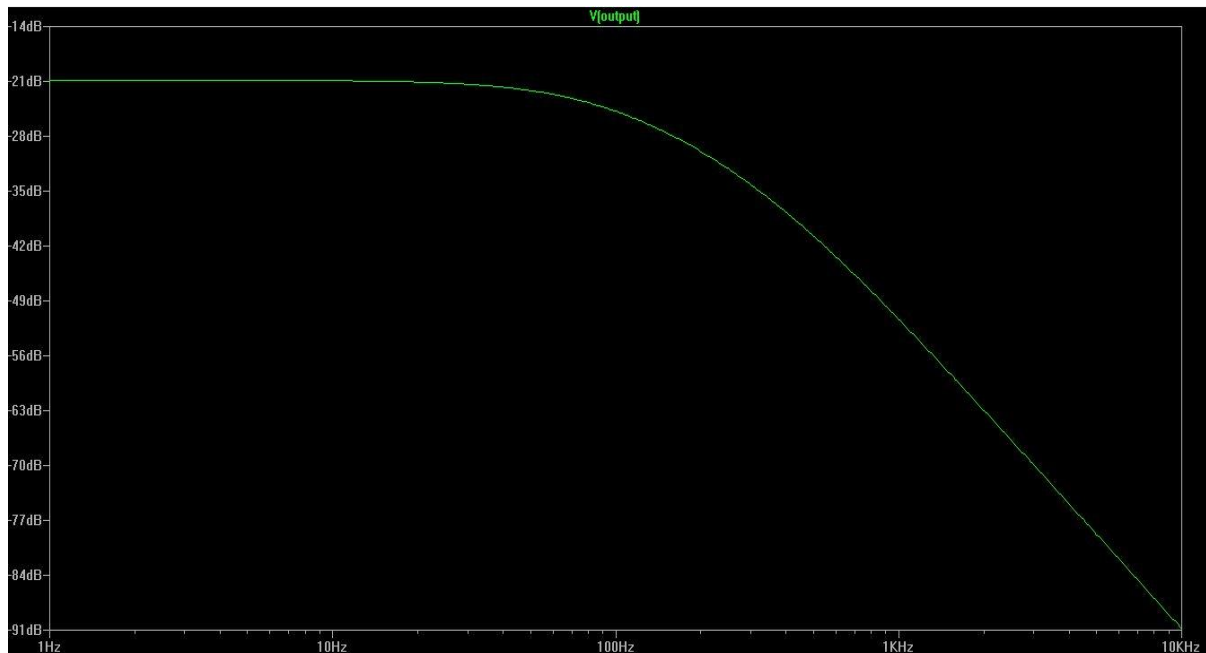


Figure 2.18 – Frequency response of the low pass filter shown in figure 2.19

2.2.6.1 -PCB design

The ECG Monitor PCB was developed in three stages with improvements being carried out on each design. The first two prototypes had the capability to be powered from the main and using a USB connection from a laptop for the ease of use. Because the first two boards were for testing purposes this was not an issue; however, the final design needed to be battery operated to consider the safety of the patient. Therefore the option for external power source from the board is removed, and the final board is only powered by a battery. The first two boards are described in Appendix 1; the third board was used to design the final PCB, with further required modifications.

A DC to DC convertor is a circuit that would, as the name suggests, convert the level of an input DC voltage from one value to another. A switched-mode boost converter uses an electronic IC to store input energy in either inductors or capacitors, and release it at a higher voltage. High efficiency of switched-mode converters help to increase the operating time of the battery operated devices and thus is a valuable option for the ECG monitor. Out of the

DC-to-DC convertors available on the market, MCP1640 is a suitable option since it provides the required voltage, is inexpensive, and does not require excessive electronic components to operate. This keeps the size of the board at its minimum.

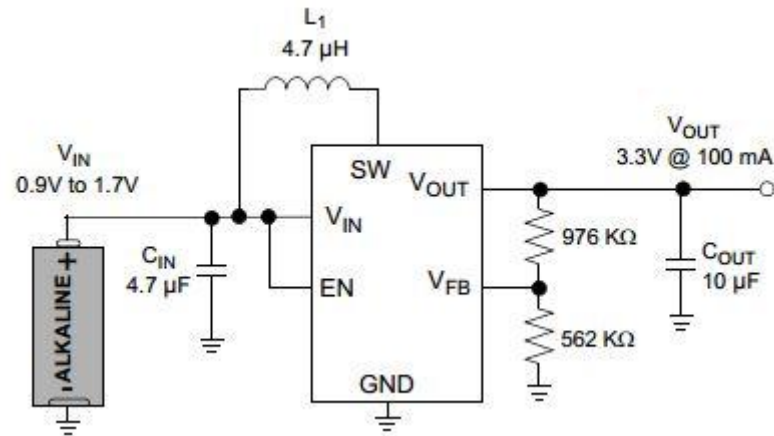


Figure 2.19 - MCP1640 application circuit [2.21, p.2]

Figure 2.19 shows the application circuit for converting voltages from 0.9-1.7 V to 3.3 V, which is within the range of operating voltage of all the components on the ECG monitor [2.21]. This circuitry is added to the final ECG monitor design. The final ECG monitor, after going through the initial IR communication and ECG capturing tests, is the board used in vivo experiments at the final stages of the project. The PCB layout and the assembled board are shown figure 2.20 and 2.21.

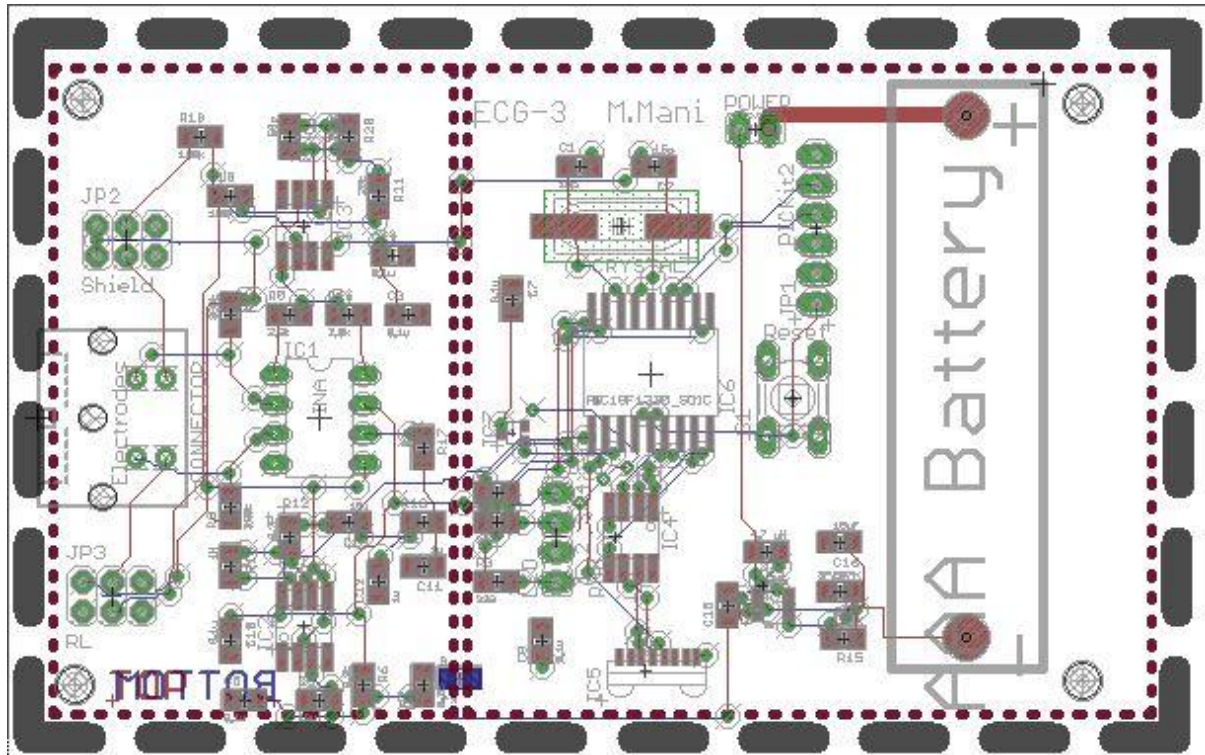


Figure 2.20 - PCB layout of the final ECG monitor



Figure 2.21 - Third PCB assembled

The results taken from the developed ECG monitor were compared to an ECG trace taken by commercial ECG monitor in the Nottingham Queen's Medical Centre (QMC). The comparison is shown in figure 2.22. The two waveforms were taken 1 day apart. The X-axis on both figures shows time in seconds and the Y-axis on the bottom trace is in milli-volts.

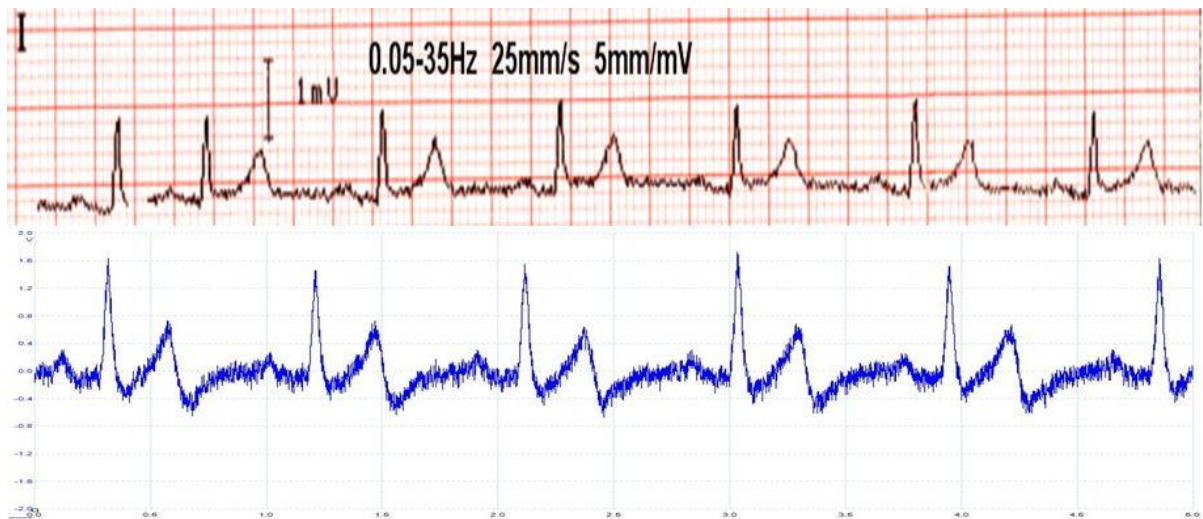


Figure 2.22 - ECG taken from commercial machine (top) and experimentally taken ECG (bottom, y-axis in mV, x-axis in ms)

As the above figure shows, the level of noise in the ECG trace taken from the developed instrument has more high frequency noise; however, this is not an issue for the purpose of the ECG monitor. This is because the ECG trace is only used as a triggering marker and would not be analysed for diagnosis of the patient. The above traces were not taken at the same time, however as it can be seen, the traces are very similar in terms of the timing of the QRS complex.

2.3 – Conclusions and summary

IR technology was selected for the wireless link between the ECG monitor and ECG processor ahead of its RF competitors. The reasoning behind this decision is that IR link is inexpensive, easy to implement and use, acceptable and widely used. Furthermore, RF technologies are not desirable due to their interference to other medical devices. In addition, a commercially available ECG monitor cannot be used in this study due to its cost, transportations issues and size. Therefore, a new IR system was designed based on current standard practices.

A circuitry for ECG monitoring of the patient was designed and developed. Three boards were developed, tested and improved achieve the most reliable, and safest design for continuous use.

Integration of the ECG monitor with the rest of the system is done through the ECG processor: the ECG monitor captures and digitises the ECG signal from the patient, and sends it directly to the ECG processor for triggering the ultrasonic scan over the IR link.

The final system was also compared to commercially available systems. Results showed that although the commercial systems may have cleaner signals and more functionality, the system required for the purpose of this research project the ECG signal will not be presented to be analysed for diagnosis of the patient but only it will be used to trigger the ultrasound pulse. For this reason the quality of the ECG waveform, as long as the R-wave can be distinguished from the rest of the QRS complex, does not have to be as good as commercially available ECG machines.

References

- 2.1 – Wikipedia(2013; August). "ISM Band"[Online]. Available:
http://en.wikipedia.org/wiki/ISM_band
- 2.2 – Maxim(2012;June). "Max70300 Datasheet"[Online]. Available:
<http://datasheets.maximintegrated.com/en/ds/MAX7030.pdf>
- 2.3 – RFM(2008; August). "DR7000 Datasheet"[Online]. Available:
<http://www.rfm.com/products/data/dr7000.pdf>
- 2.4 –Microchip. "RF Connectivity Solution"[Online]. Available:
http://www.microchip.com/stellent/idcplg?IdcService=SS_GET_PAGE&nodeId=2640¶m=en001021
- 2.5 – Bluetooth. "Bluetooth Basics"[Online]. Available:
<http://www.bluetooth.com/Pages/Basics.aspx>
- 2.6 – Zigbee Alliance. "Zigbee Technology"[Online]. Available:
<http://www.zigbee.org/About/AboutTechnology/ZigBeeTechnology.aspx>
- 2.7 – Wifi Alliance. "Wi-Fi: Discover and Learn"[Online]. Available:
<http://www.wi-fi.org/discover-and-learn>
- 2.8 – ATMEL (2012; February). "Zigbee enabled transceiver"[Online]. Available:
<http://www.atmel.com/Images/doc8168.pdf>
- 2.9 – J. Silberberg (1997; February). "Medical Device Electromagnetic Interference Issues, Problem Reports, Standards, and Recommendations"[Online]. Available:
<http://www.fda.gov/downloads/MedicalDevices/DeviceRegulationandGuidance/GuidanceDocuments/UCM072177.pdf>
- 2.10 – D. Witters et al. "Medical Devices EMI: FDA Analysis of Incident reports, and Recent Concerns for Security Systems and Wireless Medical telemetry"[Online]. Available:
<http://ieeexplore.ieee.org/stamp/stamp.jsp?arnumber=00950633>

2.11- T, Hikage et al. "Active implantable medical device EMI assessments for electromagnetic emitters operating in various RF bands," Microwave Workshop Series on Innovative Wireless Power Transmission: Technologies, Systems, and Applications (IMWS), 2011 IEEE MTT-S International , pp.109-112, May 2011

2.12 – IEEE Engineering in Medicine and Biology (2008; December). "Health Informatics - PoC Medical Device Communication - Part 00101: Guide-- Guidelines for the Use of RF Wireless Technology"[Online]. Available: <http://ieeexplore.ieee.org/stamp/stamp.jsp?tp=&arnumber=4736537>

2.13 - IEEE Committee on Man and Radiation (1998). "COMAR Technical Information Statement, Radio Frequency Interference With Medical Devices"[Online]. Available: <http://ewh.ieee.org/soc/embs/comar/interfer.htm>

2.14 – D. Hyder (2002; July). "Infrared sensing and data transmission fundamentals"[Online]. Available: <http://ewh.ieee.org/soc/embs/comar/interfer.htm>

2.15 – Microchip (2007). "MCP2122 Datasheet"[Online]. Available: <http://ww1.microchip.com/downloads/en/DeviceDoc/21894c.pdf>

2.16 – VISHAY(2004; January). "TFDU4300, infrared transceiver module Datasheet"[Online]. Available: <http://pdf.datasheetcatalog.com/datasheet/vishay/82614.pdf>

2.17 – VISHAY (2007; December). "TFDU4101, , infrared transceiver module Datasheet"[Online]. Available: <http://www.farnell.com/datasheets/87975.pdf>

2.18 – VISHAY (2006; July). "TFBS4650, infrared transceiver module Datasheet"[Online]. Available: <http://www.farnell.com/datasheets/60689.pdf>

2.19 – Microchip (2003; March). "Microchip Infrared product family"[Online]. Available: <http://ww1.microchip.com/downloads/en/DesignCenter/21627c.pdf>

2.20 – Connexion (2009; November). "Review of Data analysis methods for Denoising and Characterizing ECG"[Online]. Available: <http://cnx.org/content/m32823/1.1/>

2.21 – J. Hampton, "The ECG made easy (Third edition)", Uni.v of Nottingham, Nottingham UK, 1986

2.22 – J. Malmivou, R. Plonsey, "Bioelectromagnetism - Principles and Applications of Bioelectric and Biomagnetic Fields", Oxford Univ., New York, 1995

2.23 – Open ECG Project. "Open ECG Project"[Online]. Available: <http://www.open-ecg-project.org>

2.24 – Texas Instrument (2008; July). "INA333 Datasheet"[Online]. Available: <http://pdf1.alldatasheet.com/datasheet-pdf/view/239865/TI/INA333.html>

2.25 – Linear Technology. "LTspice IV"[Online]. Available: http://cds.linear.com/docs/en/product-info/LTspiceIV_flyer.pdf

2.26 – LochMaster. "LochMaster4.0"[Online]. Available: <http://www.abacom-online.de/uk/html/lochmaster.html>

2.27- Microchip (2011; February). "MCP1640 Datasheet"[Online]. Available: <http://ww1.microchip.com/downloads/en/DeviceDoc/22234B.pdf>

3 – Development of the ECG processor and triggering procedure

The ECG Processor is responsible for receiving and analysing ECG waveforms; and initiating and delivering the trigger signal to the ultrasound system. It also ensures accurate timing for triggering the ultrasonic scans. Moreover, the ECG Processor acts as the connecting bridge between the DAQ board and the UPR making the DAQ output signals compatible with the input of the UPR.

The development of the ECG monitor itself was discussed in detail in the previous chapter. After capturing the ECG trace from the patient, it must be analysed and used to trigger the ultrasound scans at the desired point of the cardiac cycle. The analysis of the ECG signal requires substantial amount of computing on the board in real-time. This would negatively affect the power usage of the ECG monitor board. For this reason the analysis of the ECG trace was delegated to the ECG processor board.

This chapter presents the process of developing, testing and improving the ECG processor board in order for it to become as reliable as possible in analysing the ECG signal and detecting the R-wave of the ECG trace with high accuracy and low latency. The algorithm developed for this detection is discussed in detail along with its implementation and experimental verification.

Debugging the ECG processor starts from establishing the IR communication to the ECG monitor. The combination of IR communication, ECG monitor, ECG processor and the R-wave detection algorithm is expected to fulfil the requirements for triggering ultrasound scans at a particular time of the cardiac cycle in order to significantly reduce the changes caused by blood circulation on the IMT and improve the accuracy of lumen diameter and IMT measurement.

3.1 – Requirements of the ECG Processor

The ECG Processor is the second development in this research project. Before this development, the ECG monitor is fully developed to detect the heart activity signals, and pass these signals to the PIC microcontroller. The PIC on the ECG Monitor digitises and sends this data through the MCP2122 IC to the IR module for broadcasting. The ECG processor then receives the ECG data over the IR link, and generates the trigger at the phase of the heart cycle set by the user. The block diagram of the ECG processor is presented in figure 3.1.

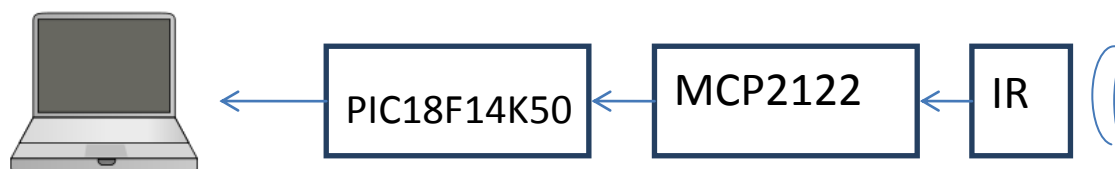


Figure 3.1 - Block diagram of the ECG processor

In addition to analysing the ECG trace and producing the trigger signal for the DAQ, the ECG processor integrates additional circuits that are responsible for matching the 0 to 1V operating levels of the DAQ to 0 to 5V operating levels of the ECG processor and the UPR as shown in figure 3.2.

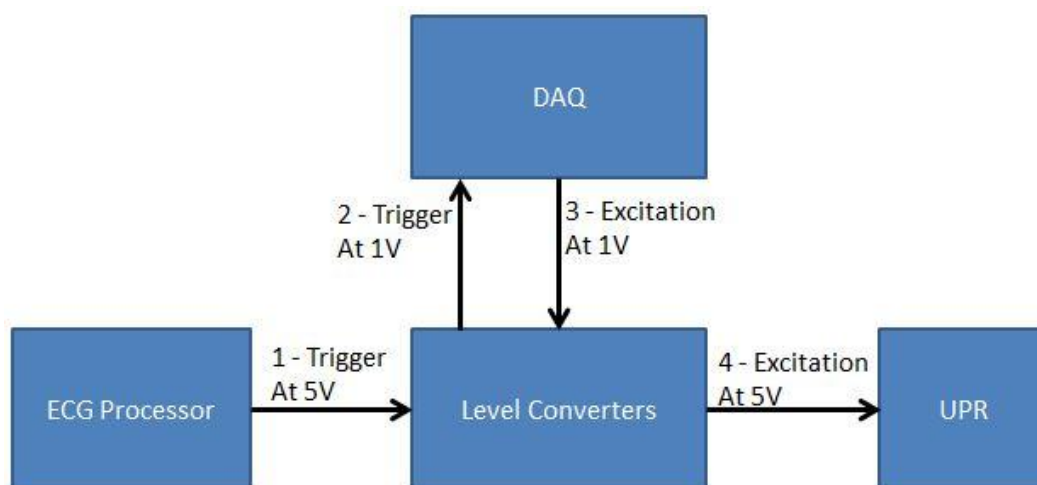


Figure 3.2 – Converting voltage levels in the ECG processor

3.2 – ECG Processor development

Over the course of this project, the ECG processor went through two stages of development and eventually became a robust, intelligent, easy to use and reliable system capable of meeting the requirements of the overall set up. The first PCB board was designed and developed to only analyse the ECG waveforms and provide the trigger signal for the UPR. This was sufficient to develop the algorithm that detected the R-wave of the ECG, and verify it in vivo

The second stage of the development process is adding the bridge between the DAQ and UPR which eliminates the need of any additional modules that were required otherwise. Second PCB was developed for this purpose, and it was used for in vivo experiments.

3.2.1 – First prototype

The ECG processor circuit, as shown in figure 3.3, includes the PIC microcontroller as the central component of the board, MCP2122 to decode the IR data, TFDU4300 to receive data over IR, and a three colour LED for indication of the state of the board. Components used for this board are very similar to the ones used in the digital part of the ECG monitor with similar connections among them. Therefore, the same detailed description of the design is not repeated here. However, there are some differences that need to be discussed in order to fully cover the operation of the ECG processor.

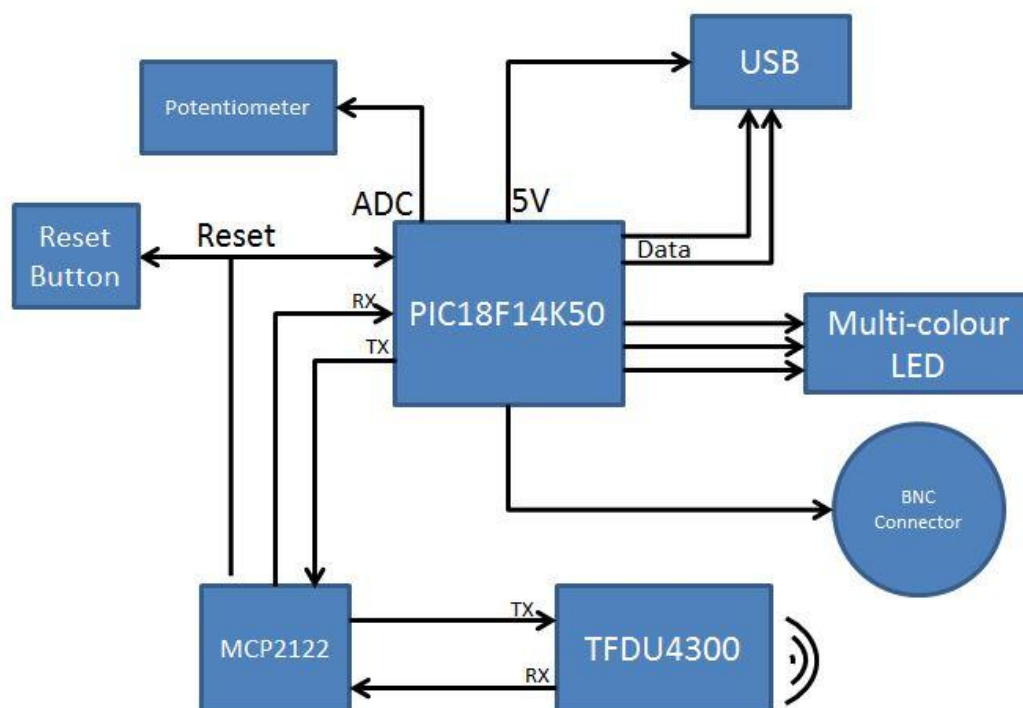


Figure 3.3 – Block diagram of the first design of the ECG processor

The first difference is the use of a potentiometer on the board. The voltage at the centre pin of the potentiometer, read by the PIC's AD, sets the time delay between the detection of the R-wave and the start of the trigger signal.

The second additional component is the USB socket placed on the board. The ECG processor was designed with the provision of using USB for powering the device to make it easier to carry around. USB ports have four different pins as shown in figure 3.4. These are power supply, ground connection, Data- and Data+. Power and ground pins are used to power the ECG processor; D+ and D- allow establishing communication via a USB cable.

The first purpose of these signal lines is to determine what type of device, if any, is connected to the host. D- and D+ lines are pulled to low state by two 15kΩ resistors; therefore, when there is no device connected to the host the value is read as '0'. As soon as a device connects to the host, it reports its communication speed to the host as follows:

1. D+ is set high and D- is set low; this combination is interpreted by the host as connection of a high speed USB device;

2. D+ is set low and D- is set high; which indicates that the device can only use the low speed configuration;
3. During the idle state, which is before and after sending data packets, depending on the speed configuration, one of the lines is set high and the other one is set to low.

For the purpose of this project, the USB cable is only used for supplying power to the ECG processor board. For this reason the state of the D+ and D- lines was irrelevant. However, selection of the PIC18F14K50 microcontroller [3.1] allows the USB communication to be added to the functionality of the ECG processor at a later stage.



Figure 3.4 - USB pin out

Table 3.1 - Purposes of the USB socket pins

Pin	Name	Cable color	Description
1	VCC	Red	+5 VDC
2	D-	White	Data -
3	D+	Green	Data +
4	GND	Black	Ground

The third and final important difference between this prototype and the ECG monitor is the presence of a BNC connector which is used to output the trigger signal to the DAQ.

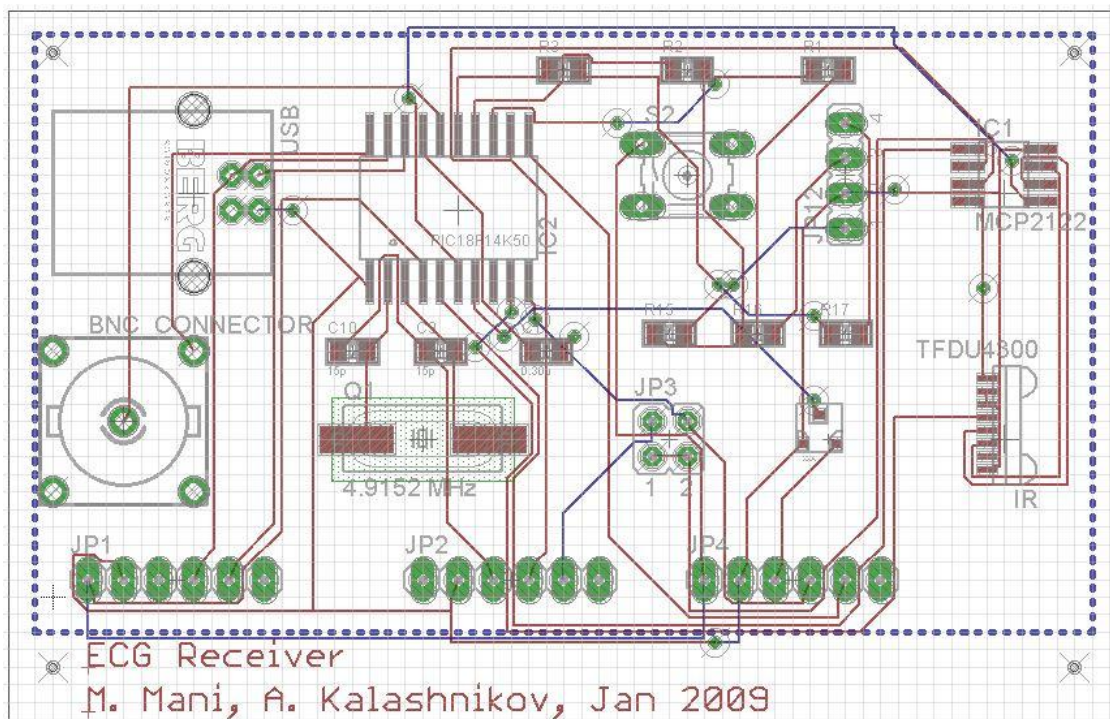


Figure 3.5 - PCB of the first ECG processor



Figure 3.6 - First ECG processor assembled

Figure 3.5 presents the PCB layout of the first ECG processor while figure 3.6 shows the assembled PCB. This board is used for debugging the IR link between the two boards (namely ECG monitor and ECG processor), development of the algorithm for the R-wave detection, and initial tests for setting the trigger delays.

3.2.2 – Level converter design

As it is shown in figure 3.2, there is a need to convert the DAQ board signal levels (0/1 V) to the 0/5 V values required by the other circuitry used. This was provided by designing the following two circuits

- ECG processor to DAQ level converter,
- DAQ to UPR level converter.

These are discussed in detail below.

3.2.2.1 – ECG processor to DAQ level converter

The DAQ board only accepts voltages of up to 1V whereas the ECG processor is powered by USB from a personal computer, generating the trigger signal with the amplitude of 5V. The reduction of this output voltage can be achieved by using a potential divider consisting of two resistors only. However, in this case this solution is not feasible because of the low input impedance of the DAQ board of 50 Ω . If this impedance is complemented by a series resistor of 200 Ω , the required reduction of the ECG processor trigger voltage can be achieved. However, the PIC needs to source $5V/250 \Omega = 20$ mA of current that is at its rated limit. This current is delivered over a long cable that could skew the trigger signal and introduce signal reflections, resulting in reduced accuracy of triggering. Additionally, the circuit would experience current rushes when the DAQ board is connected/disconnected, reducing reliability of the design. For these reasons a combination of a comparator and an opamp acting as a cable driver was used instead (figure 3.7). The comparator trips when the voltage at its positive input exceeds 1 V (set by the potential divider R1R2 connected to the negative input), shorting its open collector output to ground. When the input voltage is below 1 V, the comparator output stays at high impedance, and the potential divider R3R4 holds the input of the cable driver at 2 V. The cable driver is connected as the voltage follower, keeping this voltage at the series connection of R5 and input impedance of the DAQ board. Therefore, 1V level appears at the DAQ input. When the comparator trips, the voltage at the input of

the DAQ board decreases to 0 V. Thus this level converter inverts the trigger signal produced by the ECG processor.

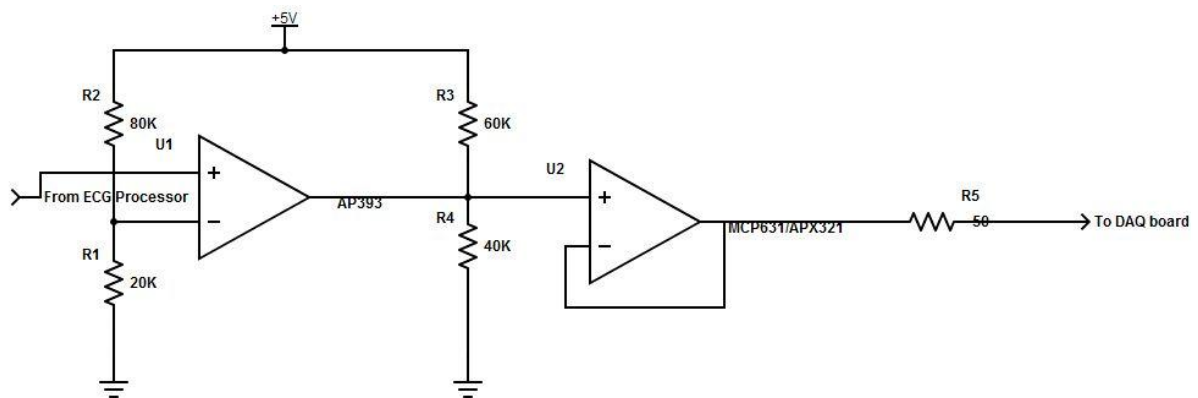


Figure 3.7 - Schematic of 5V to 1V amplifier

Initially the schematic presented in figure 3.7 was implemented on a breadboard to test both the operation, and stability of the design. Two different opamps, MCP631 [3.2] and APX321 [3.3], were employed to find the better of the two for the voltage follower. The breadboard design and the assembled breadboard itself are presented in figures 3.8 and 3.9 respectively.

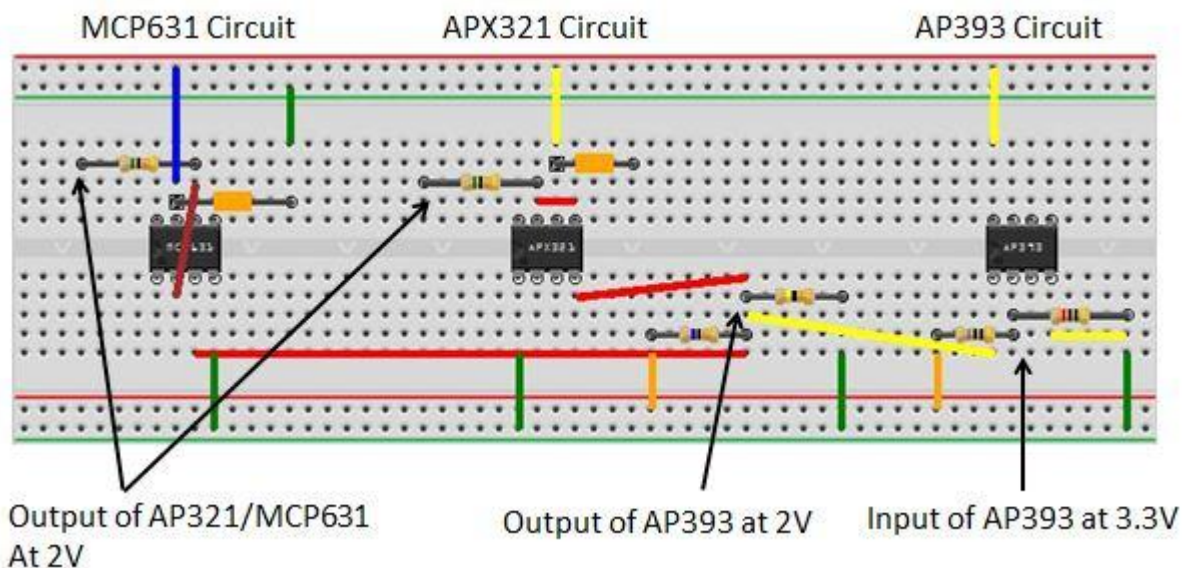


Figure 3.8 - Breadboard design for the ECG processor to DAQ level converter

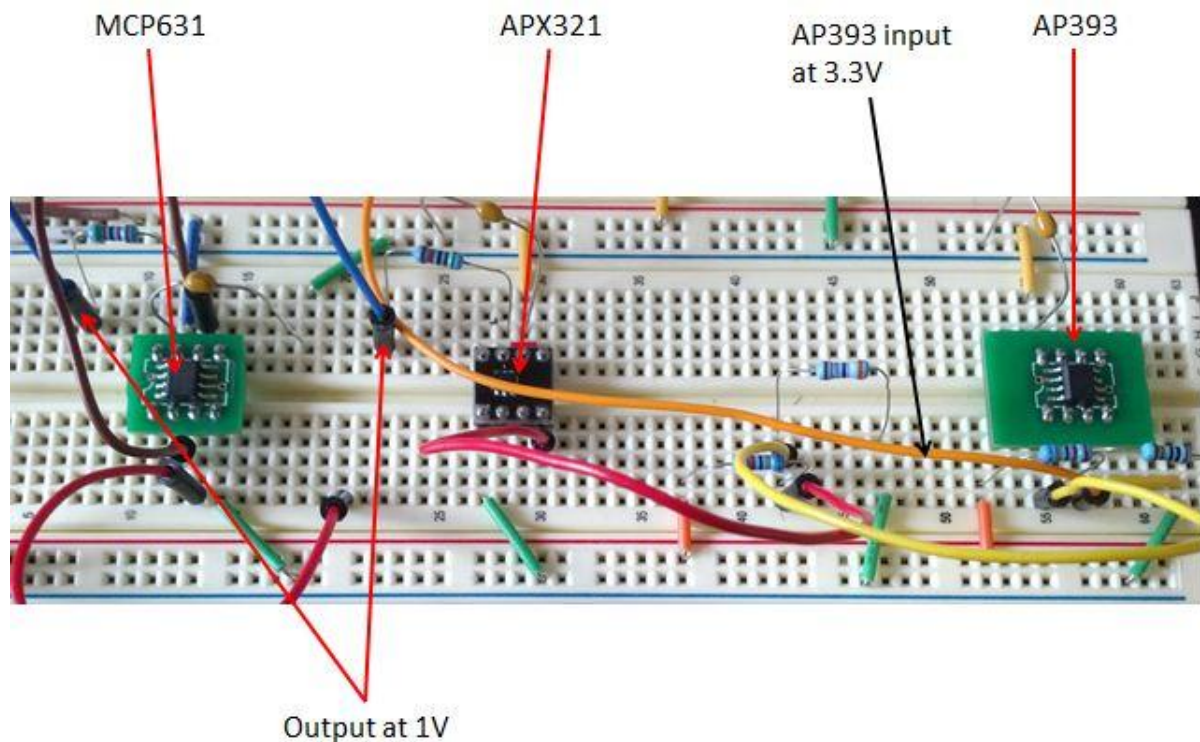


Figure 3.9 -Assembled on a breadboard ECG processor to DAQ level converter

The operation of the assembled veroboard is tested with the input voltage provided by the PicoScope at 3.3 V; three different points of the circuit are checked to track the signal throughout the circuit to ensure the correct operation of the circuit:

1. output of the comparator;
2. output of the voltage follower;
3. voltage at the DAQ input.

Unfortunately APX321 amplifier did not work on the adaptor, most likely due to the thermal damage occurred when it was soldered. Since the MCP361 operated as required, it was selected for the design without making a comparison with another APX321 IC.

The PCB design of this part was implemented using EAGLE software and the schematic is shown in figure 3.10.

Chapter 3 Development of the ECG processor and triggering procedure

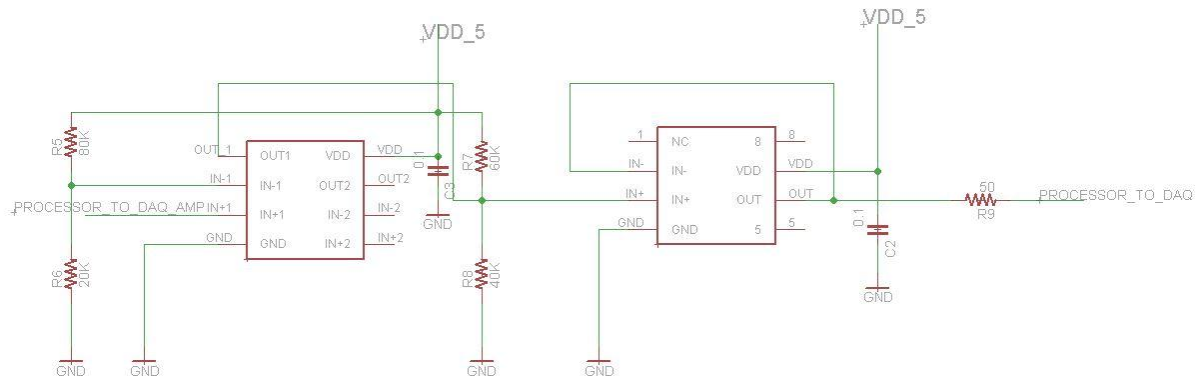


Figure 3.10 - EAGLE design of the ECG processor to DAQ level converter

3.2.2.2 - DAQ to UPR amplifier level converter

The second section of figure 3.2 is the level converter which converts the output of the DAQ (0/1 V) to 0/5 V, to be supplied to the external trigger socket of the UPR. The AP393 comparator is used here to detect when the voltage coming from the DAQ to its positive input, is above the value set by the potential divider R1R2 (1:10 at 0.5 V) at its negative input (figure 3.11).

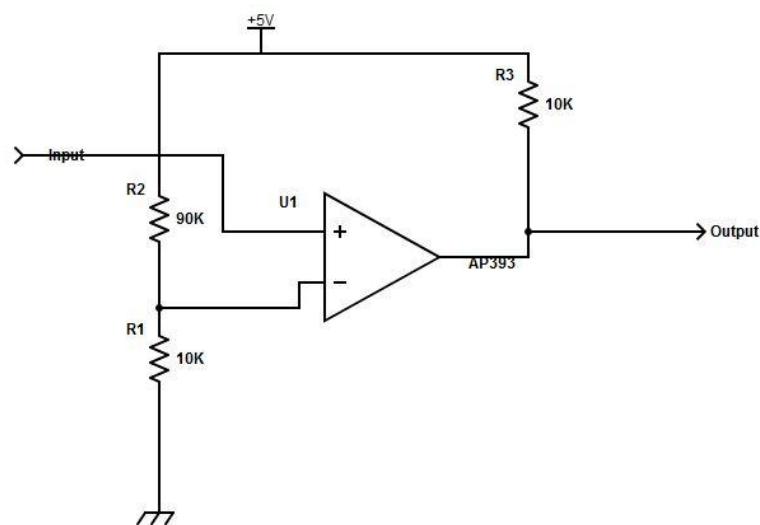


Figure 3.11 - Schematic of the DAQ to UPR level converter

To test the operation of the level converter, it is assembled on a breadboard (figures 3.12, 3.13) and tested using input signal from the PicoScope.

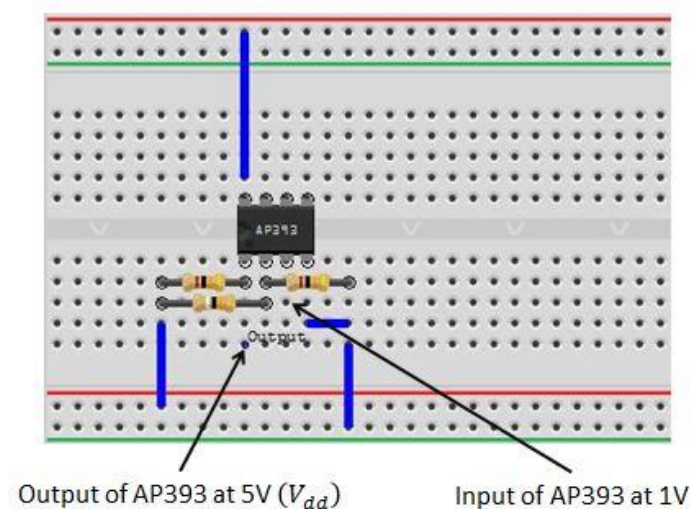


Figure 3.12 - Breadboard design of the DAQ to UPR level converter

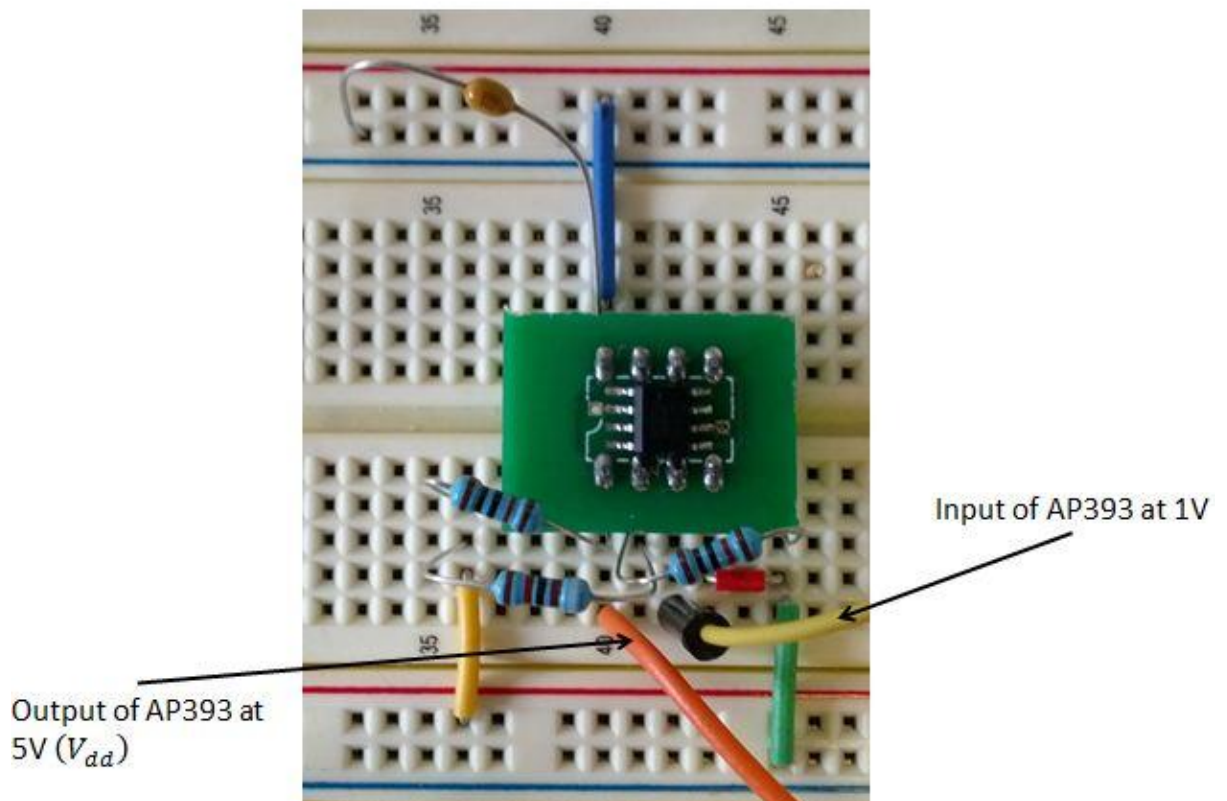


Figure 3.13 – Assembled on a breadboard DAQ to UPR level converter

The recorded waveforms are presented in figure 3.14, confirming appropriate operation of the level converter.

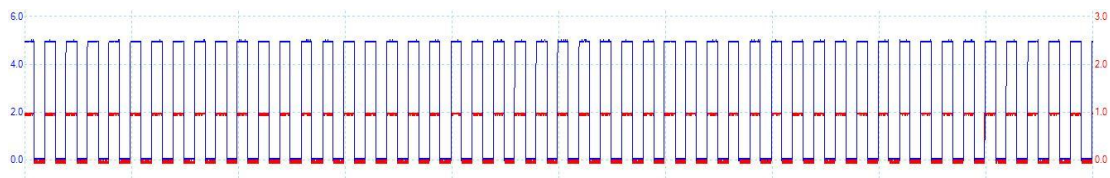


Figure 3.14 Operation of the DAQ to UPR level conversion (red curve – input signal from the PicoScope, blue curve – output signal to the UPR)

3.2.3 – Final design of the ECG processor

After designing and testing the two level converters, they were combined with the ECG processor described in section 3.1.1.1. The new board was designed using EAGLE software as before. The complete schematic was partitioned into three pages for simplicity in dealing with different parts of the design.

First page (figure 3.15) is the original ECG processor circuit with two amendments:

1. The number of BNC connectors was increased to three, to allow the output/input signals of the level converters to be connected to required parts of the overall system
2. The potentiometer was changed to a physically bigger part to ease setting the trigger delays.

Second page (figure 3.16) is the level converter which connects the processor to the DAQ board converting the output of the board to 0/1 V as required. Third page (figure 3.17) is the 1 V to 5 V level converters to connect the DAQ external trigger output to the UPR input. The operation of the level converters are shown in figure 3.2 as a separate board which is included in the final ECG processor to make the overall system more compact and easier to use.

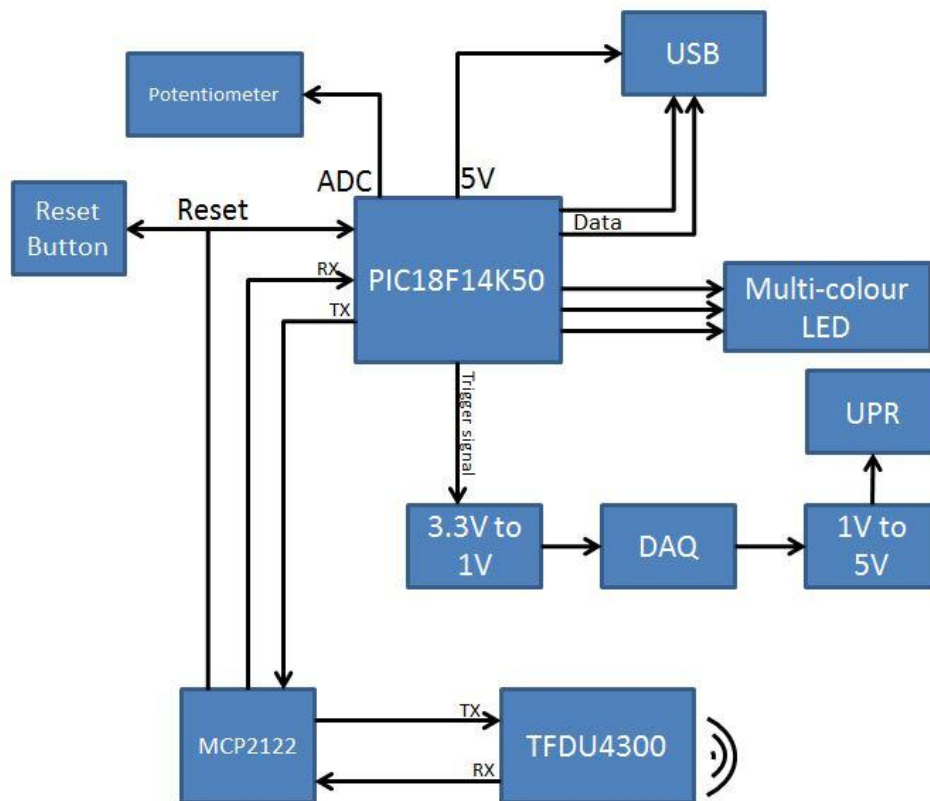


Figure 3.15 – Block diagram of the final design of the ECG processor

Figure 3.19 shows the layout of processor PCB manufactured to be used with the rest of the system. Compared to the first designed PCB shown in figure 3.6, the developed PCB of the complete circuit, shown in figure 3.17, is still a

Chapter 3 Development of the ECG processor and triggering procedure

compact board even with the additional level convertors and the two extra BNC connectors.

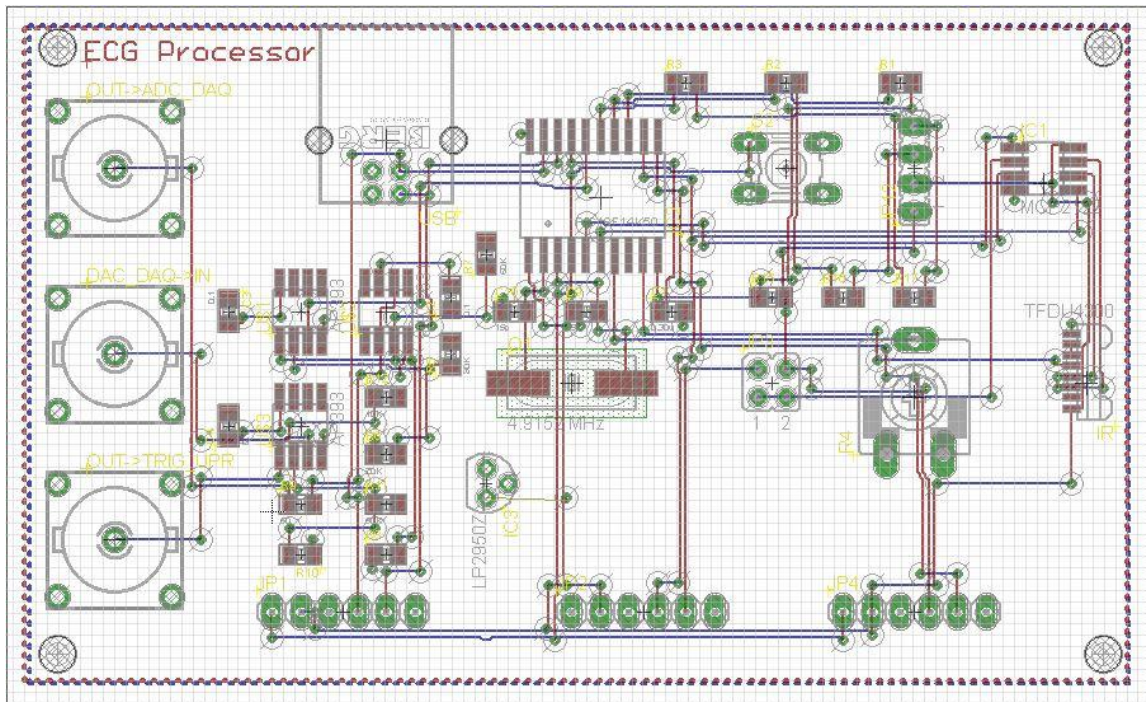


Figure 3.16 - PCB layout of the final ECG processor board



Figure 3.17 - Assembled second ECG processor board

3.3 – Establishing and debugging the IR link

In order to develop a reliable link between the ECG monitor and processor, IR communication was first established using a separate board. It consists of a Full Speed USB (FSUSB) board [3.4] which is plugged in IR custom board (figure 3.18).

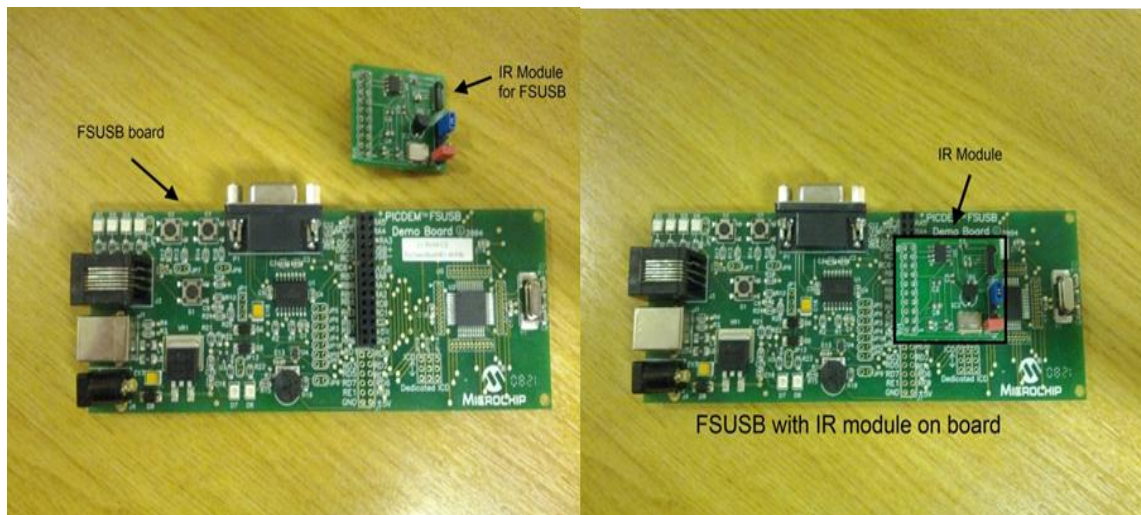


Figure 3.18 - FS USB board with IR transmitter module (left - shown separately, right - shown connected)

Each of the two buttons available on the top left corner of the FSUSB board are used to trigger transmission of a single letter, “a” or “b”, to the IR receiver (either the ECG monitor or processor board). Additionally, particular LEDs are switched on when these characters are received back. The receiver is programmed to switch on an LED of a particular colour, and transmit the received character back to the FS USB board. This ensures that the communication is running both ways at the set bitrate, and correct characters are being transmitted or received.

However, it is not possible to verify that the correct ADC data are transmitted and received continuously. This is verified using an additional IR development board from Microchip [3.5], which is capable of sniffing the ongoing IR communication, and outputting the data stream via an RS-232 port. An additional RS-232 to USB converter is used to bridge the board with a laptop (figure 3.19).

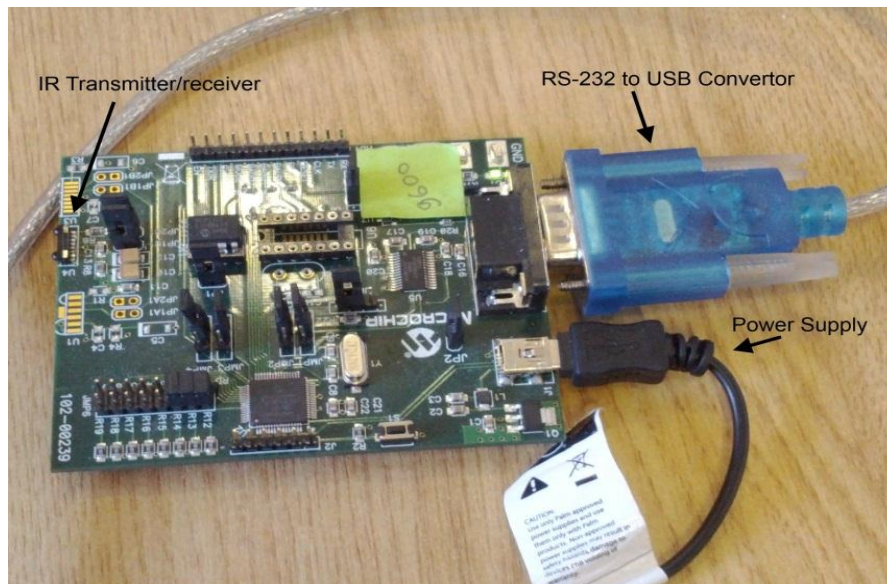


Figure 3.19 - Microchip IR transmitter/receiver board connected to a PC

A MATLAB program was developed to log the data stream on a PC. This program receives and records the ECG signal transmitted from the ECG monitor. It also sends the previously recorded or simulated ECGs to the ECG processor for a complete simulation of the detection of the R-wave. The USB cable connects the board to a PC, creating a virtual COM port. MATLAB opens this virtual port using Serial Communication functionality. The "serial" class in MATLAB creates an instance of the Serial Communication port, opens the port, sends data over the port and reads the port for any received data.

If any data is received by the Microchip IR board, it will be stored at the buffer of the COM port. "fread" can be used to read the buffer and store the received values in a MATLAB variable. It is important to ensure that every COM port is closed after the completion of communication in order for it to be reused later.

Using these debugging facilities (two IR boards and MATLAB program), the IR communication firmware was verified for the ECG monitor and processor independently. The examples of the communicated experimental waveforms are presented and discussed in the following section.

3.4 – Development and testing of the algorithm for triggering the ultrasonic scans

Because of the difficulties in debugging the triggering algorithm using live waveforms, MATLAB software was used to send a previously recorded or artificially simulated ECG signal to the ECG processor board. An intelligent algorithm was designed, verified in MATLAB and implemented in the firmware of the ECG processor, which detects the R-wave in the ECG signal in real time and generates the trigger signal to the UPR.

3.4.1 – Simulating an ECG signal

Simulating an ECG signal has the advantage of being able to get a variety of waveforms with the range of parameters, which are difficult if at all possible to record experimentally. ECGSYN, a toolbox of MATLAB, was used to generate the signal [3.6]. The ECG signal frequency, its sampling frequency, amplitude and noise level are set by the user.

For the purpose of this work the average heart rate is set to 60 beats per minute (bpm) with the standard deviation of 1 bpm. The internal sampling frequency is set to five times 612 Hz. Then 6000 samples of the simulated signal are selected as one complete cycle of the ECG, and quantised to the range from 0 to 255, ready to be transmitted to the ECG processor. The following simulation shows how noise with different amplitudes (0, 0.1, 0.2 and 0.5 in decibels respectively) distorts the waveform (figure 3.20).

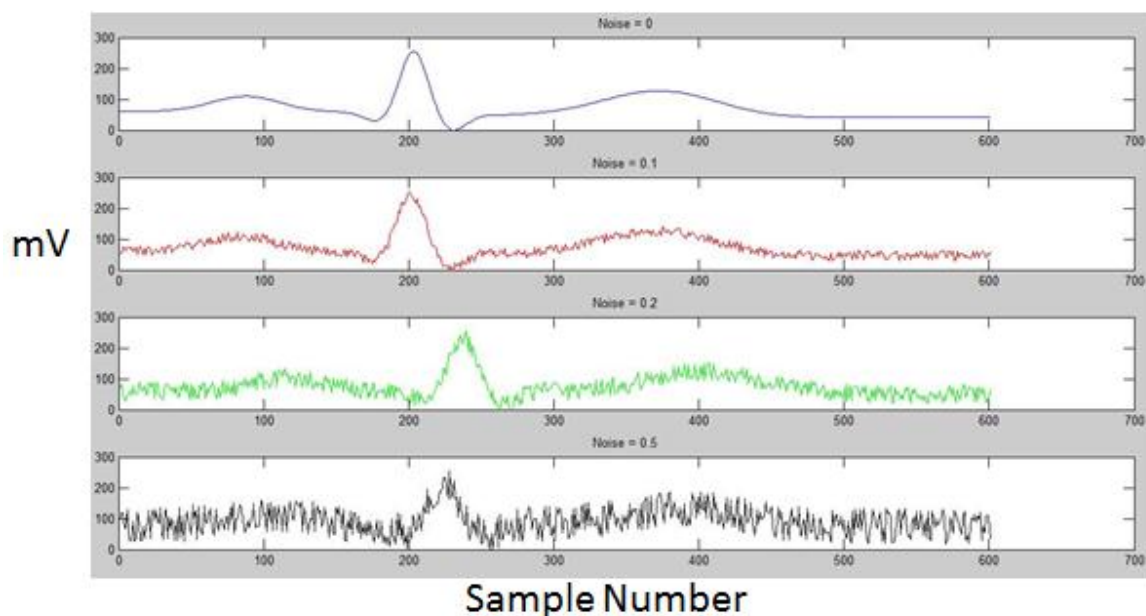


Figure 3.20 - Effect of different levels of noise on the simulated ECG

3.4.2 - Detection of the R-wave

3.4.2.1 - Methodology

Several algorithms were developed in order to determine the heart rate out of ECG records. For instance, Pan and Tompkins algorithm detects the QRS complex for the heart beat detection [3.7]. This method uses a digital bandpass filter to reduce the noise of the ECG trace, calculates the derivative of the ECG waveform, then squares the signal which makes all the points positive and finally uses a moving average window to analyse the characteristics of the QRS complex. There are two thresholds used in this method; the lower threshold is to detect the QRS complex and the higher threshold is to detect the R-wave.

According to this method, a 30 sample window (which takes 150ms in the time domain if the sampling rate is 200 samples/s) is used to analyse the QRS complex after its detection in order to find the sample with the largest value. The time position of the sample is assumed to be the time position of the R-wave. This method was originally implemented in Z80 assembly language and the highest percentage of the failed detection including both false negative and false positive is 0.675% [3.7, table 1].

Chapter 3 Development of the ECG processor and triggering procedure

The above method requires an ECG waveform to be acquired with a high SNR, and additional improvements were achieved by the use of a bandpass filter, derivative and squaring operation.

The computing power required for this method may not be readily available at microcontrollers that have limited memory available to them.

For the purpose of the R-wave detection required for this research project, a simpler algorithm was developed and verified using recorded and real time in vivo data. The algorithm was implemented using a microcontroller, and was capable of confident processing of waveforms sampled up to 1 kHz. Different methods were examined first to find the most reliable algorithm to detect the peak. The algorithm should not falsely detect an R wave from noise if the wave is absent; otherwise the IMT reading will be completely unrelated to the desired instant of the heart cycle. Triggering of the scans should ideally happen at every heart cycle, however, missing some of the R waves will only increase the measurement time without producing false readings. Therefore, in terms of the detection theory, misses of the R wave are acceptable but false alarms are not [3.8].

The simplest way to detect the maximum value during an ECG cycle is to compare each subsequent sample with the previous one; when the following sample shows smaller value, the previous sample will be the maximum. However, because an ECG waveform has three different peaks for P, R and T waves, three maxima would be detected during a single heart cycle. For this reason it is necessary to isolate the R wave first, which can be done by using a threshold that is set to a higher value than the amplitudes of both the P and T waves.

The appropriate threshold can be set, for example, by capturing 5000 ECG samples and finding the maximum value among them. Then the threshold can be set at, e.g., 75% of the maximum value that will eliminate false alarms from the P and T waves.

This method is the fastest way of detecting the R-wave since the latency for detecting an R-wave is one sample only. However, this method only works in

the case of a perfect noiseless ECG signal. The presence of noise causes misreading of the ECG value by the PIC, which can be either higher or lower than the actual value. There are two cases when the presence of noise could cause erroneous detection of the R-wave.

First, if the value of the actual ECG is not yet over the R-wave threshold, but the added noise takes a signal sample over this threshold, but the next sample is lower. In this case an R-wave will be detected without waiting for the actual peak in the ECG trace.

In the second case, the ECG signal is already above the threshold and the program is looking for the sample that is less than the previous one. At this stage, if the noise causes a drop in the actual value of an ECG sample below the previous one, this will lead to a false detection of the R-wave.

To overcome this issue, another state is added to the program to ensure that the threshold crossing is not caused by the noise. When a sample is found above the threshold, the program waits for another three samples above the threshold. When this happens, the actual ECG has crossed the threshold and the detection of the R-wave can be initiated using the same method as the previous case; capturing samples until the current sample is lower than the previous sample, counting the previous sample as the R-wave.

Even though this principle prevents any false detection of samples above the threshold, the presence of the noise can still change the value of the ECG signal in the way that a false R-wave can be detected. For this reason, when three consecutive samples above the threshold have been captured in the buffer, the ECG signal is assumed to be above the threshold and another 17 samples are added to the buffer. Total of 20 samples are compared to find their maximum value; the sample with the maximum value is assumed to be the R-wave. With the 200Hz sampling rate of the system, a window of 20 samples is 100ms long to detect the R-wave. This amount of time allows the detection of the R-wave and also reduces the chance of mistaking the T-wave for an R-wave and having a false detection.

The final method is an accurate and viable option to detect the R-waves. This method is simulated in MATLAB and verified using simulated 5000 samples.

3.4.2.2 – R-wave detection algorithm with static threshold

After successful simulation of the algorithm in MATLAB, the same method was implemented in C for the ECG processor. To verify the operation of the program, the ECG samples are sent to the ECG processor from MATLAB. To make the test more realistic the ECG samples are sent continuously to simulate a live ECG.

There are a number of tasks that the ECG processor needs to complete for it to be ready to receive and analyse ECG waveforms. Firstly, the communication between the ECG monitor and ECG processor needs to be established and confirmed. Therefore the receiver board was configured in order to send the data back to the MATLAB program. This is to test the operation of the algorithm after a set delay from the received sample. This data change based on the state of the ECG processor analysis.

The second step is to calculate the required threshold. While the threshold was being calculated, the same received data was sent back to MATLAB. This state shows the correct operation of the communication, and also that the right values are received by the receiver. When the threshold is calculated and set, its value is sent back for 255 samples. This appeared as a flat line for a small period of time on the graph.

The third and final step is to detect the R-wave and send the trigger pulse to the UPR. After sending the threshold to the MATLAB program, the program sends the received samples until the R-wave is detected and the trigger signal generated. The trigger is indicated by a flat line with the low value for 20 samples.

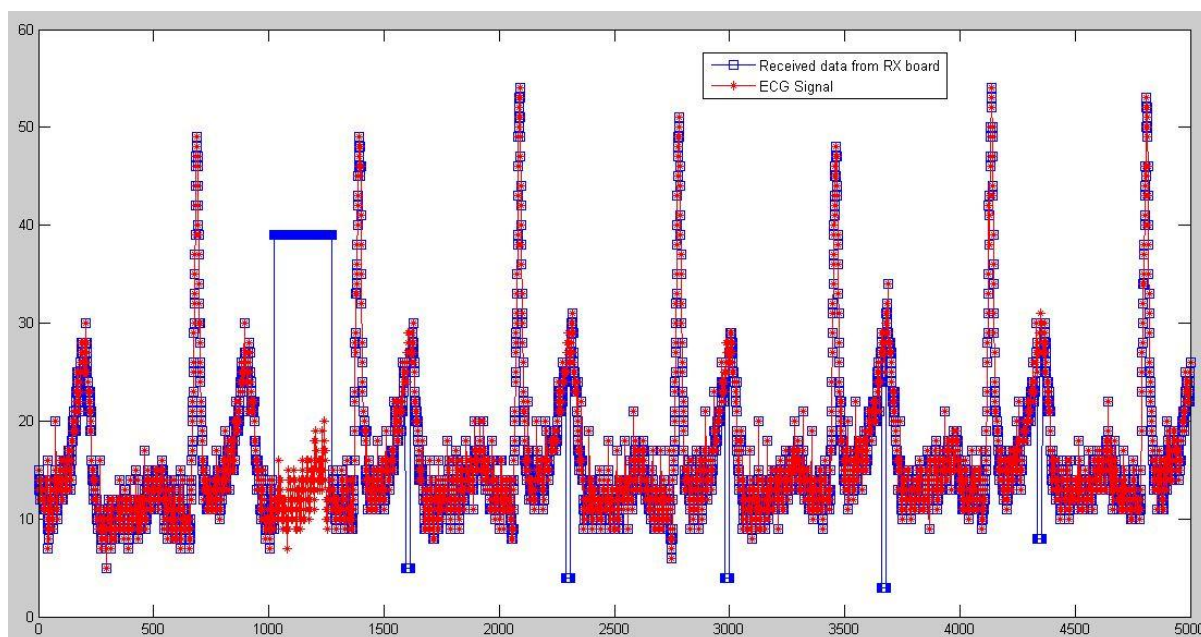


Figure 3.21 - Simulation of the R wave detection (calculated threshold is shown starting from the sample 1000; the triggers are shown by low value horizontal lines) – X-axis represents sample number and the Y-axis is in mV

Figure 3.21 shows the results of simulating the R-wave detection by the ECG processor that includes the three steps discussed above. The horizontal blue line shows the detection of the R-wave; however the triggering is not shown on the R-wave due to the implemented delay in the code. The delay can be changed based on the requirements by the user, as explained in 3.4.2.7.

3.4.2.3 - Use of time stamps

A simple counter was created in the code to produce time stamps on the trigger signal. This feature is required for testing purposes only and was removed at the final stage of testing. The primary purpose of these time stamps was to ensure that the connection between two boards was not interrupted during the experiments and the samples were being sent and received continuously. Time stamps were also used to measure the time delay between the detection of the R-wave and trigger generation.

3.4.2.4 - Experimental verification

When the algorithm was fully simulated, a 60 seconds long in vivo experiment was performed to verify the operation of the ECG processor with live ECG signals. Figure 3.22 presents the recorded trigger signals and time stamps (blue curves) and the ECG signal (red trace).

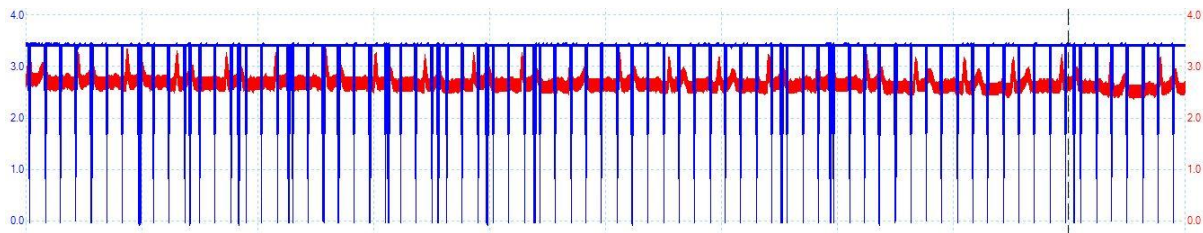


Figure 3.22 - Experimental ECG with trigger 0 to 20 seconds (amplitude in mV vs time in mS)

Assuming that the patient is at the resting state during the experiment his heart rate should be around 60 bpm producing approximately 60 trigger pulses; however figures 3.26-3.28 display only ten trigger signals. The presence of the time stamps in the blue traces of above graphs confirmed that the ECG processor operated appropriately. Therefore, the only possible explanation for the detection of only ten R-waves is a flaw in the algorithm itself.

3.4.2.5 - Adaptive calculation of the threshold

60 second ECG records were converted into MATLAB data before filtering for further analysis and plotted as shown in figure 3.23. The quantisation noise present in the graph is caused by the limited 8-bit resolution of the Picoscope which was used for recording the traces.

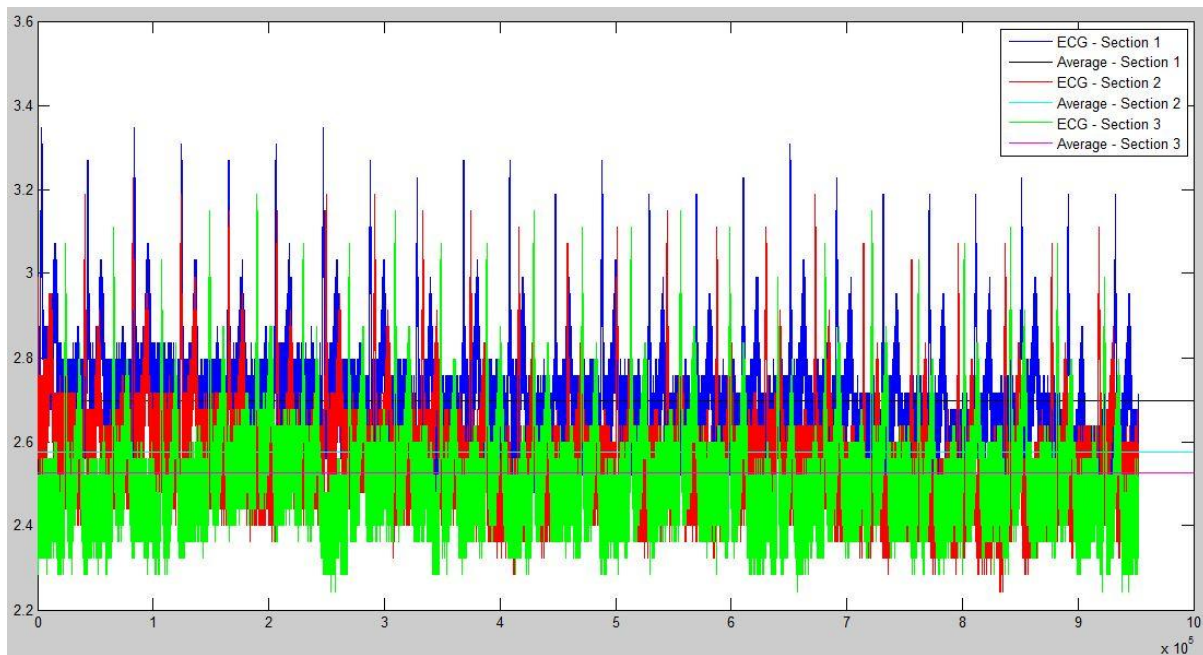


Figure 3.23 - 60s Experimentally recorded ECG

The average for every 20-second period was calculated and plotted in the graph. It was observed that the average of the ECG signal was not constant over the whole 60 second period; in fact the baseline of the ECG waveform decreased during the experiment from 2.69 V for the first 20s to 2.57 V for the second 20 s then to 2.52 V for the final 20 s periods (figure 3.31).

Analysis showed that the threshold, calculated within the first five seconds (5000 samples), became too high for the R-wave to be detected when the ECG base line drifted down. Figure 3.24 presents the results of using the detection algorithm for the experimental data figure 3.23.

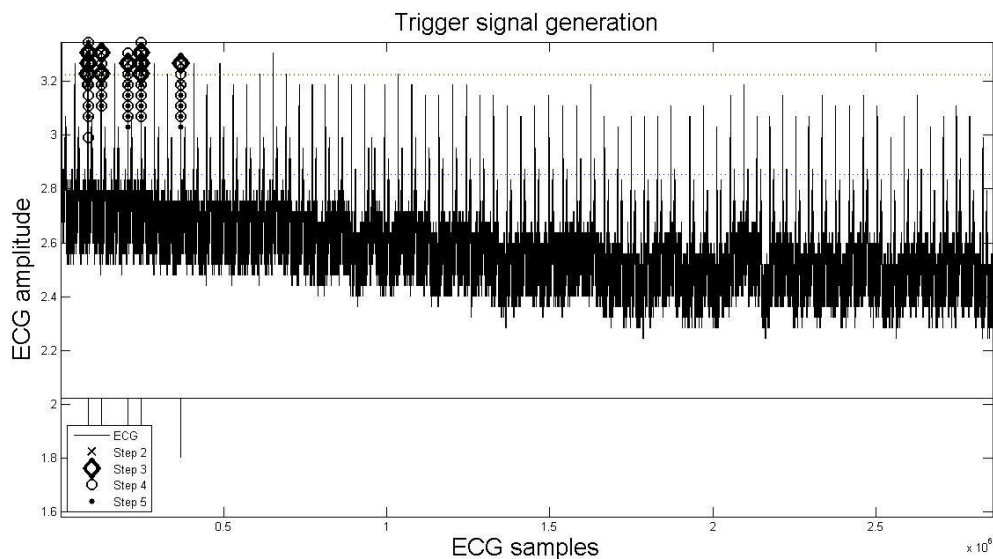


Figure 3.24 - Results of processing experimental data in MATLAB for R-wave detection

After a certain amount of time the whole ECG trace lowers below the threshold, calculated at the beginning, and hence no R-waves can be detected. In order to overcome the problem of the drop in the mean value of the ECG trace, four options were available:

1. leave the ECG to be captured by the ECG Monitor for three to four minutes before transmitting the signal. This option is time consuming and uncomfortable for the patient;
2. form a window for moving average. The size of the window needs to be at least 1000 samples, since there are about that many samples between two consecutive R-waves. If no R-wave is included in the window, the calculated average will be lower than the actual average which will result in a wrong threshold and false detection of R-waves. Unfortunately the on chip RAM of the PIC does not have capacity for storing more than 253 samples; therefore this option is not feasible;
3. an accumulator can be used to measure the average of the overall signal as the values are received. The accumulator has a constant number which every sample is multiplied by. The value of accumulator is calculated by the following equation:

$$\text{Accumulator} = \text{Current sample} \times \text{constant} + (\text{Accumulator} * (1 - \text{constant}))$$

This method was tested to calculate the average of the previously recorded ECG with the constant of 0.01 and an initial value of 120 for the accumulator. The calculated average value seemed to track the ECG average well (figure 3.25);

4. to re-calculate the threshold for another 2000 samples if an R-waves were not detected. With this option, there is a counter that is incremented at the receipt of each new sample. This counter is set to zero every time an R-wave is detected. This method was tested by using the same recorded experimental ECG and enabled detection of most R-waves (figure 3.26).

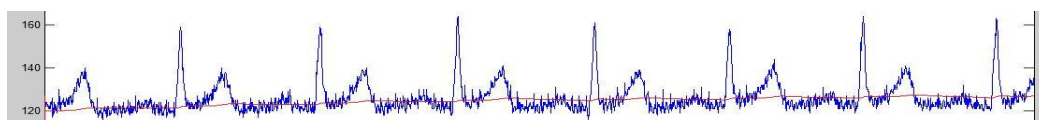


Figure 3.25 - Calculation of moving average threshold (red curve) using the accumulator

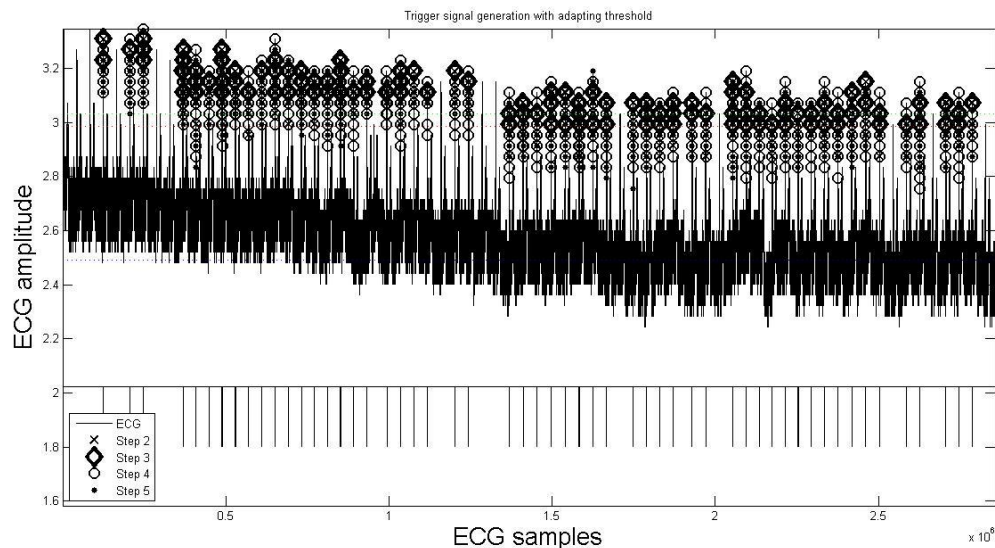


Figure 3.26 - Simulation of the R-wave detection using re-calculated threshold

As it can be seen from figure 3.26, several R-waves are missed because of the baseline drift. Firmware was modified so that the threshold was recalculated if only there was no R-wave detected after a certain number of samples. This version of the algorithm was tested with live ECG and the result is presented in

figure 3.27 – all the R-waves were correctly detected as the algorithm adapted to changes in the baseline.

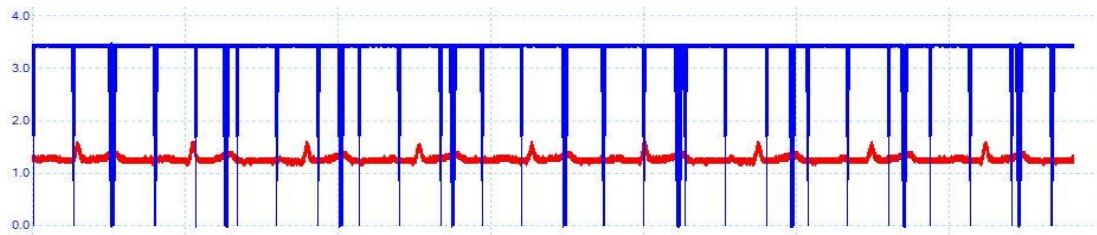


Figure 3.27 - Operation of the ECG monitor with re-calculated threshold (red line – ECG, blue line – narrow time markers and wider trigger events)

After successful experiments conducted using the re-calculating threshold program, the firmware code was modified one more time to make more debugging options available. These options help in tracking the operation of the board. A set of different experiments were carried out to finalize the operation of the algorithm-wave detection with the options to monitor the state of the ECG processor when:

- the threshold is being calculated;
- the R-wave is detected;
- ultrasonic scan is being triggered.

Figure 3.36 displays the ECG waveform (red curve) and ECG processor output (blue curve). The most frequently occurring pulses are the time stamps which help to keep track of time on the waveform. When the threshold is calculated for the first time or when it is re-calculated, the value of the trigger signal is changed for ten samples creating a square wave of 10 periods (figure 3.28).

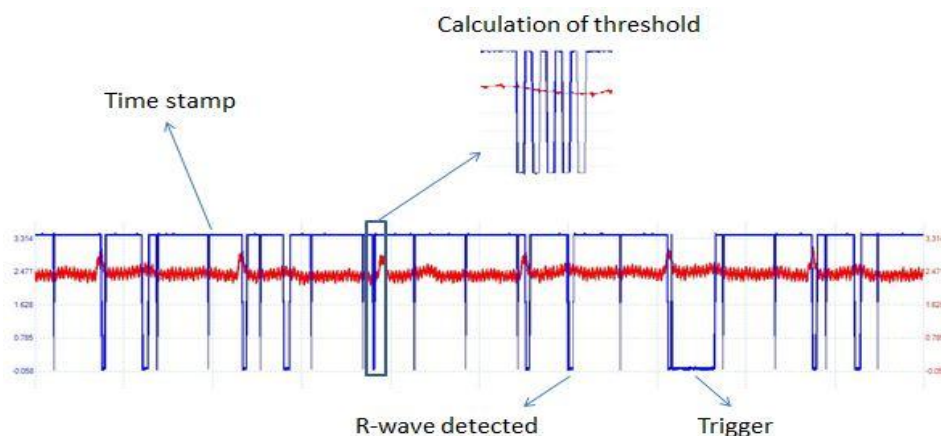


Figure 3.28 - Experimental ECG (red curve) and the ECG processor output (blue line) with all the debugging information

Chapter 3 Development of the ECG processor and triggering procedure

Every time an R-wave is detected, the value of the trigger signal is set to low for 20 samples. The trigger signal was set to appear 200 samples after the detected R-wave with the duration of 30 samples.

The availability of these three signals in figure 3.36 confirms the correct operation of the algorithm and developed system; however it is difficult to distinguish the actual trigger from the other markers. To get clearer results, three additional tests were carried out where in each test one of the variable options was eliminated from the program. The results of these three tests are shown in figures 3.29 - 3.31.

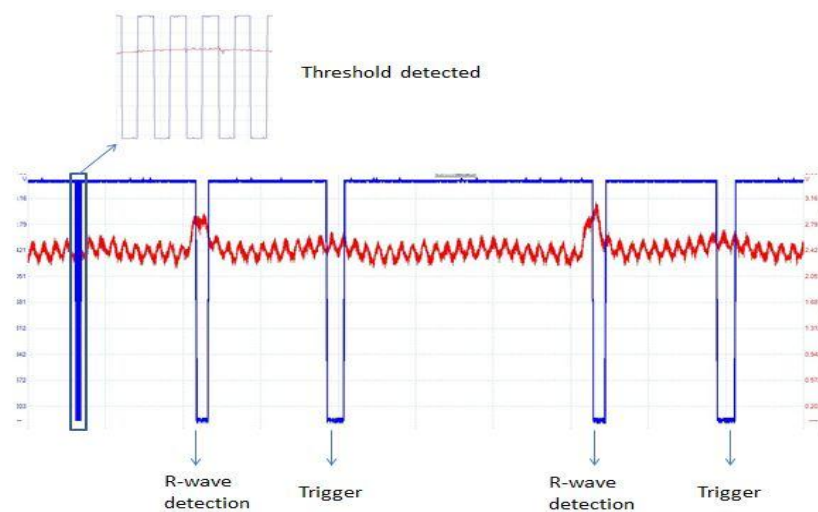


Figure 3.29 - Experimental test with threshold calculation and R-wave detection

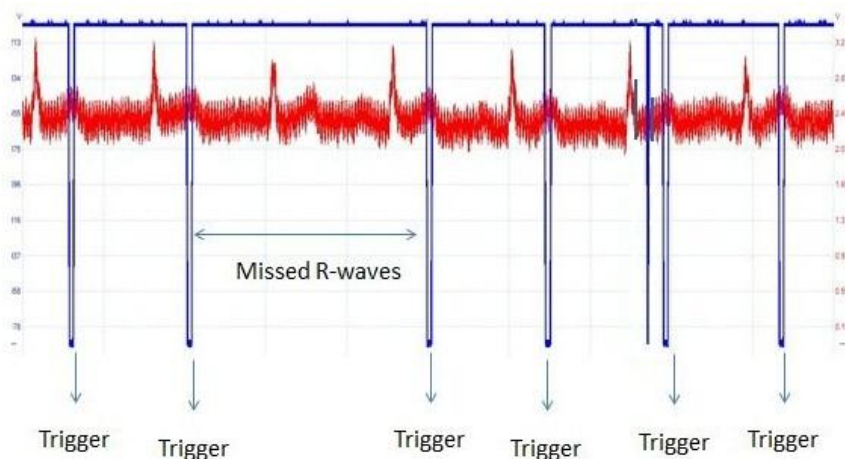


Figure 3.30 - Experimental test with threshold calculation and R-wave detection

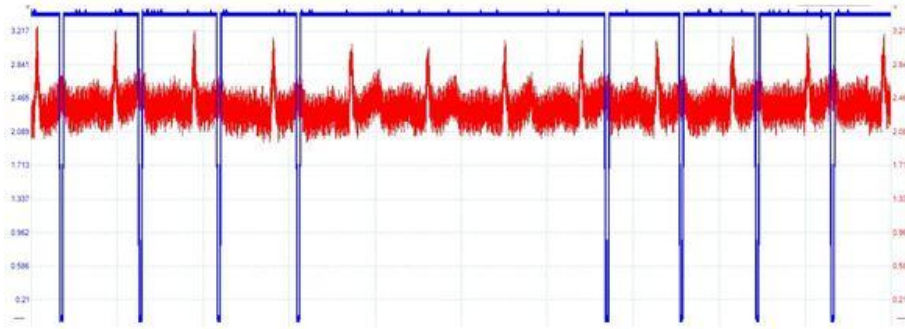


Figure 3.31 - Experimental test with threshold calculation and R-wave detection

Figure 3.31 is a good example of how the baseline of the ECG trace could suddenly drop and four R-waves were not detected by algorithm; however when the threshold was re-calculated the correct operation resumed.

One thing that also needs to be mentioned was the presence of the high frequency noise, caused by the operation of the IR transceiver, in all examples of ECG traces above. Nevertheless the developed algorithm even at such high noise presence was capable of accurate detection of the R-waves which proved the reliability of the designed system.

The last possibility of failure that needed to be explored before moving on to the next objective was to test the case when the IR connection between the ECG monitor and processor boards is terminated for a short time and resumed later. ECG processor needs to be able to adapt to this potential issue in case of blocked IR link or any other reasons that may result in a complete failure of transmitting samples. The worst case scenario would be shortage of power in the ECG monitor which will result in the loss of transmission.

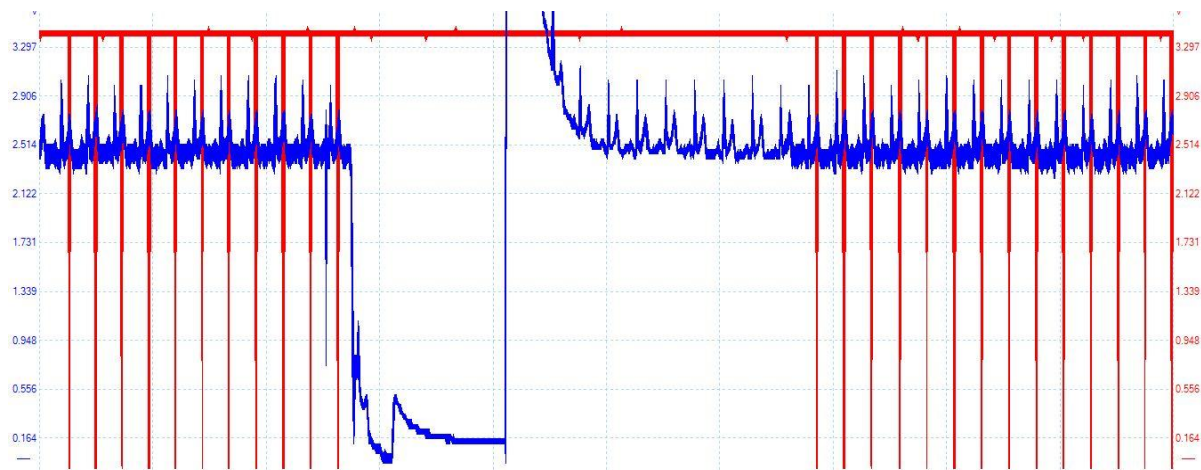


Figure 3.32 - Resetting the ECG Monitor (blue curve – ECG trace before digitization in the ECG monitor, red curve – output trigger signal of the ECG processor)

Figure 3.32 shows the operation of ECG processor before and after switching off the ECG Monitor. The blue trace is the output of ECG monitor which dropped to zero when the power was disconnected, and resumed when it was re- did not generate any trigger signals during disconnection and reconnection transients. However when the transmission was resumed (second half of the graph), threshold was calculated again and the operation of the ECG processor returned back to normal with the R-waves detected and triggers generated.

This final test proved that the algorithm could recover from normal temporary power or communication failure within a short amount of time confirming both the reliability and robustness of the ECG processor.

3.4.2.6 – Operating procedures of the ECG processor

The algorithm explained above proved to be sufficient in analysing an ECG trace and accurate detection of R-waves; therefore the next step is to use this algorithm to produce trigger signals. The procedure of sending the trigger signal to the UPR consists of the following steps:

1. capturing a digitized trace from the ECG Monitor;
2. detecting the R-wave;
3. setting required delay after the R-wave;
4. generating the trigger signal.

The first two steps have already been discussed. After the detection of the R-wave, there should be a tuneable delay before the trigger signal is sent to the UPR. This delay will be used to measure the IMT at particular stages of the heart cycle enabling fair comparison of measurements, completed, e.g., in a space of one year to make a conclusions on the state of atherosclerosis. The delay is set by counting a particular number of samples after the detection of the R-wave.

3.4.2.7 – Using a potentiometer to set the post R-wave delay

A potentiometer on the ECG processor board is connected to the ADC's channel seven of the microcontroller to be used to set the delay of trigger signal after the R-wave is detected. Movement of the dial of the potentiometer is tracked by the microcontroller as the voltage at the wiper of the potentiometer is changed. The ADC returns an 8-bit value for this voltage from 0 to 255. Because of the small size of the potentiometer, it is not possible to reproduce the exact value of the reading every time by just looking at the position of the dial. Therefore, instead of using all the 256 values produced by the ADC, the complete range was divided into five separate groups:

- 0 – 40
- 40 – 90
- 90 – 150
- 150 – 200
- 200 – 255

The wiper voltage is measured by the PIC's ADC when an R-wave is detected. This provision allows changing the delay in real time but also saves time by calculating the delay only when it is required.

To calculate the delay, a range of number of samples is set at the beginning of the program: Minimum Delay and Maximum Delay. The difference between these boundaries is divided by four and saved as the DelayInterval. These four segments plus the minimum delay generate the five possible delays for the five regions of the potentiometer dial. The value of the potentiometer is read by the ADC and saved to be used to determine the value of the delay factor. The delay factor is used to calculate the amount of delay is required by the user.

The delay that is calculated by the algorithm however is dependent on the number of samples recorded after the start of the window and the detected R-wave. This would create a delay based on the number of samples received, which enables the code to start the delay from the instant when the R-wave occurred.

To determine the value of the delay factor captured from the potentiometer, the multi-colour LED on the board was used. One example of the LED colour change based on the delay set by the user can be seen in figures 3.33

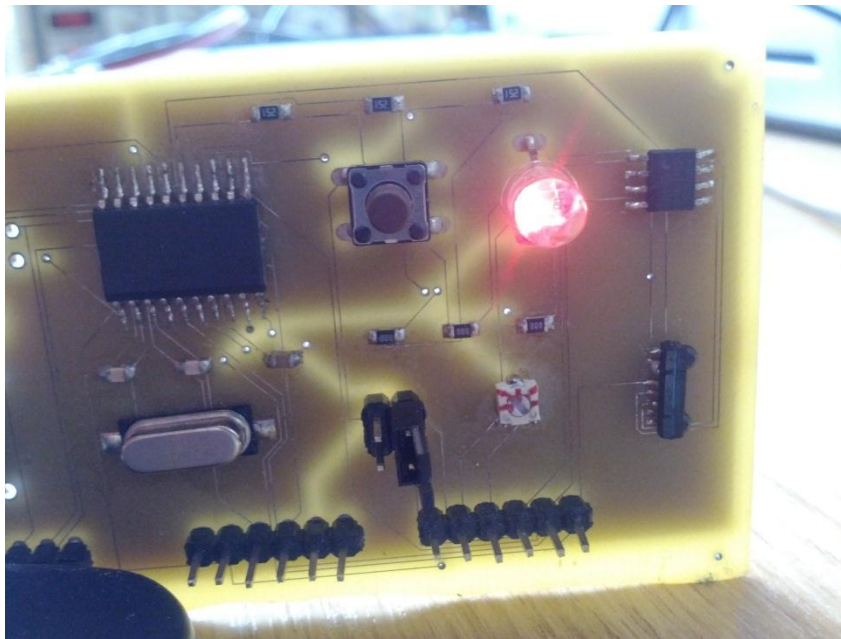


Figure 3.33 – LED indicates that DelayFactor equates to 3

Final experiment at this stage was to check the correct operation of set delay using ECG data in real time. For this test an ECG trace recorded earlier in the process (figure 3.34) was digitized by MATLAB and sent to the ECG processor; then the delay setting was varied by rotating the dial of the potentiometer. The waveform chosen for this experiment was taken from the ECG Monitor before being filtered to check if the level changes in the ECG baseline could have an effect on the operation of the developed algorithm.

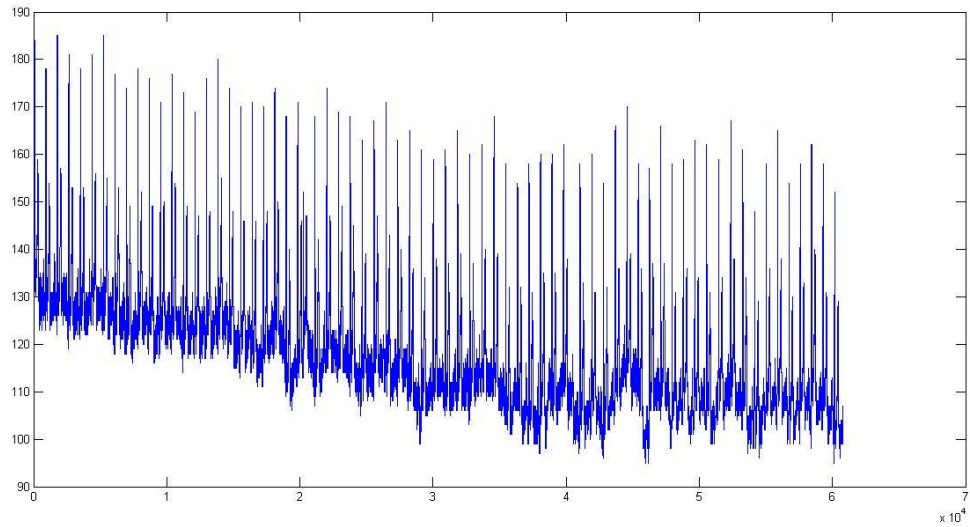


Figure 3.34 - ECG trace used for verifying set delays

The experimental delays between the detection of the R-wave and generation of the trigger are shown in table 3.2.

Table 3.2 - Changes in the post R-wave delays for different positions of the potentiometer's dial

DelayFactor	Delay
0	419 ms
1	805 ms
2	1.40 s
3	1.78 s
4	2.51 s

3.5 – Conclusion

After completion of ECG monitor and verification of its operation, the ECG processor was designed and manufactured in order to receive and analyse electrocardiogram signals from the patient and generate a trigger signal on detection of the R-wave. The main challenge for ECG processor is the accurate detection of the R-wave required in order to ensure ultrasound scans are timed with respect to the cardiac cycle of the patient to reduce the effects of blood flow on the measurements as much as possible, as explained in 1.4.1. The digital circuitry of the ECG processor was designed similarly to the ECG monitor to simplify the communications between the two boards.

As the main objective of ECG processor is to detect R-wave of the electrocardiogram, different ways of analysing the live signal received from the ECG monitor were tested and improved. This resulted in the development of the robust and reliable algorithm which was tested and verified as a stand-alone program. The algorithm was able to not only detect the R-wave with required accuracy but also to adapt to possible changes during examination, prevent false detections and ensure the high quality of the final in vivo experimental results later.

ECG processor was also chosen to act as the level converter for the required signals by the UPR and DAQ. The converter was used to make the ECG processor, DAQ and UPR compatible with each other by changing the level of the signals as necessary; which serves both points of simplicity and compact design by eliminating the need for external circuitry for these conversions.

During the electronic development phase of this research project a compact, easy to use and inexpensive system was developed for accurate monitoring of the cardiac cycle of the patient; and during the next phase this system was combined with ultrasonic scanner and data acquisition board to prepare for the in vivo experiments and measuring lumen diameter and IMT.

Chapter 3 Development of the ECG processor and triggering procedure

In this chapter the ECG processor that was designed, developed, tested and improved over the course of this research project was discussed in detail. Different options for the method of communicating between the ECG Monitor and ECG Processor were explored. The development process of both ECG Monitor and ECG processor was explained giving sufficient justification why certain schematic and/or components were chosen over others; and it was shown how the progression of electronic developments were based on their first prototype and how they evolved to the final design that was used for the final experiments of in vivo measurements of the IMT and lumen diameter.

Infrared communication between the two boards was successfully established; tested and verified using both simulated and recorded data.

A robust algorithm was developed to overcome the difficulties of detecting R-waves in ECG waveforms from the patient safely and reliably, including the presence of noise in the trace caused by infrared transceivers, possible interference from other devices in the environment and any failures in the ECG monitor.

The developed ECG processor could also include a digital filter to further improve the quality of the received ECG waveforms from the ECG Monitor. This inclusion could be useful in the case when the ECG waveform is used not only for triggering the ultrasonic scans but also for monitoring the patient's state during an examination. A filter similar to one used by Pan and Tomkins [3.7] could be applied first to see how desirable is the filter's application.

The experimental records captured by PicoScope and reported in this chapter, contained 204 heart beats. Out of these, 24 beats were missed because of changes in the ECG baseline and/or presence of the noise. These results translate to the percentage of the missed beats (false negative) of 11.76%. It is worth noting that the developed algorithm was developed with the aim not to detect the heart beat rate accurately but to make sure that every ultrasonic scan is triggered at the correct phase of the heart cycle. For this reason elimination of false positives was more important than the reduction in the number of false negatives. The ability of the algorithm to trigger ultrasonic scans correctly was experimentally verified during experimental measurement of artery thicknesses (Chapter 5). The ECG and derived trigger signals were closely

Chapter 3 Development of the ECG processor and triggering procedure

monitored at that stage as well, and the observations confirmed the robustness and appropriate performance of the developed R-wave detection algorithm.

The objectives of the electronic development, which aimed to take ECGs using inexpensive, easy to use circuitry; safely and reliably analyse recorded waveforms and trigger ultrasonic scans based on the R-wave to synchronise the heart cycle with scans to eliminate the effect of blood circulation on IMT, were all fully achieved. The next step is to combine the work discussed in the previous chapter and this chapter with the ultrasonic scanner to try and take accurate measurements.

References

- 3.1 – Microchip (2009; March). "PIC18F14K50 datasheet"[Online]. Available: <http://ww1.microchip.com/downloads/en/devicedoc/41350c.pdf>
- 3.2 – Microchop (2011; November). "MCP631/2/3/4/5/9 Datasheet"[Online]. Available: <http://ww1.microchip.com/downloads/en/DeviceDoc/22197B.pdf>
- 3.3 – Diodes Incorporated (2009; February). "APX321Datasheet"[Online]. Available: http://www.diodes.com/datasheets/APX321_358.pdf
- 3.4 – Microchip (2004; October). "PICDEM™ FS USB DEMONSTRATION BOARD USER'S GUIDE"[Online]. Available: <http://ww1.microchip.com/downloads/en/devicedoc/51526a.pdf>
- 3.5 – Mircochip (2009; March). "MCP2120/22 Developer's Board user's Guide"[Online]. Available: <http://ww1.microchip.com/downloads/en/DeviceDoc/51842a.pdf>
- 3.6 – P. McSharry et al. "A dynamical model for generating synthetic electrocardiogram signals," IEEE Transaction on Biomedical Eng., vol. 50, no. 3, pp. 289-294, March 2003.
- 3.7 – J. Pan, W. Tompkins, "A Real-Time QRS Detection Algorithm", IEEE transaction on Biomedical Engineering, vol.32, pp. 230 – 236, 1985
- 3.8 – Wikipedia (2013; March). "Detection theory"[Online]. Available: http://en.wikipedia.org/wiki/Detection_theory

4 – Phantom experiments

A series of experiments were carried out on plastic tubes in order to examine the reflection of ultrasound waves from a circularly shaped object covered by water. The purpose of these experiments was twofold: to verify the simulation results (and tweak the simulation model as appropriate if required), and to record the waveforms related to the physically scaled IMT measurements in a fully controlled and repeatable environment. These experiments have two main advantages. First is the constant dimensions of the phantom tube, unlike those of a human artery that change during a heart cycle. The second is possibility of fixing the tube securely to the setup. The latter possibility helps to record consistent waveforms, whilst it is difficult to attach the transducer to exactly the same place on the human body with the same pressure and coupling. Physical modelling in general has better connection to reality compared to mathematical modelling. This is due to model deficiencies and omissions, computational errors, insufficient simulation steps, where their combination can lead to unacceptable deviations of the modelling outcome.

This chapter describes the methodology used for physical modelling, the developed test rig, experimental procedure and experimental results obtained for various phantoms.

4.1. Methodology of physical modelling

A medical imaging model called a “phantom” could be of the same size as the living object of interest [4.1]. For the purpose of this work, making a phantom of the same dimensions as an artery would be very difficult and expensive because of the small dimensions of the artery. Objects of bigger dimensions are easier to handle, fix, scan, modify and replace. Nevertheless scanning the tubular objects used as artery phantoms should resemble wave propagation conditions occurring in vivo. This requirement should be verified against both the parameters of the transducer and dimensions of the phantom.

Linear ultrasound transducer arrays usually are 10-15 cm long and consists of 128-512 rectangular elements, each 10 mm wide [4.2], giving the approximate estimate for the pitch in the range from 0.3 mm (150mm/512) to 1mm (100mm/128). The area of such an element thus ranges from about 3 to 10 mm². The operating frequencies of most ultrasonic bio imaging arrays belong to the range from 2 to 10 MHz [4.3]. Higher operating frequencies require finer element pitch because of smaller wavelength. The ultrasound field of a transducer consists of two distinct regions: near field where Fresnel diffraction takes place and the transducer beam spreads very little [4.4], and far field (Fraunhofer diffraction [4.5]) where the beam diverges. Although there is no distinct boundary between these regions, the Fraunhofer distance d is commonly used as a reasonable estimate for its notional location [4.6]:

$$d = \frac{2D^2}{\lambda}, \quad (4.1)$$

where D is the diameter of a circular transducer and λ is the wavelength. Using the area of the transducer S instead of its diameter yields

$$d = \frac{2}{\lambda} \times \frac{4S}{\pi} = \frac{8}{\pi} \times \frac{SF}{c}, \quad (4.2)$$

where F is the operating frequency and c is the ultrasound velocity (in most human tissues it can be taken as approximately 1500m/s [4.7]). Consequently a typical array element operates at the Fraunhofer distance of approximately

$$d = \frac{8}{\pi} \times \frac{(10 \text{ to } 3\text{mm}^2)(2 \text{ to } 10\text{MHz})}{1500\text{m/s}} \approx 30 \text{ to } 50 \text{ mm}. \quad (4.3)$$

As carotid arteries are superficial, IMT measurements are undertaken in the near field.

The transducer for phantom experiment was selected from available stock of ultrasonic NDE immersion transducers of circular shape. Differentiating between echoes from the front and back wall of the phantom is easier if these echoes can be resolved in the time domain. For this reason, a high frequency wide bandwidth ultrasound transducer is preferable, and so a 20 MHz 5 mm diameter transducer was selected. Its Fraunhofer distance can be calculated from (4.2) as

$$d = \frac{8}{\pi} \times \frac{\pi \left(\frac{5\text{mm}}{2}\right)^2 20\text{MHz}}{1500\text{m/s}} \approx 660 \text{ mm}. \quad (4.4)$$

Therefore at least the front wall of the phantom should be placed at below this distance to the transducer. Ultrasound beam in the far field becomes more of a cone shape compared to the cylindrical shape of the beam within the near field. The difference between the two in this project is that if the phantom is placed in the far field, more of its area reflects the ultrasound beam. This would add to the complexity of the shape of the reflections recorded by the receiver. Although the area of the phantom covered inside the near field is less than the far field, the reflection recorded by the receiver from the objects in the near field is expected to be simpler.

Ultrasonic field patterns produced by different circular transducers with the same product of ka , where k is the wave number ($k = \frac{2\pi}{\lambda}$ [4.8]) and a is the transducer's radius, are considered the same [4.14]. It holds

$$ka = \frac{2\pi}{\lambda} a \sim F\sqrt{S}. \quad (4.5)$$

Consequently the size of the artery phantom should be scaled by the factor that equates to the ratio of ka of the transducer selected for the phantom experiment to that of a typical ultrasound array element. This scaling factor k_s was calculated as

$$k_s = \frac{20\text{MHz}\sqrt{20\text{mm}^2}}{2 \cdot 10\text{MHz}\sqrt{1 \cdot 0.3\text{mm}^2}} \approx 45 \text{ to } 16. \quad (4.6)$$

Assuming that the range of CCA/ICA diameters is between 2.5 and 9.5 mm, as it is stated in [4.9], the appropriate diameter of phantom tubes are to be within 40mm (2.5mm*16) to 400mm (9.5mm*45). When the diameter of the phantom is increased, the curvature below the transducer flattens. Therefore, experimenting at the lower end of the a.m. range should result in more profound differences in the recorded echoes compared to a flattened tube, which tends to behave like a flat object at low curvatures.

In summary, the above considerations show that conventional IMT measurements can be physically modelled, using a 20 MHz circular 5 mm transducer, and phantoms with diameters from 40 to 400 mm, placed at the distance less than 660 mm away from the transducer.

4.2 - Commissioning of the test rig

4.2.1 - Purpose and requirements

The overall setup for phantom experiments consists of:

- a plastic box, which is filled with water to propagate ultrasonic waves from the transducer to the phantom and echoes back
- a tube clamp to secure tubes in place for the duration of experiments
- a holder of the transducer to fix it in particular locations above the phantom
- The transducer holder should keep the transducer close to the surface of the phantom to satisfy the near field condition. Both the transducer and tubes of various diameters should be reliably and consistently fixed at set positions with respect to each other. The phantom and the transducer's radiating surface should be immersed in water.

4.2.2 - Test rig components

The test environment was designed to hold tubes of different sizes, which provided the option to operate objects with different dimensions in relation to the wavelength. This would enable a potential opportunity of physical simulation of smaller arteries in the body, which can be clogged like the carotid arteries, but are difficult to examine with existing instrumentation at the moment.

The phantoms need to be clamped as their movement during the test will distort the recorded echoes. Additionally, the experiments can only be repeated if the tubes can be placed at the same position every time when this is necessary. The test rig also needs to hold transducers with different sizes. Therefore, the transducer holder was designed with a detachable part, which can be changed according to the size of the particular transducer used.

The overview of the developed test rig is presented in figure 4.1.

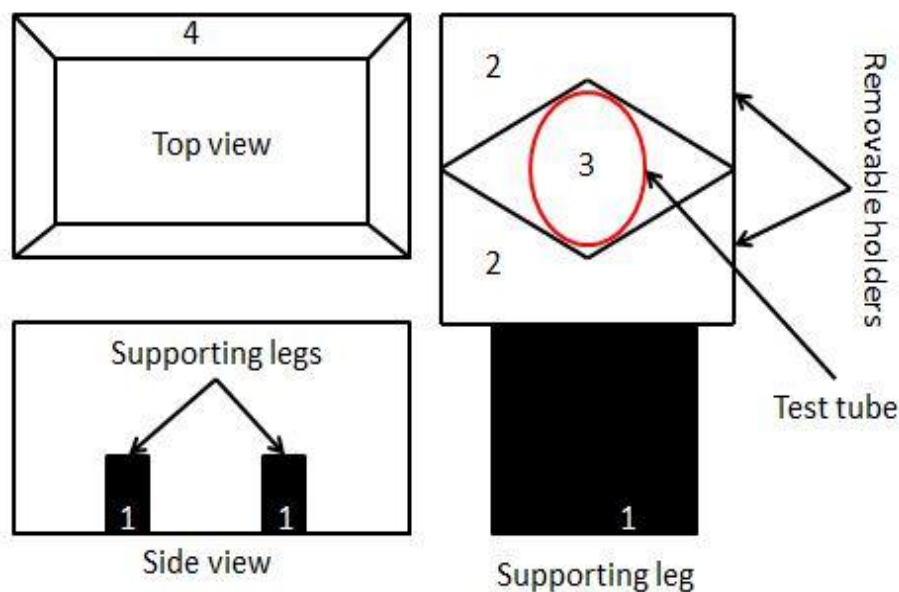


Figure 4.1 - Schematic of different parts of the experiment setup (1 - supporting legs, 2 - tube holders, 3 - test tube, 4 - test tank)

4.2.2.1 - The container

A solid plastic storage box (figure 4.1, 4) was used as a water tank. The dimensions of the box were chosen to balance the portability of the setup (table top size) to examine tubes with the diameters of interest (section 4.1). Rails for the transducer holder were attached to the storage box, and contained threaded holes to fix the transducer holder consistently and securely (figure 4.2).

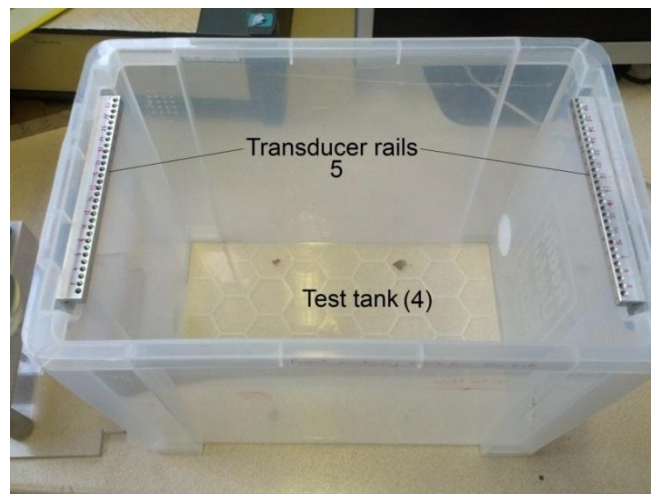


Figure 4.2 - Test cell and transducer rails

4.2.2.2 - Phantom clamp

The clamp is attached to a Plexiglass base that was shaped to fit tightly to the bottom of the storage box (figure 4.3). Four supporting legs ensured that the tube does not touch the bottom of the storage box, thus the reflections from it can be resolved in the time domain. The clamping parts were made with a V-shaped void to enable use of tubes of different diameters. All these parts were set at the threaded bars and secured with nuts that were tightened by hand.

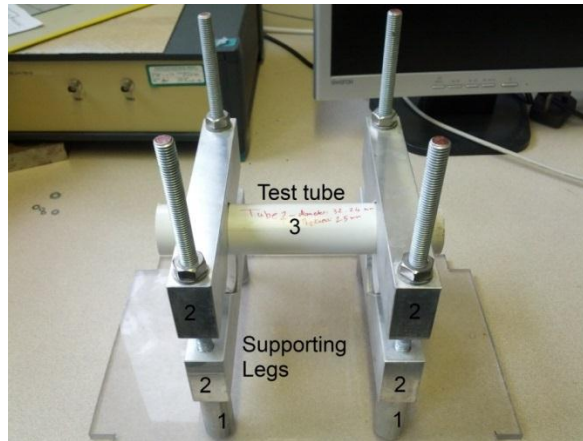


Figure 4.3 - Tube holders

4.2.2.3 - Transducer holder

The holder was designed in order to accommodate transducers with different diameters. A screw is used to secure the transducer tightly thus the experiments can be repeated under the same conditions every time (figure 4.4). It is very important to be able to reproduce the conditions of each experiment to ensure consistency of the results.

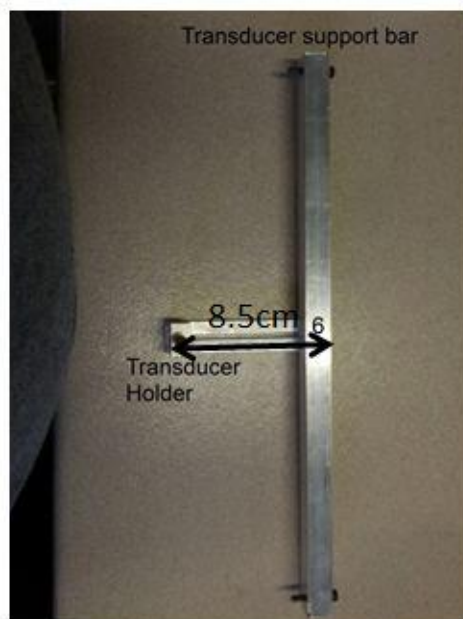


Figure 4.4 - Transducer holder

The transducer holder is connected to a metal bar that can be screwed into the rails on both sides of the tank. The screws enable movement of the transducer above the tube within the set of available positions with the pitch of 5 mm. The rails on either side have 31 holes that the transducer holder can be fixed to. The centre point of these rails is at positions 16, which form the symmetry line for the supporting legs. When the transducer is fixed at this position, its centre is placed above the central axis of the test tube.

The entire assembly is shown in figure 4.5.

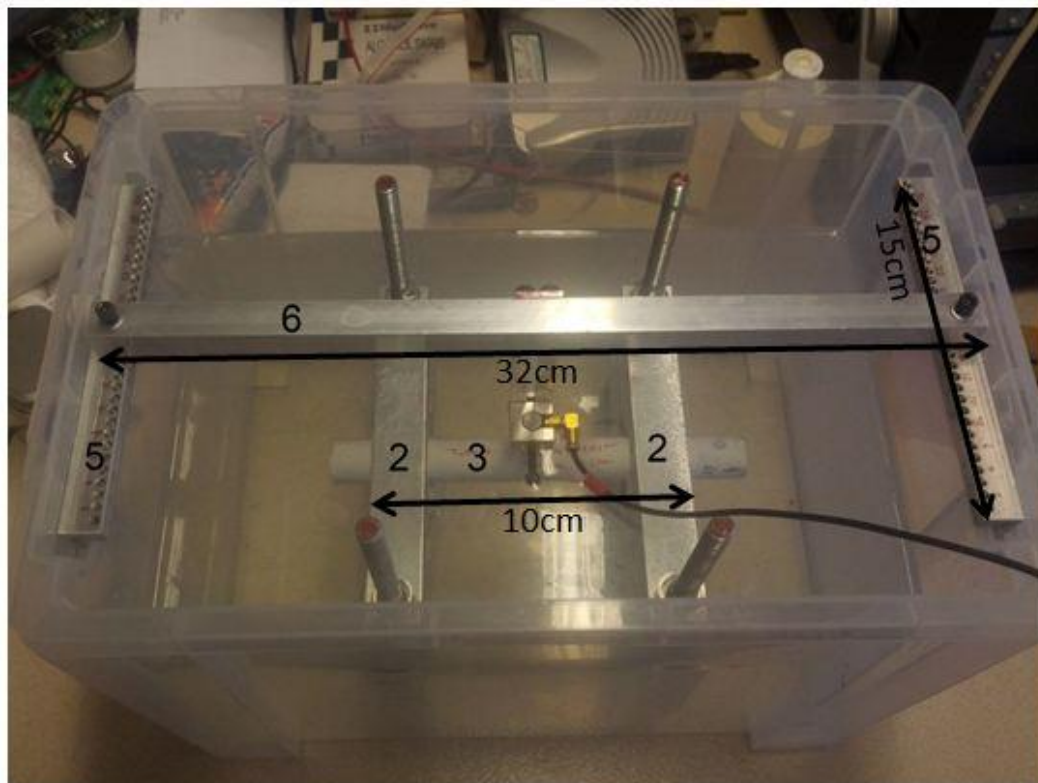


Figure 4.5 - Assembled setup with a phantom and transducer

In the above figure the transducer holder is placed at position 16 on the rails. The test rig is designed in such a way that, when the phantom is fixed (using the legs), position 16 is above the centre of the phantom. The positions on the rail are spaced 5 mm apart from each other, which enables the centre of the transducer to move by such intervals above the phantom, as it is shown in figure 4.6.

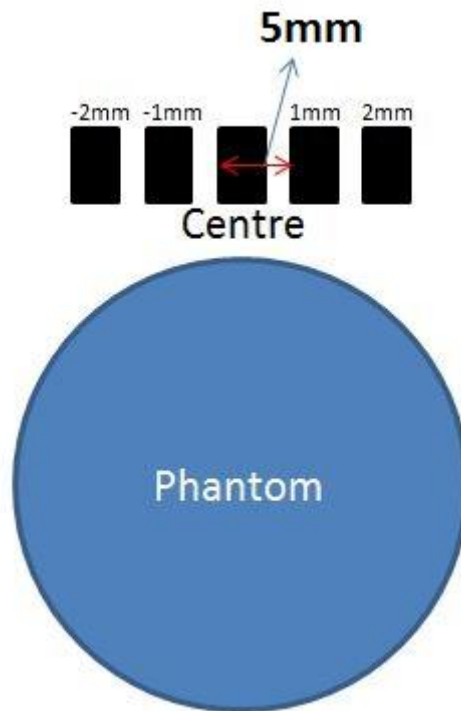


Figure 4.6 - Different positions of the transducer relative to the centre relative to the cross-section view of the tube

4.3 - Experimental Procedure

Because of the complexity of phantom experiments, and variety of different factors that can affect the outcome, a step by step guide needed to be developed and followed for each and every experiment. This ensures that the recorded waveforms are comparable to each other. This procedure must cover the selection of both the software parameters (to setup of the DAQ board), and hardware settings such as transducer placement.

4.3.1 – Software parameters

The software used to excite the ultrasound waves and capture reflections is run on a computer by MATLAB. This software allows various parameters to be altered for different experiments (figure 4.7).

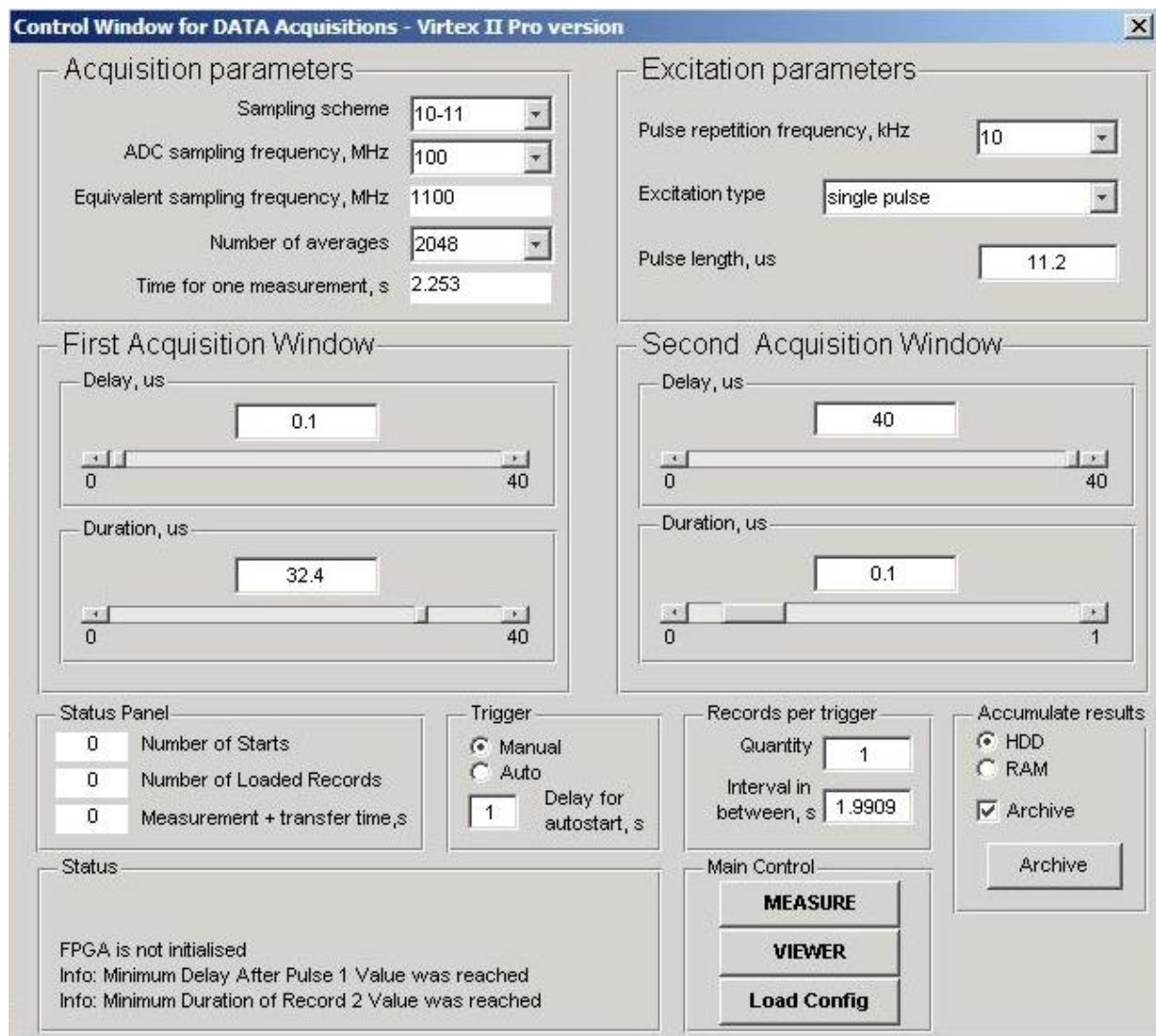


Figure 4.7 – Software parameters for phantom experiments

A single pulse is transmitted by the transducer, and reflections from objects in front of it are received by the same transducer (pulse-echo method). The advantage of this method is that only one transducer is required, which eliminates the need for the second expensive transducer and its alignment.

The software controls the averaging scheme which reduces the noise in the received signal. Averaging works on the assumption that the noise present in

subsequently recorded echoes is uncorrelated. When the average of all these records is calculated, the result features coherent enhancement of the signal, and reduction of the uncorrelated noise. Using averaging however requires finding a balance between the times required to collect separate records (for in vivo IMT measurements). This time should not exceed a small fraction of the heart cycle [4.15] and achieve noise reduction. For the purpose of phantom experiments, 2048 averages were calculated. Additionally frame interleaving was used to increase the equivalent sampling frequency.

The sampling scheme in the software provided for the DAQ is a multiplier for the base clock frequency. The sampling scheme combined with the ADC sampling frequency, will set the number of times the excitation pulse will be repeated before one measurement is completed. Setting the sampling scheme at 10-11 means the base clock runs 11 times faster than the ADC. With the sampling frequency of the ADC of 100 MHz the equivalent sampling frequency becomes 1 GHz, at the expense of the proportional increase in the measurement time. At the pulse repetition rate of 10 kHz the required 20480 (2048*10) records were collected in just over 2 seconds, which is acceptable for a steady phantom.

The final step of the procedure is to repeat each experiment three times in order to verify that these examinations are consistent. Recorded waveforms are expected to be similar in terms of timing for all the three experiments conducted on the same tube; and the differences between waveforms will be visible when the waveforms from different tubes are compared to each other.

4.3.2 – Test rig settings

The test tube is placed on the supporting legs of the test rig, and the top sections of the supporting legs are secured to the threaded bars. This ensures that the tube is tightly fixed to avoid any displacement while the test is being carried out. Then the transducer is attached to the holder and fixed to the transducer bar at the required position. This eliminates any possibility of misalignment of the transducer with respect to the tube.

After fixing the transducer to the rail, the tank is filled with water to ensure that not only the tube is fully immersed in water, but also the radiating surface of the transducer is covered with water as well. The purpose of immersing the phantom and transducer into water is to resemble ultrasound propagation in the human body, which consists of 70% water. The transducer is placed in water to eliminate any reflections caused by acoustic mismatch from air and water interfaces. Absence of these reflections is ensured during in vivo experiments by adding ultrasonic coupling gel between the transducer and the skin. Water in the tank is kept during all the experiments with a particular phantom to keep the environment the same, and also to protect the transducer from being fully immersed.

To find the starting and final transducer positions on the rails, the transducer is moved freely from one end of the rail to the other while an oscilloscope displays the echoes. The starting position corresponds to the point where the echoes become observable, and the final position corresponds to the point where the echoes cease to exist. This range is different for every tube, and the distance between the starting and final points should ideally equate to the diameter of the tube.

When the range is determined, the transducer is placed at one end of the range and fixed to the transducer rails on both sides; three measurements are taken and saved for analysis. After that the transducer is moved towards the final position by one step until this position is reached.

This combination of software and hardware settings should ensure that the properties of test environment are kept constant when experiments are repeated; therefore the recorded echoes should be very similar.

4.3.3 - Preliminary experiments

Before starting measurements on tubes made of ABS plastic, it is desirable to evaluate ultrasonic properties of this material. For example, the ultrasound velocity in the material, together with the thickness of the tube determines the ultrasound propagation delay. Manufacturers' website quote the

speed of sound in ABS plastic at 2350m/s ([4.10]). Initial experiments were carried out to evaluate this speed for the actual phantoms.

The first experiment was conducted on a piece of an ABS tube that was flattened out by the following process:

- the tube was heated to 100°C whilst subjected to flattening pressure
- It was then left to cool off overnight still under pressure to prevent the material from going back to the original shape.

This process results in the test piece to have a flat surface. This test piece was easy to use with an ultrasound transducer, with its face placed on the test piece surface directly. Recorded echoes from this test piece (figure 4.8) were used to evaluate the sound velocity for this material.

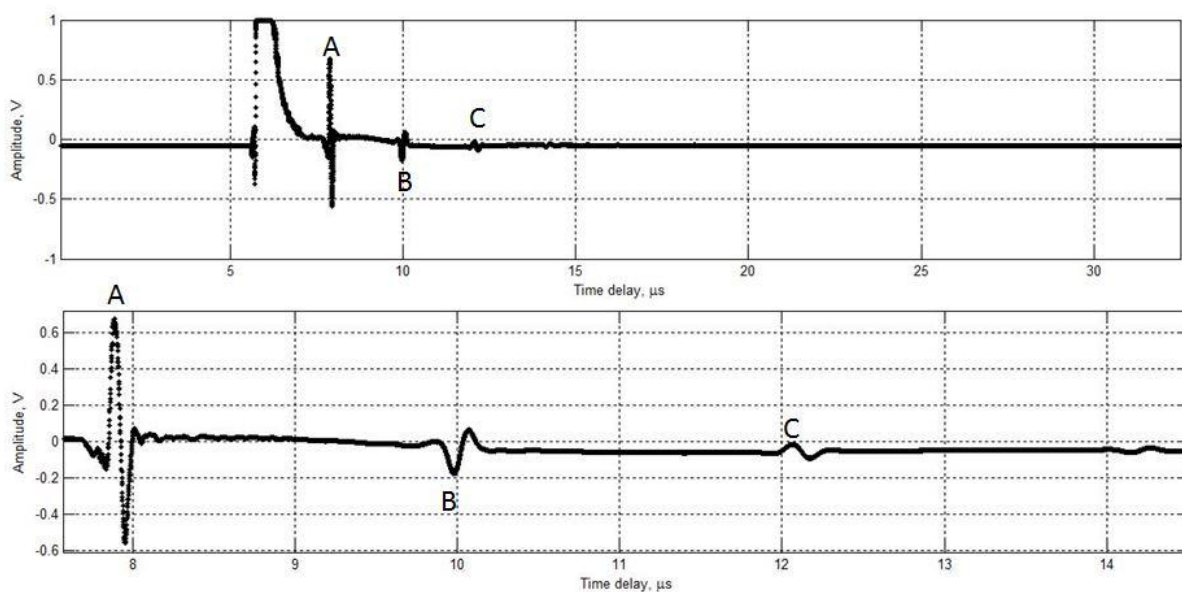


Figure 4.8 - Reflections from a flattened piece of an ABS plastic tube shown at different scales

As shown in figure 4.8, there are four clear reflections present after the excitation pulse. The time difference between the peaks of these reflections were used to evaluate the ultrasound velocity in the material. The waveform shows some drift from the base line, making it difficult to estimate delays by zero

crossings. For this reason the delays were estimated at the peak values as follows:

- Time instant at point A: 7.85 μs
- Time instant at point B: 9.98 μs
- Time instant at point C: 12.08 μs

The average time delay between the subsequent reflections is 2.115 μs , which corresponds to the ultrasound transit time from one boundary to the other and back. The thickness of the test object (x), the time delay for the wave to propagate forward and back to the transducer (τ), and the ultrasound velocity (c) are related as:

$$c = 2x/\tau. \quad (4.7)$$

The measured thickness of the flattened ABS plastic test piece at the point of transducer placement is 2.07 mm, yielding the estimated velocity of 2.04 mm/ μs or 2040 m/s. The difference between the obtained value and the one quoted by the manufacturer could originate from two main factors.

Firstly, the quoted value is a generic value for all ABS plastics, which does not account for the particular manufacturing process and chemical composition of the material used for this particular tube. Secondly, the process of making the tube flat could have resulted in some changes to its sound velocity.

Using equation 1.2, the theoretical axial resolution of the system with the above settings can be calculated as follows:

$$\text{Axial resolution} = \frac{c}{f_s} = \frac{2040\text{m/s}}{2} = \frac{1000\text{MHz}}{2} = 1.02\mu\text{m}$$

The axial resolution of around 1 μm was sufficient for these experiments as the thinnest tube used in these experiments had thickness of 1.6mm.

Another experiment was conducted on the original tube. The transducer was pressed against the tube immersed in water, and echoes were recorded (figure 4.9).

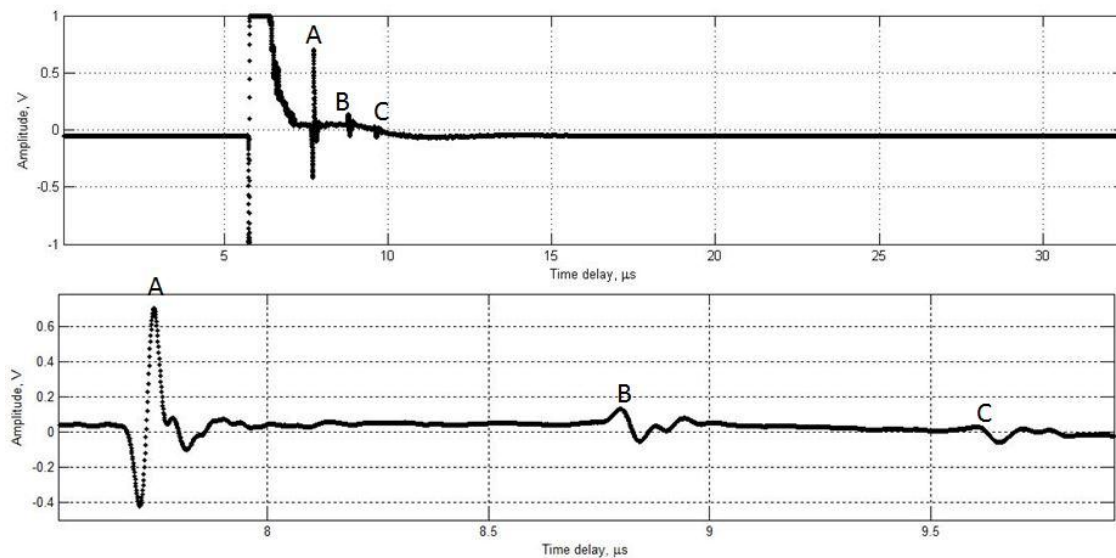


Figure 4.9 - Reflections from the original ABS tube

In addition to the reflections visible from figure 4.8 a new echo has appeared starting at approximately $8.75 \mu\text{s}$. The following time instants for the marked points were estimated from the graph:

- Time instant at point A: $7.7 \mu\text{s}$
- Time instant at point B: $8.7 \mu\text{s}$
- Time instant at point C: $9.8 \mu\text{s}$

The additional echo at point B in figure 4.8 was most likely originated from waveguiding effect inside the tube wall. Ultrasound propagates inside the wall of the tube are shown in figure 4.10. It is possible that some energy propagated inside the wall, could have leaked back to the transducer before the wave, or reflected from the far wall of the tube. It is important not to confuse this pulse with the reflection from the far wall of the tube. The time taken for the ultrasound signal to reach the other end of the wall is directly proportional to the velocity of sound inside the tube. when knowing the thickness of the tube wall, it is possible to calculate a reasonable estimate of where the reflection from the far wall should appear to avoid the confusion.

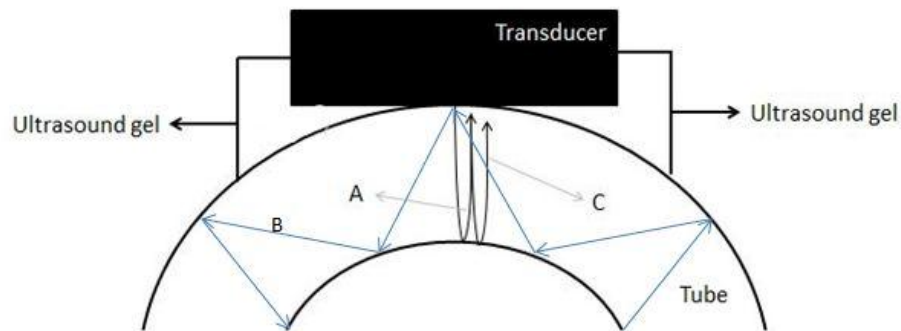


Figure 4.10 - An illustration to possibility of appearance of additional echoes in the recorded waveforms

It is important to note that this reflection appeared focused and not spread over the time axis. The second reflection from the tube boundary (point C in figure 4.9) had much lower amplitude compared to figure 4.7. This is because only part of the emitted energy entered the tube through the contact area to the transducer. The time difference between the points A and C was approximately $2.1 \mu\text{s}$ which was compatible with the average ultrasound delay estimated for the flattened tube ($2.115 \mu\text{s}$).

4.4 – Experimental records for the phantom experiments

Three different test tubes were examined during phantom experiments, with each tube having its own unique dimensions. The main difference between the tubes was the diameter and thickness of each tube, which affects the reflections due to the changes in the ratio of the size of the object to the ultrasound wavelength. The resultant waveforms were recorded for each tube, processed using MATLAB, and analysed both individually and as a part of associated group (for the same phantom or for the same transducer's position).

The number of waveforms recorded for each tube was equal to the diameter of the tube divided by the pitch of the transducer holder's rail of 5 mm.

Waveforms recorded for the same phantom were compared to each other, and to the waveforms recorded for the other phantoms. This is to identify any similarities and distinctions which could later be used in vivo experimental records.

4.4.1 - Phantom 1

The cross section of the phantom 1 is presented in figure 4.11.

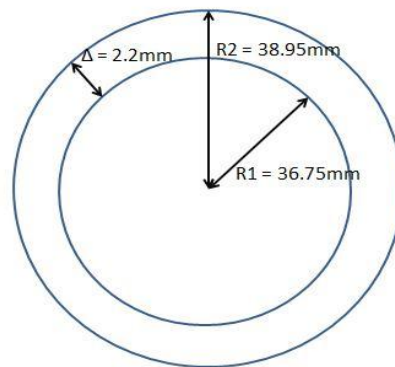


Figure 4.11 – Cross section of phantom 1

The phantom exhibited the following properties:

- Tube material: ABS
- Transducer frequency: 20 MHz
- Wavelength: $\lambda = c/f = 0.075\text{ mm}$
- Transducer diameter: $5\text{mm} = 66.7\lambda$
- Tube inner diameter: 36.75 mm
- Tube outer diameter: 38.95 mm
- Wall thickness: $2.2\text{ mm} = 29.3\lambda$

Five waveforms were recorded for this phantom as presented in table 4.1. The recorded echoes spread out considerably compared to echoes presented in figures 4.7-4.8 (obtained for the transducer touching the phantom). This is due to the increased complexity of wave propagation through the additional layer of water. The tube was placed at the distance of approximately 10 mm ($15\mu\text{s} \cdot 1500\text{m/s} / 2$) from the transducer wall within its near field. The waveforms recorded at the same distance from the centre position do not start from the same time instance. This shows that there was some misalignment

between the phantom axis and the rail position 16, which is designed to be above the centre of the curve of the phantoms. There is a well-defined echo after the main reflection from the tube observed at the position 16 only at about $17.5 \mu\text{s}$, similar to that observed in figure 4.9. This reflection was attributed to the reflections of the side waves as it was discussed in the section 4.3.3. The experiment showed that even for a manmade object of a regular well defined shape, the recorded echoes can be quite complicated and spread along the time axis. There is a possibility of recording a false reflection if the axis of the transducer is not placed directly above the centre of the phantom.

Table 4.1 – Waveforms recorded for phantom 1

Position	Recorded waveform
-2mm	<p>Tube 1 - Position 14 - Afternoon</p>
-1mm	<p>Tube 1 - Position 15 - Evening</p>
Centre of the tube	<p>Tube 1 - Position 16 - Morning</p>
1mm	<p>Tube 1 - Position 17 - Afternoon</p>
2mm	<p>Tube 1 - Position 18 - Afternoon</p>

4.4.2 - Phantom 2

The cross section of the phantom 2 is presented in figure 4.12.

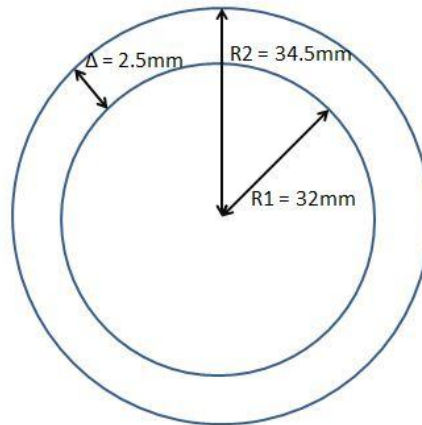


Figure 4.12 - Cross section of phantom 2

The phantom exhibited the following properties:

- Tube material: ABS
- Transducer frequency: 20 MHz
- Wavelength: $\lambda = C/f = 0.075 \text{ mm}$
- Transducer diameter: $5\text{mm} = 66.7 \lambda$
- Tube inner diameter: 32 mm
- Tube outer diameter: 34.5 mm
- Wall thickness: $2.5 \text{ mm} = 33.4 \lambda$

Five waveforms for this phantom were recorded (table 4.2).

Smaller diameter and increased thickness of this phantom led to notable changes to the recorded waveforms:

- the distance from the transducer increased to approximately 15 mm ($22\mu\text{s} \cdot 1500\text{m/s} / 2$)
- Waveforms recorded at positions next to the position 16 feature long tails
- Waveforms recorded at positions 14 and 18 show noticeable diffuse echo before the arrival of the main pulse

- Waveform at position 16 has both the additional echo at about 23 μs and reverberation from the wall at about 24 μs .

Table 4.2 - Waveforms recorded for phantom 2

Position	Recorded waveform
-2mm	
-1mm	
Centre of the tube	
1mm	
2mm	

4.4.3 - Phantom 3

The cross section of the phantom 3 is presented in figure 4.13.

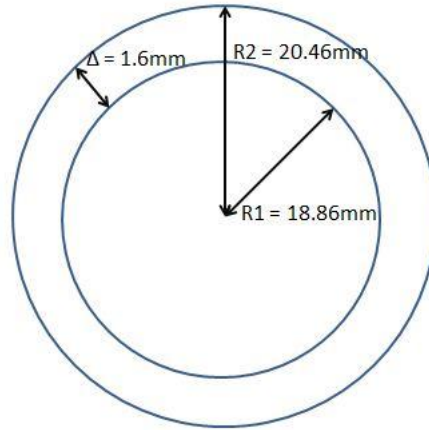


Figure 4.13 - Cross section of phantom 3

The phantom exhibited the following properties:

- Tube material: ABS
- Transducer frequency: 20MHz
- Wavelength: $\lambda = C/f = 0.075\text{mm}$
- Transducer diameter: $5\text{mm} = 66.7 \lambda$
- Tube inner diameter: 18.86 mm
- Tube outer diameter: 20.46 mm
- Wall thickness: $1.6 \text{ mm} = 21.3 \lambda$

This time only four waveforms were recorded (table 4.3) because of the smaller diameter of the tube. These records illustrate the importance of placing the transducer directly above the centre of the phantom – only one echo waveform recorded at the position 16 was relatively condensed. All other waveforms exhibited long tails. For example, the waveform recorded at position 17 starts with some diffused reflection at about the same time as the waveform recorded at the position 16, and lasts for about $3 \mu\text{s}$ instead of about $0.5 \mu\text{s}$. Additionally, this waveform looks like it was produced by several separate reflectors.

Table 4.3 - Waveforms recorded for phantom 3

Position	Recorded waveforms
-1mm	<p>Tube 3 - Position 15 - Evening</p>
Centre of the tube	<p>Tube 3 - Position 16 - Morning</p>
1mm	<p>Tube 3 - Position 17 - Evening</p>
2mm	<p>Tube 3 - Position 18 - Evening</p>

4.4.2 – Verification of the results

Each waveform presented in section 4.3.1 was recorded three times, and these separate records were found consistent with each other. Nevertheless, the observed variability among the recorded waveforms, for different phantoms, and at different transducer position, called for further verification of the results obtained. This was done by analysing differences (1) among waveforms recorded at different times of the day for the same phantom, at the same transducer position; (2) among waveforms recorded for the same (central) position for different phantoms; and (3) by evaluating the acoustic impedance of the phantoms' material from the amplitudes of the recorded echoes.

4.4.2.1 – Examining consistency among notionally the same waveform recorded at different times of the day

Each phantom was examined three times on the same day with at least three hours in between of these examinations. The transducer was moved through all the available positions during each measurement session. Waveforms shown in tables 4.1–4.3 were selected for their clarity out of the three waveforms available. All the recorded waveforms were compared to notionally the same ones collected at different time of the day. For example, figure 4.12 presents waveforms recorded for the second phantom by having the transducer above the centre of the tube.

The signal-to-noise ratio of these tests was calculated using MATLAB. The SNR of the system throughout these tests are very similar. For example, the SNR of the reflections from tube number 2 recorded during the day are -6.05dB in the morning, -8.89dB in the afternoon and -7.8dB in the evening.

Looking at these waveforms, it can be seen that the shape and timing of fragments of these waveforms are similar to each other, but far from being exactly the same. This means that, despite the experiments being performed in a controlled environment, the waveforms could substantially deviate from each other. Since the test rig is a mechanical system that needs to be assembled by

the user, it was possible to introduce some small differences during assembly even when carefully following the procedure mentioned in section 4.2. One of the differences could be related to the orientation angle of the transducer fixed to the transducer holder. This deviation may be very small that is not visible to human eye, and cannot be spotted by simply looking at the transducer. However, this small deviation could have enough effect on the angle of incidence and the reflected waveforms. Another possible reason for the observed inconsistency is related to the dependency of ultrasound velocity to the water temperature (around 2 m/s (0.14%) change per degree Celsius). This dependency will not only lead to changes in the time delay of the recorded echoes, but also will alter the wave diffraction pattern. The propagation delay for the presented records varies by about 0.3 μs (about 1.4% to the average value), which is too large to be explained by the pure temperature change. The variations were most likely caused by the combination of these two factors. Despite the observed differences, the recorded echoes seem to be good enough to be used for analysis of the in vivo experiments.

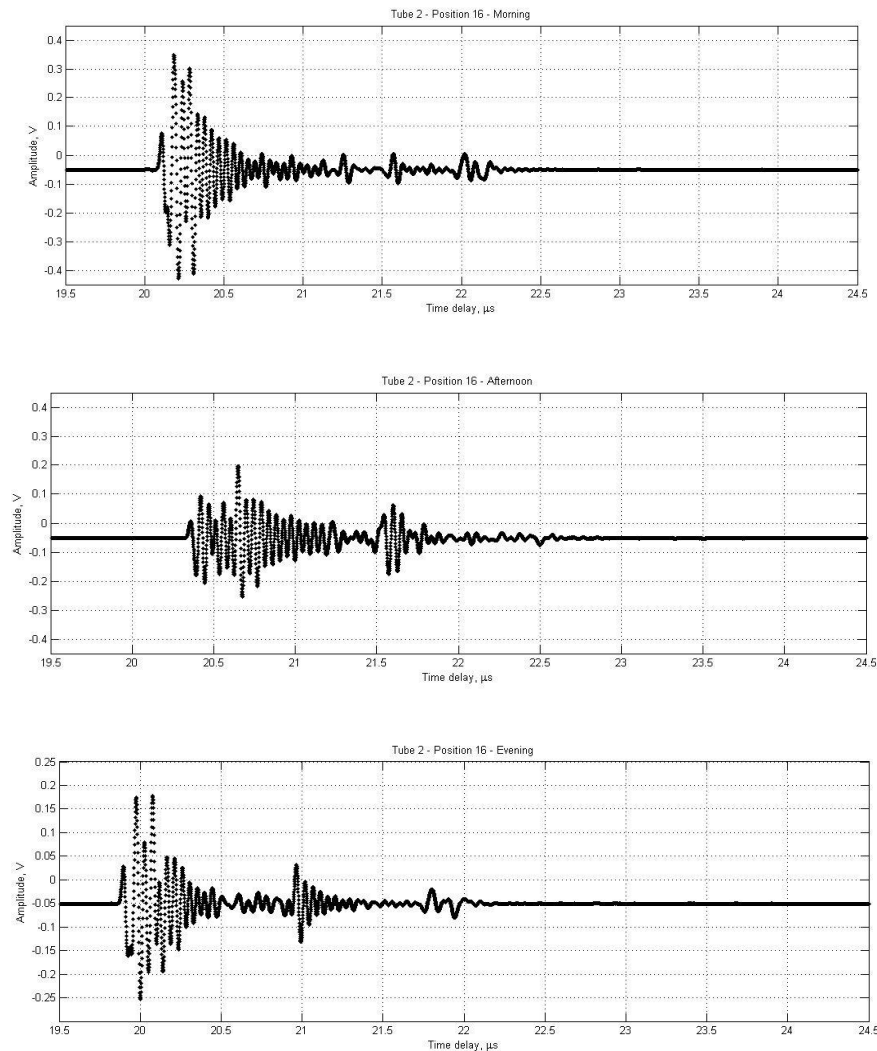


Figure 4.14 - Waveform collected for the second phantom at the centre during the morning, afternoon and evening examinations (from the top to the bottom respectively)

4.4.2.2 - Examining differences in waveforms recorded from different phantoms from the same transducer's positions

The second step in validating the results was to compare the waveforms within different sets from all three tubes to determine the similarities and differences in these waveforms. Theoretically, if the tubes are similar in all

aspects except their diameter and thickness, one can expect recording waveforms that are similar in shape. However, the timing of the first reflection and the timing between following reflections will be different because of the diameter and thickness respectively.

These similarities and differences are perfectly visible in comparison of waveforms recorded for different phantoms when the transducer was placed at the centre position 16 (figure 4.13). The difference in timing of first and later reflections and the similarity in the shape of the waveforms is clearly seen.

Comparison of the two waveforms shows that the time difference between the initial reflection in the first tube and the second tube is about 5.8 μs (14.1 μs for tube1, 19.9 μs for tube2 and 39.3 μs for tube3). This is because of the distance of the tube from the transducer, caused by the change in the diameter of the tube. These results show that the recorded echoes are not just noise or reflections from unwanted objects, as they change from tube to tube in a predictable manner. It may not be possible at this point to determine if these values are correct and correspond to the diameter or thickness of the tube due to the curved surfaces of the reflectors. However, they do prove the consistency and appropriateness of these results.

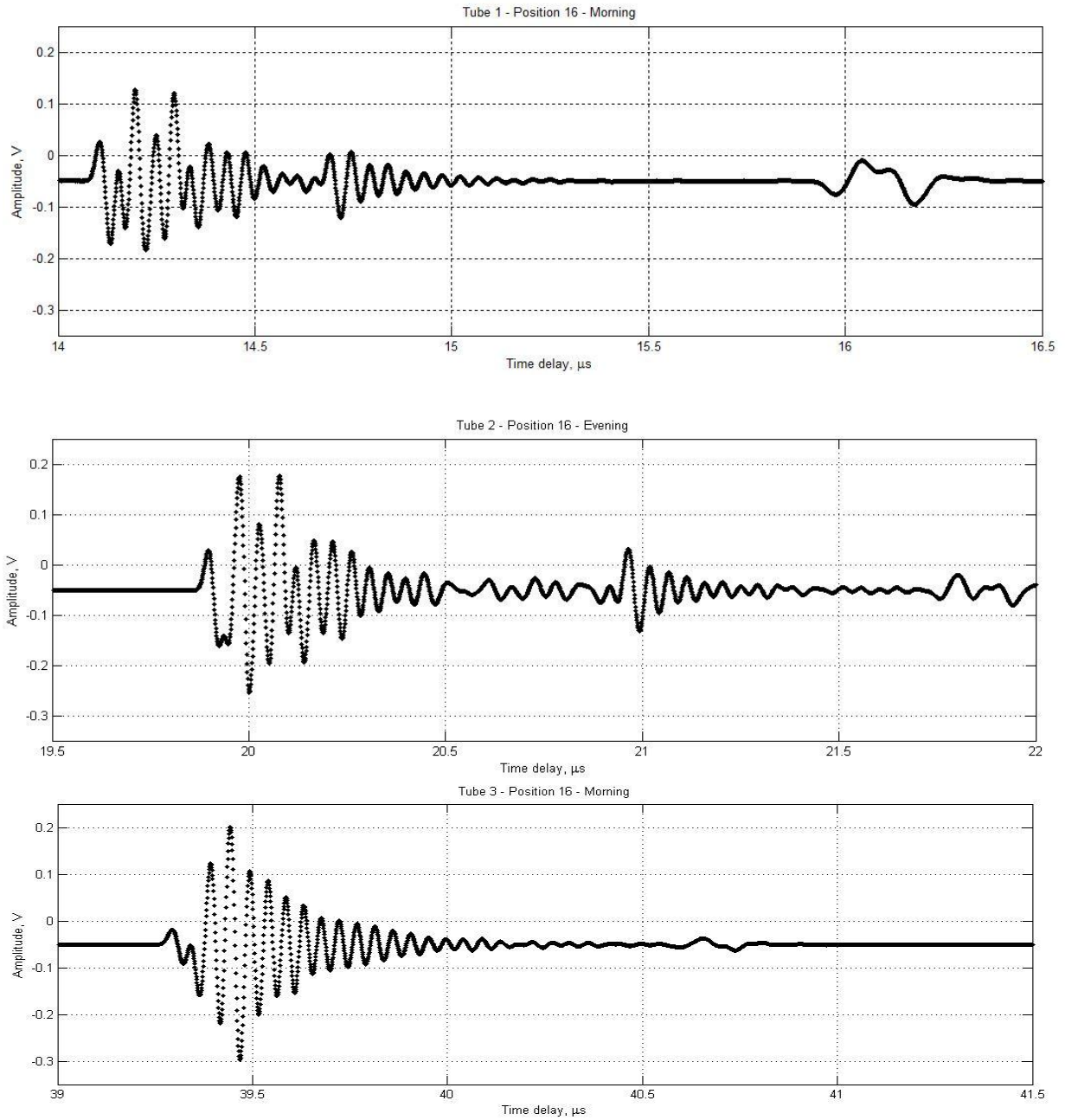


Figure 4.15 - Waveforms recorded for different phantoms at position 16 (top – for the tube 1, middle and bottom – for the tube 2)

4.4.2.3 - Evaluation of acoustic impedance

The other important ultrasonic property of materials, acoustic impedance Z [4.11], measured in Rayl'ses [4.12], determines the amount of ultrasound energy reflected from and transmitted through an interface between two media:

$$Z = \rho c, \quad (4.8)$$

where ρ is the density of the material and c is the sound velocity in the material. At the normal incidence of an ultrasonic wave with the amplitude A_I from medium 1 to medium 2 the amplitudes of the transmitted (A_T) and reflected (A_R) waves are related to the transmission (t_{12}) and reflection (r_{12}) coefficients, and acoustic impedances as follows:

$$t_{12} = \frac{A_I}{A_T} = \frac{2Z_2Z_1}{(Z_2+Z_1)^2}, \quad (4.9)$$

$$r_{12} = \frac{A_I}{A_R} = \frac{Z_2-Z_1}{Z_2+Z_1}, \quad (4.10)$$

Therefore the acoustic impedance for a test piece can be evaluated from one of the above mentioned experimentally measured coefficients. It is usually complicated to measure the incident amplitude directly without special needle probe, which was not available to this project. Reflection from a plate made from material with acoustic impedance Z_2 (ABS plastic for phantoms) surrounded by the medium with known impedance Z_1 (water) shown in figure 4.16 can be described using for following equations:

$$A_1 = A_I \times r_{12}, \quad (4.11)$$

$$A_2 = A_I \times t_{12} \times r_{21} \times t_{21}. \quad (4.12)$$

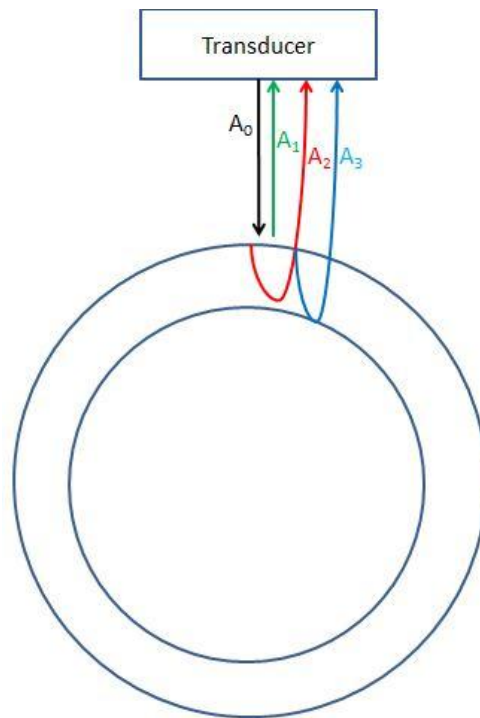


Figure 4.16 - Reflections and reverberations from the phantom

As it holds $t_{12}=t_{21}$ and $r_{12}=-r_{21}$, the ratio of the two above amplitudes yields

$$\frac{A_2}{A_1} = -t_{12}^2. \quad (4.13)$$

This ratio can be evaluated from an experimental record by relating peak amplitudes of the echoes from the front wall, and back wall of the phantom (figure 4.17).

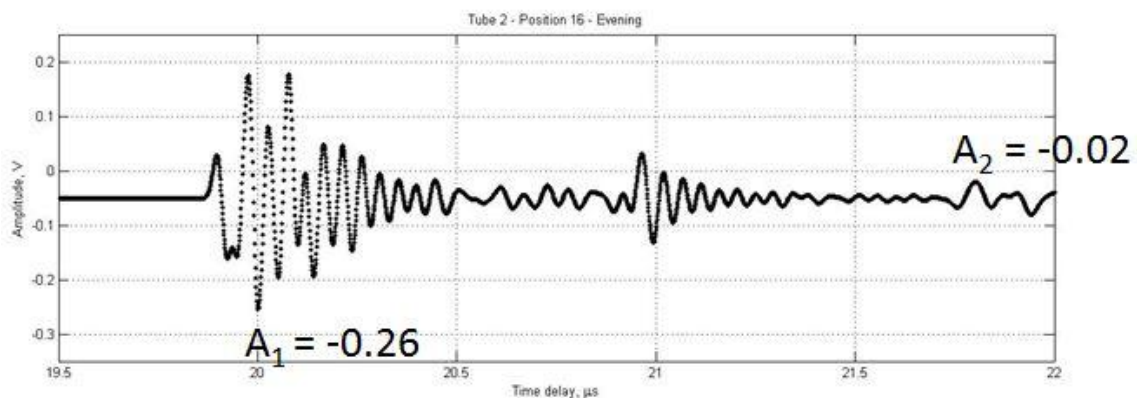


Figure 4.17 - An experimental waveform used for the acoustic impedance evaluation of the phantom

The centre pulse represents a focused reflection (as discussed in the section 4.2.3), and should be ignored for this evaluation. The base line (zero level) is offset by -0.05 thus $A_1 = -0.21$ ($-0.26 - (-0.05)$) and $A_2 = 0.03$ ($-0.02 - (-0.05)$); their ratio being approximately -7, giving $t_{12} = 0.38$. Taking the density of ABS plastic as $1.04 \times 10^3 \text{ kg/m}^3$ [4.13], and using the ultrasound velocity of 2040 m/s evaluated in section 4.3.3, its acoustic impedance equates to 2.21 MRayl. Taking the acoustic impedance of water at 1.48 MRayl ($1.00 \times 10^3 \text{ kg/m}^3 \times 1480 \text{ m/s}$), the theoretical value for the t_{12} can be calculated from (4.9) as 0.48. While these two estimates differ by about 20%, the experimental value seems reasonable because of the curved surfaces of the phantom that lead to diffusion of the incident energy, and creation of a false echo in the middle of the recorded waveform (figure 4.15). These two factors make A_2 smaller than the value expected for a flat interface.

4.5 – Conclusion

The objective of the work conducted in this chapter was to physically simulate a human artery in a controlled environment, where it is possible to change various settings to match results obtained by mathematical simulations and in vivo experiments.

This environment was commissioned using a water tank that accommodated the test fixtures, phantoms, and an ultrasound transducer, all submersed in water. The size of the tank was selected to balance portability of the test rig with the absence of unwanted reflections of ultrasound waves from the tank, and the mechanical parts present in the test rig. The procedure that needed to be followed to ensure that the test environment is consistent for every other test was developed and followed.

Three different phantoms were tested as imitators of an artery in a human body. Pulse-echo waveforms recorded from these test tubes were examined and compared to each other in order to verify their validity. It was found that the records were consistent with each other, and with expectations based on

experiments with flat objects. However the echoes became much more prolonged in the time domain.

The results showed that positioning the transducer directly above the phantom (such as the axis of the transducer intersected the axis of the phantom) helped to achieve echoes that were most sharp in the time domain. If the transducer was moved from this position, even by a small amount, the echoes became diffused, prolonged, and sometimes looked as there were several objects that caused them. This effect was especially profound for the phantom with the smallest diameter. Despite the careful handling of the transducer, and rigid mechanical fixtures used to position it, waveforms from notionally the same positions were found to be notably different when recorded at different times of the day.

The observed scatter of the waveforms contributed towards the decision to terminate further efforts for improving the simulation results. This is because scatter of this significance could not be simulated before having a thorough understanding the reasons for its existence, as simulating the same conditions must produce the same results over and over again.

The experimentally observed importance of the placement of the transducer resulted in the change to the approach for in vivo experiments. In the previous investigation [4.16] a single waveform was collected and thoroughly analysed. The physical modelling results suggest that it is better to collect many waveforms instead, putting a special attention to the transducer's placement, and sift out waveforms that do not display sought after features. This is simply because the placement of the transducer was not accurate enough.

An important observation, worthy of further investigation, was related to the appearance of an unexpected signal between the reflections from the outer and inner walls of the phantom. This signal could not appear for flat surfaces as there were no interfaces between the inner and outer walls. The possible explanation, which was given above and relates to waveguide ultrasound propagation, needs additional verification by conducting computer simulations and further experiments.

The theoretical method of axial resolution of the system was discussed in chapter 1. It is also important to be able to confirm the theory by doing a practical estimation of resolution of the system. One simple way of getting the actual resolution of the system is to run trials with thinner flat tubes. The curvature in the phantoms used in these phantom simulations will cause reflections that will complicate the waveforms obtained; therefore using a flat tube for the purpose of estimation of the axial resolution will make the interpretation of the waveforms simpler and therefore might give a more accurate indication. The clear waveform from the flat tubes would look similar to figure 4.17 with a clear delay between the pulse and reflection. By testing thinner tubes, the delay between the pulse and the reflection will get less and less to the point that these two signals may not be distinguishable which means the ultrasound scanner is not capable of seeing the two boundaries of the tube (i.e. the two surfaces) as two separate reflections. The thickness of that phantom can be a close estimation of the axial resolution of the system.

There could be a number of factors that would cause the axial resolution of the system not to be achieved. One of the reasons could be that the displacement of water inside the tank which will affect the path and the speed of the ultrasound waves. Also any motion in either the phantoms or the transducer at the time of experiment could have an impact on the recorded waveforms and have an effect on the results.

Figure 4.17 shows the excited pulse length as about 5 μ s. If the sound velocity in the ABS is assumed to be 2040 m/s, if the object is closer than 5mm to the face of the transducer, the initial pulse and the reflection will overlap. Although this may make the waveform more complicated and more difficult to analyse, however with cross-correlation techniques it might still be possible to extract the time delay between the pulse and the reflection.

To use the cross-correlation method, the reflection from the phantom must be recorded when it has a visible delay from the end of the initial pulse, for instance the third waveform of figure of 4.14. Then cross-correlation technique can be applied to this signal and the obtained signal when the two waveforms are overlapping. This will give an indication of when the signals are closest match to each other which then the actual time delay can be determined.

References

- 4.1 - Wikipedia. (2013; August). "Imaging Phantom"[Online]. Available: http://en.wikipedia.org/wiki/Imaging_phantom
- 4.2 - K. K. Shung, "The Principle of Multidimensional Arrays", Eur J Echocardiography ,vol. 3, pp.149-153, 2002
- 4.3 - Tom Nelligan. (2013; August). "Intro to Ultrasonic Phased Array"[Online]. Available: <http://www.olympus-ims.com/en/ultrasonics/intro-to-pa/>
- 4.4 - Wikipedia. (2013; July). "Fresnel diffraction"[Online]. Available: http://en.wikipedia.org/wiki/Fresnel_diffraction
- 4.5 - Wikipedia. (2013, July). "Fraunhofer diffraction"[Online]. Available: http://en.wikipedia.org/wiki/Fraunhofer_diffraction
- 4.6 - Wikipedia (2013; March). "Fraunhofer distance"[Online]. Available: http://en.wikipedia.org/wiki/Fraunhofer_distance
- 4.7 - J. Ophir. "Estimation of the Speed of Ultrasound Propagation in Biological Tissues: A Beam-Tracking Method", IEEE Transactions on Ultrasonics, Ferroelctrics and Frequency Control, vol UFFC-33, no. 4, pp. 359-368, July 1986
- 4.8 - Wikipedia. (2013; June). "Wavenumber"[Online]. Available: <http://en.wikipedia.org/wiki/Wavenumber>
- 4.9 - J. Krejza et al., "Carotid Artery Diameter in Men and Women and the Relation to Body and Neck Size", Dep. of Radiology, Univ. of Pennsylvania Philadelphia, Feb. 2006
- 4.10 - NDTnet. "Plastic Material's acoustic properties"[Online]. Available: <http://www.ndt.net/links/proper.htm>
- 4.11 - Wikipedia (May; 2013). "Acoustic impedance"[Online]. Available: http://en.wikipedia.org/wiki/Acoustic_impedance
- 4.12 - Wikipedia (2013; August). "Rayl"[Online]. Available: <http://en.wikipedia.org/wiki/Rayl>

4.13 – SS custom Electronics. "ABS Material Datasheet"[Online]. Available: <http://www.sselec.com/data/ins%20specs/ABS%20Data%20sheet.pdf>

4.14 – G. Kino. *Acoustic Waves: Devices, Imaging, and Analog Signal Processing*. New Jersey, USA, 1987

4.15 - He Yin et al. "Measurement time as a limiting factor for the accurate acquisition of repeatable waveforms", in *Intelligent Data Acquisition and Advanced Computing System: Technology and Applications*, Berlin, Germany, 2013, in press

4.16 – O. Benner, "Synchronisation of vascular ultrasonic scans with heart activity using ECG signals", MPhil thesis, Dept. Elect. Eng., Nottingham univ., Nottingham,UK

5 - Verification of the developed instrumentation *in vivo*

In vivo experiments, reported in this chapter, were conducted after obtaining an approval from the Faculty of Engineering Ethic Committee, at The University of Nottingham.

After validating individual parts of the instrument, it was necessary to integrate all to test and prove the operation of the overall system. In order to ensure the correct operation of the instrument, each separate section of the system must be operating appropriately. The overall aim of the instrument is to measure the IMT and lumen diameter of an artery.

In order to verify the ability of the system to measure IMT and lumen diameter, a series of experiments were carried out. These experiments utilised all of the tools explained in chapters 2, 3 and 4 to enable the accurate measurement of IMT and lumen diameter, after reducing the effects of blood flow. These measurements presented a comprehensive test for the correct and robust operation of the developed instrumentation. Dedicated experimental protocol needed to be developed for this purpose to standardise preparation of the instrumentation, application of the sensors, and in vivo data acquisition procedure. The acquired data were analysed offline in order to establish their validity, consistency and compliance to literature.

This chapter explains the procedure that is required to be followed in order to be able to make consistent measurements using the developed instrument. It will also shows analyses on the recorded data from in vivo experiments to verify the operation of the system.

5.1 - Experimental protocol

The experimental verification of the correct operation of the developed instrumentation must include well defined and repeatable actions, fully described custom built/prepared and off-the-shelf instrumentation and materials. Also, there has to be enough details to enable another researcher to repeat the experiment. These pieces of information are combined to define what is called an experimental protocol:

5.1.1 - Connection diagram for the instrumentation

The experimental setup includes the following instrumentation:

custom built

- ECG monitor, for digitizing the ECG signal and transmitting it over the IR link (chapter 2)
- ECG processor, for receiving the ECG data and triggering the ultrasonic scan (chapter 3)

previously developed

- ultrasound scanner with controllable number of averages and interleaving factor [5.2] triggered by an external signal for taking scans of carotid arteries;

off the shelf

- UPR [5.3], for providing high voltage excitation of the transducer and amplification of the echo signal
- LeCroy 9450A digital storage oscilloscope [5.4], for visual inspection of the signals at different nodes of the instrumentation.

These instruments were connected as shown in figure 5.1.

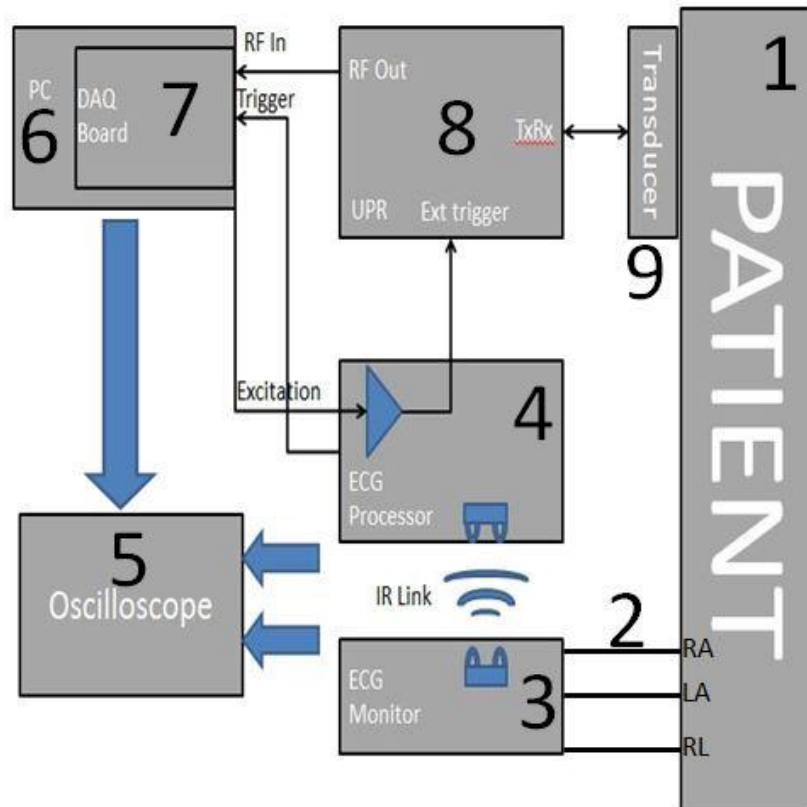


Figure 5.1 - Interconnection of custom build, previously developed and off the shelf instruments used for in vivo measurements (1 – patient; 2 – electrodes (right arm RA, left arm LA and right leg RL); 3 – ECG monitor; 4 – ECG processor; 5 – Oscilloscope; 6 – Personal Computer; 7 – DAQ Board on the PC; 8 – ultrasonic pulser receiver (UPR); 9 – ultrasound transducer)

A photograph of the experimental in vivo setup (figure 5.2) additionally shows coupling gel tubes used for the ECG electrodes and ultrasonic transducer (marked by numbers 6 and 7 in figure 5.2 respectively).

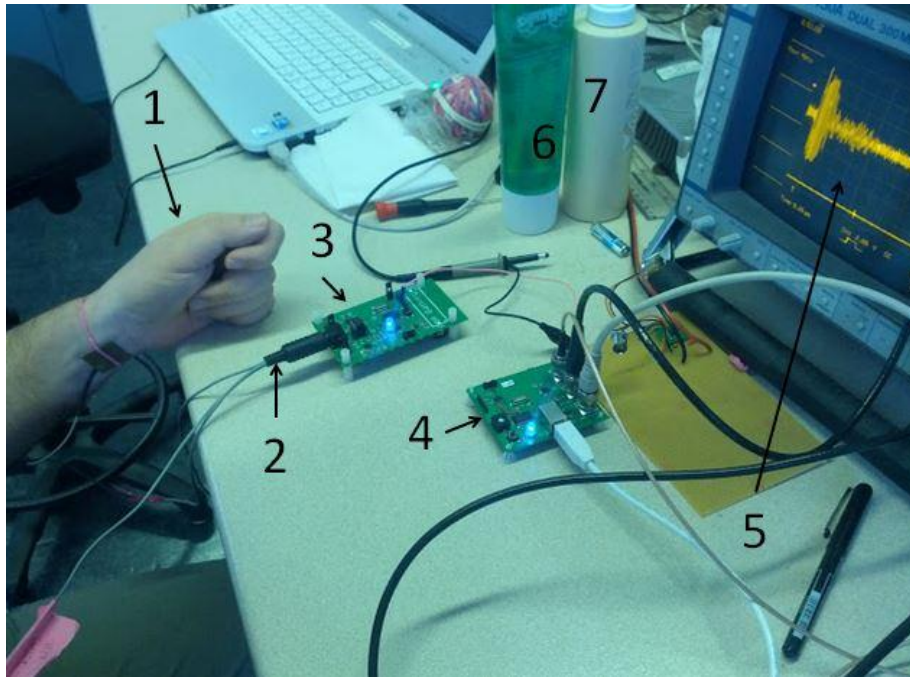


Figure 5.2 - Photograph of the setup for an experiment (1 – patient; 2 – ECG electrodes connector; 3 – ECG monitor; 4 – ECG processor; 5 – Oscilloscope; 6 – conductive gel for the ECG electrodes; 7- coupling gel for the ultrasound transducer)

After connecting the instruments, the oscilloscope was used to check all the signals among the instruments, and, after that, to display the UPR output RF signal as shown in figure 5.2.

5.1.2 - Setting up the ECG instrumentation

The waveform acquisition starts from presence of the ECG signal at the output of the ECG front end, and appropriate generation of the ultrasonic trigger. Electrodes need to be connected to the body of the volunteer as described in chapter 2. The output of the ECG front end is checked using an oscilloscope before starting, and during the experiment, to ensure that the signal supplied to the ECG processor possesses sufficient SNR.

It was observed that starting operation of the IR link led to a substantial increase in electronic noise at the output of the ECG front end, as shown in figure 5.3. The ECG front end starts functioning as soon as the board is connected to its power supply. After approximately 4.5 seconds of being powered, the microcontroller turns the IR link on, which adds a considerable amount of digital noise to the waveform. Even though this noise is heavily affecting the visible ECG signal, it is still possible to see the general shape of a typical ECG waveform and the R-waves in the signal. Therefore, the ECG Processor will still be able to pick up these R-waves.

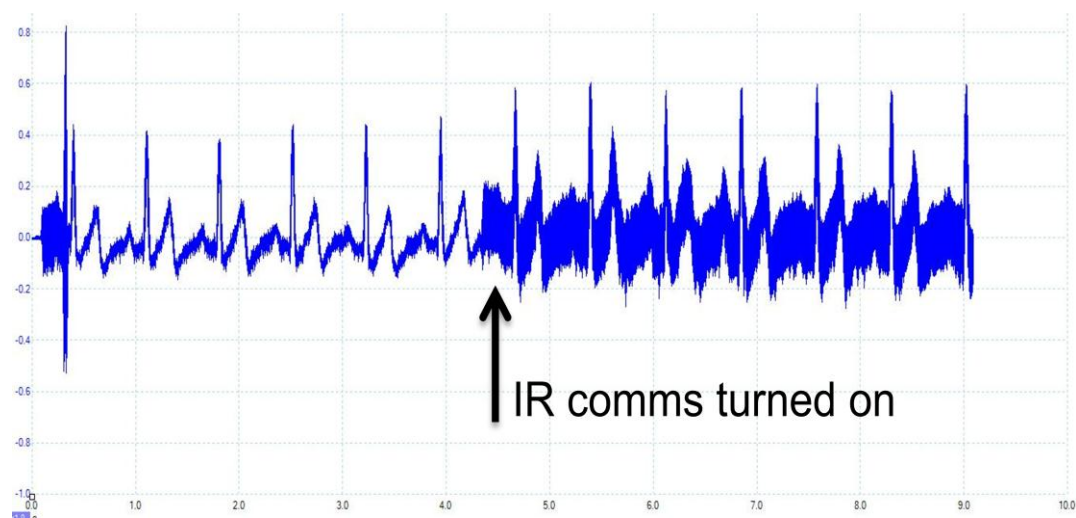


Figure 5.3 - Output signal of the ECG front end showing rapid increase

Another source identified for the noise increase was the operation of the on board DC/DC converter. If the battery on board was new (conventional battery) or fully charged (rechargeable battery), the overall noise level remained appropriate as shown in figure 5.3. However, when the battery became discharged during continuous operation, the converter started to produce such a level of noise that made the detection of R-waves impossible when the IR link operated (figure 5.4). Therefore, it is important to use a fresh, fully charged battery every time.

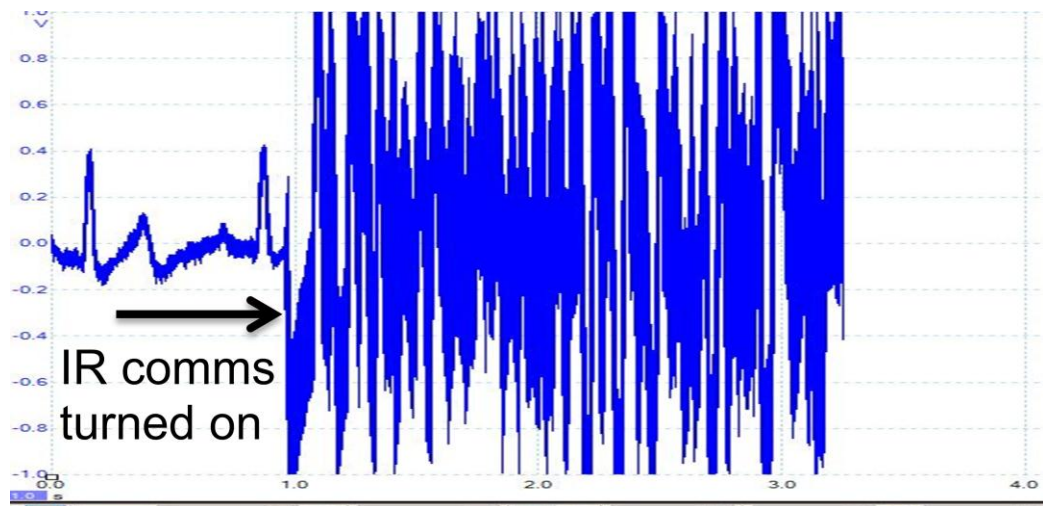


Figure 5.4 - Output signal of the ECG front end showing unacceptable increase in noise

at the start of IR communication when using discharged battery

The ECG monitor and Processor are placed in close proximity to enable reliable IR communication (figure 5.5). After powering the ECG processor up from a USB port, the on board LED should show a correct light pattern when the monitor undergoes initialisation. After that the LED should indicate that the processor receives IR data. At this point the trigger output of the ECG processor can be observed at an oscilloscope showing short pulses for almost every R-wave (some R-waves can remain undetectable because of the changes in the baseline as discussed in chapter 2). Trigger pulses should change their position relative to the R-wave at the output of the ECG front end when the dial of the ECG processor potentiometer is moved into different preset positions. Additionally, when the ECG processor is powered, it translates the 1 V output trigger pulses of the DAQ board to the 5 V pulses that are required by the UPR. When the DAQ and UPR control software is activated, the UPR excitation pulses should be constantly present at its external trigger input; and an oscilloscope should display excitation and reflection waveform at the UPR's RF output.

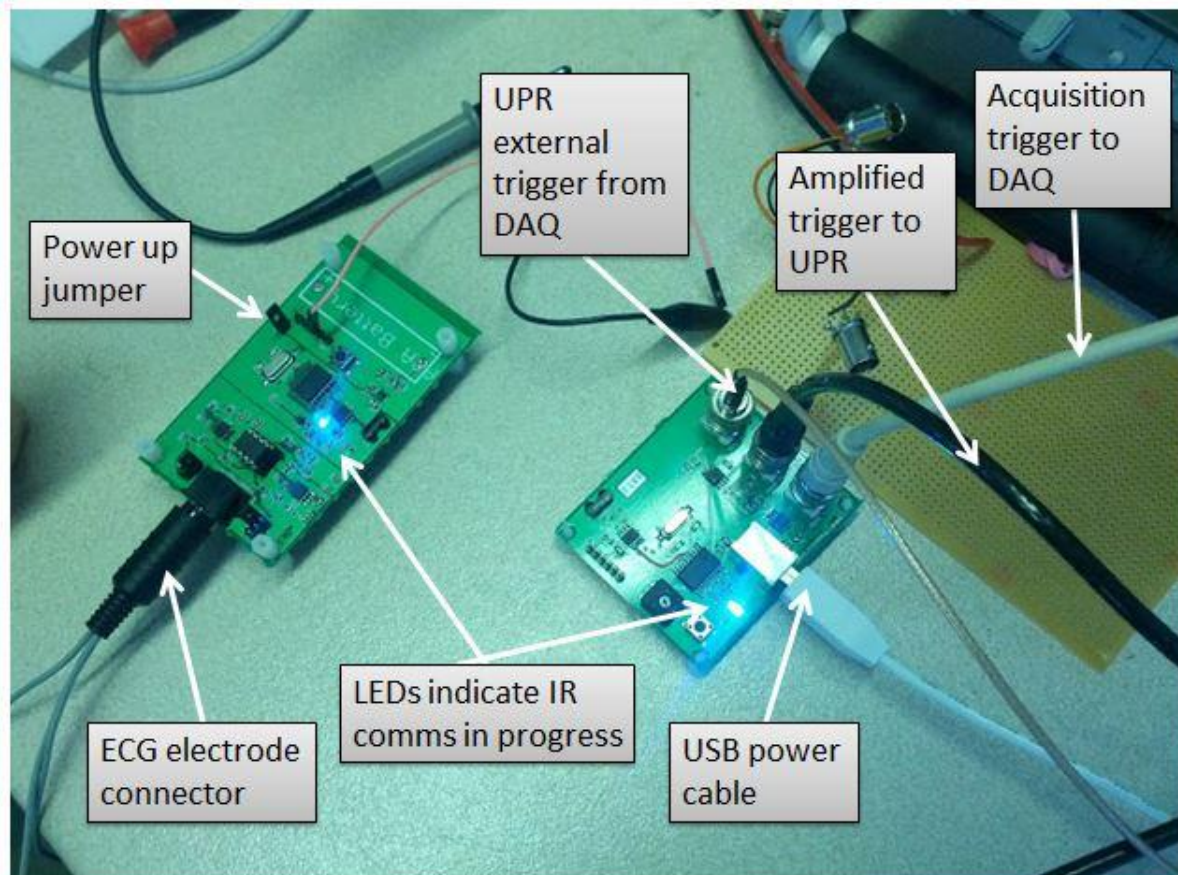


Figure 5.5 - Placement, connections and indicators for the ECG instrumentation

5.1.3 - Setting up the ultrasonic scanner

The instrumentation works in a way that the trigger signal from the DAQ to UPR is always present. Therefore, the transducer keeps sending signals and receiving reflections. When the R-wave trigger is sent to DAQ from the ECG processor, the DAQ will process the following $N_A * N_I$ reflections, where N_A is the number of averages and N_I is the interleaving factor.

The setting on the DAQ software is important to keep the acquisition time of a single waveform as low as it needs to be. Typical heart rate at a relaxed resting state of the patient should be around 60 beats per minute, which is around one beat per second. During this time the diameter of the artery cyclically changes as a result of varied blood pressure in the lumen. Using too high a value for the $N_A * N_I$ product will result in recording unsuitable waveforms because the lumen changes too much [5.22].

The quality of the received signal strongly depends on the number of averages performed on the signal. The more excitation signals and their reflections are coherently added, the less noise remains as the noise is added non-coherently, resulting in the increase of the SNR.

In making a compromise between shorter measurement time (to have a consistent snapshot of the artery without changes) and clarity of the noise-free signal, the former factor had a priority because any reflections from moving tissues will not add coherently. For this reason the $N_A * N_I$ product was set to 10, in order to ensure that the waveforms for processing were taken within 1 ms only at the pulse repetition frequency of 10 kHz. These parameters were set using the DAQ graphical user interface shown in figure 5.6.

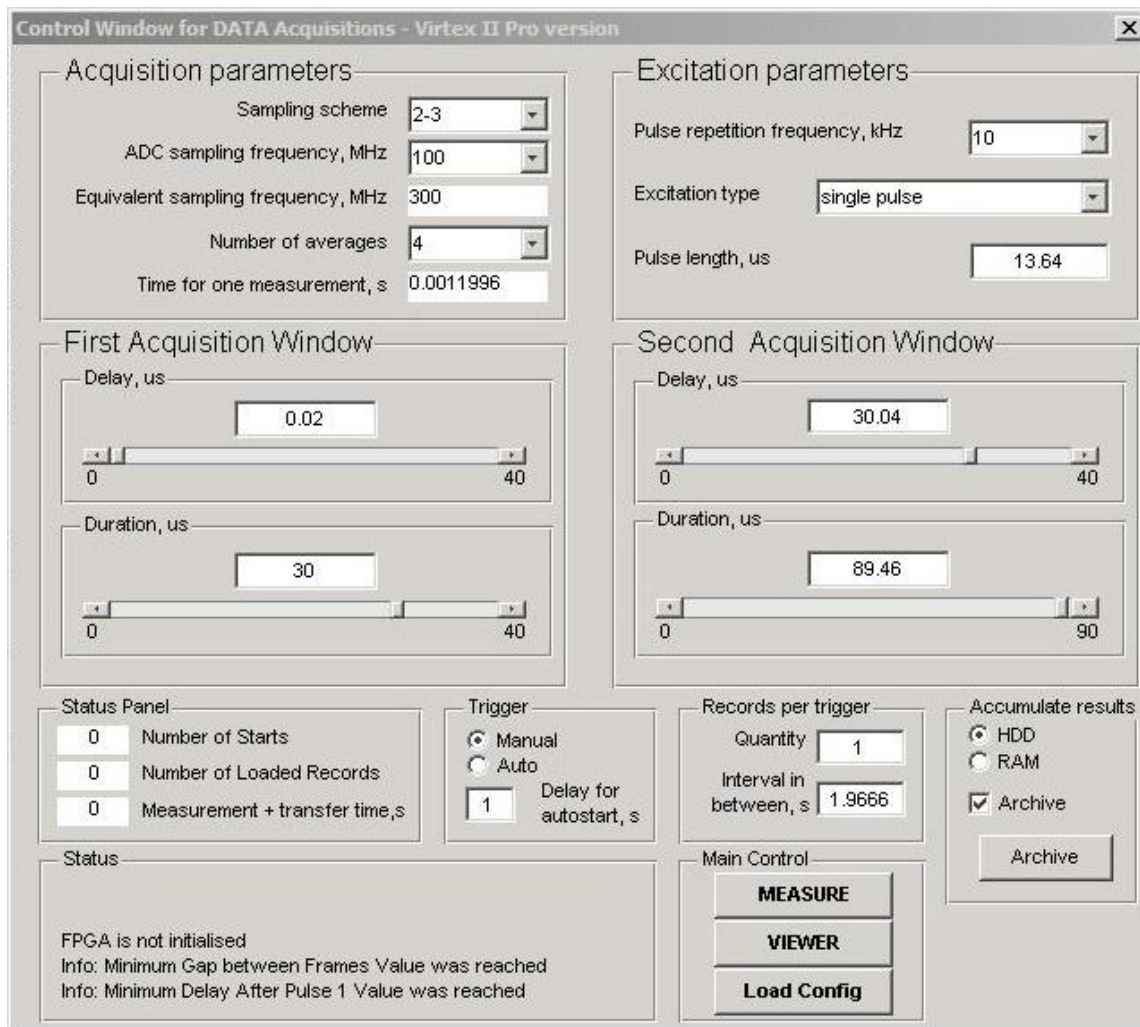


Figure 5.6 - Screenshot of the control panel

The parameters shown in figure 5.6 were already discussed for the phantom experiments in section 5.3.1. The excitation pulse was kept exactly the same as it was used for phantom experiments. The combination of the sampling scheme and number of averages however, needed change in order to keep the time for each measurement at around 1ms. This value ensured that the measurement time equated to a small fraction of the cardiac cycle time. This is so the physical characteristics of the artery, including the IMT and lumen diameter, did not change notably during the examination.

It is important to reduce the measurement time in order to be able to record waveforms when changes in the blood flow are minimal to exclude any effects from the tension inside the artery, as discussed in 1.5.1. However, achieving small axial resolution is crucial for accurate evaluation of both the IMT, and the lumen diameter. Assuming the velocity of the ultrasound in the human body to be close to water, i.e. 1500m/s and 300MHz sampling frequency, the theoretical axial resolution of the instrument can be calculated using equation 1.1 and 1.2:

$$\text{Axial resolution} = \frac{c}{f_s} = \frac{1500\text{m/s}}{300\text{MHz}} = 2.5\mu\text{m}$$

The input required by the UPR for external triggering is 5V. As explained previously in chapter 3, the DAQ board was only capable of outputting signals at maximum of 2V peak to peak. Therefore, a level converter was added to the ECG processor to provide the UPR with triggering the signal it requires. Figure 5.7 shows the output of the DAQ board (blue trace) at 2V, and input signal to the UPR (red trace) at 5 V. The timing of the triggering was also very important. Every rising edge of the trigger signal started an excitation signal by the UPR. The period chosen for the setup meant an excitation signal was produced by the DAQ board every 100 us, with high state of 20 us as required by the UPR.

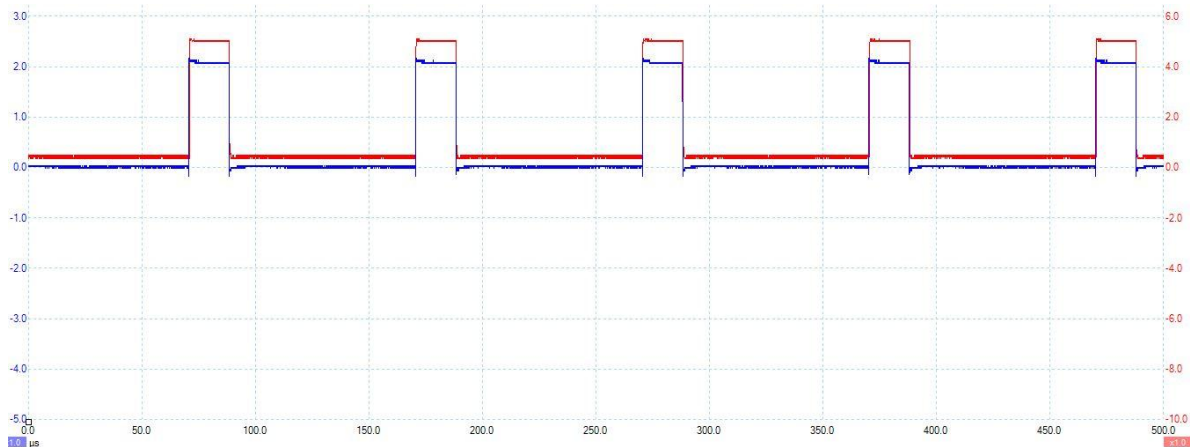


Figure 5.7 - Operation of the level converter on the ECG processor board (blue trace – input from the DAQ board, red trace- output to the UPR)

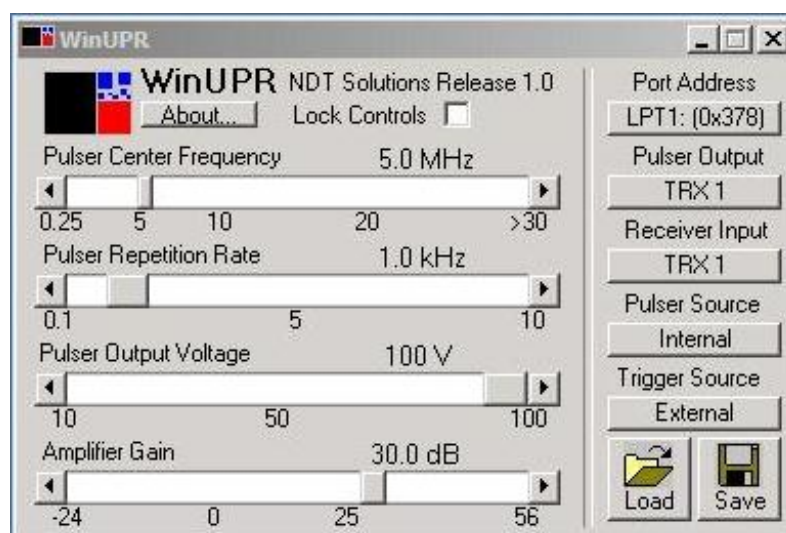


Figure 5.8 - UPR setup window

The UPR is also controlled by the personal computer, using a software called WinUPR (figure 5.8). This program allows changing the properties of the UPR excitation signals. Centre frequency is set to match that of the transducer, in this case 5 MHz. Repetition rate is irrelevant since the external trigger is used. The output voltage is set to 100 V to provide the ultrasound waves with as much energy as possible, to ensure that reflected waves are visible against the noise. The gain of the amplifier in the UPR is set to the desired value to also help with the amplitude of the received signals. There is no fixed value for the gain, as the reflections are affected by different factors such as placement of the transducer,

and amount of pressure applied to the transducer while holding it against the neck. Therefore, the gain was adjusted by observing the amplitude of the signals at the RF output socket of the UPR.

Output and Input of the UPR are both set for TRX1, which, since Pulse-echo is being used, will excite an initial wave from the transducer connected to TRX1 and receive reflections from the same transducer. The excitation signal is produced by the UPR, therefore, the Pulser source is set to internal. However, trigger source is set to external as the trigger signal is provided by the DAQ board, and fed to the UPR via the level shifter at the ECG processor (as shown in figure 5.1).

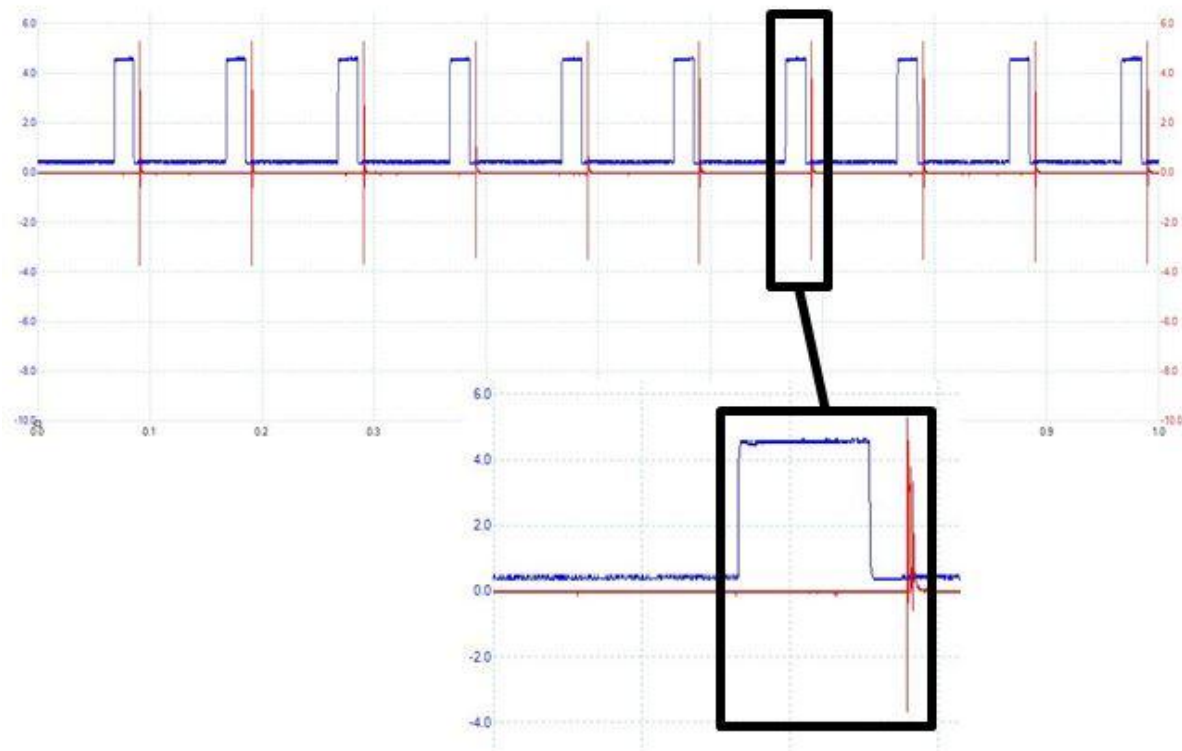


Figure 5.9 - Trigger signal at the input of the UPR and the excitation pulse it produces

Figure 5.9 shows how the excitation pulse is controlled by the trigger signal. The transducer connection of the UPR is terminated by a 50 Ω resistor. The amplitude of signal is at 5 V, which is too high for the DAQ board to convert without clipping. The gain setting for the UPR (see figure 5.8) can be changed

during examination, to fit the echo signal within the input range of the DAQ board, i.e. from -1 V to +1 V.

5.1.4 - Getting appropriate ultrasonic A-scan

5.1.4.1 - Identification of the transducer elements

The linear array transducer used for this experiment is a medical transducer, which was used in a hospital in the United States and was later discharged for unknown reasons (figure 5.10). Unfortunately, it was not possible to find any reference material, such as user manual, specifying its parameters and pin-outs. Its label reads "5 MHz Linear array".

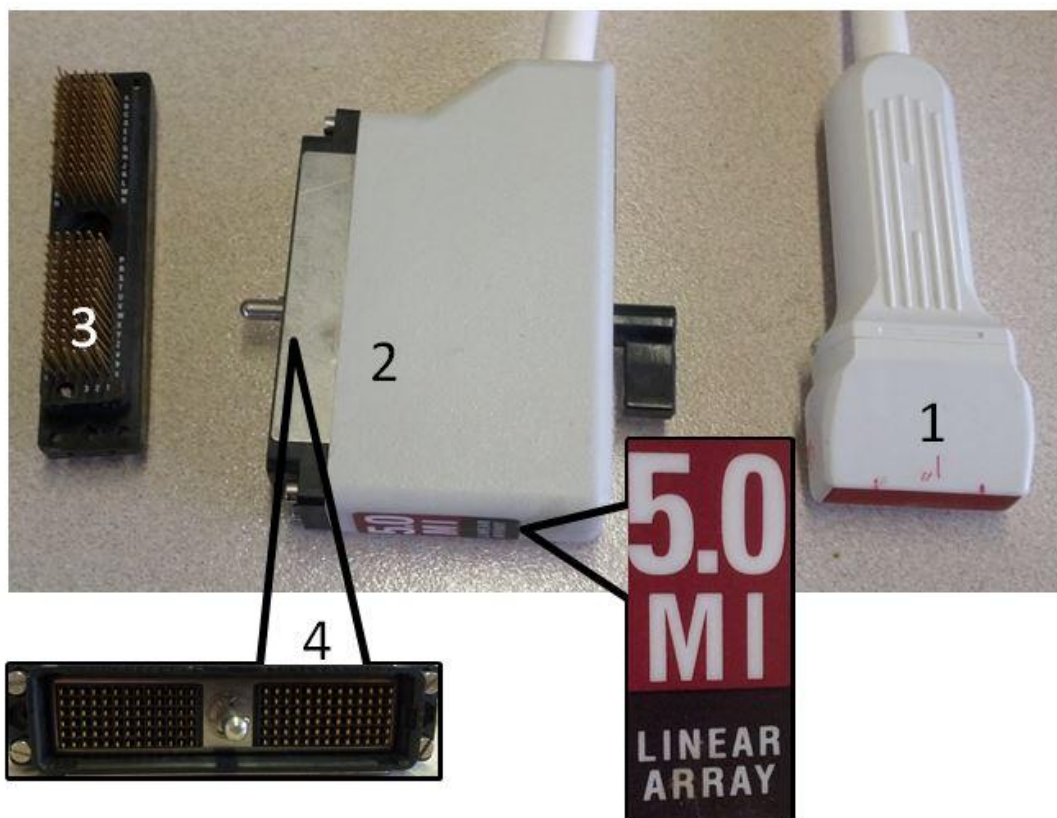


Figure 5.10 - Photograph of the transducer and its mating connector (1 - transducer's head, 2 and 4 - transducer's connecting pins, 3 - mating connector to the transducer)

All the transducer pins were tested to find which of them are signal pins and ground pins. Then the signal pins were connected in turn to the UPR to find which of them were operational. This test showed that there was a substantial number of usable elements, and the established pin-out is shown in figure 5.11.

	6	5	4	3	2	1	
A	x	x	x	0	x	x	A
B	95	51	0	x	x	x	B
C	45	x	91	0	92	43	C
D	93	41	0	46	0	x	D
E	40	x	94	0	89	37	E
F	90	38	0	52	0	77	F
G	36	x	87	0	85	35	G
H	82	30	0	39	0	81	H
J	31		83	0	84	28	J
K	76	33	0	32	0	78	K
L	86	x	79	0	80	26	L
M	73	34	0	29	0	75	M
N	25	0	69	0	74	24	N
P	68	27	0	23	0	71	P
R	21	0	67	0	72	20	R
S	60	22	0	8	0	70	S
T	15	0	64	0	65	19	T
U	66	18	0	6	0	57	U
V	16	0	56	0	61	12	V
W	62	17	0	4	0	63	W
X	13	0	58	0	59	10	X
Y	55	14	0	3	0	50	Y
Z	11	0	47	0	53	7	Z
a	54	9	0	2	0	48	a
b	88	0	44	0	49	5	b
c	x	x	0	1	0	42	c
	6	5	4	3	2	1	

Figure 5.11 - Experimentally determined pin-out of the transducer (0 denotes grounded pins, red cells with crosses showed either unused pins or connections to malfunctioning elements, numbers in the green cells relate to the order of the elements placement from one side of the transducer’s head)

As it was found by experimenting with tube phantoms (chapter 5), the best waveform was obtained when the ultrasound beam crossed the centre of the tubes. Even small deviations from this position severely complicated analysis of the reflected waveforms. Therefore, it was important to establish positions of the individual elements of the transducer array. This is to be able to acquire waveforms from definite neighbouring elements that should have covered the artery of interest. These positions were determined experimentally, by placing the array on the custom manufactured 45° aluminium prism, shown in figure 5.12.

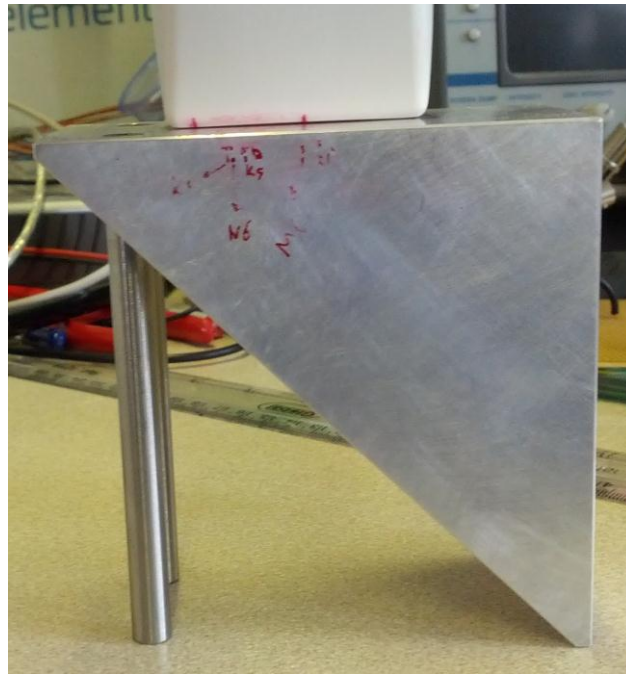


Figure 5.12 - Aluminium prism used to determine positions of array elements

When the array was placed on top of the prism, the ultrasound pathway for every transducer became different (the shortest pathway for the transducers on the left of the array) and could be estimated by the pulse transit time in the pulse echo mode. The 45° angle was selected in order to achieve a reasonable trade-off between the resolution of the estimates (the steeper the angle, the bigger the difference between the pathways of adjacent transducers) and their amplitude (the steeper the angle, the lower the amplitude of the reflection towards the element used). Analysis of the waveforms recorded from all of the array elements allows one to identify the order of the transducers in the array, as shown in figure 5.10 clearly.

5.1.4.2 - Placement of the transducer on the neck of the patient

Conventional IMT measurements are usually conducted by placing the ultrasonic array parallel to, and above the RCA with the centre of the former around the RCA bifurcation (figure 5.13). It shows that the array can be placed at different positions on the neck (compare (a) and (b)). Contact gel is used to ensure acoustic contact between the array and skin (evident in (c)), the

sonographer find the best position for the array by observing real time images (d).



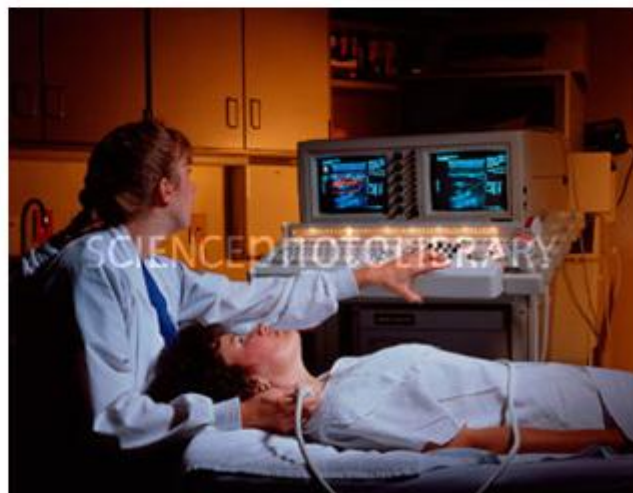
(a) [6.5]



(b) [6.6, fig.2]



(c) [6.7]



(d) [6.8]

Figure 5.13 - Examples of ultrasonic array placements for taking RCA scans

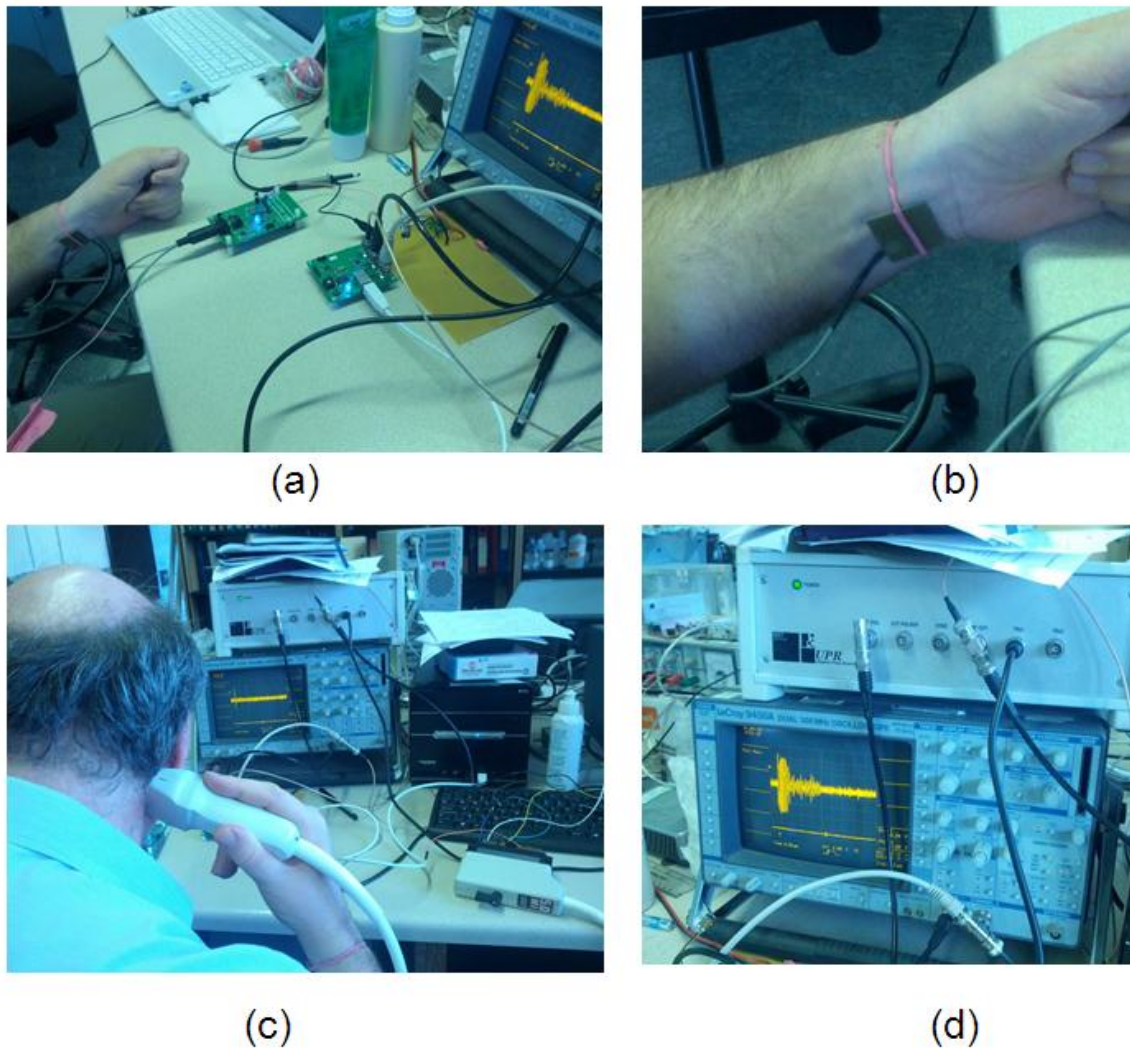


Figure 5.14 - Photographs of the subject and equipments taken during

In the case of the developed instrument, it is impossible to adjust the position of the array based on the obtained real time image as an A-scan does not permit this. Additionally, the obtained A-scans around the bifurcation point can be confusing if the bulb is not clearly visible, and Internal Carotid Artery (ICA) and External Carotid Artery (ECA) close to this point can easily be mixed up [5.14]. Because of these reasons, the developed instrument was tested away from the Right Coronary Artery (RCA) bifurcation at the ECA close to the ear. The ECA location was detected by palpation. Then, the array was placed perpendicularly to the ECA in order to be able to select a transducer whose beam crosses the centre of the artery, as shown in figure 5.16(c). The ECG electrodes were held in place by a rubber band, visible in figure 5.16(a-c). A typical noisy waveform observed at the oscilloscope is presented in figure 5.16(d).

5.1.4.3 - Selecting the right transducer for a complete in vivo measurement session

A reasonable first order approximation for the reflection of an ultrasonic pulse from the artery can be obtained, by considering the artery as a cylindrical tissue, surrounded and filled in by liquids with lower acoustic impedances. If these substances formed layers with parallel interfaces, the signs of the reflection coefficients for the incident plane wave would be as follows: liquid-tissue (+), then tissue-liquid (-), then liquid-tissue (+), and, finally, tissue-liquid (-). The following signs of the reflection coefficients were observed in the phantom experiments: (+) for the water-tube interface and (-) for the tube-water interface (figure 4.13). Also, a waveform shown in figure 5.16 [5.15, figure 1] clearly shows that the reflection coefficients at the interfaces tissue-liquid and liquid-tissue exhibited the same sign. The most likely cause of this behaviour was the diffraction of ultrasound waves, as an array element emits a spherical wave and the cross section of the artery is circular. Nevertheless, an ideal waveform should have four distinct reflections. The time delays between the first and the second, and between the third and fourth reflections, correspond to the ultrasound transit time in the proximal and distal intima-media layers respectively. These delays for the pulse-echo mode and IMT of 0.6 mm can be estimated at approximately $0.8\mu\text{s}$ ($0.6\text{mm}\times 2/1500\text{m/s}$). The time delay between the second and third reflection relates to the propagation in the lumen that can vary for males from $5.11\text{mm}\pm 0.87\text{mm}$ for the ICA to 6.52 ± 0.98 for the CCA (mean \pm standard deviation) [5.16]. Allowing the scatter of results within two standard deviations, the expected transit time can be estimated within the arteries of interest from $4.4\mu\text{s}$ ($(5.11-2\times 0.87)\text{mm}\times 2/1500\text{m/s}$) to $11.3\mu\text{s}$ ($(6.52+2\times 0.98)\text{mm}\times 2/1500\text{m/s}$).

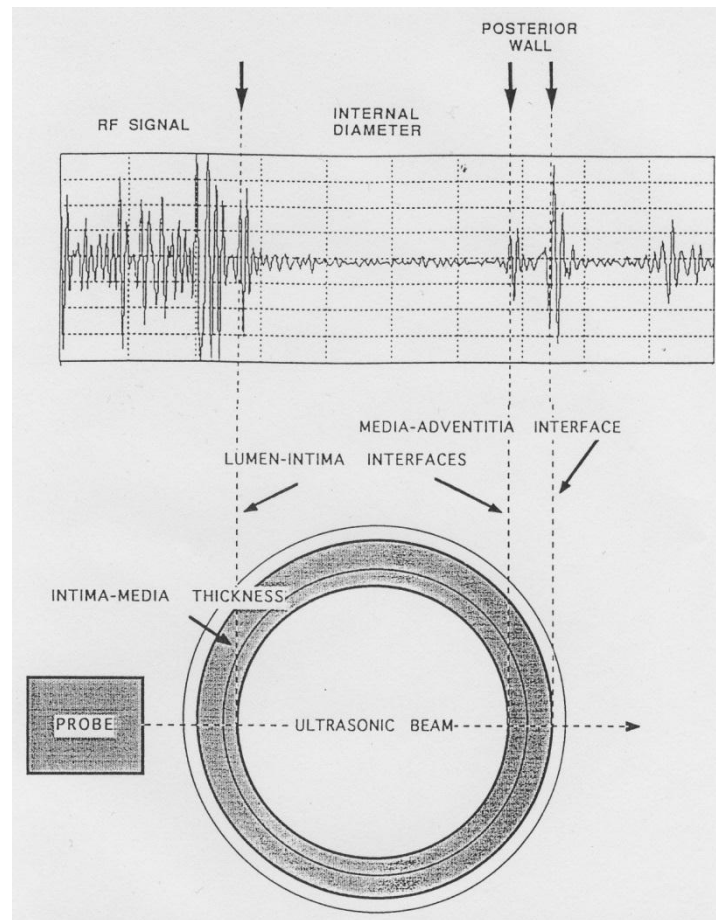


Figure 5.15 - An example of experimental waveform and its relation to arterial interfaces [5.15, figure 1]

After placing the transducer on the neck (figure 5.14, c), several transducer elements were connected in turn to the UPR transceiver port TRx1 as shown in figure 5.15, and the received echoes (similar to one shown in figure 5.14, d) were observed carefully on the oscilloscope in order to select an element producing the waveform with four well defined reflections.

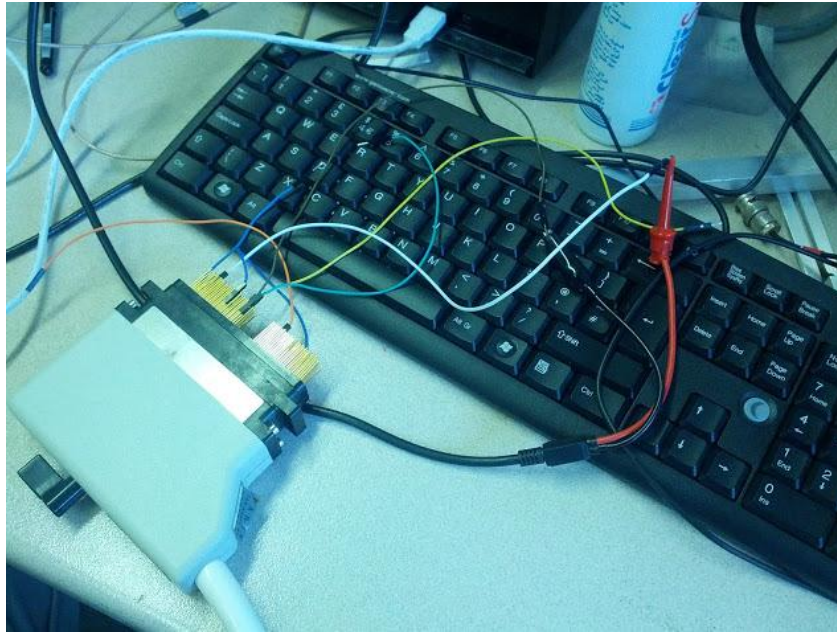


Figure 5.16 - Pins of the array's mating connector were connected to the UPR using

When the best reflection among the group of six elements (S5 [22], M5 [34], b4 [44], U1 [57], P1 [71], H1 [81] as numbered in figure 5.11) was found, the corresponding pin would be kept connected to UPR and the measurement session began.

5.1.5 - Collecting a set of waveforms for an *in vivo* measurement session

It must be noted that IMT measurements are conducted under certain conditions established by medical practitioners. A recommended setting and conditions for IMT measurement is depicted in figure 5.17.

Ultrasound examination, practical aspects

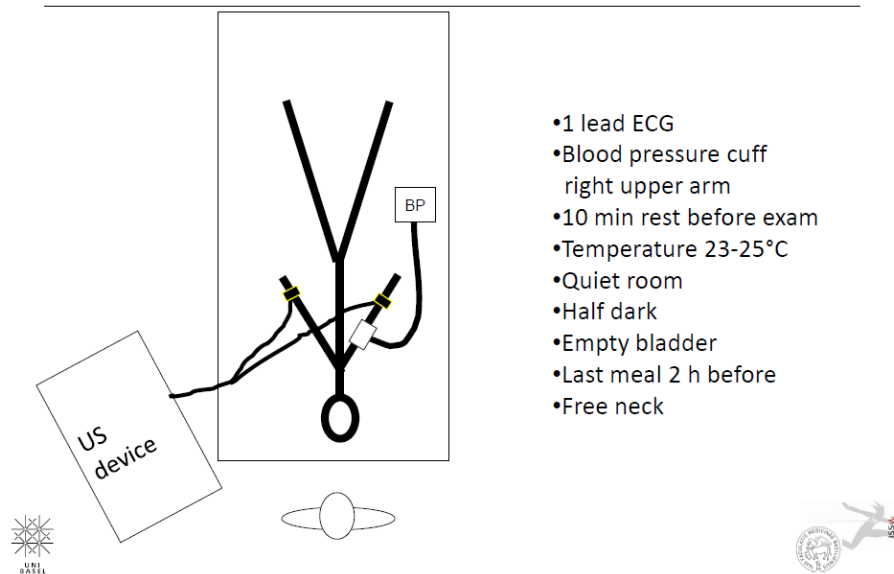


Figure 5.17 - Setting and conditions for IMT measurement

It was difficult to meet all of these conditions in an electronic laboratory. The subject was sitting on a chair in a fully lit room holding the transducer by a hand with an ECG electrode attached (figure 5.16, c). A blood pressure monitor was not used despite, the fact that variations in the blood pressure between different sessions affect the estimated IMTs.

After the instrumentation was set up, the experimenter enabled waveform acquisition that was triggered by the following pulse from the ECG processor. Every waveform was taken five times to enable consistency check. The potentiometer, controlling the trigger delay after the R-wave, was then rotated until the control LED showed the subsequent colour combination. There were four delay settings available as shown in table 5.1. These were accompanied by switching on different combinations of the on board LEDs for easy reference of the experimenter. For every session all the four settings were used, resulting in collection of 20 independent waveforms. The session took approximately 10 minutes, and it was desirable to shorten this time as the subject could accidentally move the array. The waveform analysis was decoupled from the waveform acquisition in order to avoid any misconceptions regarding the data collected.

5.1.6 - Protocol summary

In summary, the developed protocol consisted of the following steps:

- connecting the ECG electrodes, setting up and checking correct operation of the ECG instrumentation (section 5.1.2);
- setting up and checking correct operation of the DAQ board and UPR (section 5.1.3);
- positioning the ultrasonic array and selecting a particular transducer (section 5.1.4);
- collecting the set of waveforms for the present session (section 5.1.5).

5.2 - Check for consistency of the acquired records

Six experimental sessions were carried out according to the experimental protocol summarised in section 5.1.6, and total of 120 experiments were recorded. No data analysis was conducted until all the records were collected in order not to introduce any unintentional bias to the experimental procedure. No issues were observed with the developed ECG monitor, neither for operation and communication, nor triggering during the conducted in vivo experiments.

Unfortunately, some of these records were discarded as few files became written with an error or unintentionally overwritten. Session 3 started too soon after finishing the session 2; this resulted in the persistent movement of the ultrasonic transducer despite the best effort from the subject that did not get enough rest between the sessions. For this reason all the session 3 records were discarded.

All of the remaining valid records were analysed for consistency among each five records collected during the same session for the same delay where applicable. Records were considered consistent if they exhibited

- similar level of noise (a few records were found excessively noisy for unknown reason);
- comparable level of echo signals (uneven pressure applied to the transducer did result in variation of the recorded echo amplitudes);
- absence of significant echo signals not present in the other records in the set;
- presence of groups of echoes with close timings among the signals in the group.

Although these assessment criteria were not formalised any further, they helped to sift the recorded waveforms. For example, out of three valid waveforms recorded during session 1 for delay 1 (figure 5.180), second waveform shows excessive noise, and the other waveforms display different configurations of the echoes.

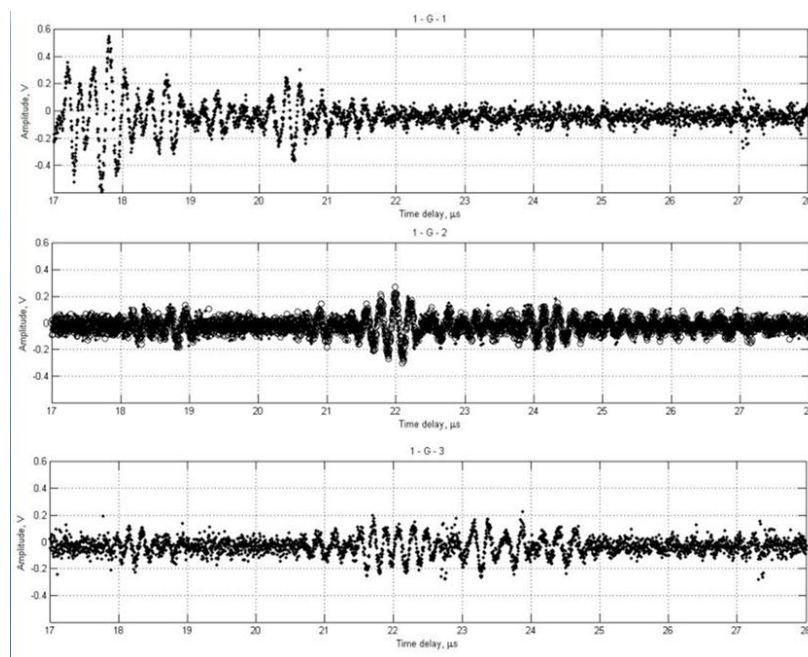


Figure 5.18 - Three valid waveforms recorded for session 1, delay 1 that show no consistency

In contrast, figure 5.24 presents five consistent records for session 4, delay 4 after filtering [5.18]. The raw waveforms taken during this session zoomed into the area of interest are presented in figures 5.19-5.23.

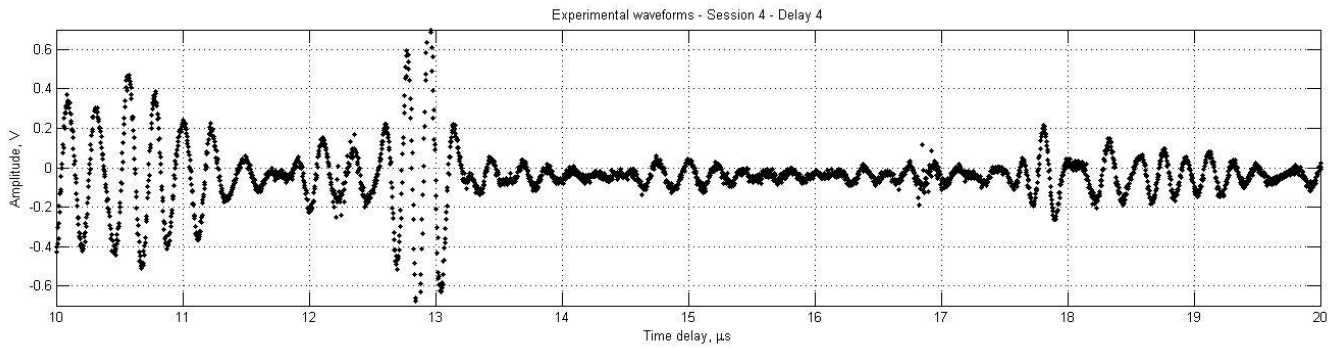


Figure 5.19 - Session 4 - Delay 4 ; First record

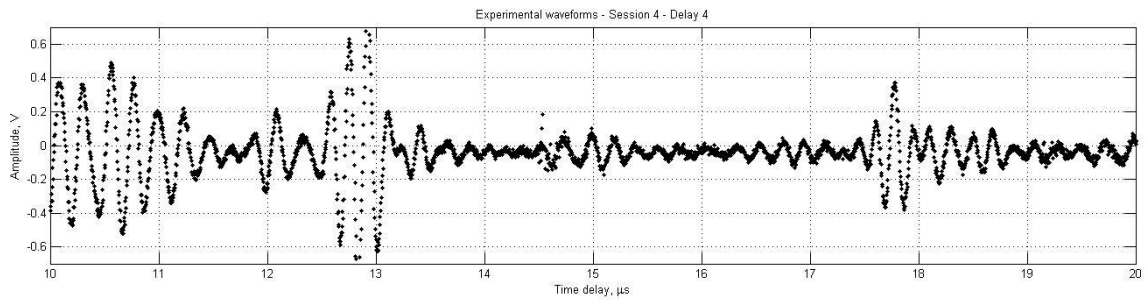


Figure 5.20 - Session 4 - Delay 4 ; Second record

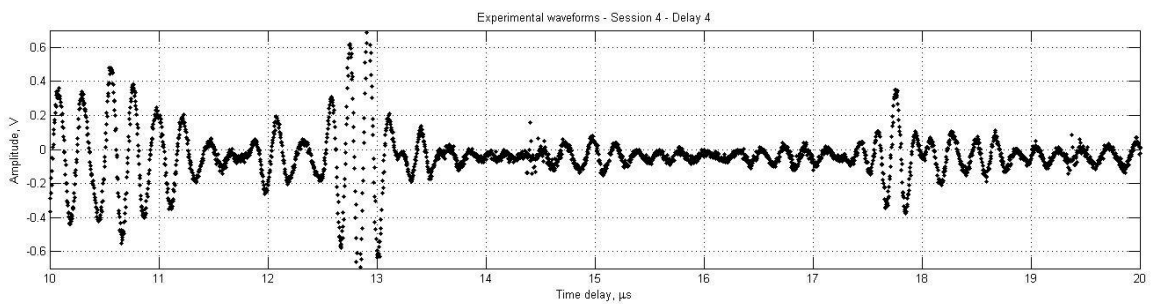


Figure 5.21 - Session 4 - Delay 4; Third record

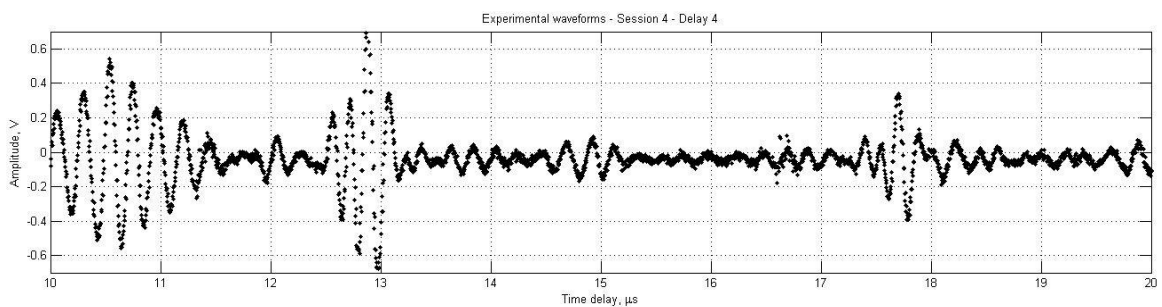


Figure 5.22 - Session 4 - Delay 4; Fourth record

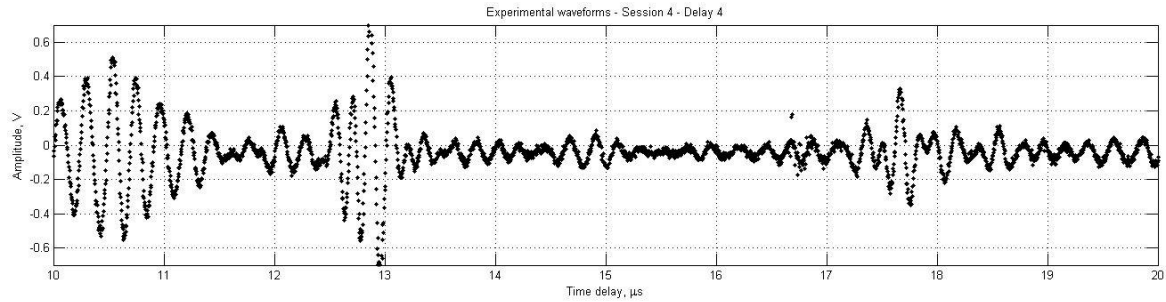


Figure 5.23 - Session 4 - Delay 4; Fifth record

The consistency of the waveforms, recorded during the 4th session, can be assessed by comparing the above waveforms. There is noise interference that makes the waveforms different from each other at some points (e.g. figures 5.22 and 5.23 show some spikes at around 14.5 μ s, which are absent from the other records); however, the overall shape, delay and amplitude of each section of the waveforms are fairly similar. The consistency can also be seen more clearly in the top graph of figure 5.24, where all five recorded waveforms are superimposed using different colours. Except some spikes at around 14.5 μ s and 16.5 μ s, the remaining waveforms are very close to each other, proving the ability of the designed system to take consistent scans.

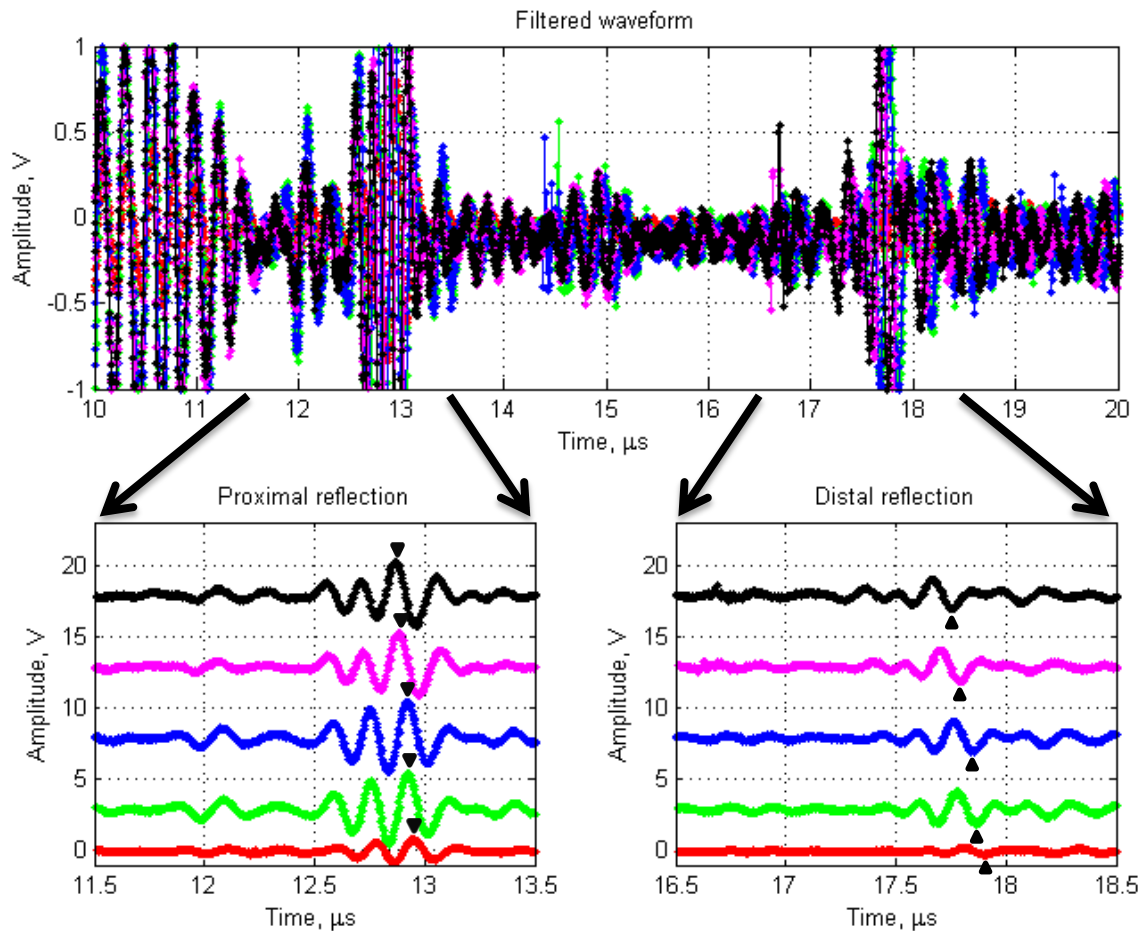


Figure 5.24 - Five consistent valid waveforms recorded for session 4, delay 4 [5.18]

The bottom two graphs in figure 5.24 magnify the areas of interest for the two main peaks in the records of session four. The graph on the left shows the pulse, reflected from the proximal wall and recorded at around 13 μs, and the graph on the right displays the distal reflection at around 18 μs.

Looking at all the waveforms recorded during this session, one can see two major reflection-type peaks before and after the assumed proximal reflections, which are both circled in figure 5.25. There is a long waveform started just before 10 μs (figure 5.25, blue circle), and another one at around 15 μs (figure 5.25, red circle).

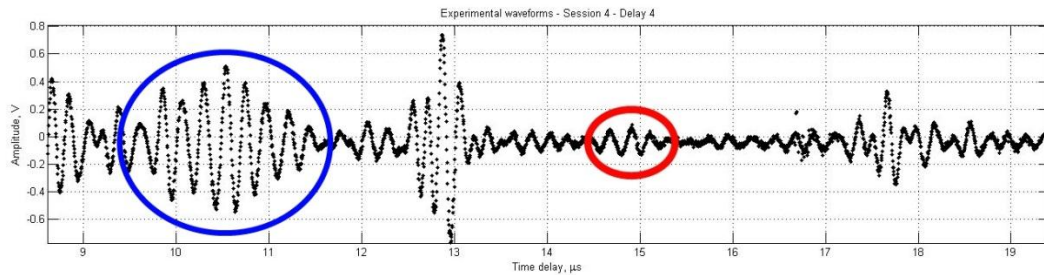


Figure 5.25 - Additional reflections in the recorded waveforms at around 10.5 and 15 μ s

The waveform on the left of the proximal reflection looks like it was constructed out of several pulses, reflected from closely located objects. The observed time delay suggests that these reflectors were situated between the skin and the outer wall of the artery. It is difficult to say which object in a human body could have produced such a wave packet. This requires further study. One possible explanation is that the changes in the acoustic impedance among different tissue layers, located between the skin and the artery, could have caused several reflections. As these layers were very close to each other, the reflections combined to form the observed pulse. The pulse, located within the red circle, may have had similar origin to the pulses that were experimentally recorded and then discussed in chapter 4, section 4.4.2.

Table 5.1 provides a summary of the analysed records. Out of the 120 recorded waveforms only 74 were found valid and, further, only 38 were found consistent. Session 4 records were found the most consistent among all the sessions.

Table 5.1 - Consistency analysis for recorded waveforms at different sessions with different delays (number of valid records / number of consistent records)

Session	Date - Time	Delay1 Green 200 samples (Minimum delay)	Delay2 Red 450 samples	Delay3 Blue Red 950 samples	Delay4 Blue Green 1200 samples (Maximum delay)
1	15/02/13 - 14:30	3/0	3/0	5/5	5/5
2	15/02/13 - 16:10	3/2	3/0	2/2	4/2
3	15/02/13 - 16:30	N/A	N/A	N/A	N/A
4	15/02/13 - 15:30	4/4	3/3	4/4	5/5
5	18/02/13 - 14:00	2/0	3/0	3/0	3/0
6	18/02/13 - 15:00	5/2	5/2	4/0	5/2

5.3 - Propagation delay estimation

Ideally a recorded waveform should feature reflections from all four interfaces from an artery in the following order:

- proximal outer wall,
- proximal inner wall,
- distal inner wall,
- and distal outer wall.

When ultrasound penetrates from the surrounding artery tissue into it, the wave does not change phase as the impedance in the artery wall is higher than that in the tissue. However, if it propagates from the wall into the lumen with lower acoustic impedance, the sign of the reflection coefficient became negative. Therefore, the four a.m. reflections should have the following phases + - + - . The propagation delay in the lumen should be estimated between the markers applied to different polarity amplitudes. An example of finding the position for the lumen markers is shown in figure 5.24, where the highest recorded amplitude at the proximal reflection was chosen as the

marker. Because of this, the lowest recorded amplitude for the distal inner wall became the second marker. The same applies for the reflections from the outer walls (change of sign) with respect to the reflections from the inner walls.

In order to estimate the propagation delays, parts of the raw waveforms were printed on the same scale. Dimensions marked A, B, C and D in figure 5.22 were measured by a ruler, where the relevant reflections could have been discriminated with some confidence. For example, reflections for the outer walls (figure 5.26, red curves) were not clear from the waveform, and the measurement of distances A and D were not taken for this record.

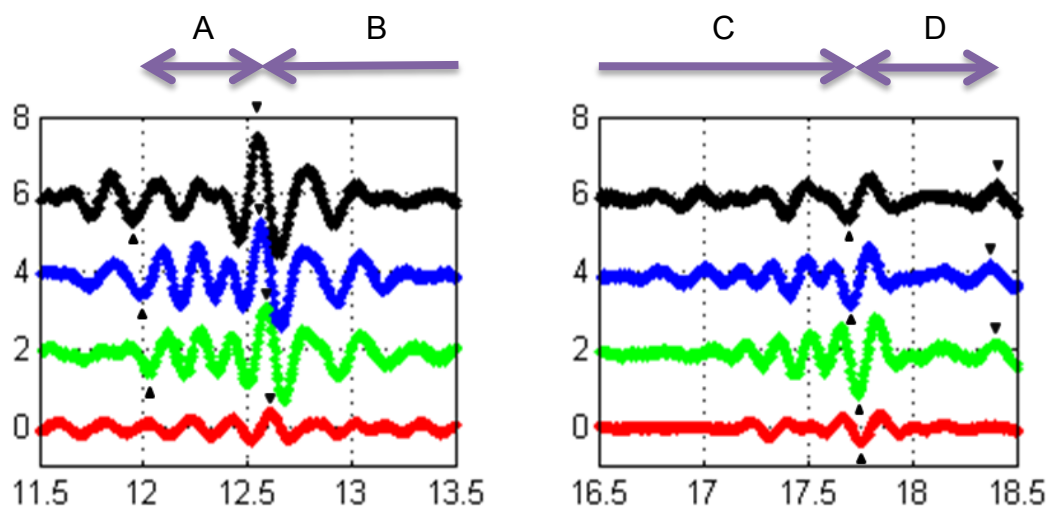


Figure 5.26 - Distances measured from the printouts for the propagation delays estimation

This procedure resembled the one that is being used by sonographers who measure the distance between marks on the recorded sonograms, e.g., [5.19]. The distances were measured with the resolution of 1 mm; 0.5 μ s divisions on the printout were spaced at 24 mm. Therefore, the temporal resolution of these estimates was about 0.02 μ s. This temporal resolution translated into the spatial resolution in the pulse echo mode of approximately 15 μ m (0.02 μ s / 2 * 1500 m/s). Such a resolution seems insufficient for the accurate IMT assessment, but adequate for the assessment of the lumen

diameter. The ultrasound propagation estimates were calculated from the averaged values according to the following equations:

$$\text{propagation delay for the lumen} = \frac{B+C}{24} * 0.5 + 3 (\mu\text{s}) , \quad (5.1)$$

$$\text{propagation delay for the proximal IMT} = \frac{A}{24} * 0.5(\mu\text{s}) , \quad (5.2)$$

$$\text{propagation delay for the proximal IMT} = \frac{D}{24} * 0.5(\mu\text{s}) . \quad (5.3)$$

The waveforms recorded for the session 4 with relevant markers are presented in figures 5.23-5.26.

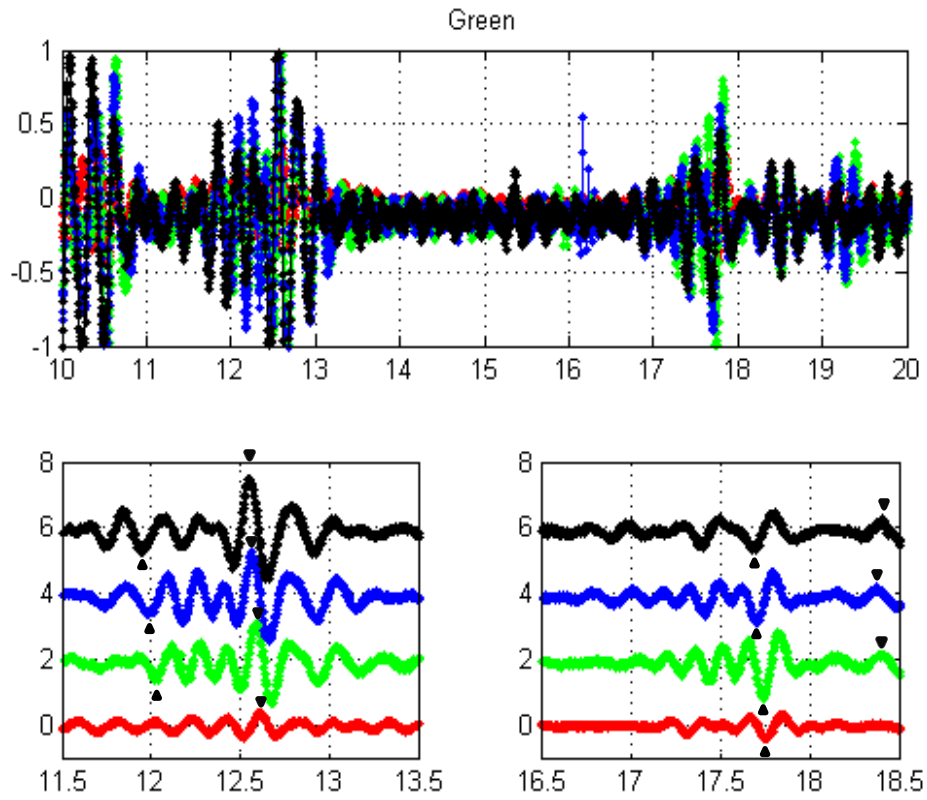


Figure 5.27 - Recorded waveforms for session 4, delay 1 with markers

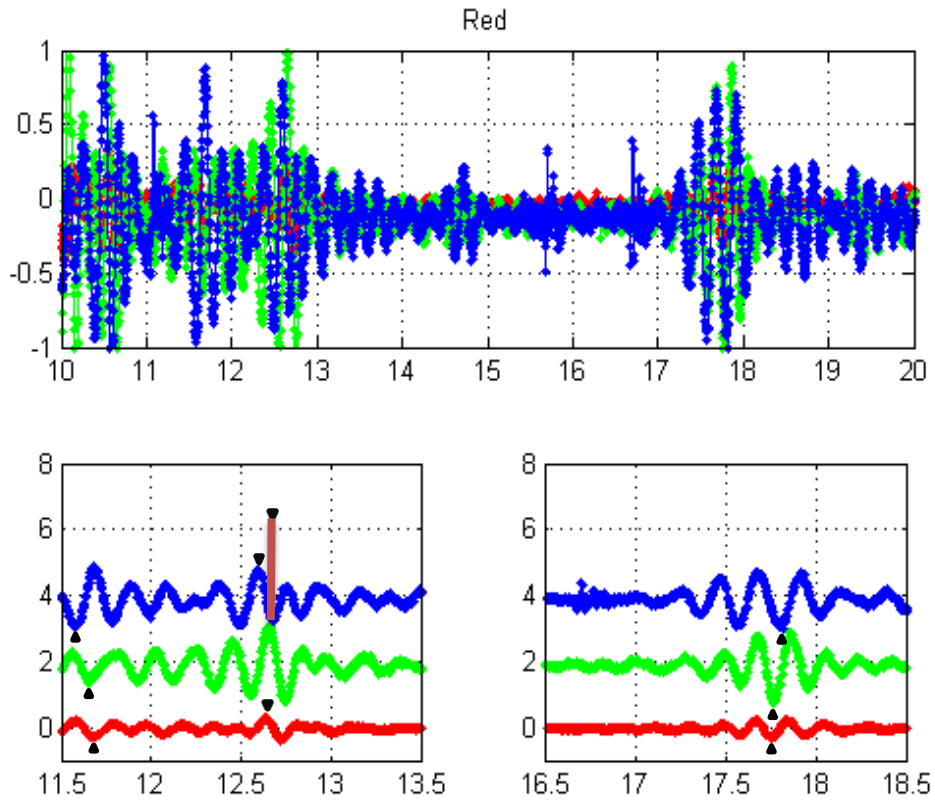


Figure 5.28 - Recorded waveforms for session 4, delay 2 with markers

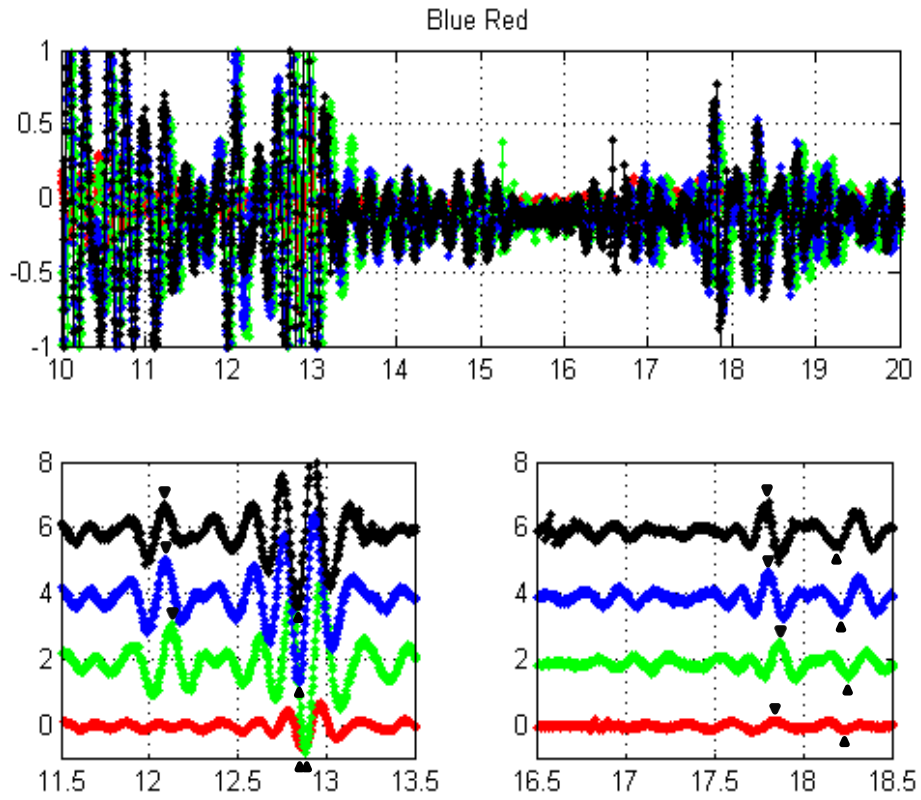


Figure 5.29 - Recorded waveforms for session 4, delay 3 with markers

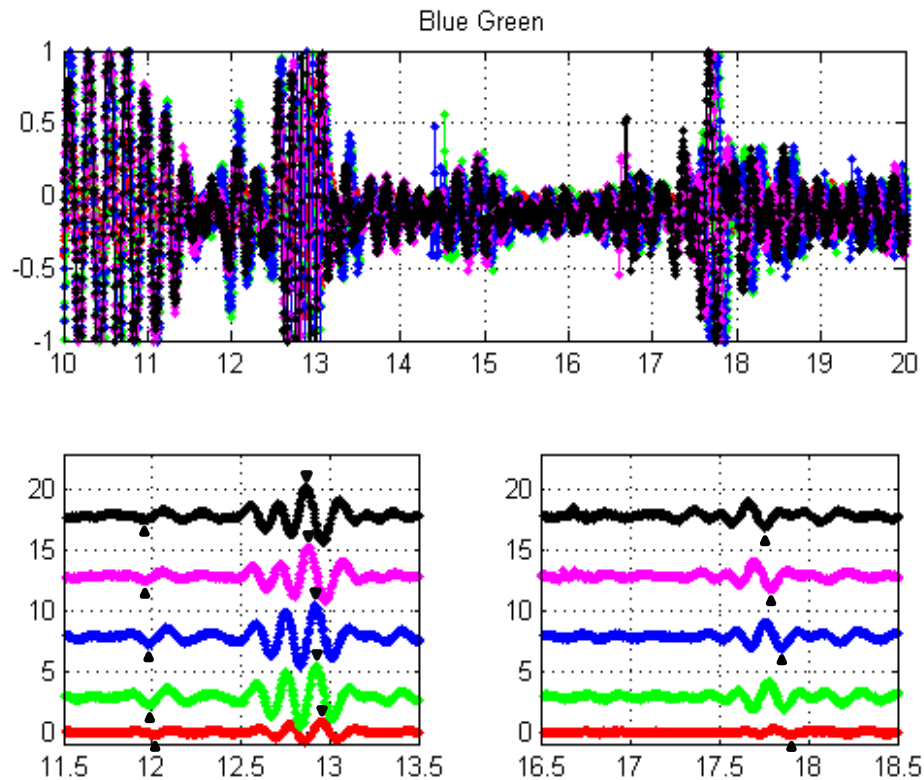


Figure 5.30 - Recorded waveforms for session 4, delay 4 with markers

The measurement and estimation results are presented in table 5.2.

Table 5.2 - Measured lengths and estimated ultrasound propagation delays

Delay	Curve colour	Measured length, mm				Calculated delay, μ s		
		A	B	C	D	Proximal IMT	Lumen	Distal IMT
Green	black	30	46	57	32	0.60	5.15	0.67
	---	---	---	---				
	blue	28	45	57	32			
	green	28	44	60	32			
	red	---	43	61	---			
	average	28.7	44.5	58.8	32.0			
Red	---	---	---	---	---	0.97	5.15	---
	---	---	---	---				
	blue	48	43	63	---			
	green	47	40	61	---			
	red	45	42	61	---			

	average	46.7	41.7	61.7	---			
Blue Red	black	37	33	63	20	0.79	5.02	0.41
	---	---	---	---	---			
	blue	37	32	64	20			
	green	36	30	68	19			
	red	---	31	66	20			
	average	37.7	31.5	65.3	19.8			
Blue Green	black	44	31	61	---	0.96	4.95	---
	magenta	46	30	63	---			
	blue	47	28	66	---			
	green	47	28	67	---			
	red	47	27	68	---			
	average	46.2	28.8	65.0	---			

Results from table 5.2, show that the estimates for the propagation delay in the lumen were consistent at around 5 μ s. This value translates into the diameter estimate of 3.8 mm (5μ s / 2×1500 m/s). Although this value is significantly lower than reported diameters for the CCA and ICA (e.g., [5.14, table 1]), the measurements in this study were taken far away from the bulb where the ECA narrows as shown in figure 5.31. For this reason this estimate can be considered appropriate.

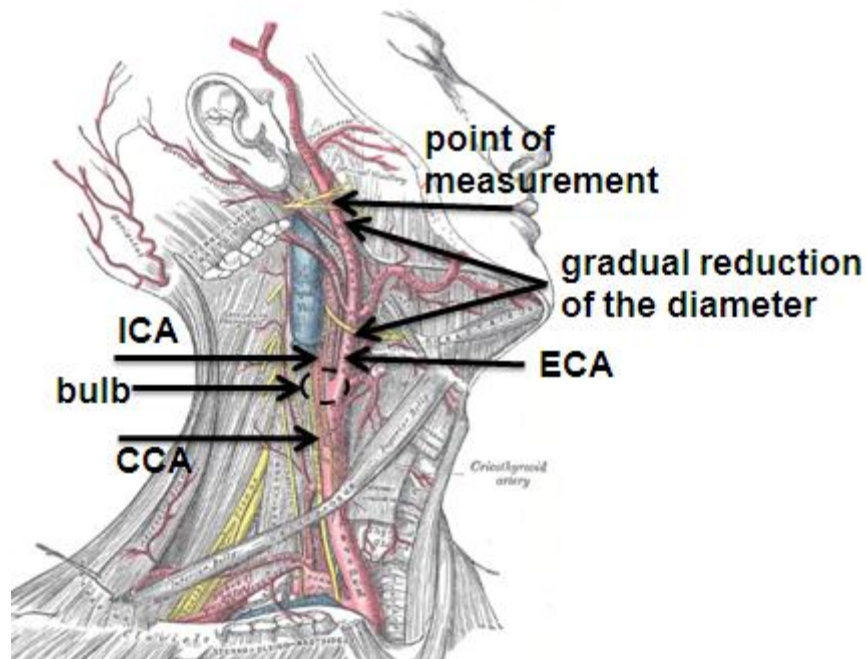


Figure 5.31 - Reduction of the ECA diameter from the bulb to the point of measurement (background image taken from [5.20, figure 507])

Unfortunately, the observed scatter of the estimated values for the IMT rules out any possibility to conclude on its value. This is because the values estimated from the proximal and distant wall were different by less than 10%, which was still too big a difference for the intended accuracy of the IMT estimation. Nevertheless, the obtained estimates for the delays in the lumen do make sense if compared to a typical heart cycle data. Figure 5.32 presents example behaviour of the arterial pressure and ECG versus time. Four equally spaced vertical lines present the possible instants when the waveforms were taken. They show that first two waveforms could have been recorded during the diastolic part of the heart cycle, giving similar values for the lumen diameter. The following two waveforms were taken at the raised values for the arterial pressure, thus the lumen diameter became reduced. Therefore, the data collected during session 4 seem consistent, reasonable and related to a feasible cardiovascular scenario.

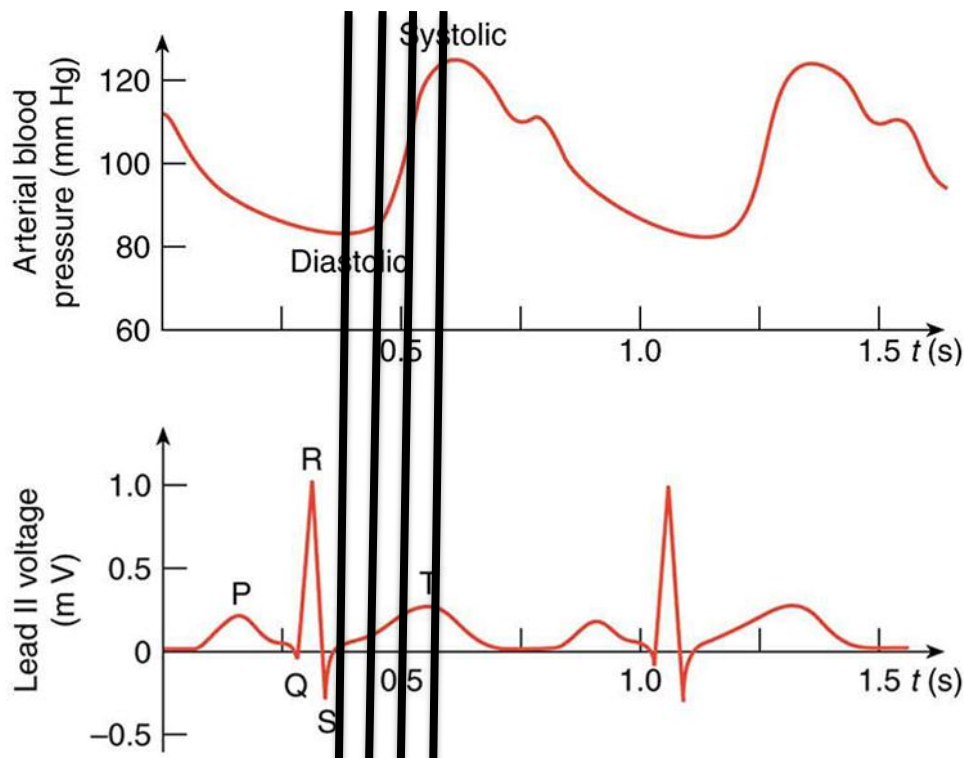


Figure 5.32 - A typical cardiovascular behaviour of the arterial pressure and ECG signal [5.21]. Vertical lines depict time instants when the echo waveforms could have been taken to result in the estimated propagation delays.

The propagation delays estimates for the lumen and IMTs were compared among different sessions. The analysis shows that, despite observed consistency for some waveforms recorded during sessions 1 and 6, shown in table 5.1, they were unfit for the confident detection of relevant echoes required for the delay estimation.

5.4 - Estimation of the SNR for the recorded waveforms

The signal to noise ratio (SNR) of the system was calculated by estimating the standard deviation of the part of the signal, where only noise was present, and parts of the signal, where both signal and noise were present. Assuming that the signal was notably stronger than the noise (which was the case), the SNR was calculated as it is shown below:

$$nRMS = RMS \text{ of Noise}$$

$$aRMS = RMS \text{ of signal and noise}$$

$$sRMS = \sqrt{aRMS^2 - nRMS^2}$$

$$SNR = 20 \times \log_{10}\left(\frac{sRMS}{nRMS}\right)$$

The most consistent set of the experimental records (fourth session, delay 4) was used for the SNR calculations. Table 5.3 presents the SNR values for each of the waveforms recorded.

Table 5.3 - SNR calculation of the system

Waveform	nRMS, V	aRMS, V	sRMS, V	SNR, dB
1	0.0431	0.2663	0.2628	15.69
2	0.0423	0.2725	0.2692	16.07
3	0.0427	0.2670	0.2635	15.80
4	0.0426	0.2694	0.2660	15.90
5	0.0420	0.2673	0.2640	15.96

From the above table, the average value of the SNR during the 4th session was 15.9 dB.

5.5 - Discussion on possible improvement to experimental procedures and data processing

Despite the fact that the developed experimental protocol was strictly followed, a large proportion of the recorded waveforms became invalid, and appropriate waveforms were consistently recorded during one session only out of the 6 conducted. One reason for this is the difficulty of locating the centre of an artery by observing the echo waveforms on an oscilloscope. This could be improved by applying a conventional ultrasound imaging system, ideally connected to the same transducer as the developed instrument.

Another experimental difficulty was related to the need of holding the ultrasonic array at the same place for the duration of an experimental session (around 10 minutes). This time could be reduced by developing control software that would automatically save the echo records. Additionally, some fixture to hold the transducer throughout an experimental session would be useful to improve the recorded waveforms' consistency.

The reflections from intima-media outer interfaces were not clear from many in vivo records. Contrary to the data presented in a presentation by Schmidt [5.17, slide 22], this happened more frequently to the distal wall. Most likely reason for this is the absence of the time gain control circuitry in the developed instrument, which is used as a standard in commercial instruments, providing extra gain for the distal reflections.

5.6 - Conclusions

The developed experimental protocol allowed taking valid and consistent echo waveforms that could be associated with some cardiovascular scenario. Finding the most suitable transducer in the ultrasound array was the most difficult part of this procedure that could be improved by employing a conventional ultrasound scanner as a reference. The absence of a reference was the likely reason for having good records for only one session among the conducted six.

Both the ECG monitor/processor and ultrasound scanner, operated appropriately without any notable malfunction. Their operation could be improved by further automation of the measurement procedures in order to avoid human errors and delays.

Despite the achieved high temporal resolution of 1ns, the estimation of the propagation delays was conducted with the resolution of about 20 ns. This was to process the waveforms in the way similar to that used by sonographers. Better automated signal processing procedures would have improved the results obtained.

For the best dataset, the echoes from the lumen were found consistent and in agreement with the possible cardiovascular scenario. At the same time, positions of the intima-media interfaces of blood and outer tissue is very difficult to locate reliably. For this reason, development of the automated procedure was not attempted at this stage, and achieving finer resolution of the ultrasonic scanner became unnecessary.

Overall, the conducted experiments confirmed the suitability of the developed instrument for taking measurements in vivo with the high notional resolution. Despite this, the resolution was not possible to utilise for the recorded experimental dataset.

References

- 5.2 - Alexander N. Kalashnikov et al. "High-Accuracy Data Acquisition Architectures for Ultrasonic Imaging", IEEE Transactions on Ultrasonics, Ferroelectrics and Frequency Control, vol. 54, no. 8, pp. 1596 – 1605, August 2007
- 5.3 – Ultrasonic pulser receiver. User manual. NDT Solutions, UK.
- 5.4 – LeCroy. "9450A Portable, Dual-Channel Digital Oscilloscope"[Online]. Available: <http://www.teknetelectronics.com/DataSheet/LeCroy/LeCro9450A.pdf>
- 5.5 – SciencephotoLibrary. "Ultrasound scan"[Online]. Available: <http://www.sciencephoto.com/media/407951/view>
- 5.6 – Xin Yang. "Ultrasound Carotid Artery Intima-Media Thickness (IMT) Segmentation Review", Huazhong univ., Wuhan, Hubei, China, 2011
- 5.7 - SciencephotoLibrary. "Ultrasound scanning of neck blood vessels"[Online]. Available: <http://www.sciencephoto.com/media/271204/view>
- 5.8 - SciencephotoLibrary. "Ultrasound scan"[Online]. Available: <http://www.sciencephoto.com/media/271142/view>
- 5.9 – Perfuse (January; 2009). "Carotid endarterectomy"[Online]. Available: http://www.perfuse.net/cms/index.php?option=com_content&view=article&id=45:cea&catid=34:infoleaflets&Itemid=53
- 5.10 – Women Health advice. "Vascular screening"[Online]. Available: <http://www.womens-health-advice.com/stroke/vascular-screening.html>
- 5.11 – HeartHealthyWomen. "Carotid Ultrasound"[Online]. Available: <http://www.hearthealthywomen.org/tests-diagnosis/index-tests/carotid-ultrasound.html>
- 5.12 - SciencephotoLibrary. "Doctor using sonogram on patient"[Online]. Available: <http://www.sciencephoto.com/media/494638/view>

5.13 - SciencephotoLibrary. "Doppler ultrasound examination of leg"[Online]. Available: <http://www.sciencephoto.com/media/271239/view>

5.14 - A Benetos et al. "Pulsed Doppler: an evaluation of diameter, blood velocity and blood flow of the common carotid artery in patients with isolated unilateral stenosis of the internal carotid artery", *Stroke*, vol. 16, no. 6, pp. 969 – 972, 1985

5.15 – X. Girerd et al. "Noninvasive ultrasound methods for the measurement of arterial wall thickness", Dept. of Internal medicine, France

5.16 – J. Krejza et al. "Carotid Artery Diameter in Men and Women and the Relation to Body and Neck Size", *Stroke*, vol. 37, pp. 1103 – 1105, 2006

5.17 - A.Schmidt-Trucksass. "Intima-media thickness: integration of arterial assessment into clinical practice", presentation at the meeting of European society for cardiology, Stockholm, August 2010

5.18 - M.Mani, A.N.Kalashnikov, "*In vivo* verification of an intelligent system for accurate measurement of intima-media thicknesses", in *Advanced information systems and technologies (AIST-2013)*, Sumy, pp.124-127, 2013

5.19 – J. Wikstrand. "Methodological considerations of ultrasound measurement of carotid artery intima-media thickness and lumen diameter", Lab. For Cardiovascular Research, Sweden, November 2007

5.20 – Yahoo Education. "The common carotid artery"[Online]. Available: <http://education.yahoo.com/reference/gray/subjects/subject/143#i507>

5.21 – Connexions (2013; June). "Nerve Conduction - Electrocardiogram"[Online]. Available: <http://cnx.org/content/m42352/latest/?collection=col11406/latest>

5.22 - He Yin et al. "Measurement time as a limiting factor for the accurate acquisition of repeatable waveforms", in *Intelligent Data Acquisition and Advanced Computing System: Technology and Applications*, Berlin, Germany, 2013

6 –Conclusions and Future Work

6.1 Summery

During the course of this research project the main goal was to develop a system for accurate measurement of the IMT and lumen diameter in human at a particular instant of the cardiac cycle. This was achieved through a set of clearly defined objectives. Each chapter of this manuscript focuses on one of the objectives in order to provide detailed presentation of what was achieved and how each objective was tackled. The particular developments were combined and tested as a complete instrument to form the measurement system that the project aimed to develop.

The first step of the project was to identify available devices enabling clinical technicians to measure the IMT with sufficient accuracy for detecting and monitoring the progression of atherosclerosis. After detailed research, it was found that there have been many studies undertaken by the medical community that proved the importance of the IMT for diagnosis of atherosclerosis. Instruments developed for this purpose were found to be bulky, expensive and complicated to work with. Moreover, these devices had difficulty measuring the small changes in the IMT caused by disruption in the cardiac system, which would result in known heart diseases. The resolution of these devices was found to be insufficient for detecting small changes of the IMT, caused by atherosclerosis, which could be as small as 10 μm during a year. Therefore, a device was designed which is user friendly, easy to implement, safe to apply in hospitals, accurate for the purpose of IMT measurements, and also potentially inexpensive to manufacture compared to the currently available commercial devices on the market.

Beside the small changes in the IMT itself in a period of one year, another concern for this project was the complications added by the variable pressure inside arteries caused by the blood flow in human body. The diameter of an artery could vary up to 700 μm during one heart cycle as the blood gets pumped by the heart. To reduce the effect of this change on the measurement results, there was a need to monitor the cardiac cycle to be able to synchronise the ultrasound scans with the heart activity. This results in the changes in the

artery, caused by blood flow, to be reduced to a minimum if not eliminated completely. This means that possible differences in IMTs measured during two different sessions, some time apart from each other can be caused by possible thickening of the arterial wall, and indicate of potential cardiovascular issues. Having looked at a number of different methods to monitor heart activity, the Electrocardiogram (ECG) was found to be the most suitable signal to use since it was an electrical signal directly caused the heart itself. For this reason the ECG was considered the most accurate signal to monitor the cardiac cycle. Finally the relative ease of capturing the ECG signal was an additional reason why it was chosen as the most convenient option.

Although the ECG triggering is a good addition to the system, there have been a number of studies and also commercial ultrasound scanners that use ECG triggering for the purpose of ultrasonic scans. The main advantage of the system developed throughout this research project over other devices is the potential of achieving higher spatial resolution with a higher sampling rate and reduction in noise by employing methods such as averaging and interleaving. Combining the ECG triggering with the higher resolution ultrasound scans will result in more accurate IMT measurements which can potentially be useful to the medical professionals to carry out examinations at a relatively lower cost.

6.2 – Knowledge contributions

6.2.1 – Development of the ECG Monitor

The first phase of development, therefore, was to design and develop the circuitry to capture and monitor the ECG signal from the patient in a comfortable and safe manner. Three schematics for ECG monitors were combined on the same PCB and tested. The results of these tests allowed selecting the schematic that enabled the most accurate and least noisy operation. The final board was put through a series of vigorous experiments to verify correct functioning and reliability of the board; which were both proven to be of the required standard. Any safety concerns were overcome by isolating the patient from any potential high voltage source. This was achieved by powering the ECG monitor from an on-board battery instead of connecting it to a mains powered supply. The ECG

monitor developed for this project was thoroughly tested, and it met its objective by capturing the heart activity of the patient safely and reliably. Comparing the results obtained by the developed circuitry to the ECG taken in the hospital showed that the developed design suffered more from the noise. This was because of the extensive filtering on the hospital monitors and also the quality of the electrodes used in ECG monitors for the purpose of the diagnosis. However, the waveforms taken by the developed system, using re-usable electrodes made in the laboratory was sufficiently clean for the purpose of triggering the ultrasonic pulses. These waveforms are not, currently, used for diagnosis or status monitoring of the patient; therefore the level of noise present was not problematic.

6.2.2 - Development of the ECG processor and triggering procedure

The ECG captured from the patient had to be processed in order to trigger ultrasonic scans at a required instant of the heart cycle. Because of the isolation of the ECG monitor itself from any direct or indirect connection to the mains powered equipment, the analysis must be done on a separate board to enable the required connection to the ultrasonic scanner. The Second phase of the electronic development was to produce a board that could receive the ECG signal from the ECG monitor, process the waveform to detect the R-wave of the ECG signal, and trigger the ultrasonic scan at the desired point of the cardiac cycle. For this purpose it was necessary to establish reliable communication between the ECG monitor and the second board, the ECG processor. Several conventional technologies for wireless communication were compared to each other. Considering a number of cases where radio frequency enabled devices in the hospitals interfered with other medical instruments (such as, and most importantly, pace makers used by patients), it was decided that the best option for communication between the two boards was the infra-red technology. It is inexpensive, easy to implement and work with, and safe for use within any medical environment. The IR capabilities of each board were enabled and tested separately using a third board that was connected to a computer running MATLAB test scripts. Then the two boards were paired and the ECG monitor continually streamed the ECG data to the ECG processor. The high level of electrical noise caused by IR chips inside the ECG monitor dictated that it was necessary to develop a robust and accurate algorithm for the ECG processor,

which would analyse the ECG received from the patient and also be capable of adaptation, if the waveform changes during the examination. Some algorithms for heart beat detection were developed in the past, and could potentially be used for the ECG processor. However these algorithms, despite being very accurate, were overly complicated for implementation on a PIC microcontroller with limited memory. For this reason, an algorithm for R-wave detection was developed that was easy to use in real time.

The algorithm was initially developed using MATLAB to ensure that it was capable of reacting properly to possible changes during each examination. Only then it was implemented on a microcontroller inside the ECG processor. The ECG processor firmware showed high accuracy in detecting the R-wave of the ECG waveforms, and continued to function normally even if the infra-red communication restarted, or the ECG base line drifted significantly.

6.2.3 – Phantom Experiments

In the next phase, to study the behaviour of ultrasonic waves on curved surfaces, phantom experiments were carried out. They were performed by submerging plastic tubes under water, which resembled an artery wall surrounded by softer tissue and filled with blood in a human body. Tubes with different diameters and thicknesses were tested during this phase and the recorded waveforms were analysed and compared to each other. It was found that the placement of the transducer with respect to the centre point of the tube played a much more important role than it was anticipated. When the transducer's axis intersected the axis of the tube, reflections from the tube were the cleanest and easiest to interpret. Even small deviations from this optimal position resulted in very convoluted waveforms, which no longer exhibited a clear correlation to the diameter and thickness of the tube.

One of the unexpected outcomes in phantom measurements was the presence of an extra pulse about half way between the reflections from the near and distal walls. This pulse possessed with high amplitude could easily be mistaken for a reflection from some inner interface of the phantom that was non-existing. This pulse can only be explained by considering the wave guiding effect. When the ultrasound beam hits the test tube, some of the energy goes through the material and some is reflected back to the transducer at each

boundary surface of the tube (e.g. water-tube or tube-water). There is also some energy that travels through the tube wall itself. These waves will travel all the way through the material and also produce some reflections back to the transducer, which could either be taken as a separate reflection or sometimes are merged with other reflections, which would make the analysis of the waveforms more challenging.

Results obtained from the phantom experiments emphasized the importance of the correct transducer placement onto the artery during in vivo experiments, and helped in developing the experimental protocol for in vivo tests that ensured that the best possible waveforms were recorded.

6.2.4 – Concluding Remarks

The final stage of the present research was to combine all the previous sections together to perform in vivo examinations. In order to ensure the results of in vivo experiments were of good quality, an experimental protocol was followed for each experiment. This step by step guide was to make sure that every part of the system functioned as expected before taking any records. The ECG monitor was connected to the patient and the output was monitored using an oscilloscope. IR communication was established between the boards and was confirmed by the trigger signals from the ECG processor, which were also monitored by an oscilloscope. A linear array transducer was placed on the neck of the patient where the ECA was expected to be. Different elements of the transducer were connected to the scanner, while the echo waveform was monitored on the oscilloscope to find the transducer's element with the best position with regard to the tested artery. Following this procedure during six in vivo experimental sessions, a total of 120 records were taken with various delays to the ECG processor-wave. These delays corresponded to different instants of the cardiac cycle, which meant that the measured IMTs would be different for different delays because of variations in the blood flow in the artery. The presence of noise, possible misalignment of transducer elements, and changes to the pressure applied on the transducer, made the analysis of most of the records very difficult. The best data set recorded during these experiments showed good accuracy for lumen diameter measurement. However, the intima-

media interface was detected with enough confidence in one record only; and, while this measurement did agree with the expected size of the IMT, it still cannot be considered as a reliable IMT measurement due to insufficient dataset.

The results from the in vivo experiments showed the lumen diameter could be confidently measured using the developed system. However, because of the presence of electronic noise and various complications during the experiments (such as transducer placement, element selection inside the array transducer and the applied pressure on the skin), IMT measurements were not as good as it was expected. Thorough examination of the waveforms, recorded during one of the experimental sessions, led to some estimates of the IMT of the ECA. However verification of these results required additional experiments in a tightly controlled environment.

Finally, experimental results confirmed that the measurement system developed during the course of this research study was capable of taking high resolution and high speed ultrasonic scans at an arbitrary instant of the heart cycle. Further improving the system will allow it to be used for monitoring lumen diameters, and/or intima-media thicknesses to help detect and monitor progression of atherosclerosis. Although the ECG triggering has been done in other studies and is available in commercial devices to improve the ultrasound scans, the addition of this feature to the developed system in the laboratory has some positive impacts. However, the main advantages of the ultrasound scanner of this research project are the high resolution high speed scans capability and the ability to perform on the fly averaging and interleaving to reduce the effect of noise to have clearer recordings.

6.3 – Future Work

The operation of the developed instrument can be further improved by additional developments and procedures that are listed below.

The analysis of the ECG can be transferred to the ECG monitor; which means that the R-wave is detected on the transmitting board. This means only a single pulse for a complete heart cycle is sent to the ECG processor. This will

further reduce the noise induced by the IR transmit circuit on the raw ECG signal, and reduce the ECG monitor power consumption significantly.

At present the desired delay after the R-wave is set by a potentiometer on board the ECG processor. It is difficult to set the same resistance every time, and this was avoided by using the five set delays only, indicated by the on board LED. A better option is to use the USB capabilities of the microcontroller on board the ECG processor, and set this delay from a graphic user interface on a computer.

Another factor that added uncertainty to the results recorded during in vivo experiments was the placement of the transducer. Since the transducer element used was very small, slightest movement of the transducer on the neck would cause a large difference to the scans. Additionally the pressure applied to the transducer on the neck affects the amplitude of the reflected signals, which could result in false reading or missing peaks. For the above reasons, it is better to have a mechanical system that can affix the transducer to the same place on the neck and hold the transducer during one examination at a constant pressure.

Finally, an electronic switch can be developed for connecting a single transducer's element out of the elements available to the scanner in a cyclical manner. The user will observe the echoes on the oscilloscope, and press a button when the waveform shows the lumen clearly, triggering the measurements using the presently connected transducer's element. This addition will be especially important for taking the instrument to the next step that involves broader range of subjects.

In addition to the electronic improvements suggested above, the research itself can be extended into studying scattering of ultrasound waves on tubular objects. Such a study will help in the analysis of the recorded reflections coming back from the near and far wall of the artery.

One other area that could add to the uncertainty of the results obtained during this research was the effects of different layers in the human body located between the skin and the arterial walls. The assumption that the ultrasound velocity in a human body is similar to water may have had an effect on the expected timings of the reflections coming back from the artery walls.

Closer look at different impedances and propagation times affecting the ultrasound waves on their way from the skin to the artery may help in the analysis of the recorded waveforms.

Future research would also need to expand the experimental results to more patients; preferably ones who have been tested using an approved medical instrument by skilled practitioners. Having more experimental results comparable to ones produced by established systems will determine the applicability of the developed instrument; and identify areas for additional research and development.

Appendix 1 - First ECG board

The schematic of the boards has been done in EAGLE which will produce the PCB layout to be sent to the manufacturer for production. Features in Eagle make the design process very simple as the schematic is turned into the PCB by the software; with the flexibility of placing the components on the board enabling the user to conveniently set the size of the board and place the components in the order that makes the board user friendly. A Detailed description of the schematic helps to understand the operation of the board.

Sheet 1

Sheet1 contains most of the components of the ECG monitor.

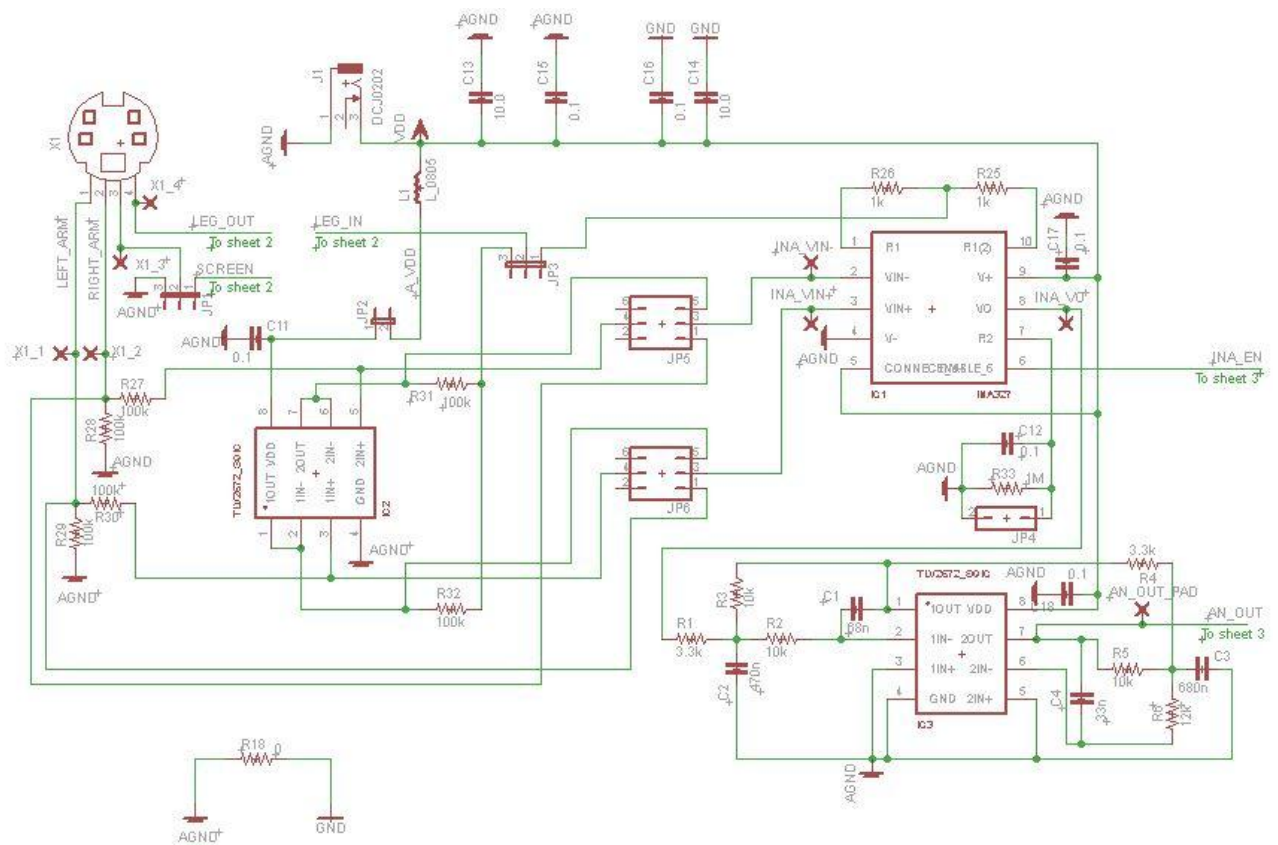


Figure 1 - ECG Monitor Schematic – Analogue section

The connector socket, unit X1, is a four way mini-din connector. The pins of the plug of this connector are connected to wires to the electrodes placed on the body of the patient, namely on the left arm, right arm, left leg and right leg. The left leg pin is connected to the ground. The other three pins are connected to different jumpers to direct the signal to different circuits.

IC1 is the main operational amplifier of the ECG monitor, INA327. The inputs of the INA327, i.e. Vin- and Vin+, are connected to the jumpers JP5 and JP6. Based on various designs, the connections of these jumpers are changed as explained later. The “enable” pin of the INA327 goes to sheet3 where it is connected to an output pin of the PIC microcontroller. The enable pin is used to switch the INA327 on or off. Pin number nine of the INA (V+) is connected to the positive pin of the power supply. There is a 0.1 μF capacitor between this pin and the ground which acts as a decoupling capacitor. Similarly other capacitors are used for decoupling at the V+ pin of all ICs in the design.

As can be seen from figure 1, pin7 of the INA is connected to ground in the case of the right leg drive (JP4 closed). If the direct connection circuit is being used, JP4 is open and pin7 is connected to the R12C33 filter.

The output of the INA goes to the low-pass filter shown in figure 1. It is implemented using IC3 and related components. The output of the right hand side op-amp in IC3 which is the final output of the low-pass filter goes to sheet3 where it is connected to one of the ADC inputs of the PIC microcontroller.

IC2 belongs to the low power circuit. It combines two operational amplifiers that the right arm (RA) and left arm (LA) are connected to. The outputs of these two operational amplifiers are connected to the INA inputs as well as they are combined and fed to the input of the left leg (LL) amplifier. The left leg amplifier is shown in the sheet2 and is discussed later.

JP3 is the jumper that determines where the right leg is connected to. It is connected either to the output of the left leg op-amp or to the middle point of the resistors R25R26 connecting pin1 and pin10 of the INA for the right leg drive design.

Each TLV2672 in this board has a jumper which can disconnect the IC from the power supply.

Sheet2

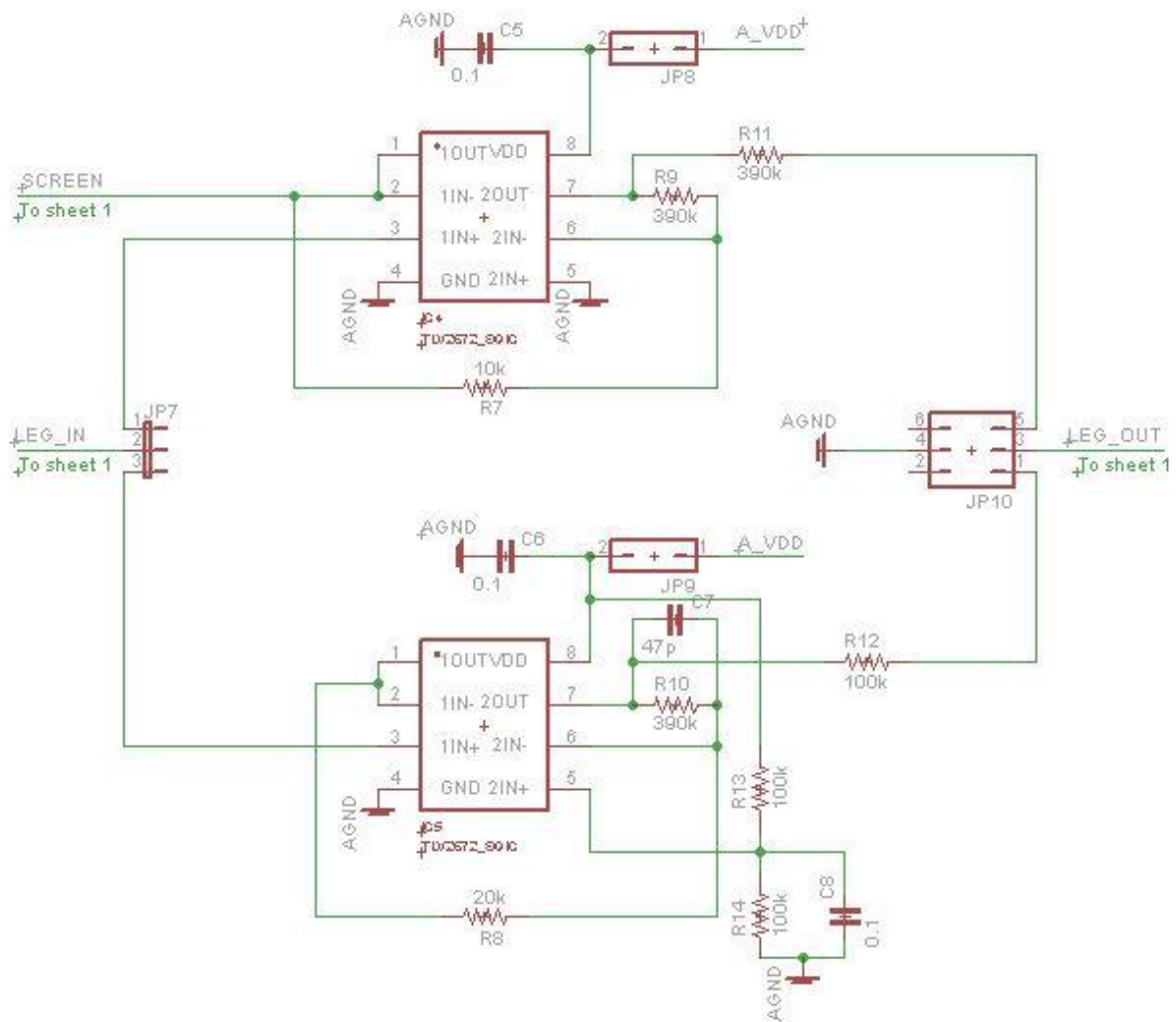


Figure 2 - ECG Monitor Digital Section

Here two TLV2672 components are used to generate the reference signal supplied to the right leg of the patient.

The electrode placed on the right leg of the patient is connected to the jumper JP10. By altering this jumper, the signal to the right leg either goes from the IC4 which is the case for the "right leg drive" circuit or from the IC5 which is the combination of the op-amps for the "low power" circuit design. Additionally the right leg electrode can be grounded.

Non-inverting inputs of each opamps are connected to the jumper JP7 which allows selecting the required opamp. Jumpers JP8 and JP9 are used to power on and off IC4 and IC5 respectively as needed.

Sheet3

Sheet3 contains all the digital components that handle the conversion of analogue signals to digital data and transmission of the data using the IR link.

IC6 is the PIC18F1330 microcontroller that controls the ECG monitor. This component receives the analogue signal from the INA and directs the digital bitstream to IC7, the MCP2122 IR controller. This component supplies the data to the TFDU4300 IR transmitter which transmits the data to the receiver.

IC8 (ADR5040) provides a stable reference voltage of 2.048 V required by the ADC of the PIC microcontroller to set the upper operating range limit. As the 8 most significant bits of the ADC output are transmitted to the ECG processor, the resolution of the code is $2.048\text{V}/256 = 8\text{ mV}$ per bit.

Switch S1 is used to reset the PIC. Jumper JP12 represents a three colour LED which was used for debugging and indicating the state of the operation (i.e. off, idle and processing). Q1 is the crystal that determines the clock speed of the microcontroller (4.9152 MHz).

JP11 is the socket to connect the in circuit debugger/programmer PICKit2. The debugger will be inserted into this component when the microcontroller is to be re-programmed or debugged to find any malfunction in the firmware.

By using EAGLE software, the board was laid out. The analogue and digital parts of the design were provided with separate GND planes in order to reduce the interference from the digital circuitry to the analogue section. Another consideration that needed to be taken into account was the placement of different components. For instance it was required to make sure the IR transmitter was located in a convenient place on the board so that its face was not blocked by other components. Figure 4 presents the layout of the first PCB board that was sent to the manufacturer; and figure 5 shows the first PCB assembled.

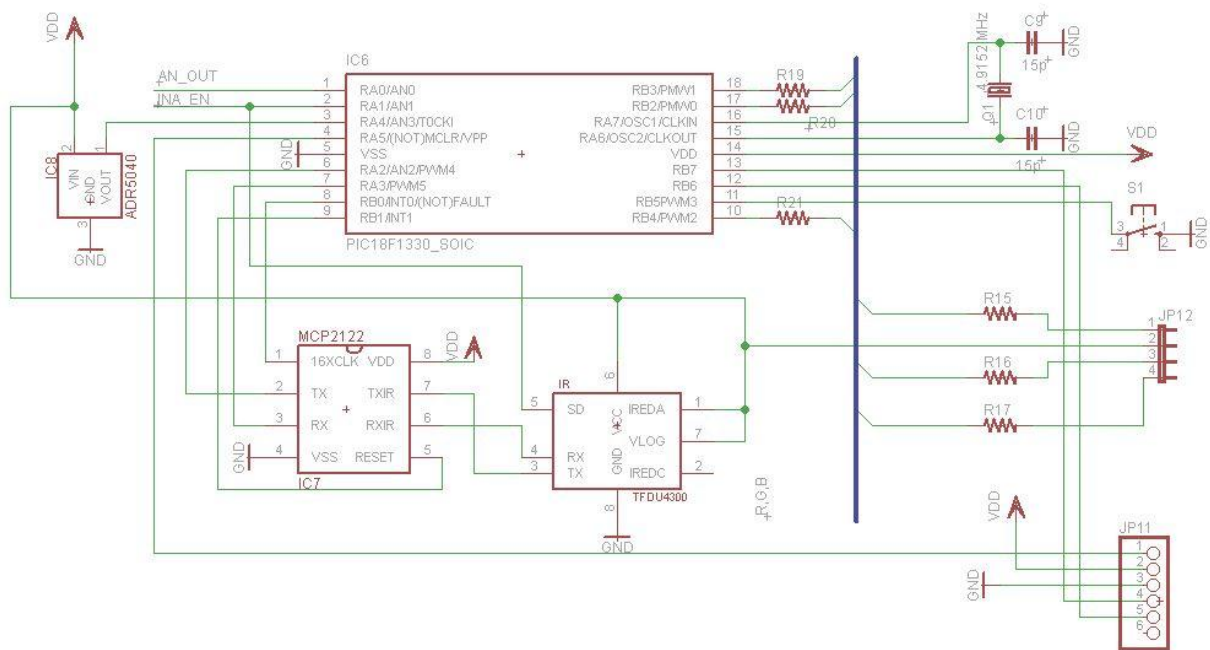


Figure 3 - ECG Monitor - Microprocessor

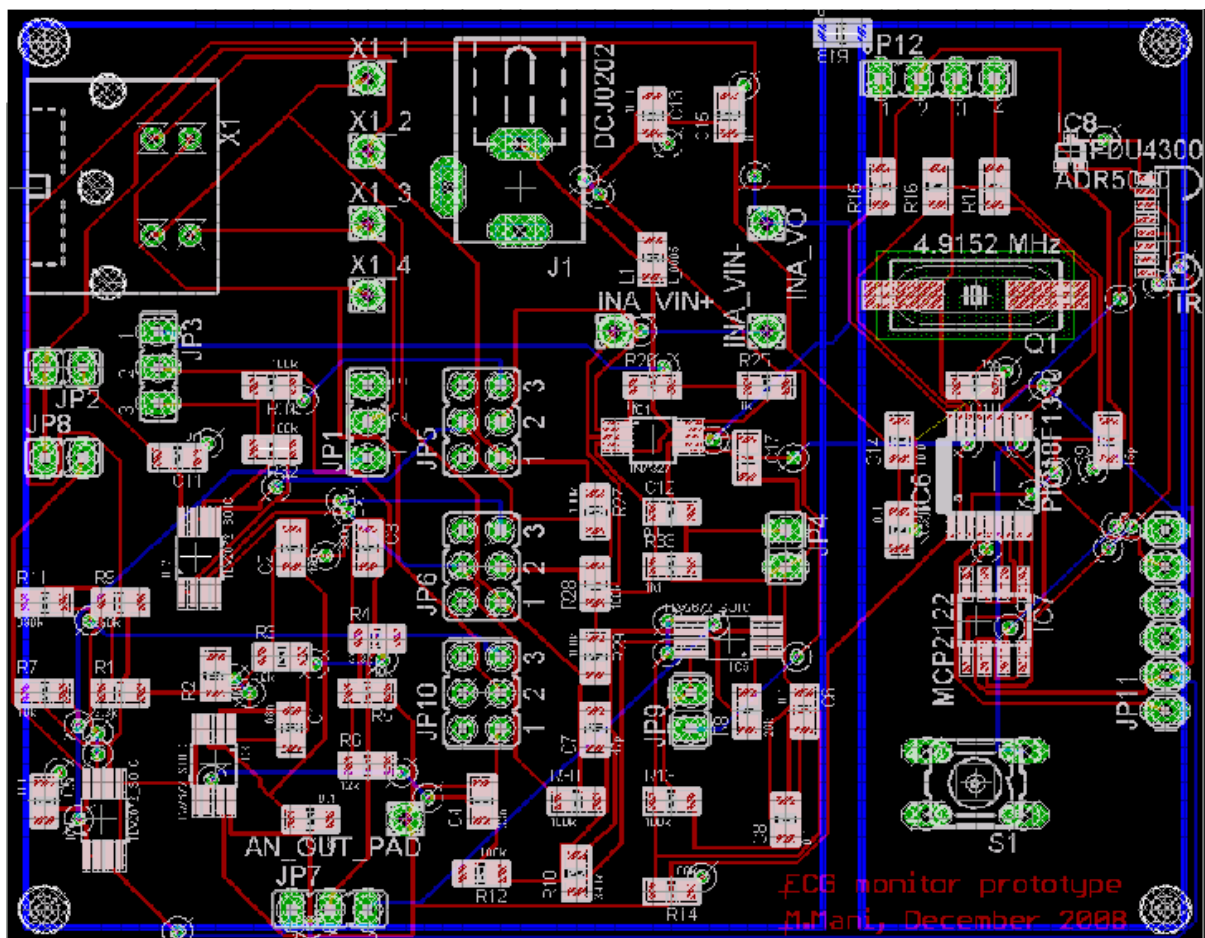


Figure 4 - ECG Monitor - PCB design

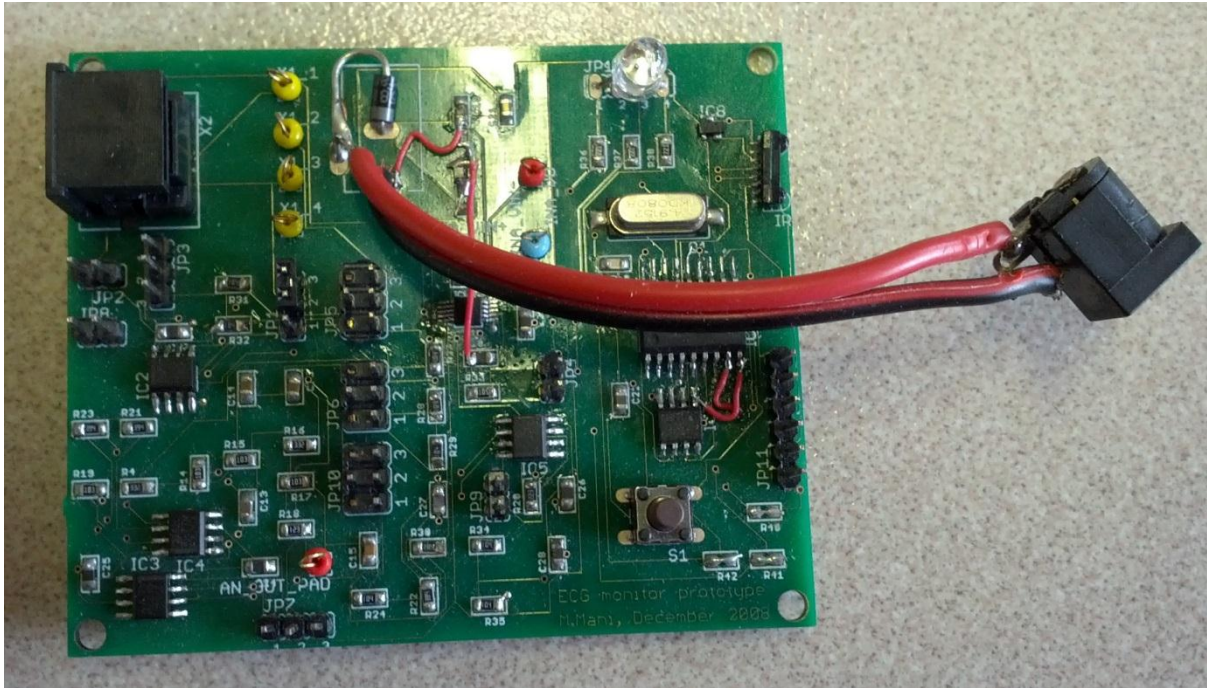


Figure 5 - First ECG Monitor prototype

Appendix 2 – Second ECG board

When the first prototype was manufactured and tested, there were a number of issues with the board that affected the operation of the ECG monitor. To fix these problems, it was necessary to remove some of the components; break some of the connections and re-solder the correct connections instead. Two main corrections to the first prototype were required: connect isolated part of the digital ground plane and correct wrong connections between the PIC and MCP2122.

The first issue was rectified by connecting the missing ground connections to the ground plane by separate wires. It required removing the solder mask from some parts of the bottom side of the board and placing wires from these pads to the ground.

The second problem required removing the connection from the clock pin of the MCP2122 to the PIC and making a new connection to the adjacent pin. The reason for this correction was that only PWM0 function of the PIC could be turned on to be used independently from the rest of the board.

The combination of the two major corrections done on the board increased the possibility of its unexpected failure. Moreover, the act of de-soldering and re-soldering required heat to be applied to the board that could damage some components. As a result, it was decided to re-design the board and manufacture the second PCB. The second PCB is shown assembled in figure 7. It was still powered from an external power supply.



Figure 6 - Second ECG Boar

The schematic of the second prototype is very similar to the previous version of the ECG monitor; therefore discussing it again is unnecessary. However, the second prototype PCB was laid out to be even more compact in size which made it easier to carry and operate; the addition of power pins allowed an external 5V power supply to operate the board instead of only using PICKIT2 and MPLAB software as before.

The second prototype PCB, presented in figure 7, was tested when received from the manufacturer and a manufacturing problem was immediately found. The placement of the reset button on the board caused discontinuity in the ground connection again and more corrections were required.

Appendix 3 – ECG Processor schematic

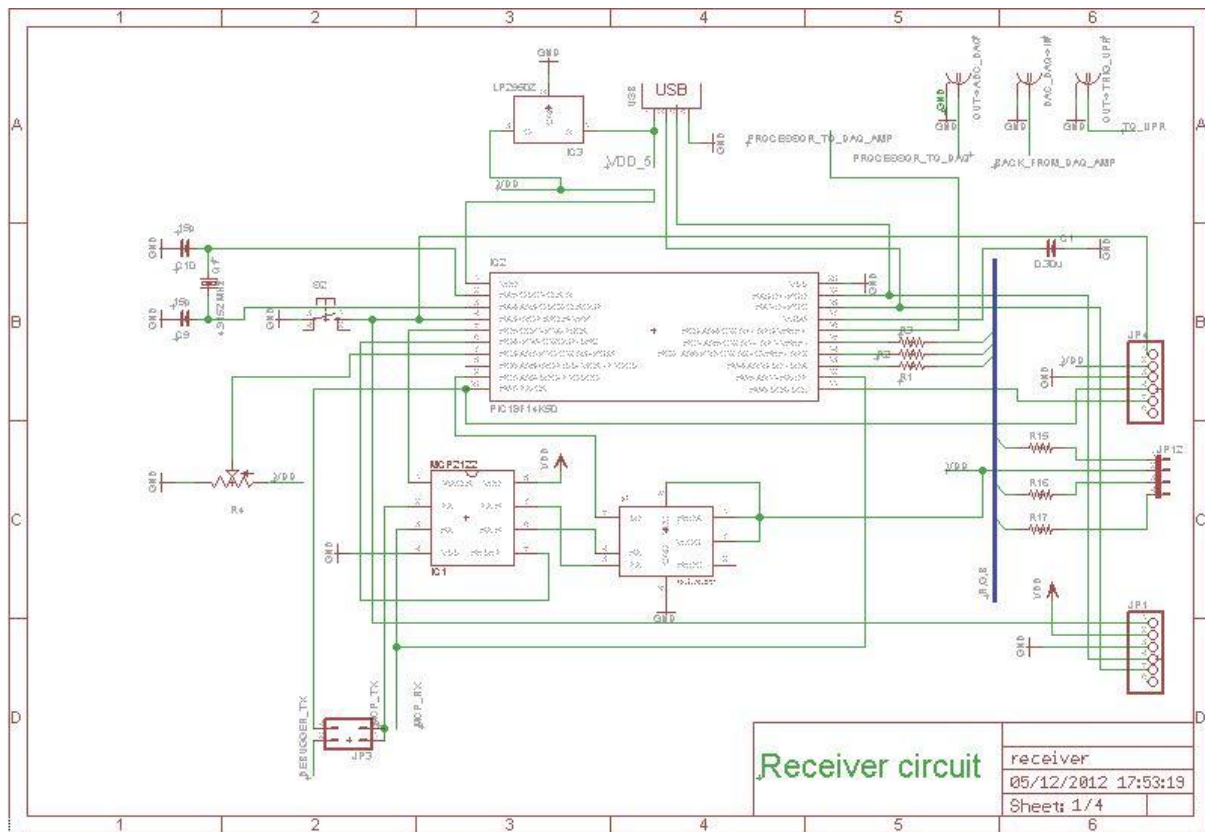


Figure 7 - ECG Processor

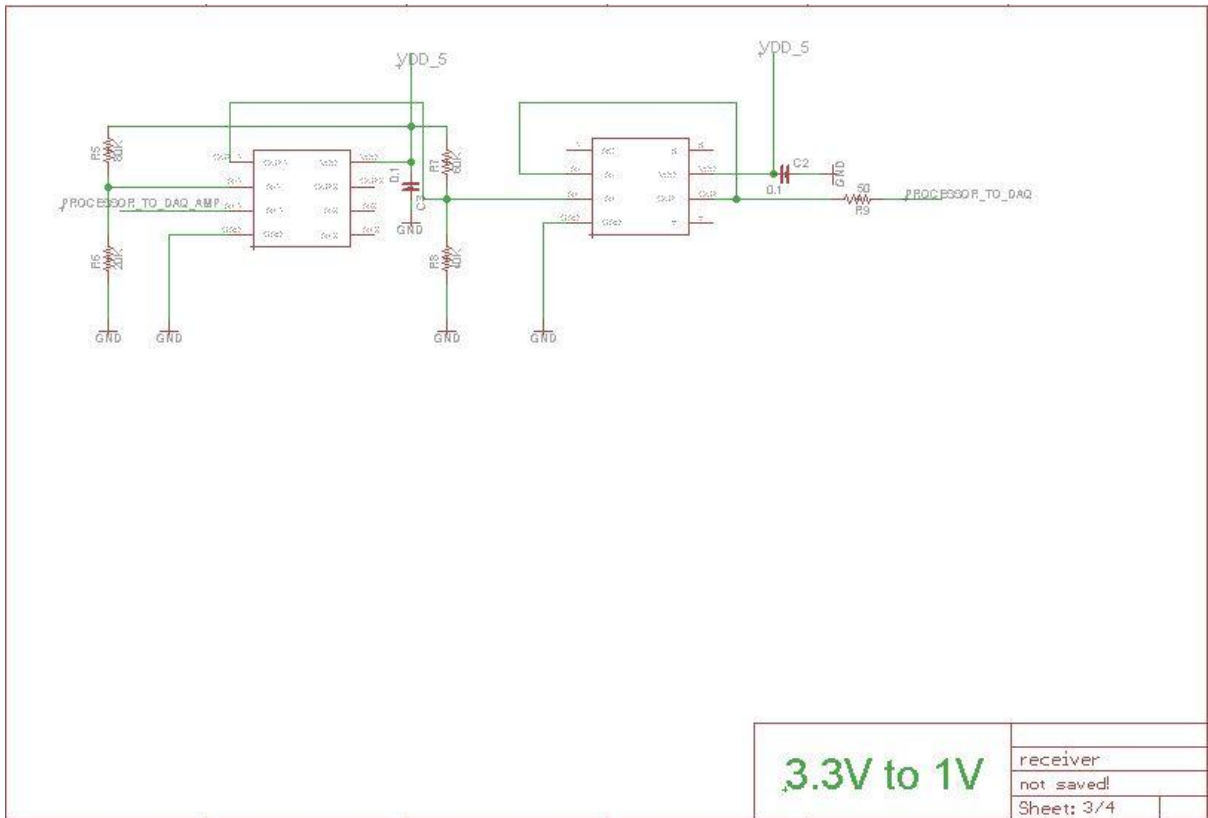


Figure 8 - ECG Processor

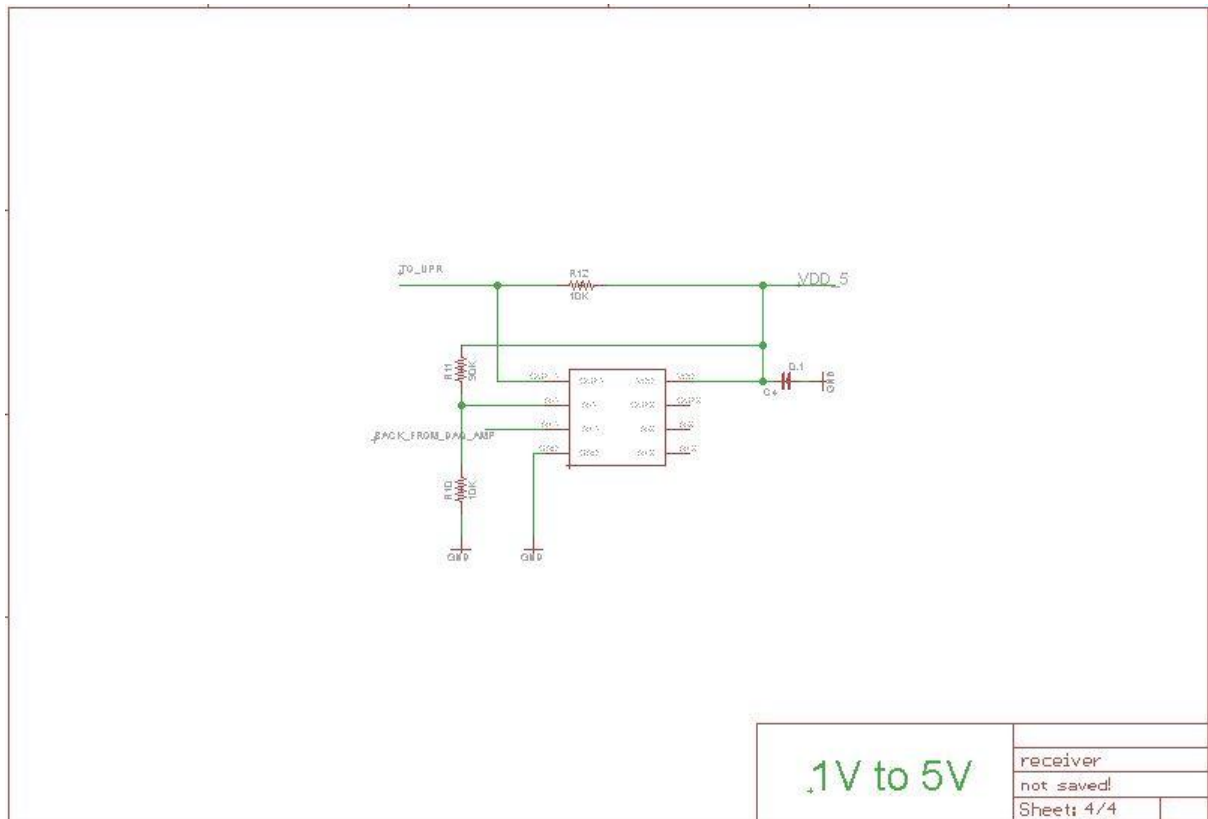


Figure 9 - ECG Processor

Appendix 4 – MATLAB code for simulating R-wave detection

```
s1=serial('COM3');
s1.BaudRate = 9600;
s1.InputBufferSize = 6;
fopen(s1);

fprintf(s1,'a');
out = fread(s1,1,'uint8');
fclose(s1);
ECGfreq=612;
[tmp1,ipeaks] = ecgsyn (ECGfreq, 10, 0, 60, 1, 0.5, ECGfreq*5);
% [s, ipeaks] = ecgsyn(sfecg,N,Anoise,hrmean,hrstd,lfhfratio,sfint,ti,ai,bi)
ECG1=tmp1(5900:6500);
ECG_Max = max(ECG1);
ECG_Min = min(ECG1);
ECG1=floor((ECG1-ECG_Min)/(ECG_Max-ECG_Min)*255);
```

Appendix 5 - Delay calculation and Potentiometer code

```
if( ! ( LongCounter & 0x000000FF ) )
{
    LATCbits.LATC0 = 0;
}
else
{
    LATCbits.LATC0 = 1;
}
```

```
DelayInterval = (MaxDelay - MinDelay) / 4;
```

```
if( Pot < 40)
    DelayFactor = 0;
else if( (Pot>= 40) && (Pot<90) )
    DelayFactor = 1;
else if( (Pot>= 90) && (Pot<150) )
    DelayFactor = 2;
else if( (Pot>= 150) && (Pot<200) )
    DelayFactor = 3;
else if( (Pot>= 200) && (Pot<255) )
    DelayFactor = 4;
```

DelayFactor will be multiplied by the DelayInterval and added to the minimum delay:

```
InitialDelay = MinDelay + (DelayFactor * DelayInterval);
```

The actual value of the delay is dependent on the number of samples recorded after the detection of samples above the threshold (size of the window), InitialDelay and the position of the detected R-wave in the window:

```
Delay = InitialDelay - WinSize + IndMax;
```

This would create a delay based on the number of samples received, which enables the code to start the delay from the instant when the R-wave occurred.

The LED on the board was used to indicate the amount of set delay (figures 3.41, 3.42). Colour of LED changed depending on the position of the potentiometer's dial:

```
switch(DelayFactor)
{
    case 0: Green_on();
           break;
    case 1: Red_on();
           break;
    case 2: Blue_on();
           break;
    case 3: Blue_on();
           Red_on();
           break;
    case 4: Green_on();
           Blue_on();
           break;
}
```